LOUIS DUFRESNE

A SPECTRAL/B-SPLINE METHOD FOR THE NAVIER-STOKES EQUATIONS IN UNBOUNDED CYLINDRICAL DOMAINS

Thèse
présentée
à la Faculté des études supérieures
de l'Université Laval
pour l'obtention
du grade de Philosophiæ Doctor (Ph.D.)

Département de génie mécanique
FACULTÉ DES SCIENCES ET DE GÉNIE
UNIVERSITÉ LAVAL
QUÉBEC

SEPTEMBRE 2001

À mes parents : Jacques Dufresne et Lucile La Rue

Résumé court

Dans cette thèse, on présente une nouvelle méthode numérique pour la solution des équations de Navier-Stokes incompressibles et instationnaires dans des domaines cylindriques non confinés. La discrétisation spatiale est constituée d'expansions vectorielles à divergence nulle, suivant l'approche proposée par Leonard. Des séries de Fourier sont utilisées dans les directions longitudinale et azimutale alors que des polynômes par morceaux de type "B-splines" sont utilisés dans la direction radiale. Le caractère local des B-splines permet en plus d'inclure une variation radiale de la troncation azimutale. Des conditions de régularité complète au centre du domaine ainsi que les taux de décroissance asymptotiques à l'infini sont pris en compte. L'intégration temporelle des sous-systèmes d'équations résultant de la formulation de Galerkine utilisée est effectuée avec un schéma mixte explicite/implicite du quasi troisième ordre. Les comparaisons faites avec d'autres méthodes purement globales, dans le calcul de stabilité hydrodynamique de certains écoulements tourbillonnaires avec symétrie axiale, ont permis de conclure que la méthode proposée ici représente une alternative avantageuse.

Prof. Guy Dumas
Directeur de thèse

Louis Dufresne
Candidat

Résumé long

Dans cette thèse, on présente une nouvelle méthode numérique pour la solution des équations de Navier-Stokes incompressibles et instationnaires dans des domaines cylindriques non confinés. Cette méthode apparaît comme une nouvelle application de la formulation des expansions vectorielles à divergence nulle proposée par Leonard et possède donc les caractéristiques suivantes : i) représentation exacte de l'équation de continuité ; ii) élimination complète de la variable de pression ; iii) intégration temporelle implicite du terme de diffusion sans coûts additionnels ; et iv) réduction du nombre d'inconnus (vitesse) de trois à deux. Une autre caractéristique importante de la méthode, qui de fait lui confère une bonne part de son originalité, est l'inclusion de polynômes par morceaux de type "B-spline" dans la direction radiale semi-infinie.

Plus particulièrement, la discrétisation spatiale est constituée d'une combinaison de séries de Fourier dans les directions longitudinale (périodicité physique des écoulements avec évolution temporelle) et azimutale (périodicité géométrique), et de B-splines projetés sur un domaine radial unitaire. La fonction de projection choisie permet une représentation exacte, jusqu'à un certain ordre, des comportements asymptotiques à l'infini. En plus de ces comportements asymptotiques, des conditions de régularité complète sont imposées au centre du domaine ($r = 0$). Grâce au caractère mixte spectral/B-spline des expansions vectorielles, un compromis intéressant est obtenu entre le découplage provenant de l'orthogonalité des séries de Fourier et la flexibilité de positionnement de résolution propre aux méthodes locales. De même, le caractère local des B-splines permet aussi d'inclure une variation radiale de la troncation azimutale. La base vectorielle ainsi construite est ensuite utilisée dans une méthode de résidus pondérés de type Galerkine, d'où on obtient une réduction du problème complet 3-D en un ensemble de sous-problèmes radiaux 1-D.

L'intégration temporelle de ces sous-systèmes d'équations est quant à elle effectuée avec le schéma mixte explicite/implicite du quasi troisième ordre proposé par Spalart *et al.* (*J. Comp. Phys.*, **96**, 297, 1991). La formulation de Galerkine est aussi utilisée pour l'obtention d'un programme de calcul de valeurs propres pour les problèmes de stabilité linéaire. Une version pour domaines confinés par une paroi cylindrique a de plus été développée. Das ce cas, la version confinée de la présente méthode devient équivalente à celle proposée par Loulou *et al.* (NASA TM-110436, 1997).

La validation des différents programmes de calcul (Navier-Stokes et valeurs propres) a été effectuée en comparant des résultats obtenus par la présente méthode avec des valeurs de référence. Les problèmes considérés pour faire ces comparaisons sont liés à la stabilité d'un modèle de tourbillon de sillage ainsi qu'à la stabilité et à l'évolution non linéaire d'un tourbillon triangulaire. Les résultats obtenus ont permis de conclure, d'une part, que le gain réalisé entre la méthode B-spline non confinée et celle confinée n'est que marginal. D'autre part, les comparaisons faites avec les autres méthodes purement globales ont permis de conclure que la méthode proposée ici représente une alternative avantageuse aux méthodes globales comparées, particulièrement pour le calcul d'écoulements avec symétrie axiale.

Prof. GUY DUMAS
Directeur de thèse

LOUIS DUFRESNE
Candidat

Abstract

In this thesis, a new numerical method to solve the incompressible, unsteady Navier-Stokes equations in unbounded cylindrical domains is presented. The method comes as a novel application of Leonard's divergence-free vector expansions approach, and therefore possesses the following characteristics: i) exact treatment of the continuity constraint; ii) complete elimination of the pressure variable; iii) implicit time integration of the diffusive term at no extra cost; and iv) reduction of the number of (velocity) unknowns from three to two. Another important feature of the method, that indeed represents the originality of the present formulation, is the introduction of mapped B-spline piecewise polynomials for the discretization of the semi-infinite radial direction.

More specifically, the spatial discretization is constructed from a combination of Fourier series, for both the longitudinal (physical periodicity of temporal evolving flows) and azimuthal (geometrical periodicity) directions, and of B-splines on a mapped unitary radial domain. The particular choice of mapping function allows for an exact representation of algebraically decaying functions, up to some finite order. Besides the imposition of proper decaying conditions in the far field, complete (finite order) regularity conditions are also imposed at the center point $r = 0$. These mixed spectral/B-spline expansions, used to form the divergence-free vector basis functions, yield an efficient compromise between the high uncoupling associated with the orthogonality of Fourier series and the resolution positioning flexibility that is characteristic of local methods. The local character of the B-splines furthermore allows for a radial variation of the azimuthal truncation. The resulting vector basis functions are applied to in Galerkin type weighted residual formulation that transforms the complete 3-D problem into a set of small 1-D radial ODE's that are marched in time. For

that latter task, the quasi-third order, mixed explicit/implicit scheme proposed by Spalart et al. (*J. Comp. Phys.*, **96**, 297, 1991) is used. The Galerkin formulation also serves for the development of an eigenvalue solver for linear stability problems. Finally, a wall-bounded version of this method, equivalent to the one presented by Loulou et al. (NASA TM-110436, 1997), is also produced in this work.

The validation of the different Navier-Stokes and eigenvalue solvers is achieved by comparing linear stability results, and nonlinear dynamics predictions with other benchmark data. The particular flow problems considered are related to the stability of a trailing line vortex, and the stability and nonlinear dynamical evolution of a special class of zero circulation vortex that leads to the formation of a triangular vortex. On one hand, comparisons made between the unbounded B-spline formulation and the wall-bounded version of the method have shown only a marginal advantage of the former method over the latter. On the other hand, comparisons made with the data obtained by purely global expansions approximation methods prove the present spectral/B-spline method to be an advantageous alternative to these global methods for the computation of unbounded flow problems having an intrinsic axial symmetry.

Prof. GUY DUMAS
Thesis Advisor

LOUIS DUFRESNE
Candidate

Avant-Propos

J'aimerais en premier lieu exprimer ma plus profonde grattitude à mon directeur de thèse, le professeur Guy Dumas. Sa grande disponibilité, ses continuels encouragements, son intérêt marqué pour ce projet de recherche ainsi que sa confiance dans ma capacité à le mener à terme ont été pour moi une indispensable source d'inspiration et de motivation. Il va sans dire que ces quelques lignes ne peuvent évidemment rendre justice à l'expression complète de mon appréciation mais j'espère néanmoins qu'elles puissent témoigner combien il m'a été agréable et profitable, autant sur le plan professionel que personnel, de travailler sous la supervision du Prof. Dumas.

Ce travail a été rendu en partie possible grâce au soutien financier du Conseil de recherche en sciences naturelles et génie (CRSNG) du Canada, via ses programmes de bourses et de subventions de recherche. De même, ont aussi contribué financièrement le Fonds pour la formation des chercheurs et l'avancement de la recherche (FCAR) du Québec, par le biais de son programme de bourses, et l'Université Laval, par le biais de son fonds de soutien au doctorat. L'appui financier de tous ces différents organismes a été grandement apprécié.

Je désire remercier les membres du jury de thèse, les professeurs Yvan Maciel, Roger Pierre et Grégoire Winckelmans. Leurs observations et commentaires en regard à ce travail de recherche ont été reçus avec beaucoup d'intérêt. En effet, la diversité de champ d'expertise des membres du jury m'a permis de bénificier de différents points de vue complémentaires fort appréciés, et ce d'autant plus que l'ensemble du processus d'évaluation s'est déroulé sur une échelle de temps relativement courte. Un merci additionnel au Prof. Maciel qui a bien voulu aussi se charger de la prélecture de la thèse.

La courtoisie et le dévouement du personnel administratif et du service informatique ont indéniablement rendu plus facile et agréable mon séjour au Département de génie mécanique. Par ces quelque lignes, j'aimerais leur témoigner mon appréciation.

J'aimerais aussi profiter de cette occasion pour saluer les nombreux collègues et amis que j'ai eu le plaisir de côtoyer au cours des dernières années. Je mentionne ici en particulier Sébastien Houde et Raphaël Brochu qui ont travaillé avec et testé une partie des codes développés dans cette thèse. Dans un contexte plus large et moins technique, j'aimerais de même souligner l'esprit d'équipe et de collaboration encouragé non seulement par le Prof. Guy Dumas mais aussi par ses collègues, les Profs. Jean Lemay et Yvan Maciel, qui m'a permis de travailler dans une atmosphère de convivialité favorisant les échanges avec l'ensemble des membres du "groupe de mécanique des fluides". À toutes ces personnes, je dis merci et leur souhaite bonne chance et bon succès.

En dernier lieu, j'aimerais plus personnellement remercier mon collègue et ami, Martin Deslauriers, pour son appui, ses encouragements et surtout pour son amitié. À ma grande amie Martine Foisy, je dis aussi merci non seulement pour son appui "logistique", son support moral, ses discussions stimulantes, qui m'ont tous été pronfondément utiles et bénifiques, mais d'abord et avant tout pour sa présence chaleureuse et son amitié sincère. À ma famille, plus particulièrement à mes parents à qui ce travail est dédié, je dis aussi merci pour tout. Finalement, et non en moindre lieu, je remercie mon épouse Patrizia pour son amour et sa patience.

Table of Contents

List of Figures

List of Tables

Chapter 1

Introduction

Over the last few decades, with the tremendous increase in computing capability and the many developments to which it was the subject, computational fluid dynamics (or CFD as it is more commonly known) has gained much acceptance as an indispensable tool for studying the dynamics of fluid flows, standing somewhere between the theoretical approach and the "lab experiments". If we now arrive at a point where numerical simulations of the Navier-Stokes equations—yielding the complete and accurate time evolution of the 3-D flow field on all physically relevant scales—can be viewed as a way of doing "numerical experiments", it still remains of a limited extent. In vortical flow stability and transition dynamics—the class of physical problems aimed at by the present work—one of the key phenomena is the apparition and rapid growth, after a certain time, of small scale structures. The amount of resolution, both in space and time, necessary to generate the detailed databases required to shed light on such complex dynamics can easily become a challenge even for today's supercomputers. To maintain the problem within tractable dimensions and cost, specialized tailor-made numerical methods are still necessary. Albeit the fact that these methods are usually restrained to very simple and regular geometries, whenever they are applicable, the richness of information at hand and the resulting absolute control over the flow parameters they provide help make of numerical simulations a very powerful investigating tool.

This thesis is primarily concerned with the development of one such specialized numerical method for the solution of the incompressible Navier-Stokes equations. To

better put in perspective the objectives and scope of our work, we will briefly go over some preliminary considerations. Then, the specific objectives aimed at by this thesis will be stated. A general outline of the material presented will also be given.

1.1 Preliminaries

When devising an efficient numerical method for problems that involve the time evolution of structures of many different length scales, one would principally look for i) wide-band, rapidly converging spatial discretization; and ii) simple, cost effective time integration. The first criterion is to be able to resolve smaller and smaller structures as they appear in the flow field with only a minimal increase of the spatial discretization. As for the second, it is obviously to maintain the time marching of the solution accurate at an acceptable cost over the relevant time scales of the flow.

Global (spectral) expansion methods are certainly well suited for the first requirement. Amongst the main advantages they offer, let us note the exact treatment of the derivatives and the very high convergence rate—typically exponential, i.e., faster than any algebraic power—achieved in practice after reaching a certain level of resolution, as well as the important spatial uncoupling resulting from the (quasi-) orthogonality relations of the basis functions. We refer the reader to the monograph by Gottlieb & Orszag (1977) and the books by Canuto et al. (1988) and by Boyd (1999) for a more detailed description of the theory and techniques of such powerful methodology.

Efficient time integration is somewhat more involved since it implies an efficient implementation of the spatial discretization for the computation of both the nonlinear and the pressure terms; the linear diffusive term is the most simple one and does not require any particular techniques. Typically a mixed explicit/implicit time integration scheme is used. The explicit integration of the nonlinear term is used to avoid the costly iterations while the implicit integration of the viscous term is used to relax the time step size restriction. Since the pioneering works of Orszag (1969, 1970 and 1971), the use of pseudo-spectral algorithms has become the standard way of avoiding the convolution sum associated with the nonlinear convective term. In incompressible flows, no such "unique" approach is available for the pressure term and many different

clever techniques have been devised (Canuto et al., 1988). They can be separated in two main classes: the coupled and the splitting methods, according to whether the system of equations (momentum and continuity) is solved at once or in a decoupled manner.

A different third special class of methods—known as divergence-free expansions methods—has been introduced by Leonard (1981). His idea is to avoid the problem of pressure computation by using special divergence-free vector expansions that implicitly satisfy the continuity constraint and the boundary conditions. The construction of such expansions is far from straightforward, though, and requires mathematical insight and craftsmanship. The challenge is hence shifted from algorithmic to analytical considerations, but the advantages are numerous:

- Exact treatment of the continuity constraint;
- Complete elimination of the pressure variable;
- Implicit time integration of the diffusive term at no extra cost; and
- Reduction of the number of unknows (velocity components) from three to two.

Divergence-free methods have successfully been used in various types of simulation problems among which we find: pipe flows (Leonard & Wray, 1982); straight and curved channel flows (Moser et al., 1983); spherical Couette flows (Dumas & Leonard, 1994); vortex rings (Stanaway et al., 1988); boundary layers, mixing layers, and wakes (Spalart et al., 1991); and trailing vortex flows (Matsushima & Marcus, 1997). Note that these last three references deal with unbounded domains in, spherical, Cartesian and cylindrical coordinates respectively.

The question as to whether use one of these already existing specialized methods or engage in the development of a new one greatly depends on the type of targeted flow problems. Here, the particular class of problems we are interested in mostly concerns the dynamics of simple vortical flows. Many interesting problems can indeed be formulated in terms of a single vortex tube interacting with some other fundamental flow structure like a straining field[1], or a circular jet for example. A better understanding of these simple models is relevant to more complex problems ranging from

[1]This particular problem has been the object of a fair amount of attention lately, especially since

the dynamics of aircraft trailing vortices (Spalart, 1998) to the dynamics of coherent structures in turbulent flows (Vincent & Meneguzzi, 1991; Cadot et al., 1995).

Taking into account these physical considerations led us to restrain our possible choices to methods having at least one (periodic) longitudinal axis that can be aligned with the main flow structure. For such axisymmetric topology though, the unbounded Cartesian formulation used by Spalart et al. (1991)—with two periodic directions—would not seem to be more advantageous than a fully periodic box, i.e., with three periodic directions. Although the advantages of the complete uncoupling and fast transforms for all directions in a fully periodic box may seem very appealing, proper resolution of very localized structures (such as a single or a pair of vortex tubes) could rapidly become too expensive because of the uniform resolution associated with Fourier series. Another penalizing element of using a Cartesian periodic box is that the periodicity lengths of the transverse directions must be large enough to avoid interactions with the neighboring structures while maintaining enough resolution for the ones of interest. This problem can be partly avoided in passing from Cartesian to cylindrical coordinates where the now unique "transverse" radial direction is no longer periodic, but the azimuthal direction has now gained a geometrical periodicity. For this reason and because some of the targeted flows for the present code have an intrinsic axial symmetry, a cylindrical coordinates frame of reference was chosen[2]. This way, not only the problem of minimizing neighbor interactions is moved into one of properly taking into account the more complex non-homogeneity of the radial coordinate, but the reference frame also allows for a more natural description of an important class of vortex problems.

Matsushima & Marcus (1997) developed an efficient spectral method for unbounded cylindrical coordinates that could certainly be used for the type of flow problems we have mentioned. Their method is based on Fourier series expansions for

Leweke & Williamson (1998) have shown that the short-wave instability of the counter-rotating vortex pair could be linked to the elliptic instability problem (Bayly, 1986; Pierrehumbert, 1986; Waleffe, 1990).

[2]If the link between the axial symmetry of the flow and the choice of a cylindrical coordinate frame of reference may seem quite natural, the choice of formulating the numerical method in terms of cylindrical coordinates instead of Cartesian did not appear to us as so obvious in the first place. Indeed, cylindrical coordinates have intrinsic difficulties due to the singularity of the differential operators at $r = 0$ that Cartesian coordinates do not have.

both the longitudinal and the azimuthal directions, and rational Legendre function expansions in the radial one. It is worth noting that, at the time the present work was undertaken, their paper had not yet been published. At any rate, their approach did not completely answer our preoccupation of the time which was the introduction of a local discretization for the semi-infinite radial direction. Indeed, the fixed "method-defined" resolution associated with global expansions may become expensive when solving very localized structures, as we already mentioned for the case of the periodic box above. The idea behind the development of a new mixed global/local method is to take advantage of the high uncoupling that comes from orthogonal expansions (e.g., Fourier series) while introducing some more "user-defined" flexibility in the resolution positioning of the unbounded radial direction.

Some preliminary work (Dufresne & Dumas, 1998a; Dufresne & Dumas, 1998b) led us to the conclusion that B-splines were better adapted than more classical finite elements for the type of discretization considered for the radial direction (see also the discussion in Sec. 2.3.2). It then came to our attention that the appropriateness of B-splines was also supported by some of the work done at NASA Ames Research Center and Stanford University. Kravchenko et al. (1996) had developed a mixed spectral/B-spline method, in Cartesian coordinates, to simulate turbulent channel flows. A similar method for cylindrical coordinates was later on presented by Loulou et al. (1997) for the simulation of turbulent (circular) pipe flows. This latter work being very close to our own, we used it as a work base for some methodological aspects, the principal differences being in the treatment of the radial basis functions and the boundary conditions. Also, since we shall frequently refer to their work throughout this thesis, we will make use of the simpler notation "LMMC", for the four authors' names: Loulou, Moser, Mansour and Cantwell.

Let us finally note that the method we present here, like the one of Matsushima & Marcus, can be viewed as an alternative approach to the "vortex methods" for the computation of free vortical flow dynamics. Indeed, the vortex methods—based on a Lagrangian discretization of the vorticity equation—certainly offer another efficient and attractive means for computing this kind of flow problems. Different formulations in terms of vortex filaments (Leonard, 1985) or vortex particles, in two or three dimensions (Winckelmans, 1989) have been devised according to the type of problem considered. A more recent account of the various aspects of these methods can be

found in Cottet & Koumoutsakos (2000). Some of the most recent developments, in relation to flow simulations past bluff bodies, can also be found in Ploumhans (2001).

1.2 Objectives

Following the aforementioned considerations, we are now in a position to formulate the principal objective of this thesis as:

- *To develop a new spectral/B-spline method for the solution of the unsteady, incompressible Navier-Stokes equations in unbounded cylindrical domains.*

This original extension, made here, of Leonard's divergence-free vector expansions method is to be complemented by the following secondary objectives:

- To develop an eigenvalue solver for the normal mode analysis of the (temporal) linear stability problem;
- To adapt the unbounded spectral/B-spline method for the solution of wall-bounded flow problems; and
- To develop an eigenvalue solver for the latter wall-bounded flow problems.

1.3 Outline of presentation

The material presented in this thesis is divided in three parts: i) the numerical method itself; ii) the implementation of the method; and iii) the numerical testing of the method. A more specific outline, by chapter, is given in what follows.

Chap. 2 is devoted to the presentation of the numerical approach. More specifically, in Sec. 2.1 we present the mathematical problem to be solved, i.e., the Navier-Stokes equations with the relevant boundary and initial conditions. Particular attention is paid to the definition of the regularity conditions that apply in the unbounded

radial direction. In Sec. 2.2, we define the weak problem to be approximated by the divergence-free vector expansions. These expansions form the core of the spatial discretization which is then presented in Sec. 2.3. Here again, special attention is paid to the radial direction and its B-spline discretization which, indeed, represents an original extension of the divergence-free method. A summary of the complete spatial discretization is presented in Sec. 2.4.

Implementation of the numerical method is discussed in Chap. 3. For the time integration, we use the mixed scheme proposed by Spalart et al. (1991), briefly presented in Sec. 3.1. Explanations on how to compute the nonlinear term are given in Sec. 3.2. In that case, special attention is again paid to the radial direction whose treatment differs from the standard pseudo-spectral algorithm. Treatment of the regularity and the boundary conditions is discussed in Sec. 3.3. The local discretization in the radial direction allows for the implementation of a modal reduction algorithm; this is covered in Sec. 3.4. At this step, we now have in hand our complete unbounded Navier-Stokes solver which is identified by the name UNCYL. The modifications that are required for the implementation of the wall-bounded version of the solver are discussed in Sec. 3.5. Implementation of these modifications results in the code BOUNCYL. Because the implementation of the eigenvalue solver is quite similar for both the unbounded and the wall-bounded method, it is discussed in a unified manner in Sec. 3.6. From this, we obtain the two new linear stability codes UNCYL-LS and BOUNCYL-LS.

The material presented so far has been of a rather technical character. The third part on the numerical testing, presented in Chap. 4, involves more physical considerations. In the first section of the chapter (Sec. 4.1), we consider the Poiseuille flow problem in relation with both the eigenvalue solver BOUNCYL-LS and the Navier-Stokes solver BOUNCYL. Comparisons with Stokes flow analytical solutions serve for a thorough validation of the B-spline discretization. Other test results are also presented to complete the validation of the two solvers. As for the remainder of the chapter, it is devoted to the numerical testing of both unbounded solvers UNCYL and UNCYL-LS. A two part approach has been adopted. First, in Sec. 4.2, we consider the stability of a trailing line vortex. For the cases studied, an excellent agreement between our results and those of other authors is observed. Comparisons with some results of Matsushima & Marcus also show that the present B-spline formulation is

indeed advantageous. For the second part, in Sec. 4.3, we consider simulations of the triangular vortex problem. Although more qualitative in this case, the agreement between our results and those used as a reference is again more than satisfactory. Since this crucial validation chapter turns out to be somewhat lengthy, a summary is presented at the end in Sec. 4.4.

Finally, conclusions are drawn in Chap. 5. Note that throughout this thesis, the more technical material has been, whenever possible, relegated to the appendices in order to alleviate the presentation.

Chapter 2

Numerical Method

The numerical methodology presented here aims at solving efficiently the unsteady, incompressible Navier-Stokes equations in unbounded cylindrical domains. As a natural first step, we begin this chapter with a more precise mathematical statement of the problem, including some particular considerations on the regularity and boundary conditions in the radial direction. The variational form, leading to a weak approximation of the problem, is then considered. The ensuing Galerkin method is obtained after the construction of a complete set of divergence-free vector expansions. These expansions are formulated in terms of both Fourier series and mapped B-spline interpolation functions. Because of its rather non-standard character, the use of B-splines for the radial direction is the object of some particular attention. For ease of consultation, a brief summary of the spatial discretization is provided at the end of the chapter.

2.1 Navier-Stokes equations

We start by assuming that the fluid flows we are interested in are well described by the incompressible Navier-Stokes equations (see, for example, Batchelor, 1967). The conservation of momentum equation, expressed in terms of the velocity vector $\mathbf{u}$ and static pressure p, is written in non-dimensional form (in an inertial frame of reference)

as

$$\frac{\partial \mathbf{u}}{\partial t} + \mathbf{u} \cdot \nabla \mathbf{u} = -\nabla p + \frac{1}{Re} \nabla^2 \mathbf{u} \,. \tag{2.1}$$

The vector field $\mathbf{u}$ and the scalar field p are both functions of space and time, i.e.,

$$\mathbf{u} = \mathbf{u}(\mathbf{x}, t) \quad \text{with} \quad \mathbf{x} \in \Omega \,,$$

and similarly for p. The vector $\mathbf{x}$ defines the spatial coordinate and t the time, Ω defines the spatial domain containing the fluid and since we consider three dimensional (unbounded) fields, $\Omega \subseteq \mathbb{R}^3$. As for the mass conservation equation, because of the incompressibility condition (assuming a homogeneous fluid), it simply reduces to the divergence-free constraint

$$\nabla \cdot \mathbf{u} = 0 \,. \tag{2.2}$$

Beside the auxiliary (boundary and initial) conditions that will be discussed into some more details below, there is only one additional parameter that completely characterizes the problem, namely the Reynolds number Re. It represents the ratio of the non-viscous (typically the inertia) to the viscous forces and is usually defined as

$$Re \equiv \frac{\bar{U}_{\text{ref}} \bar{L}_{\text{ref}}}{\bar{\nu}} \,,$$

where $\bar{U}_{\text{ref}}$ and $\bar{L}_{\text{ref}}$ are respectively the (dimensional) reference velocity and length scales of the flow, and $\bar{\nu}$ is the kinematic viscosity of the fluid. Before going any further, let us make a note regarding the notation used in this work. All constants and variables will be expressed in non-dimensional form unless otherwise stated; dimensional terms will be identified with the "overbar" notation. Because for the targeted flow problems all relevant scales are determined by the flow itself, at first we only consider the dimensional scaling factors in their general form, i.e., a reference length $\bar{L}_{\text{ref}}$ and velocity $\bar{U}_{\text{ref}}$, from which can be deduced the reference time $\bar{T}_{\text{ref}} = \bar{L}_{\text{ref}} / \bar{U}_{\text{ref}}$. Note that the Reynolds number can also be interpreted as a ratio of the viscous to the convective time scales. Explicit mention of the dimensional scaling factors, with their physical relevance will be made when considering some particular flow problem.

The set of partial differential equations (PDEs) formed by the conservation of momentum equation (2.1) and the solenoidal condition (2.2) has been the subject of

much attention since its formulation in about the mid 19th century, and may even be considered one of the most studied sets of PDEs (Ockendon et al., 1999). However, only a very small number of exact steady solutions, and an even smaller number of unsteady ones, are yet known. Some of these solutions can be found in Schlichting (1979) and Wang (1991), among others. For the great majority of problems then, one must rely on approximate (strong or weak) solutions. The questions of existence and uniqueness of such solutions, as well as the ones regarding the convergence of the different type of approximations have consequently been extensively studied (Ladyzhenskaya, 1975; Temam, 1979, for a taste of the subject). Though important steps were made, leading to a greater insight, some fundamental issues still remain open (Temam, 1995). This said, we will not go any deeper into these rather theoretical, though much interesting, considerations and assume to meet here all the minimum analytical requirements as to insure the existence of an "acceptable" solution at some finite time.

Let us now go back to (2.1), where by using the identity

$$\mathbf{u} \cdot \nabla \mathbf{u} \equiv \frac{1}{2} \nabla |\mathbf{u}|^2 - \mathbf{u} \times \boldsymbol{\omega} ,$$

with $\boldsymbol{\omega}$ being the vorticity vector defined as

$$\boldsymbol{\omega} \equiv \nabla \times \mathbf{u} ,$$

we may rewrite the equation as

$$\frac{\partial \mathbf{u}}{\partial t} = -\nabla P + \frac{1}{Re} \nabla^2 \mathbf{u} + \mathbf{F} \tag{2.3}$$

where now P ($\equiv p + \frac{1}{2}|\mathbf{u}|^2$) is the total pressure and $\mathbf{F} \equiv \mathbf{u} \times \boldsymbol{\omega}$ is a nonlinear forcing term. This equivalent "forced Stokes equation" formulation[1] of (2.1) helps relate many important analytical results obtained from the study of the linear Stokes problem to the more complex, nonlinear Navier-Stokes equations (Temam, 1979; Pasquarelli et al., 1987). Some of these particular analytical considerations will be carried over to the variational formulation of Sec. 2.2.

[1] Note that there are other possible forced Stokes formulations than the one used here. The most simple example being of course for $\mathbf{F} \equiv -\mathbf{u} \cdot \nabla \mathbf{u}$, but $\mathbf{F} \equiv -\nabla \cdot (\mathbf{u}\mathbf{u})$ is also an other acceptable form (both of these leading to p instead of P in (2.3)). Although all analytically equivalent, the discrete versions of these different terms may lead to different types of discretization errors (Kravchenko & Moin, 1997).

The set of equations (2.2)–(2.3) has to be complemented with auxiliary (initial and boundary) conditions. The initial condition is given in a general form by

$$\mathbf{u}(\mathbf{x}, t = 0) \;=\; \mathbf{U}_0(\mathbf{x}) \;, \tag{2.4}$$

where $\mathbf{U}_0(\mathbf{x})$ is a known vector field, function of the space coordinate $\mathbf{x}$ only. As for the boundary conditions, they are expressed, in the cylindrical coordinates

$$\mathbf{x} \;=\; r\,\hat{\mathbf{e}}_r \;+\; \theta\,\hat{\mathbf{e}}_\theta \;+\; z\,\hat{\mathbf{e}}_z \;=\; \{\,r,\;\theta,\;z\,\}\;,$$

as: i) periodicity in the longitudinal z direction such that

$$\mathbf{u}(\mathbf{x}, t) \;=\; \mathbf{u}(\mathbf{x} + L_z\hat{\mathbf{e}}_z, t)\;, \tag{2.5}$$

with L_z the given periodicity length, and ii) finite and uniform velocity at infinity such that

$$\lim_{r\to\infty} \mathbf{u}(\mathbf{x}, t) \;=\; \mathbf{U}_\infty \qquad \text{with} \qquad |\,\mathbf{U}_\infty\,| \;<\; \infty\;. \tag{2.6}$$

If we furthermore decompose the velocity field $\mathbf{u}$ into a homogeneous part $\mathbf{u}_\mathrm{h}$ and a non-homogeneous one $\mathbf{u}_\mathrm{nh}$ such that

$$\mathbf{u} \;=\; \mathbf{u}_\mathrm{h} + \mathbf{u}_\mathrm{nh}\;, \tag{2.7}$$

it is then always possible to choose $\mathbf{u}_\mathrm{nh} = -\mathbf{U}_\infty$ and solve (2.3) under fully homogeneous boundary conditions. For simplicity, we will drop the subscript "h" and consider for now that the vector $\mathbf{u}$ is always defined in terms of homogeneous boundary conditions, i.e., with

$$\lim_{r\to\infty} \mathbf{u}(\mathbf{x}, t) \;=\; \mathbf{0}\;, \tag{2.8}$$

Note that all the non-homogeneous contributions can easily be accounted for by a slight modification of the nonlinear forcing term, where for example,

$$\mathbf{F} \;=\; \mathbf{u}\times\boldsymbol{\omega} \;+\; \frac{1}{Re}\nabla^2\mathbf{u}_\mathrm{nh} \;+\; \text{other terms},$$

Here the vector $\mathbf{u}$ is understood in its complete form (2.7); the same remark obviously applies to the vector $\boldsymbol{\omega}$. A further generalization of the forcing vector $\mathbf{F}$ can also

allow for the inclusion of such contributions that would arise by considering the equations in a rotating frame of reference, say. In that particular case, the Coriolis acceleration $-2\boldsymbol{\Omega} \times \mathbf{u}$ ($\boldsymbol{\Omega}$ being here the angular velocity vector) would simply be added in the "other terms"; the centrifugal contribution $\frac{1}{2}\Omega^2 r'^2$ (r' is the distance from the axis of rotation) would also have to be added to the total pressure P. As a further simplification of notation, we introduce the general extra forcing vector $\mathbf{F_e}$, which includes all of the above contributions, and write

$$\mathbf{F} = \mathbf{u} \times \boldsymbol{\omega} + \mathbf{F_e} .$$

Finally, the complete mathematical problem to solve is summarized by:

$$\begin{aligned}
&\frac{\partial \mathbf{u}}{\partial t} = -\nabla P + \frac{1}{Re}\nabla^2 \mathbf{u} + \mathbf{F} \\
&\nabla \cdot \mathbf{u} = 0 \\
&\mathbf{u}(\mathbf{x}, t=0) = \mathbf{U_0}(\mathbf{x}) \\
&\mathbf{u}(\mathbf{x}, t) = \mathbf{u}(\mathbf{x} + L_z \hat{\mathbf{e}}_z, t) \quad \text{and} \quad \lim_{r \to \infty} \mathbf{u}(\mathbf{x}, t) = \mathbf{0} \\
&\text{with } \mathbf{F} = \mathbf{u} \times \boldsymbol{\omega} + \mathbf{F_e}
\end{aligned} \tag{2.9}$$

2.1.1 Radial regularity

In cylindrical coordinates, the differential operators involved in (2.9) are singular (in r) at both the origin ($r = 0$) and at infinity. If the solution $\mathbf{u}$ is to remain bounded at both these singular points—the boundedness condition at infinity is even more specific in this case since it is in fact the decaying condition (2.8)—then some regularity or "behavioral" conditions are needed. The particular restrictions that these conditions impose on the different field quantities are discussed in what follows.

We first consider the center point $r = 0$. Let us use the vector $\boldsymbol{\Psi}$ to denote a

general vector field. Using separation of variables and a Fourier series expansion for the naturally periodic azimuthal (θ) direction, we write

$$\boldsymbol{\Psi}(r,\theta) \;=\; \sum_{k_\theta=-M}^{M} \widehat{\boldsymbol{\Psi}}(r;\, k_\theta)\; e^{ik_\theta\theta} \;,$$

where $i \equiv \sqrt{-1}$ and where M may be infinite. The variable dependence on z and t is omitted or implicitly assumed without loss of generality.

The first necessary "unicity" condition requires that

$$\frac{\partial\, \boldsymbol{\Psi}}{\partial\theta} \;=\; \mathbf{0}$$

at the origin. In terms of the Fourier-transformed vector components of $\boldsymbol{\Psi}$, this gives[2]

$$\begin{aligned} ik_\theta\widehat{\psi}_r \;-\; \widehat{\psi}_\theta \;&=\; 0\;, \\ ik_\theta\widehat{\psi}_\theta \;+\; \widehat{\psi}_r \;&=\; 0\;, \\ ik_\theta\widehat{\psi}_z \;&=\; 0\;, \end{aligned}$$

which simplifies to

$$\boxed{\begin{aligned} \widehat{\psi}_r \;=\; \widehat{\psi}_\theta \;&=\; 0 \quad \text{for} \quad |k_\theta| \neq 1\;, \\ \widehat{\psi}_r \;+\; ik_\theta\widehat{\psi}_\theta \;&=\; 0 \quad \text{for} \quad |k_\theta| = 1\;, \\ \widehat{\psi}_z \;&=\; 0 \quad \text{for} \quad |k_\theta| > 0\;. \end{aligned}} \tag{2.10}$$

Note that any scalar component in general, such as the pressure, follows the same type of conditions as $\widehat{\psi}_z$.

The radial behavior of each component can even be further specified if the vector field is required to be analytic in the neighborhood of the origin. There are different ways to derive the next result, one of them is presented in App. A.2. By considering first the Cartesian vector components[3], we may show that the analyticity condition

[2]Recall that in cylindrical coordinates: $\partial\,\hat{\mathbf{e}}_r/\partial\theta = +\hat{\mathbf{e}}_\theta$ and $\partial\,\hat{\mathbf{e}}_\theta/\partial\theta = -\hat{\mathbf{e}}_r$.

[3]In this case, each vector component behaves as a scalar because the Cartesian basis vectors are independent of the position, i.e., they all have zero derivatives.

requires that (see (A.21))

$$\{ \widehat{\psi}_x,\ \widehat{\psi}_y,\ \widehat{\psi}_z \} \ = \ \mathcal{O}(r^{|k_\theta|+2p}) \ ,$$

as $r \rightarrow 0$, and where p is a non-negative integer, i.e., $p = 0, 1, 2, \ldots$. In terms of the polar vector components (see (A.25)), the complete set of parity or pole conditions become

$$\begin{aligned}
r\,[\,\widehat{\psi}_r + i\,\widehat{\psi}_\theta\,] &= \mathcal{O}(r^{k_\theta+2p+2}) \quad \text{for} \quad k_\theta \geq 0 \ , \\
r\,[\,\widehat{\psi}_r - i\,\widehat{\psi}_\theta\,] &= \mathcal{O}(r^{k_\theta+2p}) \quad \text{for} \quad k_\theta \geq 1 \ , \\
r\,[\,\widehat{\psi}_r + i\,\widehat{\psi}_\theta\,] &= \mathcal{O}(r^{|k_\theta|+2p}) \quad \text{for} \quad k_\theta \leq -1 \ , \\
r\,[\,\widehat{\psi}_r - i\,\widehat{\psi}_\theta\,] &= \mathcal{O}(r^{|k_\theta|+2p+2}) \quad \text{for} \quad k_\theta \leq 0 \ , \\
\widehat{\psi}_z &= \mathcal{O}(r^{|k_\theta|+2p}) \quad \text{for} \quad |k_\theta| \geq 0 \ .
\end{aligned} \tag{2.11}$$

The unicity conditions (2.10) can obviously be directly deduced from (2.11) by simply considering the limit point $r = 0$.

Two additional points are worth noting at this moment. The first is related to the general nature of (2.11), and thus (2.10). Any analytical operations on the vector $\boldsymbol{\Psi}$ will obviously leave the radial behavior unchanged, i.e., the vectors resulting from $\nabla \times \boldsymbol{\Psi}$ or $\nabla^2 \boldsymbol{\Psi}$ will follow the exact same behavior as in (2.11). The same applies to scalar components which, as we already mentioned, follow the z vector component behavior. The second point regards the nature of the boundary conditions that need to be imposed for solving (2.9). Borrowing from the finite element literature (Strang & Fix, 1988), the conditions in (2.10) can be described as "essential" while those in (2.11) would be referred to as "natural" boundary conditions. If the two conditions are analytically equivalent they, on the other hand, lead to different types of approximation functional spaces. We leave this matter pending for now as we shall return to it in the construction of the radial basis functions, later on in this chapter.

At the other extremity of the radial coordinate, i.e., as r tends to infinity, the decaying condition (2.8) is somewhat less stringent on the vector fields. For example, if the initial condition (2.4) is related to a vorticity field having a compact support, the flow in the far field could then be considered irrotational since the vorticity there would be at most exponentially small, in the presence of diffusion. The same problem

could also be formulated in terms of a more general class of flows that would allow algebraically decaying (i.e., with some negative power of r) vorticity instead. This would obviously lead to a different (decaying) radial form that would encompass the potential flow condition as a particular case. With such level of flexibility, the final choice of a specific decaying behavior—assuming the minimum requirements imposed by the type of flow considered—will therefore usually end up being determined by practical reasons related to the construction of the approximation functions.

Following this last remark, let us consider the harmonic[4] decaying behavior of the vector field Ψ. Details on the derivation on this particular condition will be found in App. A.3. As for the practical motivations, they will become clear in the light of the choice of the radial basis functions, particularly when considering the implementation of the boundary conditions. Now, if a vector field is to decay harmonically as $r \to \infty$, we can show (see (A.26)–(A.31)) that its Cartesian components should be in the form

$$\{ \widehat{\psi}_x,\ \widehat{\psi}_y,\ \widehat{\psi}_z \} \ = \ \mathcal{O}(r^{-|k_\theta|}) \ , \tag{2.12}$$

with the additional constraint (see (A.32)) that

$$\lim_{r\to\infty} r^{|k_\theta|}\ \widehat{\psi}_x \ = \ i\,\mathrm{sgn}(k_\theta) \lim_{r\to\infty} r^{|k_\theta|}\ \widehat{\psi}_y \ , \tag{2.13}$$

where $\mathrm{sgn}(k_\theta) \equiv k_\theta/|k_\theta|$. The coupling between $\widehat{\psi}_x$ and $\widehat{\psi}_y$ can be viewed as result of the Cauchy-Riemann equations because both real functions ψ_x and ψ_y form a pair of harmonic conjugates in the complex r–θ plane. The complete conditions (2.12) and (2.13) expressed in terms of the cylindrical vector components give

$$\boxed{\begin{aligned} &\{ r\widehat{\psi}_r,\ r\widehat{\psi}_\theta,\ \widehat{\psi}_z \} \ = \ \mathcal{O}(r^{-|k_\theta|}) \ , \\ &\lim_{r\to\infty} r^{|k_\theta|+1}\ \widehat{\psi}_r \ = \ i\,\mathrm{sgn}(k_\theta) \lim_{r\to\infty} r^{|k_\theta|+1}\ \widehat{\psi}_\theta \ . \end{aligned}} \tag{2.14}$$

[4]The term "harmonic" refers here to the complex analysis meaning of the word. Each of the Fourier-transformed vector components can be represented by a complex valued function. If such vector components behave as (complex) analytic, or equivalently harmonic, functions they must then follow the above described behavior. See also App. A.3 for more details.

Before closing this section, some last observations are worth noting. First, both (2.11) and (2.14) are the result of analyticity considerations, but were derived from different perspectives (see App. A.2 and A.3). Around the origin, the real vector components were assumed to be defined at the point $r = 0$ itself, and were then extended analytically in some neighborhood of that point. After that, the results were transposed into the (complex) Fourier spectral space. Analyticity at infinity was, on the other hand, considered directly in the complex (Fourier-transformed) plane. The vector components were assumed to be defined at some finite radius in the complex plane, and then were extended analytically to infinity.

Second, analyticity at the origin applies to all vector fields whereas the condition at infinity must be imposed on a specific vector field. In the present case, the harmonic decaying behavior is imposed on what will be defined as the vector potential $\boldsymbol{\Psi}$ — anticipating on the material related to the construction of the approximation vector functions in Sec. 2.3—from which the velocity vector field $\mathbf{u}$ will be defined as $\mathbf{u} = \nabla \times \boldsymbol{\Psi}$. As we already mentioned this choice of decaying condition is motivated by practical implementation considerations that will be better explained later. It can also be shown that this condition is general enough to include far field potential flow conditions as a particular case.

2.2 Variational formulation

Before we get into the details of the numerical method developed to solve (2.9), let us briefly consider some of the analytical background material on which rests the method. More precisely, in this section we present the variational formulation used to construct the general approximation of (2.9). Since the purpose of our presentation, here, is only to help sit the numerical method on firm mathematical ground, we shall limit ourselves to a general overview only. A rigorous account of the complete analytical framework would involve a fair amount of functional analysis material that goes far beyond the scope of the present work. For a more complete treatment of the subject we therefore refer the reader to some of the specialized works dedicated to the approximation theory of the Navier-Stokes equations, from which we may cite Temam (1979) and Temam (1995) amongst others. Other theoretical and practical aspects of

approximation theory, in the more specific context of spectral methods, can also be found in Boyd (1999), Canuto et al. (1988) and also Gottlieb & Orszag (1977).

The general variational approximation of the Navier-Stokes equations was introduced in a series of papers by Leray (1933), (1934a) and (1934b) (cited from Temam, 1979). In this approach the approximation of the solution is constructed by taking the inner product of (2.9) with some "weight" basis vector function $\mathbf{\Phi}$ such that

$$\left\langle \mathbf{\Phi}, \frac{\partial \mathbf{u}}{\partial t} \right\rangle = -\langle \mathbf{\Phi}, \nabla P \rangle + \frac{1}{Re} \langle \mathbf{\Phi}, \nabla^2 \mathbf{u} \rangle + \langle \mathbf{\Phi}, \mathbf{F} \rangle , \tag{2.15}$$

where

$$\langle \mathbf{v}, \mathbf{u} \rangle \equiv \int_\Omega \mathbf{v}^* \cdot \mathbf{u} \, dV . \tag{2.16}$$

The inner product (2.16) is defined in a general sense where both $\mathbf{u}$ and $\mathbf{v}$ may be complex valued, the superscript "$*$" stands for the complex conjugate. Solutions of (2.15) are sought for $\mathbf{u} \in X$ and $\mathbf{\Phi} \in Y$ where both functional spaces are given by

$$X = \{ \mathbf{v} : \mathbf{v} \in \mathbf{H}^2 \cap \mathbf{H}_0^1 , \nabla \cdot \mathbf{v} = 0 \} ; \tag{2.17}$$

$$Y = \{ \mathbf{v} : \mathbf{v} \in \mathbf{H}_0^1 , \nabla \cdot \mathbf{v} = 0 \} . \tag{2.18}$$

$\mathbf{H}^n$ defines a general Hilbert (inner product) space for which all the vector basis functions $\mathbf{v}$ and their derivatives up to order n are square integrable. We furthermore define a subspace $\mathbf{H}_0^1 \subset \mathbf{H}^1$ such that

$$\mathbf{H}_0^1 = \{ \mathbf{v} : \mathbf{v} \in \mathbf{H}^1 , \mathbf{v}(\mathbf{x}) = \mathbf{v}(\mathbf{x} + L_z \hat{\mathbf{e}}_z) \text{ and } \lim_{r \to \infty} \mathbf{v} = \mathbf{0} \} .$$

This subspace defines the set of basis functions $\mathbf{v} \in \mathbf{H}^1$ that satisfy the general homogeneous boundary conditions of (2.9).

It can now be shown, making use of the following vector identity

$$\int_\Omega \mathbf{\Phi} \cdot \nabla P \, dV \equiv \int_{\partial\Omega} P \, (\mathbf{\Phi} \cdot \mathbf{n}) \, dS - \int_\Omega P \, (\nabla \cdot \mathbf{\Phi}) \, dV , \tag{2.19}$$

that if $\mathbf{\Phi} \in X$ then

$$\langle \mathbf{\Phi}, \nabla P \rangle = 0 , \tag{2.20}$$

i.e., that the pressure term in (2.15) drops out. In (2.19), $\partial\Omega$ symbolizes the surface enclosing the volume Ω; this surface must obviously be understood here in its limiting

sense since Ω is theoretically unbounded. The actual requirements to obtain such a result are that

$$\nabla \cdot \mathbf{\Phi} \;=\; 0 \qquad \text{and} \qquad \lim_{r\to\infty} \mathbf{\Phi}\cdot\mathbf{n} \;=\; 0\;,$$

More specifically, the vanishing of the pressure surface integrals (the first integral on the right hand side of (2.19)) requires that the integrand $P(\mathbf{\Phi}\cdot\mathbf{n})$ decays at least as $\mathcal{O}(r^{-2})$ or faster. This last condition is in turn granted as long as the total pressure P satisfies a decaying condition in the form of

$$P \;=\; \mathcal{O}(r^{-1})$$

in the far field. For P to tend to some finite value at infinity, we would then obviously need to have that $\mathbf{\Phi}\cdot\mathbf{n} = \mathcal{O}(r^{-2})$. It is interesting to note that in bounded domains, there is no requirement for the pressure value on the bounding surface, as long as the value remains with a finite amplitude of course. Only the no-through flow condition $\mathbf{\Phi}\cdot\mathbf{n} = 0$ is sufficient to ensure the vanishing of the pressure term.

Reduction of the requirements on the differentiability of $\mathbf{u}$ can be achieved by integration by parts of the viscous term. This result can be derived in different ways, here, it is obtained by first making use of the following identity

$$\nabla^2\mathbf{u} \;\equiv\; \nabla(\nabla\cdot\mathbf{u}) \;-\; \nabla\times\nabla\times\mathbf{u}\;, \tag{2.21}$$

for which the first term on the right hand side is identically zero. Then, with the second identity

$$\begin{aligned}\int_\Omega \mathbf{\Phi}\cdot(\nabla\times\nabla\times\mathbf{u})\,dV \;\equiv\;& \\ -\int_{\partial\Omega}\left[\,\mathbf{\Phi}\times(\nabla\times\mathbf{u})\,\right]\cdot\mathbf{n}\,dS \;+\; \int_\Omega(\nabla\times\mathbf{\Phi})\cdot(\nabla\times\mathbf{u})\,dV\;,&\end{aligned} \tag{2.22}$$

we obtain

$$\int_\Omega \mathbf{\Phi}\cdot\nabla^2\mathbf{u}\,dV \;=\; -\int_\Omega(\nabla\times\mathbf{\Phi})\cdot(\nabla\times\mathbf{u})\,dV\;, \tag{2.23}$$

under the provision that the normal component of $\mathbf{\Phi}\times(\nabla\times\mathbf{u})$ decays fast enough, a condition granted by the fact that both $\mathbf{\Phi}$ and $\mathbf{u}$ belong to $\mathbf{H}_0^1$. The weak form of

(2.9) is finally obtained by replacing (2.23) in (2.15) taking into account the complex conjugate of the inner product definition (2.16), combined with (2.20), and is written

$$\left\langle \mathbf{\Phi},\, \frac{\partial \mathbf{u}}{\partial t} \right\rangle \;=\; -\frac{1}{Re}\,\langle \nabla \times \mathbf{\Phi},\, \nabla \times \mathbf{u} \rangle + \langle \mathbf{\Phi},\, \mathbf{F} \rangle \;, \tag{2.24}$$

where now both $\mathbf{\Phi}, \mathbf{u} \in Y$.

In summary, the problem of finding solutions for (2.9) has now been transformed into the variational, initial value problem

$$\boxed{\begin{array}{c} \mathbf{u} \in Y \;\text{ and }\; \mathbf{u}(t=0) = \mathbf{U}_0 \\[2ex] \left\langle \mathbf{\Phi},\, \dfrac{\partial \mathbf{u}}{\partial t} \right\rangle \;=\; -\dfrac{1}{Re}\,\langle \nabla \times \mathbf{\Phi},\, \nabla \times \mathbf{u} \rangle + \langle \mathbf{\Phi},\, \mathbf{F} \rangle \\[2ex] \forall \mathbf{\Phi} \in Y \end{array}} \tag{2.25}$$

A last remark can be made regarding the equivalent projection formulation of (2.25). Based on the Helmholtz-Hodge vector decomposition (Chorin & Marsden, 1993), the strong form of the above mentioned variational problem can be formulated in terms of a divergence-free projection operator $\mathbb{P}$, such that the new problem is written as

$$\frac{\partial \mathbf{u}}{\partial t} \;=\; \mathbb{P}\left(-\frac{1}{Re} \nabla \times \nabla \times \mathbf{u} \;+\; \mathbf{F} \right) .$$

Using a similar procedure as for the above variational formulation[5] we obtain, for $\mathbf{v} \in Y$, that

$$\mathbb{P}\,\mathbf{v} \;=\; \mathbf{v} \qquad \text{and} \qquad \mathbb{P}\,(\nabla P) \;=\; \mathbf{0} \,.$$

Theoretical considerations related to this type of projection operators can be found in Ebin & Marsden (1970). In the path of Leonard & Wray (1982), the numerical

[5]Here again, the standard results are established for bounded domains with a no-through flow condition at the boundary. For unbounded domains, special considerations on the decay rate of the various terms must be taken into account.

method presented here can then be viewed as a means for constructing an approximation of such a projection operator. Examples of application to the numerical approximation of Navier-Stokes equations are given in Chorin (1969) and also in Moser & Moin (1984).

2.3 Basis vector functions

The overall idea behind the present numerical methodology, first introduced by Leonard (1981), is to construct a finite dimensional approximation of the variational problem (2.25). In the mathematical formulation of the previous section, we need to construct a finite dimensional space V^J (of dimension J) such that, V^J is dense in Y in the limit of $J \to \infty$. Our first objective in this section is therefore to construct a basis $\mathbf{V}_j$ such that $V^J = \text{span}\{\ \mathbf{V}_j\ \}$. Once the basis is determined, the velocity vector $\mathbf{u}$ is then expanded in terms of this basis, viz.,

$$\mathbf{u}(r,\theta,z,t) \ = \ \sum_{j=1}^{J} \alpha_j\,(t)\ \mathbf{V}_j(r,\theta,z)\ . \tag{2.26}$$

The next step is to construct a weighted residual method that mimics the variational formulation (2.25). The weight functions are chosen as the complex conjugate of the $\mathbf{V}_j$; keeping in mind the definition of the inner product (2.16). This spatial discretization process—from which is obtained the set of time evolution equations for the $\alpha_j(t)$ coefficients—gives rise to a Galerkin method. The Galerkin method is well known for its many advantageous properties: energy conservation (in the absence of dissipation), minimization of the approximation error, positive definiteness of the discrete operators, to cite a few; more can be found in Canuto et al. (1988) for example.

From this general outline, let us first start with the construction of the $\mathbf{V}_j$. It can be shown, although it may become quite involved, that solutions of either (2.9) or (2.25) may be constructed by separation of variables (see, for example, Morse &

Feshbach, 1953). It is thus possible to start with a generic expression in the form of

$$\mathbf{V}_j(r,\theta,z) \;=\; \left\{ \begin{array}{ll} R_1(r)\,\Theta_1(\theta)\,Z_1(z)\,\hat{\mathbf{e}}_r & + \\ R_2(r)\,\Theta_2(\theta)\,Z_2(z)\,\hat{\mathbf{e}}_\theta & + \\ R_3(r)\,\Theta_3(\theta)\,Z_3(z)\,\hat{\mathbf{e}}_z & \end{array} \right\}_j \;. \tag{2.27}$$

For V^J to constitute a dense subspace of Y, we must then have

$$\nabla\cdot\mathbf{V}_j \;=\; 0 \quad , \quad \mathbf{V}_j(\mathbf{x}) = \mathbf{V}_j(\mathbf{x}+L_z\hat{\mathbf{e}}_z) \quad \text{and} \quad \lim_{r\to\infty}\mathbf{V}_j \;=\; \mathbf{0} \quad \forall j \;, \tag{2.28}$$

and also have that the set of generic functions $\{\,R_i\,,\Theta_i\,,Z_i\,\}$ $(i=1,2,3)$ be complete for each of the vector components.

Since both the longitudinal (z) and the azimuthal (θ) directions are periodic, Fourier series (trigonometric polynomials) form a natural basis for these directions and (2.26) may be directly simplified to

$$\mathbf{u}(r,\theta,z,t) \;=\; \sum_l\sum_m\sum_n \alpha_{lmn}\,(t)\;\mathbf{W}_l(r\,;\,k_\theta,k_z)\,e^{ik_\theta\theta}e^{ik_z z} \;, \tag{2.29}$$

where

$$k_\theta \;=\; m\,\frac{2\pi}{L_\theta} \qquad \text{with} \qquad -N_\theta \;\le\; m \;\le\; N_\theta \;,$$

$$k_z \;=\; n\,\frac{2\pi}{L_z} \qquad \text{with} \qquad -N_z \;\le\; n \;\le\; N_z \;,$$

and $1 \le l \le N_r$. In terms of the basis functions $\mathbf{V}_j$, (2.29) implies the following definition

$$\mathbf{V}_j \;\equiv\; \mathbf{W}_l(r\,;\,k_\theta,k_z)\,e^{ik_\theta\theta}e^{ik_z z} \;, \tag{2.30}$$

in which the global index j has been split into the three indices l, m, and n associated respectively with the r, θ, and z coordinates. According to the different ranges covered by the new indices, the global index j may now be written

$$j \;=\; l \;+\; (m+N_\theta) \;+\; (n+N_z) \;.$$

In (2.29), the Fourier periodicity lengths L_θ and L_z are both adjustable parameters that can be modified according to the natural periodicities of the problem under

consideration. In the azimuthal direction though, because the point $r = 0$ belongs to the domain, L_θ is constrained to entire fractions of the basic periodicity 2π and k_θ to integer values, i.e.,

$$L_\theta = \frac{2\pi}{p} \qquad \text{and} \qquad k_\theta = pm \,,$$

where here p is a positive integer. An example in which such particular periodicity (symmetry) of the flow problem can advantageously be taken into account is given in Sec. 4.3, with $p = 3$. Let us also make a note on the identification of the Fourier "modal pairs". According to the values of L_θ and L_z, the Fourier summation indices m and n and the corresponding wavenumber k_θ and k_z will obviously only differ by a constant value. Thus, for a particular problem in which both periodicity lengths are given and fixed we may identify a particular modal pair by either its characteristic wavenumbers k_θ, k_z or by its modal indices (m, n), in parenthesis.

The use of Fourier series in (2.29) also calls for an other comment. Since the vector field $\mathbf{u}$ is limited to real values, the general complex conjugate symmetry of the Fourier basis (for the modal pair k_θ, k_z), viz.,

$$e^{-ik_\theta\theta}e^{-ik_z z} = \left[e^{ik_\theta\theta}e^{ik_z z}\right]^* \qquad \text{and} \qquad e^{-ik_\theta\theta}e^{ik_z z} = \left[e^{ik_\theta\theta}e^{-ik_z z}\right]^* \,,$$

can therefore be applied to the coefficients α_{lmn}, such that

$$\alpha_{l\,-m\,-n} = \alpha^*_{lmn} \qquad \text{and} \qquad \alpha_{l\,-mn} = \alpha^*_{lm\,-n} \,. \tag{2.31}$$

The number of coefficients that need to be effectively accounted for can thus be reduced by half. For practical reasons that will be considered in Sec. 3.4, we shall only consider explicitly, for now on, the set of coefficients for which $m \geq 0$, i.e., the α_{lmn} and $\alpha_{lm\,-n}$ (where in this case $m \geq 0$ and $n \geq 0$). Note that the second half of the coefficients is always accounted for implicitly according to (2.31).

2.3.1 Divergence-free vector functions

Following (2.29), the next step is the construction of the divergence-free basis vectors $\mathbf{W}_l(r\,;\, k_\theta, k_z)$. This is indeed the step at the heart of Leonard's divergence-free expansions method. Now, it can again be shown that if the general vector $\mathbf{W}_l$ is

divergence-free, then only two independent basis vectors are actually required to completely define it (see again Morse & Feshbach, 1953). These vectors are associated with a "+" and "−" class, as in Leonard & Wray (1982), and are written such that

$$\alpha_{lmn}\,\mathbf{W}_l \;=\; \alpha^{+}_{lmn}\,\mathbf{W}^{+}_l \;+\; \alpha^{-}_{lmn}\,\mathbf{W}^{-}_l \;. \tag{2.32}$$

There are many possibilities for the construction of the $\mathbf{W}^{\pm}_l$, the choice of one over another being usually determined from practical implementation reasons. In this case, because of the similarities that bear the present method with the one developed by LMMC, we directly make use of the same set of vector expansions given in their report. From the vectorial identity

$$\nabla\cdot(\nabla\times\Psi)\;\equiv\;0\;,$$

result, according the modal pair k_θ, k_z, the following vector basis function families:

- $k_\theta > 0\,;\; k_z \neq 0$

$$\mathbf{W}^{+}_l \;=\; \widehat{\nabla\times}\left\{\begin{array}{c}0\\0\\-k_z r G_l\end{array}\right\} \;=\; k_z\left\{\begin{array}{c}-ik_\theta G_l\\(rG_l)'\\0\end{array}\right\}\;, \tag{2.33}$$

$$\mathbf{W}^{-}_l \;=\; \widehat{\nabla\times}\left\{\begin{array}{c}-iG_l\\G_l\\0\end{array}\right\} = \left\{\begin{array}{c}-ik_z G_l\\k_z G_l\\G_l' + (1-k_\theta)r^{-1}G_l\end{array}\right\}\;. \tag{2.34}$$

The $\widehat{\nabla\times}$ stands for the Fourier-transformed curl operator and the $G_l(r)$ are real valued functions that form a basis for the radial direction (the variable dependence has been omitted to simplify the notation). This construction will be seen to be particularly advantageous when considering the imposition of the regularity/boundary conditions later on in Sec. 3.3. The details of the G_l functions are also postponed, but only until later on in this section. Because (2.33) and (2.34) are incomplete when $k_z = 0$ (no radial nor azimuthal components), the following expansions must be added:

- $k_\theta > 0\ ;\ k_z = 0$

$$\mathbf{W}_l^+ = \widehat{\nabla\times}\left\{\begin{array}{c} 0 \\ 0 \\ -rG_l \end{array}\right\} = \left\{\begin{array}{c} -ik_\theta G_l \\ (rG_l)' \\ 0 \end{array}\right\}, \tag{2.35}$$

$$\mathbf{W}_l^- = \widehat{\nabla\times}\left\{\begin{array}{c} -iG_l \\ G_l \\ 0 \end{array}\right\} = \left\{\begin{array}{c} 0 \\ 0 \\ G_l' + (1-k_\theta)r^{-1}G_l \end{array}\right\}, \tag{2.36}$$

Both of the above families of expansion are also incomplete when $k_\theta = 0$. This maybe less obvious observation is related to the fact that for an axisymmetric vector field the divergence-free constraint only links the radial and the longitudinal components together[6]. The azimuthal component must therefore remain independent. According to this requirement, the "+" class family of expansion is modified to give:

- $k_\theta = 0\ ;\ k_z \neq 0$

$$\mathbf{W}_l^+ = \widehat{\nabla\times}\left\{\begin{array}{c} -iG_l \\ 0 \\ 0 \end{array}\right\} = \left\{\begin{array}{c} 0 \\ k_z G_l \\ 0 \end{array}\right\}, \tag{2.37}$$

$$\mathbf{W}_l^- = \widehat{\nabla\times}\left\{\begin{array}{c} -iG_l \\ G_l \\ 0 \end{array}\right\} = \left\{\begin{array}{c} -ik_z G_l \\ k_z G_l \\ G_l' + r^{-1}G_l \end{array}\right\}. \tag{2.38}$$

Finally, when both wavenumbers are simultaneously zero, i.e., for a uniform, axisymmetric field, all vector components are decoupled (the radial component becomes identically zero) and the following set of vectors is used:

[6]The Fourier-transformed divergence-free constraint is given by (see (A.4) in App. A)

$$\frac{\widehat{u}_r}{r} + \widehat{u}_r' + i\,\frac{k_\theta}{r}\widehat{u}_\theta + i\,k_z\widehat{u}_z = 0$$

The axisymmetric condition is simply obtained by putting $k_\theta = 0$.

- $k_\theta = 0\,;\; k_z = 0$

$$\mathbf{W}_l^+ = \left\{ \begin{array}{c} 0 \\ G_l \\ 0 \end{array} \right\} , \tag{2.39}$$

$$\mathbf{W}_l^- = \left\{ \begin{array}{c} 0 \\ 0 \\ r^{-1} G_l \end{array} \right\} . \tag{2.40}$$

Now that the set of vector expansions has been defined, let us recapitulate. First, it may clearly be seen that the requirements in (2.28) for the $\mathbf{V}_j$ to form an acceptable basis are satisfied, under the provision that the G_l satisfy the appropriate decaying behavior which will be confirmed later. Second, proceeding from (2.25), the Galerkin method is obtained through the following steps: i) both $\mathbf{\Phi}$ and $\mathbf{u}$ are replaced by their respective discrete expansion, (2.30) and (2.29); ii) in each of these expansions, we introduce the "+" and "−" vector decomposition of (2.32); and iii) the different integrals of the inner product (2.16) are then evaluated. A simple example should probably better illustrate these general steps. Let us consider the inertia term of (2.25). Making use of the different definitions, we obtain

$$\begin{aligned} \left\langle \mathbf{\Phi}, \frac{\partial \mathbf{u}}{\partial t} \right\rangle = & \int_0^{L_\theta} \int_0^{L_z} \int_0^{\infty} \left[\mathbf{W}_{l'}^{\pm} e^{ik'_\theta \theta} e^{ik'_z z} \right]^* \cdot \\ & \frac{\partial}{\partial t} \left[\sum_l \sum_m \sum_n \alpha_{lmn}^{\pm} \mathbf{W}_l^{\pm} e^{ik_\theta \theta} e^{ik_z z} \right] r \, dr d\theta dz \quad , \quad \forall\, l', m', n' \end{aligned} \tag{2.41}$$

which must be evaluated for the whole set of weight function indices l', m' and n'. These are the analogs of the expansion coefficients of $\mathbf{u}$, i.e., they span the same values as l, m and n. Now, because of the orthogonality of Fourier series, both integrals in θ and z can be performed, resulting in a complete decoupling of these two directions. Making use of these orthogonality properties, we end up with the much simpler expression

$$\left\langle \mathbf{\Phi}, \frac{\partial \mathbf{u}}{\partial t} \right\rangle = L_\theta L_z \sum_l \int_0^{\infty} \left[\mathbf{W}_{l'}^{\pm *} \cdot \mathbf{W}_l^{\pm} \right] r \, dr \, \frac{d}{dt} \alpha_{lmn}^{\pm} \quad , \quad \forall\, l', m, n \tag{2.42}$$

The same procedure applies to the viscous and the nonlinear terms of (2.25). Note that in the latter case the procedure is somewhat more involved and will be the object of Sec. 3.2; at nay rate the details are not so important here. The final result of all this is a set of small systems of differential-algebraic equations, one for each modal pair k_θ, k_z, or their equivalent modal indices[7] (m,n). These systems of ordinary differential equations (ODE's)—that are the evolution equations of the $\alpha^{\pm}_{lmn}$ coefficients—are symbolically written

$$\boxed{\begin{aligned} \mathsf{A}^{+}_{+}\dot{\alpha}^{+} + \mathsf{A}^{-}_{+}\dot{\alpha}^{-} &= \mathsf{B}^{+}_{+}\alpha^{+} + \mathsf{B}^{-}_{+}\alpha^{-} + \mathsf{F}^{+}\,, \\ \mathsf{A}^{-}_{-}\dot{\alpha}^{-} + \mathsf{A}^{+}_{-}\dot{\alpha}^{+} &= \mathsf{B}^{-}_{-}\alpha^{-} + \mathsf{B}^{+}_{-}\alpha^{+} + \mathsf{F}^{-}\,. \end{aligned}} \tag{2.43}$$

The $\dot{\alpha}^{\pm}$ represents the time derivative of $\alpha^{\pm}$; the various indices, as well as the summation in l are implicitly assumed. The time marching of (2.43), including the computation of the nonlinear vectors $\{\mathsf{F}^{\pm}\}_{l'}$, will be discussed in Chap. 3. As for the different terms of the inertia $\mathsf{A}^{\gamma}_{\delta}$, and viscous $\mathsf{B}^{\gamma}_{\delta}$ matrices, they are respectively given by

$$[\mathsf{A}^{\gamma}_{\delta}]_{l'l} = \int_0^{\infty} \left(\mathbf{W}^{\delta}_{l'}\right)^{*} \cdot \left(\mathbf{W}^{\gamma}_{l}\right) r\,dr \tag{2.44}$$

$$[\mathsf{B}^{\gamma}_{\delta}]_{l'l} = -\frac{1}{Re}\int_0^{\infty} \left(\widehat{\nabla\times}\mathbf{W}^{\delta}_{l'}\right)^{*} \cdot \left(\widehat{\nabla\times}\mathbf{W}^{\gamma}_{l}\right) r\,dr \tag{2.45}$$

with δ and γ being equal to "+" or "−" according to the respective class coupling. The specific form that will take (2.44) and (2.45) varies in correspondence with the modal pair considered and the relevant set of vector functions defined in (2.33)–(2.40). The detailed forms are given in App. C.

The present choice of vector expansions leads to a coupling of the "+" and "−" classes in (2.43). Although it may sometimes be more advantageous to avoid such a coupling, in order to minimize the matrices' bandwidth (Leonard & Wray, 1982), it will be shown later on that the choice of radial function G_l discussed next, combined with a proper reordering of the unknowns, will have no major impact on the global bandwidth of the system of equations.

[7] The reader may recall that only half of the total modal indices are effectively accounted for in this procedure. See (2.31) and the related discussion.

2.3.2 Radial direction: Background

The numerical solution of (2.25) requires essentially two levels of approximation. The first and main one consists of approximating the infinite dimension functional space Y by a finite one, i.e., passing from the continuum problem to the discrete Galerkin method. This part is being taken care of by constructing specific vector basis functions in terms of $e^{ik_\theta\theta}$, $e^{ik_z z}$, and $G_l(r)$ leading to (2.43). The second level is, in certain manner, an indirect one. The numerical evaluation of the $G_l(r)$ can only be done for finite values of r, so the unbounded domain has to be somehow approximated by one of some finite size. In other words, an approximation of the boundary conditions must be made. The problem is not new, and many different techniques have already been developed. Excellent reviews on this subject, applied in the context of spectral methods, are presented in Boyd (1999) and in Canuto et al. (1988). We also mention the article of Grosch & Orszag (1977) which is entirely devoted to the latter problem of unbounded domain approximations. Before considering the present choice of B-spline discretization for the G_l (presented next in Sec. 2.3.3), let us first begin with a brief description of the two principal methods[8] for approximating unbounded domains: "domain truncation" and "mappings". This will be followed by some additional considerations regarding the use of piecewise polynomials in the latter method.

One of the most direct and simple way of dealing with unbounded domains is to impose the decaying condition (2.8) at some finite distance. This mimics what is the common situation found in any laboratory experiments where some no-slip, or any other type of wall bounded condition is always present. This approach is often called domain truncation. One of the main advantages of such a choice is the direct application of many already existing numerical methods (spectral or not). A list of spectral methods designed for bounded cylindrical coordinates is given in Boyd (1999). As long as the solutions sought have a "fast" (exponential, or faster than algebraic) decaying behavior, the approximation error on the boundary condition remains (exponentially) small. In the presence of "slow" or algebraically decaying fields—typical of many problems in fluid dynamics—special care must be taken before

[8]We do not discuss the Laguerre functions (Abramowitz & Stegun, 1964), that do form an orthogonal basis for the semi-infinite interval $[0, \infty[$, because they are limited to exponentially decaying behaviors and are seldom used for Navier-Stokes approximations. See Boyd (1999) and also Gottlieb & Orszag (1977) for additional comments on this set of functions.

applying the equivalent no-slip condition at some finite radius. Of course this does not lead to any particular problems as long as the boundary effects (e.g., the presence of a boundary layer) do not propagate too far inside the domain as to affect the dynamics of the main flow structures. This may be interpreted as a time limit before which the unbounded approximation remains valid. To minimize the effects associated with the presence of the artificial boundary, other type of approximate conditions can be used. A slip or shear-free condition, instead of the possibly too simple no-slip, may certainly help prevent/retard the propagation of the spurious boundary effects. This of course does not include the pressure "confinement effects" that are throughout supposed to be negligible. The elliptic character of the pressure in incompressible flows obviously results in an instantaneous (infinite speed of propagation) effect on the whole flow field.

A different way of considering the approximation of the boundary conditions is by working with a mapped domain. The main idea is to map the semi-infinite interval $r \in [0, \infty[$ onto the finite interval $\eta \in [0, 1]$, say, and then use a standard polynomial approximation in terms of the η coordinate. It has been argued by Grosch & Orszag (1977) that, for the type of problems found in fluid dynamics (i.e., smoothly decaying fields), algebraic mappings are better suited than exponential ones[9]. The authors compared both types of mapping with the truncated domain approximation for many different problems, including those considered typical of fluid dynamics. One of the advantages of the algebraic mapping is that algebraically decaying functions can be exactly represented by polynomial expressions in the mapped domain. Note that, when using such algebraic mappings, it only becomes a matter of convention to talk about a polynomial approximation in terms of the mapped η coordinate instead of a rational function approximation in r. One way or the other, this may certainly be seen to represent a better approximation of the infinite than just a simple domain truncation.

On the other hand, at the same time as they provide a better approximation of the asymptotic behavior of the field equations, mappings also have the foreseeable side-effect of steepening the already existing gradients. In that context, some flexibility

[9]There is the notable exception of Spalart et al. (1991) who used an exponential mapping for the boundary layer problem. In that case, extra functions were added to take into account the specific slower decaying behaviors.

in the resolution positioning would seem a desirable feature since standard global polynomial expansions only provide very regular resolution spreadings. This last characteristic can in turn result in an important efficiency loss in the approximation of functions having very steep gradients, i.e., the requirement of a practically too great number of expansion functions to reach spectral convergence, or even only a certain level of error. To gain in resolution flexibility, more sophisticated mapping functions can be used, e.g., as in Stanaway et al. (1988), but the price to pay in that case was the systematic loss of spectral convergence, and full matrices in (2.44) and (2.45).

Another way of gaining in resolution flexibility is by considering domain partitioning. Instead of using polynomial approximations over the whole mapped domain, the latter can be partioned into sub-domains in which, then, polynomial approximations are used. In other words, this means using a piecewise polynomial approximation instead of a polynomial one. The use of piecewise polynomials, i.e., of a *local* approximation, brings us back to the definition of the functional space Y in (2.18). The requirement that the approximation space V^J form a dense subspace of Y combined with the set of vector expansions defined in (2.33)–(2.40) leads to the necessary condition that G_l has a continuous first order derivative, i.e., that

$$\boxed{G_l \in C^1} \tag{2.46}$$

This condition is defined in terms of the standard radial coordinate r and must be preserved under mapping transformations.

Because of the "continuity constraint" (2.46), the choice of basis, or interpolation functions, for the G_l becomes somewhat more limited in practice. Indeed, the explicit imposition of this C^1-condition would result in cumbersome implementation technicalities that could be avoided by using a set of basis functions that naturally satisfy (2.46). This of course precludes, among other things, the use of spectral elements (Patera, 1984) which only satisfy a C^0-condition. On the other hand, following the standard formulation used in the finite element method (Strang & Fix, 1988), C^1-continuity can be implicitly taken into account by considering the function derivative value as a degree of freedom. Hermite interpolation functions are a good example of such built-in C^1-continuity. Higher order interpolation functions can also be built by a generalization of this approach, i.e., by increasing the number of nodal unknowns

(function or derivative values). There are many clever ways of doing this and we directly refer to the abundant literature for more details (see for example Zienkiewicz & Taylor, 1989 and 1991).

It is nevertheless important to note that, in the context of the present numerical method, imposing the continuity by nodal derivative values is limited in practice to C^1, at most C^2, i.e., the first or second order derivative. A spectral/finite element method, similar to the Petrov-Galerkin formulation of Leonard & Wray (1982), but using a C^2 Birkhoff interpolation (Hamming, 1973) for the radial direction—instead of the shifted Jacobi polynomials—was developed by Dufresne & Dumas (1998a). Although workable, the method showed some stiffness problems that impaired its use as an efficient Navier-Stokes solver (see also Dufresne & Dumas, 1998b, for additional comments). Finally, there is another important type of local interpolation functions that can satisfy an almost arbitrary level of continuity without the stiffness drawback just mentioned: the B-spline interpolation functions, that are discussed next.

2.3.3 Radial direction: B-spline interpolation

In the light of the previous observations, we are now in a position to completely define the radial discretization of (2.43). In order to do so, we first introduce the mapping function that determines the bounded domain, $\eta \in [0,1]$, on which the B-spline discretization will be considered. Then, we get into the presentation of the B-spline interpolation functions themselves.

As precedently discussed, for the type of boundary conditions considered earlier in Sec. 2.1.1, i.e., for smooth (algebraically) decaying functions, algebraic mappings are better suited. In that regard, one the most simple relation that allows to go from the unbounded radial domain, $r \in [0,\infty[$, into the new bounded one, $\eta \in [0,1]$, is certainly

$$\boxed{\eta = \frac{r}{r+L}\,,} \tag{2.47}$$

with L as the adjustable scaling parameter. There are no requirements for a more

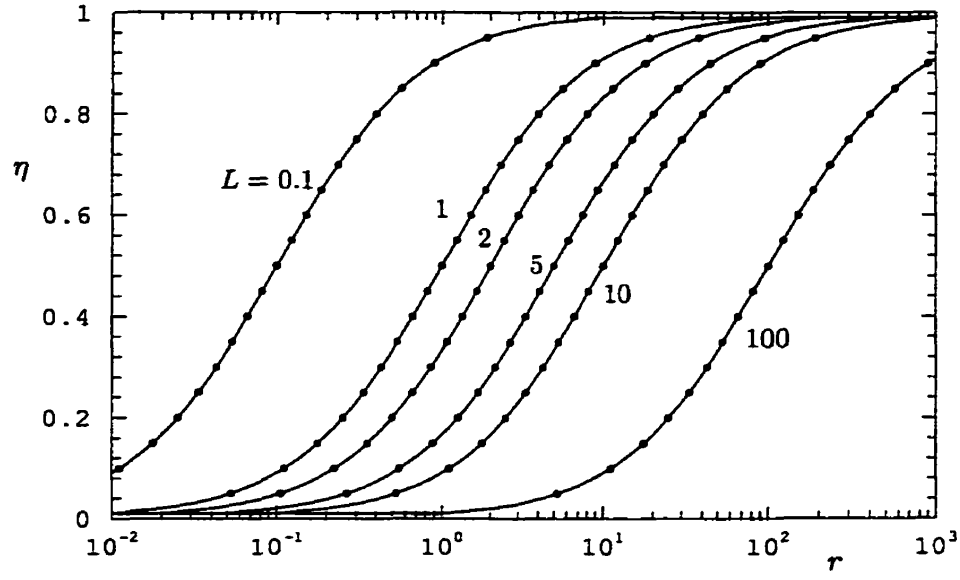

FIGURE 2.1. The mapping function $\eta = r/(r + L)$ for the different values of L directly shown on the figure. The "•" symbols identify a sequence of 20 subdomains uniformly distributed along the η-axis ($\Delta\eta = 0.05$).

complex function to improve resolution positioning, as in Stanaway et al. (1988) for example, since it can all be directly taken into account by the local B-spline discretization. A plot of (2.47) is shown in FIG. 2.1, for some values of L. For a uniform domain partitioning of $\Delta\eta = 0.05$, the resulting Δr discretization is also shown by the set of points on each curve. We may observe that for a given value of L, Δr increases with r, and also that the position of the penultimate point increases with L. At the opposite, the smaller the value of L, the closer to the origin the points are located. As a quick scaling rule of thumb between the two systems of coordinates, let us mention the following simple equivalences:

$$\eta = \frac{1}{4} \Leftrightarrow r = \frac{1}{3}L \quad ; \quad \eta = \frac{1}{2} \Leftrightarrow r = L \quad ; \quad \eta = \frac{3}{4} \Leftrightarrow r = 3L\,.$$

Other complementary information can be found directly in the paper of Grosch & Orszag (1977).

As a consequence of the mapping function (2.47), the algebraic decaying behavior,

expressed by (2.14), is transformed as follows. If a function $g(r)$ behaves as

$$\lim_{r\to\infty} g(r) \;=\; \mathcal{O}(r^{-k_\theta}) \;, \tag{2.48}$$

then it can be shown, after only a few manipulations, that the equivalent condition transforms to

$$\lim_{\eta\to 1} f(\eta) \;=\; \mathcal{O}((1-\eta)^{k_\theta}) \;, \tag{2.49}$$

in terms of the mapped coordinate η. Here, without loss of generality k_θ is assumed to be non-negative (i.e., $k_\theta \geq 0$), and the new function $f(\eta)$ is simply defined by

$$f(\eta) \;\equiv\; g(r(\eta)) \;, \tag{2.50}$$

where $r(\eta)$ is the inverse of (2.47), viz.,

$$r \;=\; \frac{\eta L}{1-\eta} \;. \tag{2.51}$$

One may consequently note that the condition (2.49) is exactly representable by a polynomial of degree k_θ. More specifically, (2.49) is expressed as a k_θ-fold zero condition at $\eta = 1$, i.e., the function $f(\eta)$ and its $k_\theta - 1$ first derivatives are zero at that point. As for the regularity conditions in (2.11), they remain practically unchanged because $\eta \sim r/L$ as r tends to zero. Further considerations and details related to the implementation of these specific conditions are presented in Sec. 3.3.

Now that we have determined the bounded coordinate domain $\eta \in [\,0, 1\,]$, through the mapping function (2.47), we may complete the radial discretization process by giving a specific definition for the basis functions G_l in (2.33)–(2.40). The piecewise polynomial approximation in the η coordinate allows us to directly define

$$\boxed{G_l(r(\eta)) \;\equiv\; B_l(\eta) \;,} \tag{2.52}$$

where B_l is a basis spline function, or B-spline for short. This simple and direct definition is made possible by the Curry & Schoenberg theorem that establishes B-splines as a basis for spline functions (de Boor, 1978). This statement is explained in the presentation of the B-spline basis functions, with some relevant definitions, that is introduced in the remainder of this section.

Before we begin the presentation, let us only mention that a more complete analytical and "practical" description of B-splines can be found in the reference book of de Boor (1978). The material presented here—some of the more technical material being put in App. B—comes, for the major part, from that reference book. It is repeated here for both convenience and completeness purposes only.

As a first step, let us consider the partition of the mapped interval $[0,1]$ into N_d *sub-domains*. The set of N_d+1 partition points that define these sub-domains is called the set of *breakpoints* and is defined such that

$$\{\,\eta_1 = 0 < \eta_2 < \eta_3 < \cdots < \eta_{N_d} < \eta_{N_d+1} = 1\,\}\,, \tag{2.53}$$

written $\{\,\eta_i\,\}_{i=1}^{N_d+1}$ for short. To simplify the presentation, we define here the spline function $f(\eta)$, of order k (or equivalently of degree $k-1$), as a piecewise polynomial function having $k-2$ continuous derivatives[10] at each inner breakpoint $\{\,\eta_i\,\}_{i=2}^{N_d}$, which gives $f(\eta) \in C^{k-2}$. B-splines actually are normalized spline functions[11] having the smallest support in terms of sub-domains. More specifically a B-spline of order k spans exactly k sub-domains. An example of a cubic ($k=4$) B-spline function is shown in FIG. 2.2. We now define an additional set of points $\{\,t_i\,\}_{i=1}^{N_d+2k-1}$, called *knots*, such that

$$\begin{aligned} \eta_1 \;=\; t_1 = t_2 = \cdots = t_k \;\;;\;\; \eta_2 \;=\; t_{k+1} \;\;;\;\; \cdots \\ \cdots \;\;;\;\; \eta_{j+1} \;=\; t_{k+j} \;\;;\;\; \cdots \\ \cdots \;\;;\;\; \eta_{N_d+1} \;=\; t_{k+N_d} = t_{k+N_d+1} = \cdots = t_{k+N_d+k-1}\,. \end{aligned} \tag{2.54}$$

This particular definition implies considerations related to the level of continuity imposed at the breakpoints. A one to one correspondence between knots and breakpoints implies the imposition of $k-1$ conditions of continuity at the breakpoints, while k knots for a breakpoint implies no continuity condition at the breakpoint (see

[10]This more restrictive definition is indeed a particular case of the general spline functions introduced in the Curry & Schoenberg theorem, for which the level of continuity may vary from an inner breakpoint to another. Such general spline functions, to which are associated "generalized" B-splines, are presented in App. B.

[11]The normalization is based of the fact the B-splines are constructed to form a partition of unity. The precise meaning of this statement will be made clearer after a few more definitions.

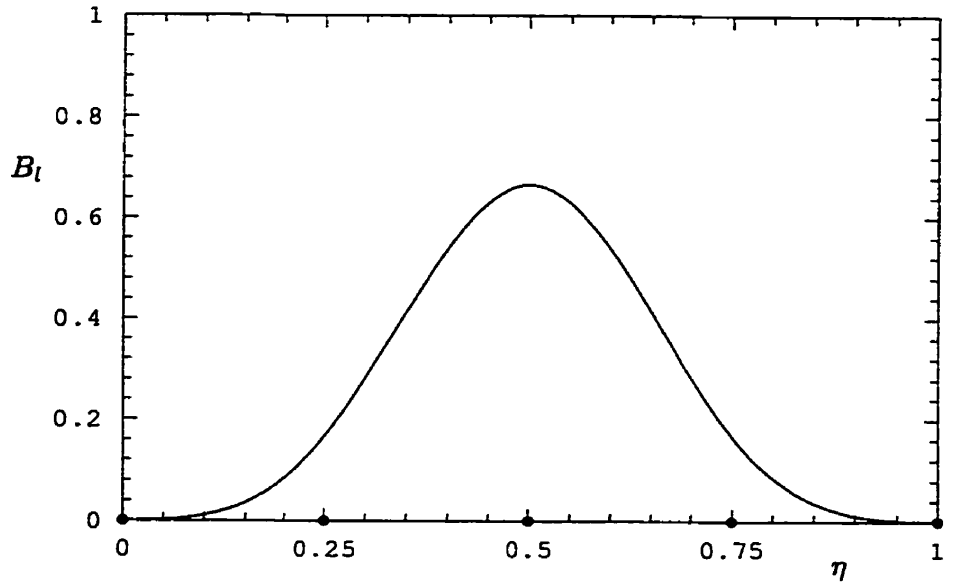

FIGURE 2.2. A cubic B-spline function ($k = 4$). The 4 sub-domains spanned by the function are delimited by the breakpoints identified by the "•" symbols.

App. B for the details). The difference between the knots associated with the inner breakpoints and those of the frontier breakpoints (η_1 and η_{N_d+1}) is a consequence of such considerations and will be explained a little later. For a given set of knots, the lth B-spline of order k, noted here $B_l^{(k)}$—this more general notation will be used for B-splines of generic order k, the more simple notation B_l being used otherwise—can be directly evaluated by the recurrence relation

$$B_l^{(k)}(\eta) = \frac{\eta - t_l}{t_{l+k-1} - t_l} B_l^{(k-1)}(\eta) + \frac{t_{l+k} - \eta}{t_{l+k} - t_{l+1}} B_{l+1}^{(k-1)}(\eta) \,. \tag{2.55}$$

First order B-splines are simply defined as unitary "top hat" functions, viz.,

$$B_l^{(1)}(\eta) = \begin{cases} 1 & ; \quad t_l \leq \eta < t_{l+1} \\ 0 & ; \quad \text{otherwise} \end{cases} \,. \tag{2.56}$$

From the above definitions, many important B-spline properties can be deduced. For example, the recurrence relation (2.55) combined with the first order B-spline

definition (2.56) leads to the support rule

$$B_l^{(k)}(\eta) \;=\; 0 \quad \text{for} \quad \eta \notin [\,t_l,\, t_{l+k}\,]\;. \tag{2.57}$$

Application of this rule to the product of B-splines gives

$$B_{l'}^{(k)}(\eta)\, B_l^{(k)}(\eta) \begin{cases} \neq 0 \;\;;\;\; l'-k+1 \;\leq\; l \;\leq\; l'+k-1 \\ = 0 \;\;;\;\; \text{otherwise} \end{cases}\;. \tag{2.58}$$

This latter result will prove useful in the computation of the different matrices in (2.43) since it confines the non-zero values to a narrow bandwidth of $2k-1$ (see also Sec. 3.3 and App. C for additional information regarding these matrices). It can also be shown, from the above result, that the complete set of B-spline functions—for a given order k and a given set of knots $\{\,t_i\,\}_{i=1}^{N_d+2k-1}$—form a partition of unity, i.e.,

$$\sum_{l=1}^{N_r} B_l^{(k)}(\eta) \;=\; 1\;, \tag{2.59}$$

where the number of B-spline functions N_r is given by

$$\begin{aligned} N_r \;&=\; N_d k - (N_d-1)(k-1)\;, \\ &=\; N_d + k - 1\;. \end{aligned} \tag{2.60}$$

The value of N_r is obtained, in a general manner, by taking the total number of piecewise polynomial coefficients minus the number of continuity conditions. Note that the number N_r also represents the dimension of the B-spline space. The value determined in (2.60) may therefore be seen to be the smallest dimension that can bear a piecewise polynomial space[12], of a given order k, defined by the set of breakpoints $\{\,\eta_i\,\}_{i=1}^{N_d+1}$. This particular property of B-splines is indeed due to their great smoothness, which in turn leads to their relative spreading.

On the other hand, because B-splines extend over various sub-domains, they cannot be considered as a strictly local basis. For that reason, special considerations

[12]If additional continuity conditions are added between any two sub-domains, to reduce the number of coefficients, then the two adjacent piecewise polynomials will collapse into one. Ultimately, imposing k continuity conditions at all the inner breakpoints would result in a single polynomial, of order k, for the whole domain.

must be given to basis functions lying near the edges of the domain. Regular or standard B-splines, i.e., spanning k sub-domains, would need to extend outside the physical boundaries. One way of coping with that would be to extend the domain with an artificial buffer region. Another more convenient and consistent way—the interpolated function making no sense outside the physical limits—would be to reduce the continuity at the edges from C^{k-2} to zero-continuity (or C^{-1} by extension of notation). In other words, it means collapsing the buffer region into the frontier points themselves. Note that this is the procedure implied by the knot definition in (2.54). This will partly affect the $k-1$ B-splines located near the edges. A resulting simple but complete set of basis functions is shown in FIG. 2.3, for both a uniform and a non-uniform domain partitioning with $N_d = 4$ and $k = 4$. A more realistic picture of what would typically be used for a radial discretization is shown in FIG. 2.4 where again $k = 4$ but with this time $N_d = 50$ (uniform distribution of breakpoints).

In terms of the basis function G_l used in the definition of the vector expansions (2.33)–(2.40), the radial equivalent of all of the above B-spline results can be rewritten by simply applying the coordinate transform (2.47) to the definition (2.52). An illustration of the function G_l that corresponds to the B-spline of FIG. 2.2 is given in FIG. 2.5, for different values of L. Since it only becomes a matter of convention to use $G_l(r)$ instead of $B_l(\eta)$, we do not elaborate any further except maybe to stress the point that in the vector expansions, as they were defined, all derivatives are given in terms of the radial coordinate r. In terms of the coordinate η and the B-spline B_l, the first order radial derivative of $G_l(r)$ is thus given by

$$\frac{d}{dr} G_l(r(\eta)) = \frac{d\eta}{dr} \frac{d}{d\eta} B_l(\eta) , \tag{2.61}$$

with

$$\frac{d\eta}{dr} = \frac{L}{(r+L)^2} = \frac{(1-\eta)^2}{L} . \tag{2.62}$$

Higher order derivatives are obtained by a successive application of this operation.

We conclude this presentation by the introduction of the modal (complex valued) spline functions that will serve for the implementation of the regularity/boundary conditions, discussed in the following chapter. For each modal pair (m, n), the two "+"

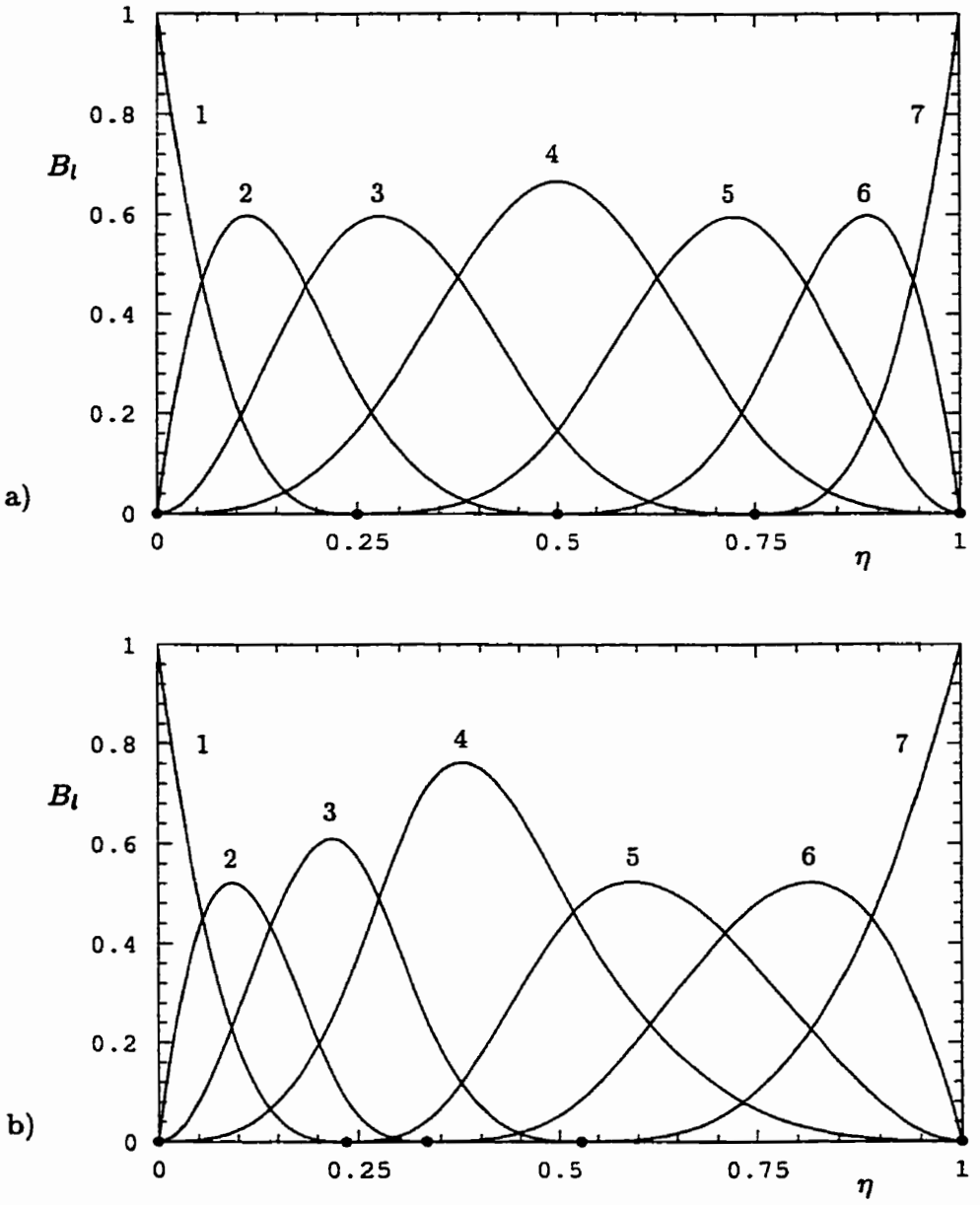

FIGURE 2.3. A uniform a) and non-uniform b) B-spline partition for the domain $[0,1]$. The number of sub-domains is $N_d = 4$ (identified by the "•" symbols) and the order of the B-splines is $k = 4$; for a total of 7 basis functions. The respective index l is shown on top of each function. The B-spline of FIG. 2.2 corresponds to B_4 of a). Also note the "irregularity" of the 3 adjacent B-splines at each one of the end points 0 and 1.

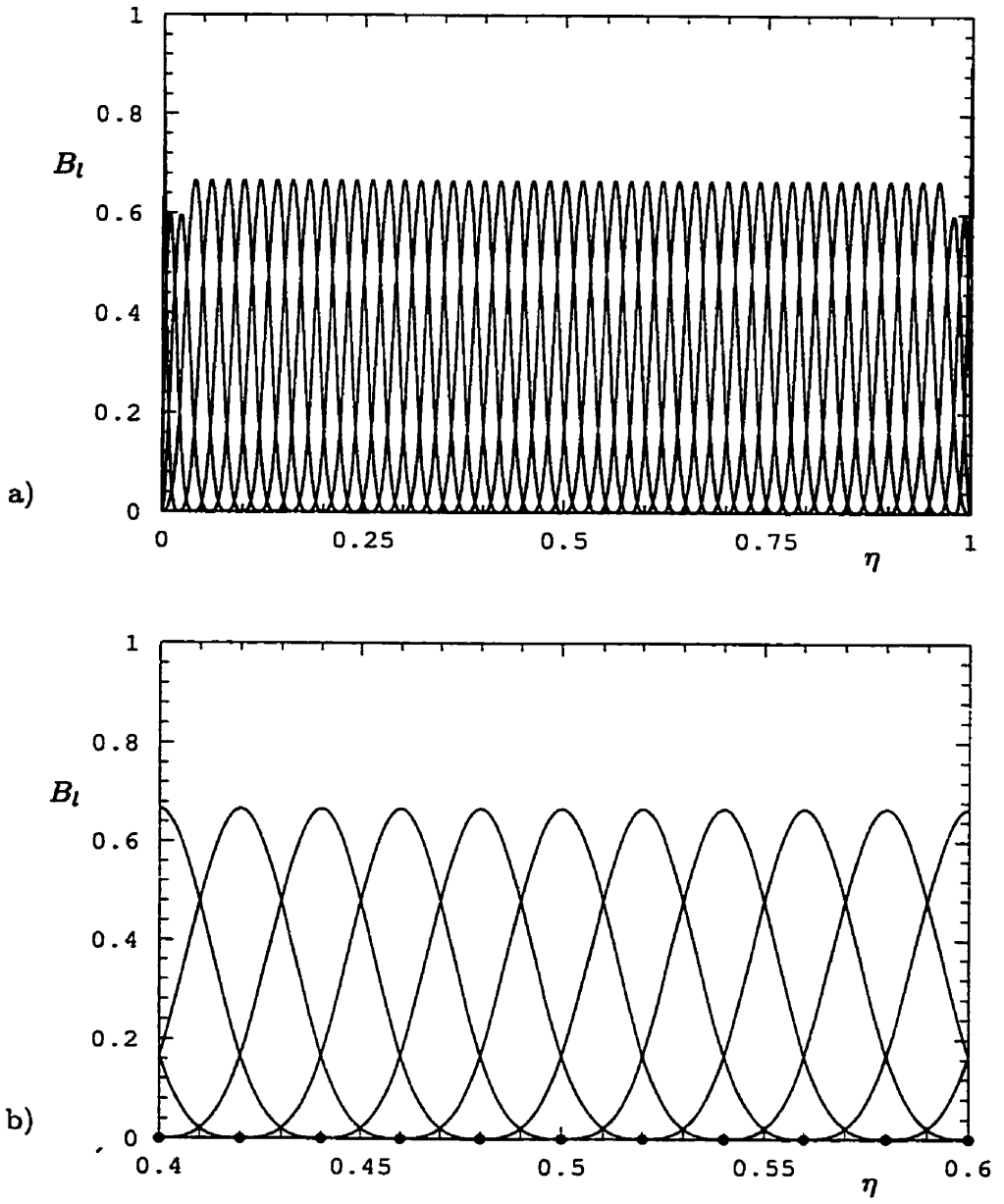

FIGURE 2.4. A uniform B-spline partition for the domain $[0,1]$ with $N_d = 50$ and $k = 4$. The complete domain and B-spline partition is shown in a). A close-up vue of the interval $[0.4, 0.6]$ is shown in b); the uniformly distributed breakpoints (the "•" symbols) are also shown in that second figure.

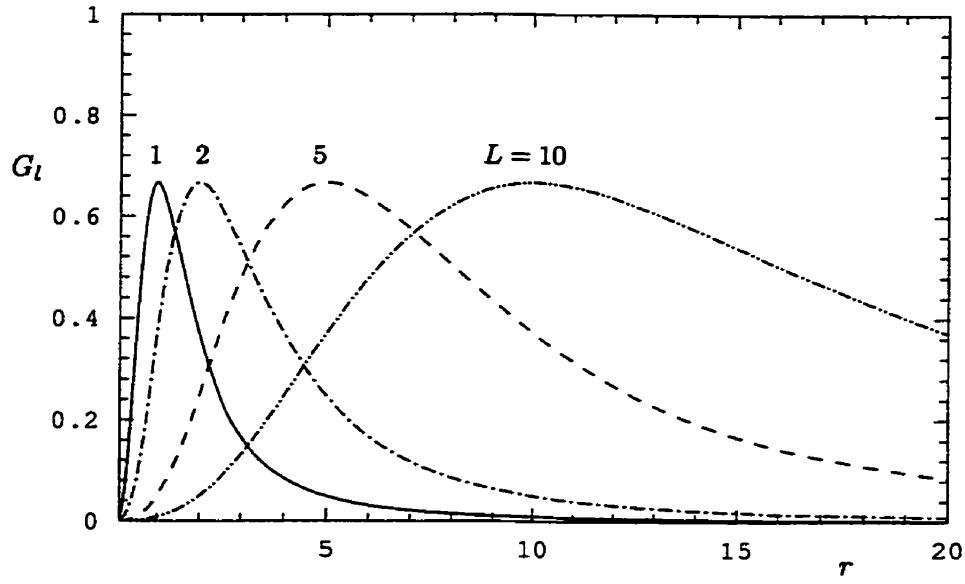

FIGURE 2.5. The basis functions G_l corresponding to the B-spline of FIG. 2.2 for the different mapping parameters $L = 1, 2, 5, 10$. The values are shown on top of each respective function.

and "$-$" functions can either be written in r or in η to give

$$g^{\pm}_{mn}(r) = \sum_{l=1}^{N_r} \alpha^{\pm}_{lmn}\, G_l(r) \quad \Longleftrightarrow \quad f^{\pm}_{mn}(\eta) = \sum_{l=1}^{N_r} \alpha^{\pm}_{lmn}\, B_l(\eta)\ . \tag{2.63}$$

This completes the spatial discretization and thus completely determines the nature of the semi-discrete (continuous in time) system of differential-algebraic equations in (2.43).

2.4 Spatial discretization: Summary

This section provides a synoptic presentation of the spatial discretization described in this chapter.

- The equation to be discretized

$$\left\langle \mathbf{\Phi},\, \frac{\partial \mathbf{u}}{\partial t} \right\rangle = -\frac{1}{Re} \langle \nabla \times \mathbf{\Phi},\, \nabla \times \mathbf{u} \rangle + \langle \mathbf{\Phi},\, \mathbf{F} \rangle$$

with

$$\mathbf{F} \;=\; \mathbf{u} \times \boldsymbol{\omega} \;+\; \mathbf{F}_e$$

- Definition of the inner product

$$\langle \mathbf{v}\,, \mathbf{u} \rangle \;\equiv\; \int_0^{L_z} \int_0^{L_\theta} \int_0^{\infty} \mathbf{v}^* \cdot \mathbf{u}\; r\, dr d\theta dz$$

- Velocity and weight vector expansions

$$\mathbf{u}(r, \theta, z, t) \;=\; \sum_l \sum_m \sum_n \alpha_{lmn}\,(t)\; \mathbf{W}_l(r\,;\; k_\theta, k_z)\, e^{ik_\theta \theta} e^{ik_z z}$$

$$\mathbf{\Phi}(r, \theta, z) \;=\; \mathbf{W}_{l'}(r\,;\; k'_\theta, k'_z)\, e^{ik'_\theta \theta} e^{ik'_z z}$$

- Vector decomposition (the $\mathbf{W}_l^{\pm}$ are specified in TABLE 2.1 that follows)

$$\alpha_{lmn}\, \mathbf{W}_l \;=\; \alpha^+_{lmn}\, \mathbf{W}^+_l \;+\; \alpha^-_{lmn}\, \mathbf{W}^-_l$$

- Mapping function

$$\eta \;=\; \frac{r}{r + L}$$

- Radial basis functions

$$G_l(r) \;\equiv\; B_l(\eta)$$

- B-spline recurrence relation

$$B_l^{(k)}(\eta) \;=\; \frac{\eta - t_l}{t_{l+k-1} - t_l}\, B_l^{(k-1)}(\eta) \;+\; \frac{t_{l+k} - \eta}{t_{l+k} - t_{l+1}}\, B_{l+1}^{(k-1)}(\eta)$$

with

$$B_l^{(1)}(\eta) \;=\; \begin{cases} 1 \;\;;\;\; t_l \le \eta < t_{l+1} \\ 0 \;\;;\;\; \text{otherwise} \end{cases}$$

- Radial scalar (spline) functions

$$g^{\pm}_{mn}(r) \;=\; \sum_{l=1}^{N_r} \alpha^{\pm}_{lmn}\, G_l(r) \quad \Longleftrightarrow \quad f^{\pm}_{mn}(\eta) \;=\; \sum_{l=1}^{N_r} \alpha^{\pm}_{lmn}\, B_l(\eta)$$

- Modal evolution equations for the $\alpha^{\pm}_{lmn}$ coefficients

$$\begin{aligned} \mathsf{A}^{+}_{+}\dot{\alpha}^{+} \;+\; \mathsf{A}^{-}_{+}\dot{\alpha}^{-} \;&=\; \mathsf{B}^{+}_{+}\alpha^{+} \;+\; \mathsf{B}^{-}_{+}\alpha^{-} \;+\; \mathsf{F}^{+} \\ \mathsf{A}^{-}_{-}\dot{\alpha}^{-} \;+\; \mathsf{A}^{+}_{-}\dot{\alpha}^{+} \;&=\; \mathsf{B}^{-}_{-}\alpha^{-} \;+\; \mathsf{B}^{+}_{-}\alpha^{+} \;+\; \mathsf{F}^{-} \end{aligned}$$

- Inertia and viscous matrices

$$\begin{aligned} [\,\mathsf{A}^{\gamma}_{\delta}\,]_{l'l} \;&=\; \int_0^{\infty} \left(\mathbf{W}^{\delta}_{l'}\right)^{*} \cdot \left(\mathbf{W}^{\gamma}_{l}\right)\, r\, dr \\ [\,\mathsf{B}^{\gamma}_{\delta}\,]_{l'l} \;&=\; -\frac{1}{Re} \int_0^{\infty} \left(\widehat{\nabla\times}\mathbf{W}^{\delta}_{l'}\right)^{*} \cdot \left(\widehat{\nabla\times}\mathbf{W}^{\gamma}_{l}\right)\, r\, dr \end{aligned}$$

TABLE 2.1. The four modal families of vector expansions defined in (2.33)–(2.40).

	$k_\theta > 0$	$k_\theta = 0$
$k_z \neq 0$	$\mathbf{W}_l^+ = k_z \begin{Bmatrix} -ik_\theta G_l \\ (rG_l)' \\ 0 \end{Bmatrix}$, $\mathbf{W}_l^- = \begin{Bmatrix} -ik_z G_l \\ k_z G_l \\ G_l' + (1-k_\theta) r^{-1} G_l \end{Bmatrix}$ $\mathbf{\Psi}_l^+ = \begin{Bmatrix} 0 \\ 0 \\ -k_z r G_l \end{Bmatrix}$, $\mathbf{\Psi}_l^- = \begin{Bmatrix} -iG_l \\ G_l \\ 0 \end{Bmatrix}$	$\mathbf{W}_l^+ = \begin{Bmatrix} 0 \\ k_z G_l \\ 0 \end{Bmatrix}$, $\mathbf{W}_l^- = \begin{Bmatrix} -ik_z G_l \\ k_z G_l \\ G_l' + r^{-1} G_l \end{Bmatrix}$ $\mathbf{\Psi}_l^+ = \begin{Bmatrix} -iG_l \\ 0 \\ 0 \end{Bmatrix}$, $\mathbf{\Psi}_l^- = \begin{Bmatrix} -iG_l \\ G_l \\ 0 \end{Bmatrix}$
$k_z = 0$	$\mathbf{W}_l^+ = \begin{Bmatrix} -ik_\theta G_l \\ (rG_l)' \\ 0 \end{Bmatrix}$, $\mathbf{W}_l^- = \begin{Bmatrix} 0 \\ 0 \\ G_l' + (1-k_\theta) r^{-1} G_l \end{Bmatrix}$ $\mathbf{\Psi}_l^+ = \begin{Bmatrix} 0 \\ 0 \\ -rG_l \end{Bmatrix}$, $\mathbf{\Psi}_l^- = \begin{Bmatrix} -iG_l \\ G_l \\ 0 \end{Bmatrix}$	$\mathbf{W}_l^+ = \begin{Bmatrix} 0 \\ G_l \\ 0 \end{Bmatrix}$, $\mathbf{W}_l^- = \begin{Bmatrix} 0 \\ 0 \\ r^{-1} G_l \end{Bmatrix}$ $\mathbf{\Psi}_l^+$, $\mathbf{\Psi}_l^-$ indeterminate†

† The corresponding stream vector components (the stream functions) are determined from the integral of the velocity components and are therefore only known up to a constant value in this case (see also Sec. D.5.3 in the appendices).

Chapter 3

Implementation

In this chapter we cover some specific considerations related to the implementation of the spatial discretization presented in Chap. 2. More specifically, we discuss the time discretization and the computation of the nonlinear term. Related to these two main topics are the implementation of the regularity/boundary conditions on the effective matrices as well as the inclusion of an azimuthal modal reduction algorithm. Due to their relative importance, these two latter subjects are the object of a separate presentation. Also discussed in this chapter are the bounded domain formulation, and the application of the spatial discretization to obtain a linear stability eigenvalue solver.

For the presentation of the material in this chapter, we have voluntarily chosen a simplified notation, trying to avoid the sometimes quite cumbersome implementation details. The more technically oriented reader may however be referred to the appendices in which we have relegated most of that specific information. Frequent references will indeed be made to both App. C and D. In the first, is included all the material related to the construction of the different matrices (Sec. C.1) as well as some of the material related to the treatment of the nonlinear term (Sec. C.2). The rest of the implementation information is found in App. D, e.g., regularity and boundary conditions, time integration, modal reduction, etc. Because of the similarity that bears the present method with the one presented by LMMC, some of the material included in these appendices may appear redundant with what can be found in their report. We nevertheless chose to include it here too for reasons of completeness and

ease of access.

Finally, let us simply mention that all the coding was done in standard, double precision, FORTRAN 77. The different resulting codes were run on various types of Unix platforms, ranging from HP workstations to a SGI Origin2000 supercomputer. Some smaller 2-D versions of the different codes (Houde, 2001) have also been ported on Pentium personal computers.

3.1 Time integration

At this point, the system of ODE's in (2.43) only remains to be discretized in time. Standard time integration for such a set of equations is usually carried out using mixed explicit/implicit schemes (Canuto et al., 1988; Gottlieb & Orszag, 1977). The nonlinear term is integrated explicitly to avoid the costly iterations associated with the nonlinearities while implicit integration is used for the linear viscous term to avoid the too stringent stability criterion that comes with the second order Laplacian operator. Because of the time step size imposed by the stability criterion of the explicit part of the scheme, time discretization errors generally remain significantly below spatial errors and standard integration techniques—finite difference type discretization of the time derivative—are sufficient. Common practice makes use of at least second order time schemes to prevent the leading order error term to directly affect the physical viscous dynamics of the problem.

Note that there are some lower order exceptions—like in Matsushima & Marcus (1997) who used a first order scheme—that could possibly be well justified by a more proper balance between spatial and temporal errors. The presence of "numerical diffusion" could also be used to filter the high wavenumber structures and hence prevent the saturation of the spatial discretization when using marginal resolution but it should be considered an unorthodox procedure that deserves caution. Instead, the use of an additional higher order dissipation term (e.g., the biharmonic term $-\nu_4\nabla^4\mathbf{u}$) should be considered for this particular task.

For the present implementation, we adopted the mixed low-storage, Runge-Kutta type scheme presented by Spalart et al. (1991), and suitably called here the SMR

scheme (for Spalart, Moser and Rogers). The scheme is formally third order for the convective and crossed terms, and second order for the viscous one. The marginal stability curve of this scheme is presented in FIG. D.1. Supplementary information regarding this scheme can be found directly in the reference paper or in the appendices (Sec. D.1). Some comparison results with the other mixed Crank-Nicolson/Adams-Bashforth-2 scheme are also included in Sec. D.1. The application of the 3 sub-steps of the SMR scheme (see also (D.4)–(D.6)) to the differential-algebraic system of equations (2.43) is shown in TABLE 3.1.

The $\widetilde{\mathsf{A}}$ and $\widetilde{\mathsf{B}}$ are respectively the inertia and diffusion matrices introduced earlier in Chap. 2, but in a reorganized form that combines simultaneously the "+" and "−" classes. The computation of these matrices is discussed in more details in Sec. 3.3. The $\widetilde{\mathsf{F}}_{l'}$ is the "+/− combined" nonlinear term, to be detailed in Sec. 3.2. As for the spectral/B-spline coefficients $\widetilde{\alpha}_l$, they follow the same convention used for the other terms. The modal pair (k_θ, k_z) dependence of the various expressions has been implicitly assumed through out. Finally, the subscripts "$*$" and "$**$" identify the two intermediary sub-time steps used when marching from time step n to $n+1$.

The implementation of these sub-steps can be synthesized by the algorithm given in TABLE 3.2. Since the same algorithm applies almost identically for the three sub-steps, we make use here of a generic notation in which the index i identifies the sub-step number and the subscripts 1 and 2 identify respectively the present known time level (viz., n, $*$ or $**$), and the next one to be computed. Note that for the first sub-step ($i = 1$), the $\{\widetilde{\mathsf{F}}\}_0$ vector is zero, and so the transfer in line 3 need not be executed at the end of the third sub-step ($i = 3$). Some of the operations described in the algorithm are themselves the object of a specific section in this chapter; the relevant section numbers are directly pointed out in TABLE 3.2.

TABLE 3.1. The SMR time integration scheme proposed by Spalart et al. (1991) and applied to the algebraic system of equations (2.43). The " ~ " symbol stands for a combination of the "+" and "−" classes. See text for further information

- Sub-step 1

$$\left[\widetilde{\mathsf{A}} - \alpha_1 \Delta t \widetilde{\mathsf{B}}\right] \left\{ \widetilde{\alpha}_l \right\}_* = \left[\widetilde{\mathsf{A}} - \beta_1 \Delta t \widetilde{\mathsf{B}}\right] \left\{ \widetilde{\alpha}_l \right\}_n + \gamma_1 \Delta t \left\{ \widetilde{\mathsf{F}}_{l'} \right\}_n$$

$$\alpha_1 = \frac{29}{96} \qquad \beta_1 = \frac{37}{160} \qquad \gamma_1 = \frac{8}{15}$$

- Sub-step 2

$$\left[\widetilde{\mathsf{A}} - \alpha_2 \Delta t \widetilde{\mathsf{B}}\right] \left\{ \widetilde{\alpha}_l \right\}_{**} = \left[\widetilde{\mathsf{A}} - \beta_2 \Delta t \widetilde{\mathsf{B}}\right] \left\{ \widetilde{\alpha}_l \right\}_* + \gamma_2 \Delta t \left\{ \widetilde{\mathsf{F}}_{l'} \right\}_* + \zeta_1 \Delta t \left\{ \widetilde{\mathsf{F}}_{l'} \right\}_n$$

$$\alpha_2 = -\frac{3}{40} \qquad \beta_2 = \frac{5}{24} \qquad \gamma_2 = \frac{5}{12} \qquad \zeta_1 = -\frac{17}{60}$$

- Sub-step 3

$$\left[\widetilde{\mathsf{A}} - \alpha_3 \Delta t \widetilde{\mathsf{B}}\right] \left\{ \widetilde{\alpha}_l \right\}_{n+1} = \left[\widetilde{\mathsf{A}} - \beta_3 \Delta t \widetilde{\mathsf{B}}\right] \left\{ \widetilde{\alpha}_l \right\}_{**} + \gamma_3 \Delta t \left\{ \widetilde{\mathsf{F}}_{l'} \right\}_{**} + \zeta_2 \Delta t \left\{ \widetilde{\mathsf{F}}_{l'} \right\}_*$$

$$\alpha_3 = \frac{1}{6} \qquad \beta_3 = \frac{1}{6} \qquad \gamma_3 = \frac{3}{4} \qquad \zeta_2 = -\frac{5}{12}$$

TABLE 3.2. Generic time marching algorithm for each one of the sub-time steps of the time integration scheme of TABLE 3.1. The particular sub-time step is identified with the index i. See text for further information.

1. From $\{\widetilde{\alpha}\}_1$ evaluate $\left\{\widetilde{\mathsf{F}}\right\}_1 \Rightarrow$ Sec. 3.2 ;
2. For each modal pair $k_\theta \geq 0$ and k_z:
   (a) Compute the effective matrices $\left[\widetilde{\mathsf{A}}\right]$ and $\left[\widetilde{\mathsf{B}}\right] \Rightarrow$ Sec. 3.3 ;
   (b) Evaluate the RHS vector $\{\mathsf{f}\}$:
      i. Evaluate $[\mathsf{K}_1] = \left[\widetilde{\mathsf{A}} - \beta_i \Delta t \widetilde{\mathsf{B}}\right]$;
      ii. Evaluate $\{\mathsf{f}_\mathsf{K}\} = [\mathsf{K}_1]\{\widetilde{\alpha}\}_1$;
      iii. Sum the contributions from the nonlinear vector(s): $\{\mathsf{f}\} = \{\mathsf{f}_\mathsf{K}\} + \gamma_i \Delta t \left\{\widetilde{\mathsf{F}}\right\}_1 + \zeta_{i-1} \Delta t \left\{\widetilde{\mathsf{F}}\right\}_0$;
   (c) Evaluate $[\mathsf{K}_2] = \left[\widetilde{\mathsf{A}} - \alpha_i \Delta t \widetilde{\mathsf{B}}\right]$;
   (d) Impose the regularity/boundary conditions on the system of equations $[\mathsf{K}_2]\{\widetilde{\alpha}\}_2 = \{\mathsf{f}\} \Rightarrow$ Sec. 3.3 ;
   (e) Solve $[\mathsf{K}_2]\{\widetilde{\alpha}\}_2 = \{\mathsf{f}\}$;
3. Replace $\left\{\widetilde{\mathsf{F}}\right\}_0$ by $\left\{\widetilde{\mathsf{F}}\right\}_1$;

Because of the explicit integration of the nonlinear convective terms, the scheme is only conditionally stable. The stability condition is characterized by a ratio between the magnitude of the local convective velocity over the "grid velocity": the CFL number (Ferziger, 1981). Here, we use the following hyperbolic type definition

$$\mathrm{CFL} \equiv \frac{2}{3}\pi \, \Delta t \, \max\left[\frac{|u_r|}{\Delta r} + \frac{|u_\theta|}{r\Delta\theta} + \frac{|u_z|}{\Delta z} \right], \tag{3.1}$$

where Δr, $\Delta\theta$ and Δz are the collocation points spacing (see also Sec. 3.2), and the "max" is taken over the whole computational domain. The 2/3 and the π factors come from the spectral equivalent of the condition where, for example, the maximum wavenumber $k_{z\,\mathrm{max}}$ is related to the "de-aliased" grid (collocation points) spacing Δz

by $k_{z\,\max}\,\Delta z = \frac{2}{3}\pi$. This is a matter of convention that only affects the critical limit value of the CFL condition. The effective stability limit of a particular computation, whatever the definition used, can obviously always be found by numerical testing. With definition (3.1) though, the scheme has a critical stability limit, for purely convective flows, of CFL $\leq \sqrt{3} \approx 1.73$, as shown by the marginal stability curve in FIG. D.1. Note that this numerical value actually comes from a 1-D linear analysis of the scheme, but its application to the conservative 3-D criterion (3.1) certainly poses no problem. When diffusion is present, values up to 2 (and possibly higher) can be used, as reported by Spalart et al. and confirmed by our own testing.

The evaluation of the maximum time step allowable (granting stability) is done at regular intervals during a simulation to ensure that (3.1) is indeed satisfied throughout the computational domain. Thus, each one of the velocity vector components has to be computed on all the collocation points. In cylindrical coordinates, there is a clustering of these collocation points near the center of the domain (i.e., as $r \rightarrow 0$) and this may lead to some very severe limitations on the time step size if no special care is taken. This particular but important issue is one of the main topics of Sec. 3.4. For this reason, we put that matter aside for now as we shall come back to it in a little later. Let us note, in addition, that some specific examples of collocation grids are also presented in that latter section.

Another point worth mentioning when evaluating the time step size is that the CFL condition has to be considered in terms of the total velocity field (2.7)

$$\mathbf{u} \;=\; \mathbf{u}_{\mathrm{h}} + \mathbf{u}_{\mathrm{nh}} \;.$$

The background flow velocity, if different from zero, must therefore be added to the homogeneous (computational) velocity

$$\mathbf{u}_{\mathrm{h}}(r_l, \theta_m, z_n, t) \;=\; \sum_{l}\sum_{m}\sum_{n} \alpha_{lmn}\,(t)\;\mathbf{W}_l(r_l\,;\,k_\theta, k_z)\,e^{ik_\theta\theta_m}e^{ik_z z_n}\;,$$

in (3.1). The set $\{r_l, \theta_m, z_n\}$ defines the set of collocation points on which the "max" is determined. The particular evaluation of each one of the velocity components is detailed in App. C, more specifically in (C.10)–(C.12). Since this operation is quite similar to what is done in the computation of the nonlinear term (see more in Sec. 3.2), the time step update procedure is inserted there. On the other hand, because the

B-spline evaluation (the summation in l) represents an additional cost—as will also be seen in Sec. 3.2—the time step is updated only after a certain, user-defined, time interval (or number of time steps). In rapidly evolving flows, the update interval must be chosen with some care, otherwise numerical instability could possibly set in.

Some care should also be taken in very diffusive flows (low Reynolds number) when only using (3.1) to determine the time step size. The SMR scheme does tend to unconditional stability in the limit of pure diffusion, as can be seen again from FIG. D.1, and large values of Δt may result. The computation would then remain stable but with possibly important precision losses. Note that this type of problem is not a concern here because the flows of interest are dominated by convection. It would nevertheless be advisable, for low Reynolds number flows, to include a diffusive time step criterion based on accuracy rather than stability. From the typical 1-D result

$$\frac{\nu \Delta t}{\Delta x^2} = \left(\frac{|u| \Delta t}{\Delta x}\right) \Big/ \left(\frac{|u| \Delta x}{\nu}\right) < \mathcal{O}(1) ,$$

a 3-D generalization is proposed as

$$\frac{4}{9}\pi^2 \Delta t \max \left[\frac{1}{Re_\Delta} \left(\frac{|u_r|}{\Delta r} + \frac{|u_\theta|}{r \Delta \theta} + \frac{|u_z|}{\Delta z} \right) \right] < \mathcal{O}(1) , \tag{3.2}$$

where the local "grid Reynolds number" may in turn be defined as

$$Re_\Delta \equiv Re \left[(u_r \Delta r)^2 + (u_\theta r \Delta \theta)^2 + (u_z \Delta z)^2 \right]^{\frac{1}{2}} .$$

This accuracy check can easily be implemented by comparing the ratio of the CFL number with the local Reynolds number Re_Δ when updating the time step size.

3.2 Nonlinear term

The computation of the nonlinear term (line 1. of TABLE 3.2) is certainly one of the most complex parts of the Navier-Stokes solver. For its implementation, we followed the procedure described by LMMC which is based on a modified version of the classical pseudo-spectral algorithm (Canuto et al., 1988; Boyd, 1999). In the presentation given below, emphasis is mostly put on the non-standard treatment of the B-spline radial direction. Because the mathematical expressions that result from

this particular treatment are quite involved, we have relegated them in the second half of App. C, making use here of only generic formulas. In this attempt at keeping the expressions as light as possible, we admittedly sacrificed some rigor of notation for simplicity.

First, let us recall from Chap. 2 that the nonlinear term is given, according to the definition of the inner product in (2.16), such that

$$\frac{1}{L_\theta L_z}\,\langle \mathbf{V}_j\,,\mathbf{F}\rangle \;=\; \frac{1}{L_\theta L_z}\int_0^{L_\theta}\!\!\int_0^{L_z}\!\!\int_0^{\infty} (\mathbf{V}_j)^*\cdot\,\mathbf{F}\,r\,dr d\theta dz\;, \tag{3.3}$$

where

$$\mathbf{F} \;=\; \mathbf{u}\times\boldsymbol{\omega} \;+\; \mathbf{F}_e\;,$$

and $\mathbf{V}_j$ as given in (2.30). Both vectors $\mathbf{u}$ and $\boldsymbol{\omega}$ are understood to be homogeneous, according to the notation convention set in that chapter. All the non-homogeneous extra forcing known terms are included in $\mathbf{F}_e$, where for example

$$\mathbf{F}_e \;=\; \mathbf{u}_{\rm nh}\times\boldsymbol{\omega} \;+\; \frac{1}{Re}\nabla^2\mathbf{u}_{\rm nh} \;-\; \frac{\partial\,\mathbf{u}_{\rm nh}}{\partial t} \;+\; \text{other terms}\;. \tag{3.4}$$

The vorticity field follows, by definition, a similar decomposition and may also lead to rotational non-homogeneous forcing.

Now, since the nonlinear term is treated explicitly in the time integration scheme (see TABLE 3.1), the integrals in (3.3) are evaluated at a specific time where all quantities are known. In a general manner, the integrals in (3.3) can be evaluated numerically by some general quadrature rule. This requires that the integrand

$$\left[\;(\mathbf{V}_j)^*\cdot\,\mathbf{F}\,r\;\right]_{\{\,r_l,\theta_m,z_n\,\}}\;,$$

needs to be evaluated on some set of quadrature points defined by $\{\,r_l,\theta_m,z_n\,\}$. The particular choice of quadrature points obviously depends on the type of expansions used to represent the basis vector functions $\mathbf{V}_j$, and the forcing vector $\mathbf{F}$.

To get a better idea of the algorithm, let us go one step ahead by substituting the vector expansions defined in (2.29) and (2.30) into (3.3). For simplicity, we only

consider the homogeneous part of the nonlinear term, and obtain

$$\frac{1}{L_\theta L_z}\iiint \mathbf{W}^{\pm\,*}_{l'm'n'}\, e^{-ik'_\theta\theta}e^{-ik'_z z}\cdot\left[\sum_l\sum_m\sum_n \alpha^{\pm}_{lmn}\mathbf{W}^{\pm}_{lmn}\, e^{ik_\theta\theta}e^{ik_z z}\times \nabla\times\left(\sum_{l_*}\sum_{m_*}\sum_{n_*}\alpha^{\pm}_{l_*m_*n_*}\mathbf{W}^{\pm}_{l_*m_*n_*}\, e^{ik_{\theta_*}\theta}e^{ik_{z_*}z}\right)\right] r\,dr\,d\theta\,dz\ . \tag{3.5}$$

The pseudo-spectral algorithm is a very standard, well documented (Canuto et al., 1988; Boyd, 1999), efficient procedure for evaluating the sequence of operations illustrated in (3.5). The reader is therefore directly refered to the specialized books just cited for a complete description, and additional considerations regarding the particular technical details.

However, to better explain how the present B-spline treatment differs from the standard procedure, we first give a brief qualitative description of the sequence of operations of a standard pseudo-spectral approach applied to (3.5):

1. The physical velocity and vorticity vectors are evaluated on a collocation grid. This means that the two triple sums (in l, m, n and l_*, m_*, n_*) are evaluated first. In terms of the Fourier components, for example, it amounts to the inverse transform. The choice of collocation points is simply the zeros of the Fourier expansions, and because of particular symmetry properties that come with this choice of points, the operation can be done in a fast way, i.e., by a Fast Fourier Transform (FFT). A similar procedure—that depends on the particular choice of basis functions—is used for the radial direction.

2. Once the physical components are obtained on the collocation/quadrature grid, the nonlinear product $\mathbf{u}\times\boldsymbol{\omega}$ is simply evaluated at each point. Note that since the complete velocity field is now available at this step, the evaluation of the CFL condition (Sec. 3.1) may be done here.

3. Then, the triple integral is evaluated. Because the choice of collocation points corresponds to the quadrature points of the different expansions, the transformation integrals can be computed exactly. Considering again the Fourier directions for example, this step simply corresponds to a direct transform which is

again done with a FFT. According to the type of (global) expansions used for the radial direction, the integral can be evaluated with either a fast transform (using Chebyshev polynomials) or with a slow one (using Jacobi polynomials for example), as in step 1.

In brief, these three steps state that because of the fast (Fourier) transforms, it is more efficient to start from the spectral space, go into the physical space to carry out the nonlinear product, and then come back into the spectral space. Of course the equivalent result could be obtained much more expensively by doing the operation in reverse order, i.e., by evaluating first the integrals (analytically) and then compute the summations. This implies that one stays at all times in the spectral coefficients space. The computational cost associated with this second approach would be far more expensive, as mentioned, because of the convolution sum that would then need to be computed[1].

Before considering in more depth the technical aspects of using B-splines in (3.5) that led us to a different algorithm, let us first introduce a more symbolic notation in which we completely separate the spectral-Fourier functional dependency from the radial B-splines[2]. Following this, the spectral velocity and vorticity vectors components—expressed in detailed form in App. C by (C.10)–(C.12) and (C.7)–(C.9) respectively—can be written in terms of some scalar functionals, symbolized by

$$\begin{aligned} \hat{\mathbf{u}}(r;\, k_\theta, k_z) \cdot \hat{\mathbf{e}}_p &= \left[\sum_l \alpha^{\pm}_{lmn} \mathbf{W}^{\pm}_l(r;\, k_\theta, k_z) \right] \cdot \hat{\mathbf{e}}_p \\ &= \sum_l \widehat{\mathcal{U}}^p_{lmn}(\alpha^{\pm}_{lmn}, k_\theta, k_z)\; \mathcal{G}^p_l(G_l, G'_l)\;; \end{aligned} \tag{3.6}$$

[1]This result is a natural consequence of the convolution theorem associated with Fourier (or other) transforms that states in simple terms that: the product of two functions in one space (physical) amounts to the convolution of these two functions in the transformed (spectral) space, and vice versa.

[2]This operation is feasible in principle because of the separation of variables approach that was used to construct the expansions in the first place. It can be technically achieved by rewriting the problem in terms of the scalar functions used to construct the vector expansions. Again, see Sec. C.2 for details.

and

$$\widehat{\omega}(r;\, k_\theta, k_z)\cdot\hat{\mathbf{e}}_q \;=\; \left[\widehat{\nabla\times}\;\widehat{\mathbf{u}}(r;\, k_\theta, k_z)\right]\cdot\hat{\mathbf{e}}_q$$

$$= \sum_l \widehat{\mathcal{W}}^q_{lmn}(\alpha^{\pm}_{lmn}, k_\theta, k_z)\;\mathcal{H}^q_l(G_l, G'_l, G''_l)\;. \qquad (3.7)$$

The unit directional vector $\hat{\mathbf{e}}_p$ (or $\hat{\mathbf{e}}_q$) takes either one of the three values of $\{\hat{\mathbf{e}}_r, \hat{\mathbf{e}}_\theta, \hat{\mathbf{e}}_z\}$. To keep the notation as simple as possible, we also discard spatial variable dependencies that should be made clear from the context.

The physical scalar coefficients $\mathcal{U}^p_l(\theta_m, z_n)$ and $\mathcal{W}^q_l(\theta_m, z_n)$ are simply obtained, for the set of collocation points $\{\,\theta_m, z_n\,\}$, by an inverse Fourier transform such that

$$\mathcal{U}^p_l \;=\; \sum_m\sum_n \widehat{\mathcal{U}}^p_{lmn}\, e^{ik_\theta\theta_m} e^{ik_z z_n}\;, \qquad (3.8)$$

$$\mathcal{W}^q_l \;=\; \sum_m\sum_n \widehat{\mathcal{W}}^q_{lmn}\, e^{ik_\theta\theta_m} e^{ik_z z_n}\;, \qquad (3.9)$$

and where here

$$-\frac{3}{2}N_\theta \;\le\; m \;\le\; \frac{3}{2}N_\theta \quad \text{and} \quad -\frac{3}{2}N_z \;\le\; n \;\le\; \frac{3}{2}N_z\;.$$

The additional, zero valued, Fourier coefficients (see (2.29) for reference) are included for the complete elimination of aliasing errors that may arise from evaluating the Fourier transform of the resulting product: the "3/2 de-aliasing rule" (Canuto et al., 1988). As for the set of Fourier collocation/quadrature points, it is simply defined by

$$\theta_m \;=\; m\,\Delta\theta \;+\; \frac{L_\theta}{2} \quad ; \quad z_n \;=\; n\,\Delta z \;+\; \frac{L_z}{2}\;, \qquad (3.10)$$

with

$$\Delta\theta \;=\; \frac{2}{3}\frac{L_\theta}{2N_\theta} \quad ; \quad \Delta z \;=\; \frac{2}{3}\frac{L_z}{2N_z}\;.$$

Replacing the new symbolic expressions (3.8) and (3.9) in (3.5) we obtain, after rearranging,

$$\frac{1}{L_\theta L_z}\int_0^{L_\theta}\!\!\int_0^{L_z}\left[\sum_{l_*}\sum_{l}\mathcal{U}^p_{l_*}\mathcal{W}^q_l\;\mathcal{P}^{pqs}_{l'l_*l}\;\varepsilon_{pqs}\right]_{l'} e^{-ik'_\theta\theta}e^{-ik'_z z}\,d\theta dz\;, \qquad (3.11)$$

where ε_{pqs} stands for the conventional permutation operator. With the symbolic notation used, a formal summation rule is somewhat awkward to define, but the result can be seen in the expressions (C.14) and (C.15) in the appendix. In passing, we have also introduced the radially integrated trilinear product

$$\mathcal{P}^{pqs}_{l'l_*l} \equiv \int_0^\infty \mathcal{G}^s_{l'}\,\mathcal{G}^p_{l_*}\,\mathcal{H}^q_l\; r\,dr\;. \tag{3.12}$$

The integral (3.12) is a purely radial expression composed of a set of 22 expressions in the form of (see also (C.13))

$$\int_0^\infty G^{(i)}_{l'}(r)\,G^{(j)}_{l}(r)\,G^{(k)}_{l_*}(r)\;r^p\;dr\;,$$

that can be pre-computed before entering the time marching procedure. The superscripts i, j and k refer here to different orders of derivative, and p is some integer (positive or negative).

The present method precisely differs from the standard pseudo-spectral one in what follows, namely the evaluation of the convolution sum

$$\sum_{l_*}\sum_{l} \mathcal{U}^p_{l_*}\mathcal{W}^q_l\;\mathcal{P}^{pqs}_{l'l_*l}\;\varepsilon_{pqs}\;, \tag{3.13}$$

in (3.11). Because of the locality of B-splines, their inner product is non-zero for only a limited number of indices, as one may recall from (2.58), i.e.,

$$\int B_{l'}\,B_l\,d\eta \;\neq\; 0 \qquad \text{for} \qquad -k < l' - l < k\;,$$

so, for a given value of l', there are only $2k-1$ values of l (similarly for l_*) that give a non-zero integral. This result is a consequence of the locality of the basis functions and is accordingly not affected by mapping considerations; it may therefore be directly applied to (3.12). Extension of this spatial "quasi-orthogonality" result to the trilinear product leads to a few more zeros (see FIG. C.1 and C.2 in the appendices), but globally the scaling remains the same. At a given index value l', the convolution sum requires only $\mathcal{O}([2k-1]^2)$ operations instead of $\mathcal{O}(N_r^2)$. From this result, it can be shown that the total operation count for the computation of the nonlinear term scales like

$$\mathcal{O}(\,N_r\,k\,N_\theta\,N_z\,[c_1\log(N_\theta N_z) + c_2 k + c_3]\,)\;,$$

without having to explicitly evaluate the physical field components (which would require a complete B-spline evaluation). The c_i represent the principal relative scaling constants.

Note that in a classical pseudo-spectral approach the velocity and vorticity components would be computed on a radial quadrature grid—if we put aside mapping considerations for the moment and work with a B-spline basis of order k—with at least $k-1$ points per sub-domain. These new quadrature points are associated with the different higher order B-spline discretization required to represent the nonlinear product. This is roughly the equivalent of the 3/2-rule used in the Fourier directions. For B-splines of order k, the velocity would be in $k-1$ (see TABLE 2.1), the vorticity in $k-2$, and therefore their product in $2k-3$, whence the minimum of $k-1$ quadrature (collocation) points. Machine precision numerical integration would require more points, on one hand, to account for the additional weight B-spline functions, and mostly, on the other hand, to account for the negative powers of r that appear in some of the expansions (see Sec. C.2). This same last comment applies a fortiori if mapping considerations are taken into account. The total operation count in this case would then scale like

$$\mathcal{O}(\, N_r\, k\, N_\theta\, N_z\, [d_1 \log(N_\theta N_z) + d_2 k^2 + d_3 k + d_4]\,) \ .$$

Although the two estimates scale almost equally, the clever but less obvious construction of products (3.13) developed by LMMC that we have just presented above leads to a more efficient implementation of the modified convolution sum algorithm.

Once the convolution sum (3.13) is computed (the expressions (C.14) and (C.15)), there remains only one final step: the evaluation of the double integral in (3.11), viz.,

$$\frac{1}{L_\theta L_z} \int_0^{L_\theta} \int_0^{L_z} [\,\ldots\,]_{l'}\, e^{-ik'_\theta \theta} e^{-ik'_z z}\, d\theta dz \ ,$$

which will be recognized as the definition of a double Fourier transform. The integrand being determined on a proper set of collocation/quadrature points, this operation is again done by means of the FFT. The complete procedure is synthesized in TABLE 3.3 (see also Sec. C.2 in the appendix for a more technical description).

Our last observation relates to the evaluation of the velocity field required for the determination of the time step size Δt via the CFL condition (3.1). As discussed

TABLE 3.3. Generic description of the algorithm for the nonlinear term computation.

1. For each index l';
   (a) From the $\alpha^{\pm}_{lmn}$, evaluate the relevant spectral scalar coefficients $\widehat{\mathcal{U}}^{p}_{l_{\bullet}m_{\bullet}n_{\bullet}}$ and $\widehat{\mathcal{W}}^{q}_{lmn}$;
   (b) Compute the inverse Fourier transform (3.8) and (3.9);
   (c) Compute the convolution sum (3.13);
   (d) Compute the Fourier transform of (3.13).

in Sec. 3.1, each one of the velocity components, defined in (C.10)–(C.12), needs to be evaluated on the collocation grid. Since the velocity field is never explicitly determined in the present computation of the nonlinear term, a supplementary step must be added. By (3.8), the scalar physical coefficients $\mathcal{U}^{p}_{l_{\bullet}}$ are obtained; the velocity vector components can thus be determined by the B-spline evaluation

$$\mathbf{u}(r_l, \theta_m, z_n) \cdot \hat{\mathbf{e}}_p \;=\; \sum_{l_{\bullet}} \mathcal{U}^{p}_{l_{\bullet}}(\theta_m, z_n)\; \mathcal{G}^{p}_{l_{\bullet}}(G_{l_{\bullet}}(r_l), G'_{l_{\bullet}}(r_l)) \;. \tag{3.14}$$

The radial collocation points r_l are chosen here as the B-spline breakpoints. This additional evaluation can naturally be inserted between lines 1.(b) and 1.(c) of TABLE 3.3. Because (3.14) represents an extra computational cost though, the evaluation of the time step size is only done at certain predetermined time intervals, as already mentioned in Sec. 3.1.

3.3 Effective matrices, regularity and boundary conditions

In this section, we discuss the construction of the effective matrices of TABLE 3.1 (see also TABLE 3.2 line 2.(a)) and the imposition of the regularity and boundary conditions (TABLE 3.2 line 2.(d)). Note that the construction of the matrices is exposed in more details in Sec. C.1, while the imposition of the regularity and boundary

conditions are detailed in Sec. D.2 and Sec. D.3 respectively.

3.3.1 Effective matrices

To better understand how the effective matrices $\widetilde{\mathsf{A}}$ and $\widetilde{\mathsf{B}}$ of Sec. 3.1 are constructed, let us first start with a brief recapitulation. The inertia and viscous matrices were initially defined in Chap. 2, and respectively given by (2.44) and (2.45). By replacing the different vector expansions of TABLE 2.1 in these definitions, we obtain a set of parametric relations, in terms of purely radial sub-matrices, bearing the generic form (see also (C.1))

$$\int_0^\infty G_{l'}^{(i)}(r)\, G_l^{(j)}(r)\, r^p\, dr \ ,$$

where i and j are derivative order indices, and p some integer (positive or negative). There are 14 of these generic matrices—pre-computed before entering the time marching procedure—that completely define the general inertia and viscous matrices. As the reader will have probably noticed, this holds a certain resemblance with what was already described for the nonlinear term in Sec. 3.2.

Because the radial basis functions $G_l(r)$ are locally defined, the matrices A_δ^γ (or B_δ^γ) are mostly zero except for a narrow band of $2k-1$ values (one may recall this result from (2.58)). The general coupling between the "+" and "−" classes, on the other hand, requires that the systems of equations (2.43) be solved in a coupled manner in the time marching algorithm (TABLE 3.1), i.e., with matrices in the form shown in FIG. 3.1. To these matrices correspond the following sequences of coefficients, for each modal pair k_θ, k_z,

$$\left\{\alpha_1^+, \alpha_2^+, \ldots, \alpha_{N_r}^+, \alpha_1^-, \alpha_2^-, \ldots, \alpha_{N_r}^-\right\}_{mn}^T \ ,$$

where ^{T} stands for the transpose. By a simple reordering of the coefficients into the sequences

$$\left\{\alpha_1^+, \alpha_1^-, \alpha_2^+, \alpha_2^-, \ldots, \alpha_{N_r}^+, \alpha_{N_r}^-\right\}_{mn}^T \ ,$$

accompanied by consequent reordering of the equations (i.e., of the corresponding weight functions), the block banded matrix of FIG. 3.1 can easily be transformed

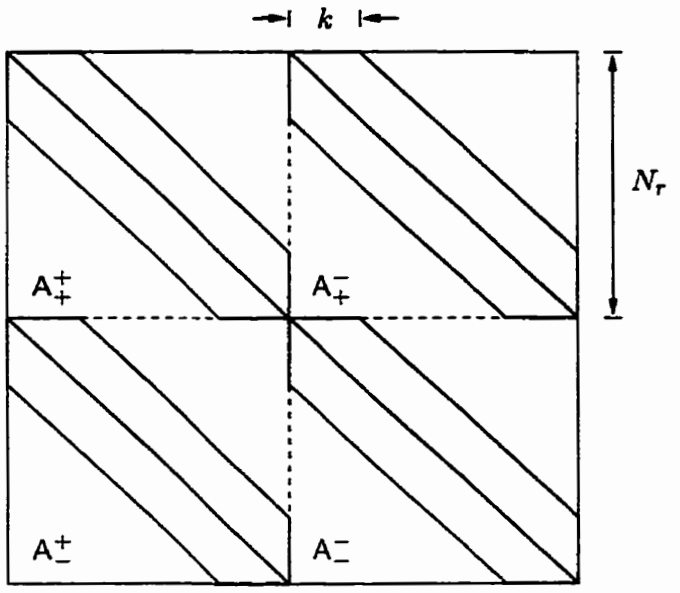

FIGURE 3.1. Topology of the coupled inertia matrix $\widetilde{\mathsf{A}}$ of TABLE 3.1 before re-ordering and imposition of regularity/boundary conditions. The shaded areas identify the non-zero values. The total bandwidth of each one of the sub-matrices A_δ^γ is $2k-1$. A similar figure could be sketched for the viscous matrix $\widetilde{\mathsf{B}}$.

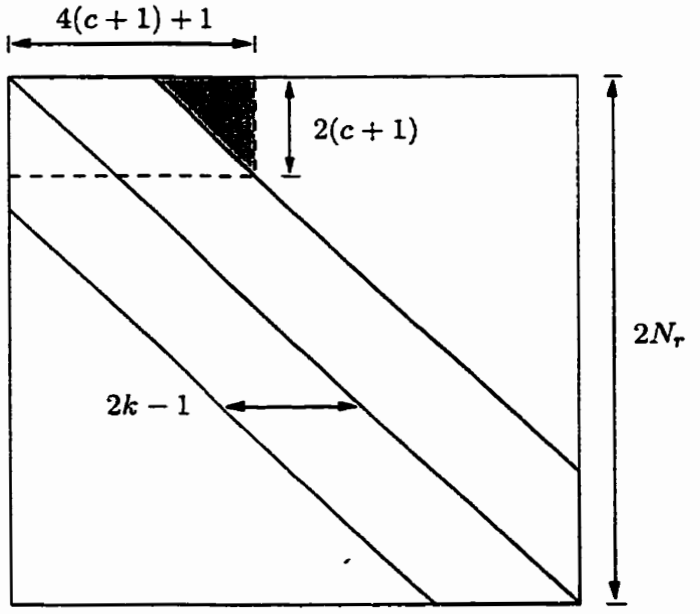

FIGURE 3.2. Topology of the coupled effective inertia matrix $\widetilde{\mathsf{A}}$ of TABLE 3.1 after reordering and imposition of the regularity/boundary conditions; matrix $\widetilde{\mathsf{B}}$ is identical. As in FIG. 3.1, the shaded area identify the non-zero values of the matrix. The total bandwidth is now of $4k-1$. The top left rectangle identifies the modified zone affected by the imposition of the regularity conditions, and c is for the B-spline continuity (see text for more information).

into a single band (new dimension of $4k-1$) "effective" matrix as the one shown in FIG. 3.2. Note that a specific index by index value example, for $k=3$, is shown in FIG. D.4. Since the sketch in FIG. 3.2 represents the global effective matrices that result from both data reordering and imposition of the regularity/boundary conditions, some further explications need to be given. The reordering procedure does indeed confine the non-zero values of the different A_δ^γ (the light shade areas) of FIG. 3.1 to the single band area (also in light shade) of $\widetilde{\mathsf{A}}$ in FIG. 3.2. The top left rectangle is the result of the imposition of the regularity condition which is now discussed.

3.3.2 Regularity conditions

The local B-spline discretization does not naturally satisfy any specific type of boundary (including regularity) conditions. These must therefore be imposed explicitly (line 2.(d) of TABLE 3.2) before solving the algebraic system of equations (line 2.(e)). The whole process of imposing these conditions can become quite tedious if presented at the algorithmic level, and so we will again limit ourselves here to the main ideas, relegating the technical details to Sec. D.2 (regularity conditions) and Sec. D.3 (boundary conditions).

The set of vector expansions defined in Chap. 2 is not unique. One of its main advantages though relates to the imposition of the regularity conditions. Indeed, one needs to recall that the vector expansions were constructed in Sec. 2.3.1 by taking the curl of some vector potential such that

$$\mathbf{W}_l^\pm \;=\; \widehat{\nabla\times}\,\mathbf{\Psi}_l^\pm\,.$$

Obviously, if one of these two vectors satisfies the regularity conditions then so must the other. Without much trouble, one can argue (see again TABLE 2.1) that it is easier to impose the regularity on the $\mathbf{\Psi}_l^\pm$ rather than on the $\mathbf{W}_l^\pm$. This is where the cleverness of LMMC's construction comes to light. For each one of the "+" and "−" class, the different components of $\mathbf{\Psi}_l^\pm$ naturally satisfy the relative behaviors expressed in (2.10) and (2.11). The imposition of the vector regularity conditions is thus reduced to the imposition of a single parity condition simultaneously on both

$(\pm)$ spline functions $g^{\pm}_{mn}$, defined in (2.63),

$$g^{\pm}_{mn}(r) \;=\; \sum_{l} \alpha^{\pm}_{lmn}\, G_l(r)\;.$$

As will be seen further down, this result will also significantly ease the imposition of the regularity condition on the weight vectors.

The imposition of an even (odd) behavior near $r = 0$ on $g^{\pm}_{mn}$ is done by constraining all odd (even) derivatives to zero at the point itself, with the appropriate number of zeros according to the value of k_θ. Let us illustrate this with an example. For $k_\theta > 0$, we have from the combination of (2.11) with the expansions of TABLE 2.1,

$$\lim_{r\to 0} g^{\pm}_{mn}(r) \;=\; \mathcal{O}(r^{k_\theta - 1 + 2p})\;,$$

with $p = 0, 1, 2 \ldots$. So, if we consider the particular case $k_\theta = 2$, it reduces to the odd behavior

$$\lim_{r\to 0} g^{\pm}_{2n}(r) \;=\; \mathcal{O}(r^{1+2p})\;,$$

and all even derivatives (including 0th order, i.e., the function value itself) must therefore be zero. More specifically, this writes:

$$g^{\pm}_{2n}(0) \;=\; 0 \;\;;\;\; \frac{d^2}{dr^2}\, g^{\pm}_{2n}(0) \;=\; 0 \;\;;\;\; \cdots \;\;;\;\; \frac{d^q}{dr^q}\, g^{\pm}_{2n}(0) \;=\; 0\;, \tag{3.15}$$

where q is an even integer such that $q \leq c$, and c being the continuity level of the spline function, viz., $g^{\pm}_{mn} \in C^c$. Here, because we use maximum continuity spline functions, $c = k - 2$. Our choice of using c instead of $k - 2$ in this example is motivated by the fact that regularity is more closely related to continuity than order, and that, most importantly, all the implementation has actually been done in terms of generalized B-splines, i.e., with $c \leq k - 2$.

According to the particular spline construction used near the edges (see Sec. 2.3.3), constraining the value of the qth derivative at a frontier point can affect at most $q + 1$ coefficients, instead of the standard k coefficients for regular splines. By a combination of the B-spline relations (D.16) and (D.17) with the conditions expressed in (3.15), we finally obtain for our example

$$\alpha^{\pm}_{12n} \;=\; 0 \;\;;\;\; \alpha^{\pm}_{22n} \;=\; -\alpha^{\pm}_{32n}\, \frac{G_3''(0)}{G_2''(0)} \;\;;\;\; \ldots \tag{3.16}$$

Other sets of algebraic relations for the $\alpha^{\pm}_{lmn}$ coefficients can be similarly derived for the other values of k_θ.

Because we use a Galerkin method—the weight functions belong to the same functional space as the basis functions—regularity must also be imposed on the weight vectors. This is done in a similar manner by considering the equivalent of a weight spline function

$$h^{\pm}_{m'n'}(r) \;=\; \sum_{l'} \beta^{\pm}_{l'm'n'}\, G_{l'}(r) \;.$$

The parity conditions are also applied on $h^{\pm}_{m'n'}(r)$, thus giving a series of coupling relations between the $\beta^{\pm}_{l'm'n'}$ coefficients. Note that in the spline weight functions, the coefficients $\beta^{\pm}_{l'm'n'}$ are arbitrary except for the linear relations that result from the parity conditions.

Another advantages of the present choice of vector expansions is that since the weight function regularity conditions are identical for both the "+" and "−" classes, they do not need to be applied separately for each sub-system of equations but can be applied at once on the effective coupled system (line 2.(d) of TABLE 3.2). More specifically, the linear combinations are applied on the $2(c+1)$ first lines of the global K_2 matrix and the vector f of TABLE 3.2. In the matrix, these coupling relations will partially alter the band structure; the region affected by these modifications is represented by the dashed-line rectangle in FIG. 3.2. The dark shade triangle covers the area where non-zero values from the lower lines are brought up by the coupling relations. An example of a modified global matrix (with index by index values) is given in FIG. D.4, in the appendix.

3.3.3 Boundary conditions

Again from the construction of the vector expansions, imposition of the harmonic decaying behavior (2.14) to the stream vector Ψ_l is also done in a straightforward manner; the implementation details are presented in Sec. D.3. Written in terms of the spline functions, the conditions require for $k_\theta \geq 0$ that (see (2.48))

$$\lim_{r\to\infty} g^{\pm}_{mn}(r) \;=\; \mathcal{O}(r^{-k_\theta-1}) \;.$$

In the mapped coordinate η $(= r/(r+L))$, this becomes (see also (2.49))

$$\lim_{\eta \to 1} g^{\pm}_{mn}(r(\eta)) \;=\; \mathcal{O}((1-\eta)^{k_\theta+1}) \;.$$

This $(k_\theta+1)$-fold zero is imposed by simply setting the $k_\theta+1$ last spline coefficients $\alpha^{\pm}_{lmn}$ to zero. For example, using again our value of $k_\theta = 2$, this would require that

$$\alpha^{\pm}_{(N_r-2)\,2n} \;=\; 0 \;\;;\;\; \alpha^{\pm}_{(N_r-1)\,2n} \;=\; 0 \;\;;\;\; \alpha^{\pm}_{N_r\,2n} \;=\; 0 \;. \tag{3.17}$$

When $k_\theta > c$, only the $c+1$ first coefficients are imposed to zero. The reason for this is based on similar considerations than those discussed in relation with regularity conditions at $r = 0$.

Let us look more specifically at the basis functions in terms of the mapped coordinate η, rather than the physical coordinate r, i.e., in the true B-spline space. Imposing, say, the last $q+1$ spline coefficients—as in (3.17) with $q = 2$—is equivalent to imposing the function value up to the qth derivative at the end point $\eta = 1$. The highest order derivative that can be imposed at that frontier point is c, all other derivatives being zero by construction there, whence the limit value of $c+1$ coefficients[3]. The decaying condition is equally applied to the spline weight functions $h^{\pm}_{m'n'}(r)$, leading to the same restrictions for the $\beta^{\pm}_{l'm'n'}$ coefficients. Note that the complete set of boundary conditions is given in TABLE D.1, in the appendix.

There are still two points, regarding the implementation of both the regularity and the boundary conditions, that deserve some attention. The first one is algorithmic. The very particular topologies of the matrices that result from the radial discretization require the use of an specialized Gaussian elimination solver. In this case, we have implemented a Gaussian elimination (without pivoting) especially designed for matrices with a structure as shown in FIG. 3.2. The operation count of this solver scales as $\mathcal{O}(N_r k^2)$, the same as for narrow bandwidth solvers. For this very specialized solver, we chose to maintain the topology of the matrices fixed for all k_θ, and have therefore also chosen to impose all the conditions explicitly.

[3] A possible ambiguity may arise if working with generalized B-splines of less that maximal continuity, i.e., $c < k-2$, as to whether impose the boundary conditions in terms of $k-1$ (for which indeed all other higher order derivatives would be identically zero) or $c+1$ (for which some higher order derivatives could then remain non-zero). At any rate, the question is eluded in the present case since we have restricted the B-spline discretization to regular splines ($c = k-2$) even though the implementation allows for any type of generalized splines.

The second point regards the effectiveness of such regularity/boundary conditions. At both frontiers, the conditions imposed represent some asymptotic behaviors, valid in the respective limits $r \to 0$ and ∞. In our discrete B-spline world however, these behaviors extend over some finite distance inward, and therefore represent an approximation of the formal conditions. The spatial extent of the finite order approximation of these boundary/regularity conditions may be limited in effect by some B-spline clustering near the edges; a procedure which we may recommend in most cases, to stay consistent with the asymptotic nature of the conditions. On the other hand, applying the full regularity conditions directly to high order B-splines, on a tightly clustered grid, may lead to some degradation in the conditioning of the matrices because

$$\frac{d^q}{dr^q} g^{\pm}_{mn}(r) \;=\; \mathcal{O}(\Delta r^{-q}) \;.$$

This drawback, in practice, contributes to limit the order of splines to values not much higher than about $k = 5$, as was also recommended by LMMC.

The practical advantages of imposing elaborate behavioral conditions at the frontiers should not only be of theoretical interest. A more formally restrained approximation space, with proper boundary conditions, allows for a reduction in the number of degrees of freedom without affecting completeness. In addition, imposing the regularity condition at the center of the domain (i.e., at $r = 0$) has the effect of making that particular point a regular one like any others in the domain, i.e., with the same approximation order. In terms of the error, this should also prove advantageous, but no formal investigations were conducted on this particular topic in the present study.

3.4 Modal reduction

The modal reduction algorithm—or zonal mesh embedding as its is sometimes referred to—allows in a general manner for the radial variation of the Fourier truncations N_θ or N_z, or both. It was first presented by Kravchenko et al. (1996) for a spectral/B-spline discretization in Cartesian coordinates, and by LMMC for a similar method in cylindrical coordinates. The purpose of the procedure is not only to reduce the number of (non-essential) degrees of freedom, as will be seen below, but also and

mostly in this case to alleviate the severe time step size restriction that may result from the compliance with the CFL condition near $r = 0$, with a uniform truncation in the azimuthal direction. In the present implementation of the procedure, because of its critical importance, we have given priority to the azimuthal truncation N_θ. However, the general and flexible set up of the algorithm used here—which can be seen as a generalization of the algorithm presented by LMMC in their report—could be extended to include the modal truncation in the longitudinal direction in a relatively straightforward manner. Finally, as previously, we limit ourselves in this section to the essential considerations and relegate the technical detail to, this time, Sec. D.4.

Let us begin our presentation of the procedure by considering the CFL constraint. In Sec. 3.1, we mentioned that the CFL condition (3.1) was evaluated on the collocation grid. The definition of the set of collocation points $\{ r_l, \theta_m, z_n \}$ was in turn given in Sec. 3.2, by (3.10) for the Fourier directions, and by the B-spline breakpoints for the radial coordinate.

A simple but important point to note regards the uniform Fourier discretization in θ, i.e., the evenly spaced "collocation angles". This does not actually lead to a uniform resolution for that direction, as opposed to the longitudinal (z) direction. Indeed, as it appears in (3.1), the azimuthal resolution is in fact associated with $r\Delta\theta$, and since $\Delta\theta$ has a constant value,

$$r\Delta\theta \to 0 \quad \text{as} \quad r \to 0 \,.$$

The module of the velocity component u_θ need not be very large near the center of the domain for the ratio $|u_\theta|/r\Delta\theta$ to become dominant there. This narrowing of $r\Delta\theta$ is pictured in FIG. 3.3.a by the convergence of the radial lines, where each line corresponds to a collocation angle θ_m. In the same figure, each circle (constant r_l) is associated with a B-spline breakpoint. The discretization parameters used for the illustration are $N_d = 25$ and $N_\theta = 16$. For the present discussion, the longitudinal direction, with its uniform discretization, does not lead to any particular restrictions on the time step, and therefore needs not be explicitly considered here.

As shown in Sec. 2.1.1, the analytical regularity of the fields (as $r \to 0$) requires the "fast dying" of the high azimuthal wavenumber modal components. This result forces many of the modal spline coefficients $\alpha^{\pm}_{lmn}$ to be practically zero near the center

(low index values of l and high values of m). The small wavenumber flow structures that effectively remain in that region are then convected through an over-resolved grid, leading to an artificially severe restrictions on Δt because of the CFL condition (3.1). One way to better reflect the analytic behavior (2.11) and alleviate the CFL constraint is by letting the truncation level N_θ (or equivalently the $\Delta\theta$) be a function of r. More specificly, this means letting $N_\theta = N_\theta(l)$. In terms of the spline functions, this becomes equivalent to introducing an "azimuthal filter".

A new filtered function $\check{g}^{\pm}_{mn}(r)$ can thus be written such that

$$\check{g}^{\pm}_{mn} = \sum_{l=1}^{N_r} s_{lm}\, \alpha^{\pm}_{lmn}\, G_l \;, \tag{3.18}$$

where the filtering coefficients s_{lm} are simply defined by

$$s_{lm} = \begin{cases} 1 \;\; ; & \text{if } l \in \{l_1, l_2, \ldots, l_{d_m}\}^{(q)} \\ 0 \;\; ; & \text{otherwise} \end{cases} \;, \tag{3.19}$$

and where the set of d_m index values $\{l_i\}^{(q)}$ forms a *modal group* (identified by the index q), i.e., the set of spline indices that share the same cut-off truncation level $N^{(q)}_{\theta Z}$, see Sec. D.4 for further details. These modal groups are a generalized form of the modal zones presented by LMMC. Seen at the algorithmic level, this filtering procedure amounts to the removal of some of the $\alpha^{\pm}_{lmn}$ coefficients, for some pre-assigned values of the azimuthal index m, whence the name "modal reduction". Similar procedures were implicitly applied by Orszag (1974) in spherical coordinates, by Leonard & Wray (1982) in cylindrical coordinates, and by Shen (1997) (cited from Lopez & Shen, 1998) aslo in cylindrical coordinates, by directly incorporating the analytical behavior to their global expansions.

For the collocation grid and the CFL condition, the repercussions of letting N_θ vary as a function of l are also probably best illustrated by an example. In FIG. 3.3, we show both a standard collocation grid and a modally reduced version. The number and distribution of radial sub-domains (breakpoints) are identical for both cases ($N_d = 25$). The standard grid has a unique truncation level of $N_\theta = 16$ while the reduced version was obtained with the set of trucation levels $N_{\theta Z} = \{4, 8, 16, 8\}$, from the center out. The frontiers between the modal zones are marked by the "bold" lines. The different truncation levels $N_\theta(l)$ have now been defined as functions of

the spline index l. The modal zone grid must therefore be obtained with some specific radial spline discretization. The grid shown in FIG. 3.3.b was produced with quadratic ($k = 3$) splines for which $1 \leq l \leq 27$. The precise functional link between the qth truncation levels $N_{\theta Z}^{(q)}$ and the index l is not so important here, but the reader will find all the relevant details again in the Sec. D.4. Let us only note that in this particular case, there are 8 B-splines with $N_{\theta Z}^{(3)} = 16$, 22 with $N_{\theta Z}^{(2)} = N_{\theta Z}^{(4)} = 8$, and obviously 27 with $N_{\theta Z}^{(1)} = 4$.

When comparing the two grids, one easily perceives the relaxation of the $r\Delta\theta$ factor near the center of FIG. 3.3.b. One may also recall that the modal reduction not only serves to alleviate the CFL constraint, as we already mentioned, but may additionally serve to remove some of the negligibly small B-spline coefficients. This possible adjustment can equally be applied in the far field where the decaying conditions require the fast dying of the high azimuthal wavenumber field components, thus allowing for a possible modal reduction in the outer region too ($N_{\theta Z}^{(4)} = 8$ in the last zone of the example). This globally leads to a reduction in the total number of B-spline coefficients that need to be computed. For example, with the quadratic splines used, the 1 zone truncation (standard collocation grid in FIG. 3.3.a) contains 432 B-spline coefficients (per longitudinal k_z mode) whereas the 4 zones truncation of FIG. 3.3.b contains only 260 coefficients: a 40% reduction.

Because of the B-spline overlapping, the efficient implementation of the variable truncation $N_\theta(l)$ requires some special care near the zonal frontiers. Recall from the computation of the nonlinear term (Sec. 3.2) that the convolution sum (3.13),

$$\sum_{l_\bullet} \sum_{l} \mathcal{U}_{l_\bullet}^{p} \mathcal{W}_{l}^{q} \, \mathcal{P}_{l' l_\bullet l}^{pqs} \, \varepsilon_{pqs} \, ,$$

is done in the physical B-spline space. The physical coefficients $\mathcal{U}_{l_\bullet}$ and $\mathcal{W}_l$ are obtained via the inverse Fourier transforms (3.8) and (3.9), viz.,

$$\mathcal{U}_{l_\bullet}^{p} = \sum_{m=-\frac{3}{2}N_\theta(l_\bullet)}^{\frac{3}{2}N_\theta(l_\bullet)} \sum_{n} \widehat{\mathcal{U}}_{l_\bullet mn}^{p} \, e^{ik_\theta \theta_m} e^{ik_z z_n} \, ,$$

$$\mathcal{W}_{l}^{q} = \sum_{m=-\frac{3}{2}N_\theta(l)}^{\frac{3}{2}N_\theta(l)} \sum_{n} \widehat{\mathcal{W}}_{lmn}^{q} \, e^{ik_\theta \theta_m} e^{ik_z z_n} \, .$$

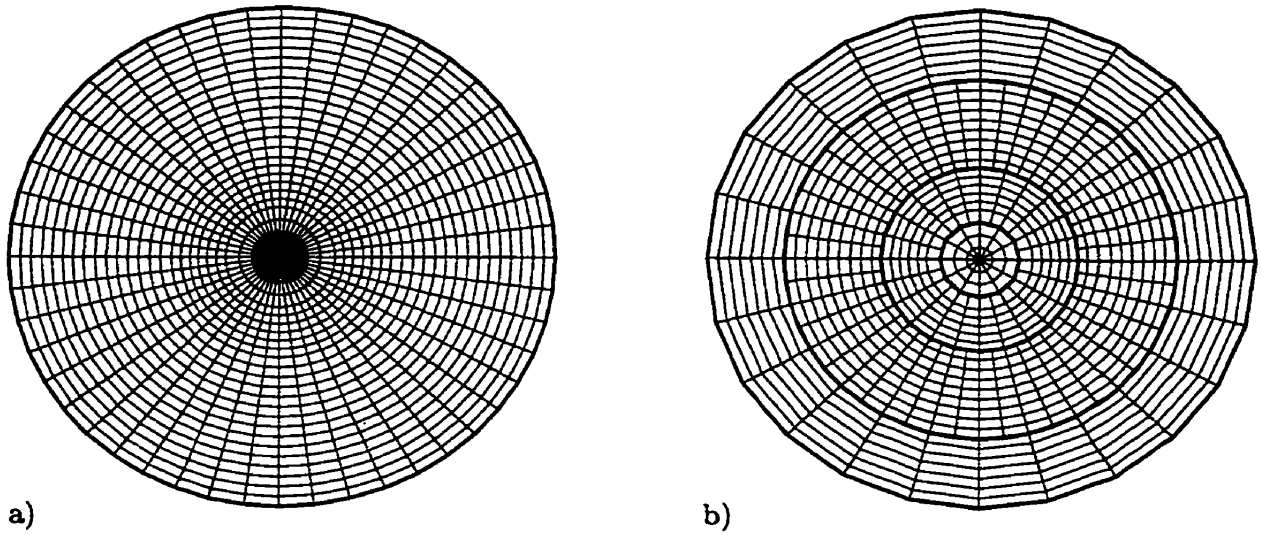

a) b)

FIGURE 3.3. De-aliased collocation grid with $N_d = 25$, uniformly distributed in the mapped η-domain, for both cases: a) Uniform modal truncation $N_\theta = 16$; b) Modal reduction with 4 zones, from inside out $N_{\theta Z} = \{ 4, 8, 16, 8 \}$. See text for additional information.

If $N_\theta(l_*) > N_\theta(l)$ for a given l' in (3.13), then the larger of the two values must be used in the Fourier transforms of both $\widehat{\mathcal{U}}^p_{l_* mn}$ and $\widehat{\mathcal{W}}^q_{lmn}$. This particularity is taken into account a priori when constructing the modal groups $\{ l_i \}^{(q)}$ mentioned earlier[4]. When a zonal frontier index l is detected such that $N_\theta(l) < N_\theta(l+1)$, then the effective modal group associated with the larger truncation is extended over the next $k-1$ spline indices (the overlapping extent) into the smaller truncation zone; in this case, the effective frontier would be set at $l + 1 - (k-1)$. The procedure would be similar if $N_\theta(l) > N_\theta(l+1)$ except that the extension would have been on the other side, i.e., from l up to $l + (k-1)$.

One of the drawbacks that comes with the azimuthal truncation jumps is that they require an extra Fourier transform—for all the overlapping B-spline coefficients that are in contact with the point at which the jump occurs—every time one of these jumps is reached. According to the level of specialization with which the algorithm is implemented, this extra work has the effect of limiting the number of allowable modal

[4]The two superscripts q should not be confused. In $\widehat{\mathcal{W}}^q_{lmn}$, the value of q identifies the vector component whereas in $\{ l_i \}^{(q)}$, it identifies the modal group.

zones in practice. A limit of 6 zones was suggested by LMMC for their near uniform azimuthal resolution applied to the simulation of turbulent pipe flows. Kravchenko et al., on the other hand, presented turbulent channel flow simulation results that were obtained with 9 zones.

In our present implementation of the algorithm in the nonlinear term, the very general formulation used for setting up the procedure does not lead to any specific overhead limitations for the number of zones. This is because the variable truncation Fourier transforms are applied in a rather systematic way for every l' index in the algorithm shown in TABLE 3.3. This approach obviously requires some additional work that could be saved in a more specialized (optimized) version of the implementation. In terms of global code performance for a typical flow simulation problem, the time spent in the computation of the nonlinear term (with the modal reduction algorithm) accounts for about 85% of the total computational time in the cases reported by LMMC while this figure is of about 92% in our tested cases.

We conclude this section, on the modal reduction algorithm, by briefly considering some of the practical points involving the possible choices of value and positioning for the different truncation levels $N_{\theta Z}^{(q)}$. The effects associated with the passage of some vortical flow structures through a change of modal resolution has been checked by Kravchenko et al.. For their test case—the rebound of a counter-rotating vortex pair on a "no-slip" wall—they showed that if the resolution jump was of approximately less than or equal to a factor 2, then there were no noticeable impacts of the zonal boundary on the dynamical evolution of the vortex-wall interaction; a minimum resolution level must obviously be assumed on either side of the jump. This leads us to suggest that, in general, the choice of modal truncation jumps in our case should satisfy a similar criterion such that

$$\frac{1}{2} \lesssim N_\theta(l)/N_\theta(l+1) \lesssim 2\,,$$

in regions where significant flow structures are present.

Another, maybe more important, point regarding the determination of a particular modal zoning is the position of the zonal boundaries. In Houde et al. (2000), a criterion based on the radial distribution of the modal (azimuthal) kinetic energy of the flow was proposed. A predetermined cut-off energy ratio is first determined.

That ratio depends on the smallest flow structure that must be resolved, and the level of precision sought for the solution. Then, the radial distribution of the minimum truncation level, required to meet the energy ratio criterion, is evaluated. From that distribution, the zonal frontiers and truncation levels can in turn be determined in a straightforward manner. Although not always easily applicable in problems involving stability and transition flow dynamics—because the cut-off criterion must be applied on a known solution field whereas the required outcome solution is not necessarily known or available a priori in these cases—the procedure, when applicable, does provide an almost optimal determination of the zonal truncation levels and positioning. Otherwise, one has to rely on more empirical distributions that should mimic a relatively uniform resolution, where the main flow structures are located, while maintaining an affordable time step size. At any rate, some particular care should always be taken to make sure that the modal truncation imposes no dynamical restrictions on the solution.

Our last point is only to mention that near the center of the domain ($r = 0$) the lowest truncation permitted to alleviate the CFL constraint, without requiring particular symmetry properties of the flow field, is $N_{\theta Z}^{(\eta)} = 4$. Indeed, the first two modes $k_\theta = 0, 1$ are sufficient to completely determine all (even and odd) field quantities at the point $r = 0$, but as we depart from the point, they only provide the equivalent of a 0th order approximation in (2.11). The additional 1st order terms (even and odd), required for $r > 0$, are obtained by including the next two modes $k_\theta = 2, 3$.

3.5 Bounded domain solver

The flexibility provided by the radial B-spline discretization in the present numerical method allows us consider the transformation of the unbounded formulation described in Chap. 2 into a bounded one, similar to LMMC's method. Indeed, if we replace the mapped B-spline coordinate η, in (2.47), by the simple equivalence

$$\eta = r ,$$

then the physical coordinate r and the mapped coordinate η coincide, and we have

$$G_l(r) = B_l(r) = B_l(\eta) .$$

In other words, we directly use the B-spline functions of FIG. 2.2 with the radial coordinate, in the vector expansions (2.33)–(2.40), instead of the rational piecewise basis functions of FIG. 2.5. This change affects the evaluation of the inertia and viscous matrix integrals in (2.44) and (2.45) respectively, as well as the trilinear product integral in (3.12). Note that the new bounded radial domain is now defined in terms of the finite interval $r \in [0, R_o]$.

If the regularity conditions discussed in Sec. 3.3 remain unaffected by this change, the outer boundary conditions, on the other hand, must be adapted. Let us for now consider the simple no-slip condition $\mathbf{u} = \mathbf{0}$, at the outer radius R_o. In terms of the spline functions $g^{\pm}_{mn}$, the following conditions, given according to the family of vector expansions of TABLE 2.1, need then to be imposed:

- $k_\theta > 0\,;\ k_z \neq 0$

$$g^{\pm}_{mn}(R_o) \;=\; 0 \qquad \text{and} \qquad \frac{d}{dr}\, g^{\pm}_{mn}(R_o) \;=\; 0 \tag{3.20}$$

- $k_\theta > 0\,;\ k_z = 0$

$$g^{\pm}_{m0}(R_o) \;=\; 0 \qquad \text{and} \qquad \frac{d}{dr}\, g^{\pm}_{m0}(R_o) \;=\; 0 \tag{3.21}$$

- $k_\theta = 0\,;\ k_z \neq 0$

$$g^{+}_{0n}(R_o) \;=\; 0 \quad ; \quad g^{-}_{0n}(R_o) \;=\; 0 \qquad \text{and} \qquad \frac{d}{dr}\, g^{-}_{0n}(R_o) \;=\; 0 \tag{3.22}$$

- $k_\theta = 0\,;\ k_z = 0$

$$g^{\pm}_{00}(R_o) \;=\; 0 \tag{3.23}$$

A recapitulative index, in terms of the spline coefficients $\alpha^{\pm}_{lmn}$, is supplied in TABLE D.2, in the appendix. Note that in (3.21), a double zero condition must be imposed on the "$-$" class spline function in order to avoid the indeterminateness associated with purely Neumann boundary conditions on g^{-}_{10} when $k_\theta = 1$.

A bounded domain Navier-Stokes solver is obtained by applying the above modifications to the rest of the implementation discussed in the precedent sections. Besides

an additional mass flow conservation algorithm—which may be equivalently treated here in term of some non-homogeneous background flow $\mathbf{u}_{\text{nh}}$—this closely reproduces the spectral/B-spline method for cylindrical coordinates introduced by LMMC.

3.6 Linear stability and eigenvalue problems

The spatial discretization method presented in Chap. 2 may not only be used for the implementation of a complete unsteady Navier-Stokes solver, but can also very well serve for the numerical approximation of linear stability eigenvalue problems. In order to show how can this be done, we first briefly review the normal mode formulation of the linear stability problem. A more complete presentation can be found in Drazin & Reid (1981), for example. From there, we can show how to advantageously make use of our spectral/B-spline discretization to obtain the targeted eigenvalue solver. We describe here only the principal steps, some detailed information is however provided in App. E.2.

Let us begin by considering the following velocity field decomposition

$$\mathbf{u}(\mathbf{x},t) \;=\; \mathbf{U}(\mathbf{x}) \;+\; \mathbf{u}'(\mathbf{x},t)\;, \tag{3.24}$$

where $\mathbf{U}$ is a known equilibrium solution and $\mathbf{u}'$ some perturbation field. Both of these vector fields satisfy the divergence-free constraint, and $\mathbf{u}'$ the boundary conditions discussed in Sec. 2.1. A similar decomposition is also used for the pressure variable. After replacing (3.24) in the Navier-Stokes equation (2.1), and elimination of the quadratic terms in $\mathbf{u}'$, we obtain the following linear perturbation equation

$$\frac{\partial \mathbf{u}'}{\partial t} + \mathbf{u}' \cdot \nabla \mathbf{U} + \mathbf{U} \cdot \nabla \mathbf{u}' \;=\; -\nabla p' + \frac{1}{Re}\nabla^2 \mathbf{u}'\;. \tag{3.25}$$

One may note that because exact equilibrium solutions of the Navier-Stokes equations are in fact scarce (see Wang, 1991, for a list), in many practical instances, equilibrium solutions of the Euler equations are used instead. An example of such a situation will be found in Chap. 4, when considering the linear stability results of a trailing line vortex (Sec. 4.2).

The perturbation vector $\mathbf{u}'$ is in turn decomposed into normal modes (similarly

with p') such that

$$\mathbf{u}'(\mathbf{x},t) \;=\; \widehat{\mathbf{u}}(r;\,k_\theta,k_z)\,e^{i(k_\theta\theta+k_z z)\,+\,\lambda t} \;+\; \text{c.c.}\;, \tag{3.26}$$

where "c.c." stands for the complex conjugate. By simply replacing (3.26) in (3.25), we now obtain

$$\lambda\mathbf{u}' + \mathbf{u}'\cdot\nabla\mathbf{U} + \mathbf{U}\cdot\nabla\mathbf{u}' \;=\; -\nabla p' + \frac{1}{Re}\nabla^2\mathbf{u}'\;, \tag{3.27}$$

which can in turn be formulated in terms of the variational principle of Sec. 2.2 to ultimately give

$$\lambda\,\langle\boldsymbol{\Phi}\,,\mathbf{u}'\rangle \;=\; -\frac{1}{Re}\,\langle\nabla\times\boldsymbol{\Phi}\,,\nabla\times\mathbf{u}'\rangle - \langle\boldsymbol{\Phi}\,,\mathbf{u}'\cdot\nabla\mathbf{U}\rangle - \langle\boldsymbol{\Phi}\,,\mathbf{U}\cdot\nabla\mathbf{u}'\rangle\;. \tag{3.28}$$

We open here a short parenthesis to mention that in temporal stability analysis—which is what is actually being considered in the present formulation—we are concerned with the determination of the complex eigenvalues λ, and corresponding eigenvectors $\widehat{\mathbf{u}}$, that depend on the real-valued wavenumbers k_θ and k_z, and also on the Reynolds number Re, for a given base flow field $\mathbf{U}$. Furthermore, since the eigenvalues λ are complex, i.e., $\lambda = \lambda_r + i\lambda_i$, we have

$$\widehat{\mathbf{u}} \;\propto\; e^{\lambda_r t}\,e^{i\lambda_i t},$$

and the eigenmode solution $\widehat{\mathbf{u}}$ will be said to be either unstable (exponential growth) for $\lambda_r > 0$ or stable (exponential decay) for $\lambda_r < 0$. We speak of neutral stability in the particular case of $\lambda_r = 0$. We close the parenthesis by noting that, in general, the eigenvalues will be ordered here according to the decreasing amplitude of their real part, viz.,

$$\mathrm{Re}(\lambda_1) \;\geq\; \mathrm{Re}(\lambda_2) \;\geq\; \mathrm{Re}(\lambda_3) \;\geq\; \ldots$$

The vector expansions introduced in Chap. 2 (see TABLE 2.1) allow for a natural base to approximate the eigenmode $\widehat{\mathbf{u}}$ in (3.26), and application of the same Galerkin approximation to (3.28) yields the following generalized eigenvalue problem (for a given pair of modes k_θ, k_z),

$$\boxed{\lambda\,\widetilde{\mathsf{A}}\,\widetilde{\alpha} \;=\; \left[\widetilde{\mathsf{B}} \;-\; \widetilde{\mathsf{O}}\right]\,\widetilde{\alpha}\,.} \tag{3.29}$$

The effective matrices $\widetilde{\mathsf{A}}$ and $\widetilde{\mathsf{B}}$ will be recognized as identical to those appearing in the Navier-Stokes solver (see Sec. 3.3). On the other hand, following the same notation used for both the inertia and viscous matrices in (2.44) and (2.45), the new linearized transport matrix $\widetilde{\mathsf{O}}$ is given by,

$$[\,\mathsf{O}_\delta^\gamma\,]_{l'l} \;=\; \int_0^\infty \left(\mathbf{W}_{l'}^\delta\right)^* \cdot \left(\mathbf{W}_l^\gamma \cdot \widehat{\nabla}\widehat{\mathbf{U}} \;+\; \widehat{\mathbf{U}} \cdot \widehat{\nabla}\mathbf{W}_l^\gamma\right) r\,dr\,, \tag{3.30}$$

according to the combination of the "+" and "−" classes of the vector expansions; the details are included in App. E.2. To solve (3.29), we use the LAPACK implementation of the QZ-method (Golub & Van Loan, 1996), and compute all the corresponding discrete eigenvalues. Finally, a bounded domain version of the eigenvalue solver can simply be obtained by applying the modifications considered in Sec. 3.5

Chapter 4

Numerical Tests

From the numerical method, presented in Chap. 2, and the implementation considerations, discussed in Chap. 3, result a set of four numerical codes: for unbounded domains, there is a Navier-Stokes solver named UNCYL and an eigenvalue solver named UNCYL-LS; and there are the other two equivalent codes for bounded domains, named respectively BOUNCYL and BOUNCYL-LS. The validation of all four codes is the task we undertake in this important chapter.

At first, we shall consider the validity of the code BOUNCYL and its eigenvalue solver BOUNCYL-LS in the context of Poiseuille flow. Complete validation of the viscous and inertia matrices as well as the B-spline interpolation can be carried out by comparison with the analytical solution of the "Stokes flow stability problem". The testing of the time marching procedure as well as the nonlinear term evaluation comes next. Note that since both Navier-Stokes solvers UNCYL and BOUNCYL share the same nonlinear term and time marching algorithms, the validation of these procedures is carried out here, at once, for both codes. Indeed, the radial discretization (with the mapping function) and the boundary conditions are the two principal elements that distinguish the bounded formulation code from the unbounded one (see Sec. 3.5).

Let us also note that because there are no closed-form analytical solutions available for the fully nonlinear problem, quantitative validation can only be done by comparisons with other benchmark numerical or experimental data. High precision results are usually very limited in parametric extent and, outside of it, validation

relies more on qualitative than truly quantitative comparisons. Consistency checks between the eigenvalue and the Navier-Stokes solvers may partly serve to compensate this. Indeed, even if these two different solvers make use of the same inertia and viscous matrices, their convective transport term follows a very different formulation and implementation. Once the validity of the eigenvalue solver, say, has been established by comparison with (highly) precise external data, then systematic quantitative consistency checks between both the eigenvalue and the Navier-Stokes solvers can be used to increase the level of confidence in the implementation of either one of the two solvers. Such a procedure will not only be used in the first section, but throughout the whole validation process.

The validation of the codes UNCYL and UNCYL-LS is discussed next, and is carried out in two steps. The first one is presented in Sec. 4.2 and considers the stability of trailing line vortices. At this point, the general algorithms of the code have been verified, and emphasis is put more specifically on the radial direction, i.e., the mapped B-splines and the boundary conditions. Our main objective for that particular section is the validation of the two families of expansions for which $k_z \neq 0$ (see TABLE 2.1). At the end of the section, we open a parenthesis to briefly consider the use of the code BOUNCYL for unbounded flow problems, following the domain truncation approach mentioned in Chap. 2.

The other two families of expansions, with $k_z = 0$, are examined in the second part of the validation, presented in Sec. 4.3. For that purpose, the simulation of the instabilities of a special class of zero circulation vortex flows is considered. In that case, available quantitative data are more scarce, and we will thus have to rely to a greater extent on qualitative comparisons of the fully nonlinear evolution and saturation of the instability. Here again, consistency checks between the eigenvalue and the Navier-Stokes solvers will come as an additional support. The chapter's fourth and final section will serve as summary of the various test results presented.

4.1 Preliminary validation and Poiseuille flow

The preliminary validation is concerned with the verification of sub-parts of the code such as matrix computations, time marching and nonlinear term computation, etc. In each case, the verification starts with implementation consistency checks. These typically consist in the corroboration of some relatively "low-level" algorithmic procedure (e.g., numerical integration) with an analytically known counterpart. These consistency verifications form an essential requirement and were systematically used during the implementation process, but because of their rather tedious nature they are not formally presented here.

We directly pass to the next level of validation which will be divided in two main parts. In the first part, we consider the validation of the B-spline interpolation in relation with both the inertia and viscous matrices. The general time marching algorithm, including the evaluation of the nonlinear term, is the object of the second part. For all cases in this section, these verifications are made for the bounded codes BOUNCYL and BOUNCYL-LS. The main reason for this rests on the availability of exact, non-trivial Stokes flow solutions (in cylindrical coordinates) for bounded domains only. As will be shown below, these solutions provide a complete reference for the systematic verification of the matrices, and indirectly for the B-spline interpolation.

4.1.1 Matrices and B-spline interpolation

For the Stokes flow problem (the limit $Re \to 0$), the nonlinear convective terms of the Navier-Stokes equations are completely neglected. By applying our divergence-free method to such cases, only the inertia (temporal acceleration) and the viscous terms remain present. If, in addition, we limit ourselves to the linear stability of such flows, then the time integration is even further simplified (see Sec. 3.6) and the generalized eigenvalue problem (3.29) reduces itself to

$$\lambda \, \widetilde{\mathsf{A}} \, \widetilde{\alpha} \; = \; \widetilde{\mathsf{B}} \, \widetilde{\alpha} \, , \tag{4.1}$$

for a given pair of wavenumbers k_θ, k_z. Note that the Re^{-1} factor of the viscous matrix in (2.45) can be omitted here, i.e., set to 1, without loss of generality since it

only comes as a scaling factor for the eigenvalue λ. Because (4.1) only involves the radial discretization, it provides a good framework to assess the B-spline interpolation. Now, from the Rayleigh-Ritz approximation theory[1] of elliptic eigenvalue problems (of order $2d$), the following eigenvalue error bounds can be derived (Strang & Fix, 1988),

$$0 \;\leq\; \lambda_s^h - \lambda_s \;\leq\; C_1\, h^{2(k-d)} \lambda_s^{k/d} \,. \tag{4.2}$$

Here, λ_s^h is the approximation of the sth eigenvalue λ_s, k is the order of approximation, h is a measure of the local discretization ($h \propto N_r^{-1}$ in our case) and C_1 is some constant, independent of h. The error estimate for the corresponding eigenfunction u_s is

$$\| u_s^h - u_s \| \;\leq\; C_2 \left[h^k + h^{2(k-d)} \right] \lambda_s^{k/2d} \,. \tag{4.3}$$

The norm $\| \cdot \|$ is given by

$$\| u_s \|^2 \;\equiv\; \int_0^{R_o} | u_s |^2 \, dr \,, \tag{4.4}$$

following the standard L^2-space definition; R_o being the outer limit of the bounded domain. Note that, unless otherwise stated, all norms will be understood in this sense. For our particular case, $d = 1$, these estimates give

$$0 \;\leq\; |\lambda_s^h - \lambda_s| \;\leq\; C_1\, N_r^{-2(k-1)} \, |\lambda_s|^k \,, \tag{4.5}$$

$$\| \widehat{\mathbf{u}}_s^h - \widehat{\mathbf{u}}_s \| \;\leq\; C_2\, N_r^{-k} \, |\lambda_s|^{k/2} \,. \tag{4.6}$$

The absolute value of the eigenvalues is used to account for the fact that in the Stokes problem all eigenvalues are (real) negative while the estimates are derived for positive values. This is only a matter of convention because, as suggested by Strang & Fix, a large but finite value could be added to every λ_s in order to shift the whole

[1]This is related to the problem of finding the extremum of a quadratic functional (usually the minimum energy) and bears very close kinship with the Galerkin approximation theory. The former is a particular case of the latter because in the Galerkin approximation only a stationary point is sought, not necessarily an extremum. At any rate, this distinction poses no problem here since the Stokes flow problem, by the self-adjointness of the operators, can also be formulated as the minimum of some quadratic functional.

(discrete) spectrum into the positive domain. Some validation of our matrices and the assessment of the B-spline discretization will be carried out by the numerical testing of these estimates.

For this task, complete analytical solutions of Stokes flow stability problem (in a circular pipe) are however required. They were derived by Salwen & Grosch (1972) for $k_z \neq 0$—by means of vector potential expansions—and extended to include the case $k_z = 0$ by LMMC. The complete set of solutions can be found in the latter reference but, for ease of access, it is also included here in App. E.

Let us first consider the verification of the matrices for the general family of expansions $k_\theta > 0$, $k_z \neq 0$ (see TABLE 2.1 for reference). In FIG. 4.1, we show the convergence rates for the 10th eigenvalue of $k_\theta = 2$, $k_z = 3$; results obtained with the code BOUNCYL-LS. This particular choice of wavenumbers is justified by the fact that they are the smallest values different from 1 (to account for the different powers of k_θ and k_z in the construction of the matrices), and different from each other. As for the eigenvalue number, it was so chosen for its more demanding character (recall that higher eigenvalues are more difficult to approximate) without being too difficult. The effective convergence rates, obtained by a best fit of the data, are shown in TABLE 4.1 in which the theoretical estimates are given for comparison. Note that since the vector expansions include B-spline derivatives, the estimates (4.5) and (4.6) must be evaluated with the value of $k-1$ instead of k. This is because the qth order derivative of a B-spline of order k is exactly representable by B-splines of order $k-q$. One observes that the tested convergence rates are all below the theoretical estimates; higher order B-splines having a faster convergence rate. In all cases, both the eigenvalue and the eigenfunction rates are consistent between themselves, viz.,

$$\text{if} \quad \| \widehat{\mathbf{u}}_s^h - \widehat{\mathbf{u}}_s \| \propto N_r^{-\kappa} \quad \text{then} \quad |\lambda_s^h - \lambda_s| \propto N_r^{-2(\kappa-1)} ,$$

where κ is either the observed or the theoretical value.

The present B-spline approximation not only allows for error reduction by increasing the number of splines N_r for a given order k (h-convergence), but also by increasing the order k for a given number of splines (p-convergence). The (quasi-) spectral convergence that results from this second approach is shown in FIG. 4.2. Theory also predicts that the eigenvalues should be approximated from above (i.e.,

$\lambda_s \leq \lambda_s^h$). Although this is not apparent from the data shown, it has indeed been confirmed by our tests. Furthermore, the higher the eigenvalue, the more difficult it becomes to approximate it. This can be seen from the eigenvalue dependence of the right hand side term of estimate (4.5). In FIG. 4.3, we show the relative error as a function of the eigenvalue index s. In this case, the number of B-splines was set to $N_r = 30$ for the same order values used in FIG. 4.1. Again the observed values are in accordance with the theoretical behavior. It can be shown that in this case, the eigenvalue spectrum gives $\lambda_s = \mathcal{O}(s^2)$. The relative error is then expected to be of $\mathcal{O}(s^{2(k-1)})$. From a best fit of the data, we obtained exponent values of approximately 4, 7, 9 and 12 in comparison with the theoretical values of 4, 6, 8 and 10 (for respectively $k = 4$, 5, 6 and 7). This is again consistent with our other results.

The above results—the accurate prediction of the eigensolutions and convergence rates—strongly contribute to validate the matrices $\widetilde{\mathsf{A}}$ and $\widetilde{\mathsf{B}}$ for the general family of expansions $k_\theta > 0$, $k_z \neq 0$. Validation of the particular cases, for which either one or both $k_\theta = 0$, $k_z = 0$ apply (again see TABLE 2.1), is carried out in a more focussed manner.

In FIG. 4.4, we show the relative eigenvalue error (5th eigenvalue) for these particular cases. The results are shown only for quartic B-splines ($k = 5$); the respective convergence rates are presented in TABLE 4.2. When the "+" and "−" classes are decoupled, the verification is made independently for each class, yielding the two curves in FIG. 4.4.a and 4.4.c. The difference of convergence rates between the $k_\theta > 0$, $k_z = 0$ and the $k_\theta = 0$, $k_z = 0$ cases (FIG. 4.4.a and 4.4.c respectively) is consistent with the fact that in the former, velocity expansions include B-spline derivatives (first order) while in the latter, the expansions are formed without derivatives. In the general axisymmetric case $k_\theta = 0$, $k_z \neq 0$, both classes are coupled through the azimuthal swirl component but, according to the structure of the eigenmode, the convergence rate may exhibit or not (as it is the case here) the "first order derivative rate".

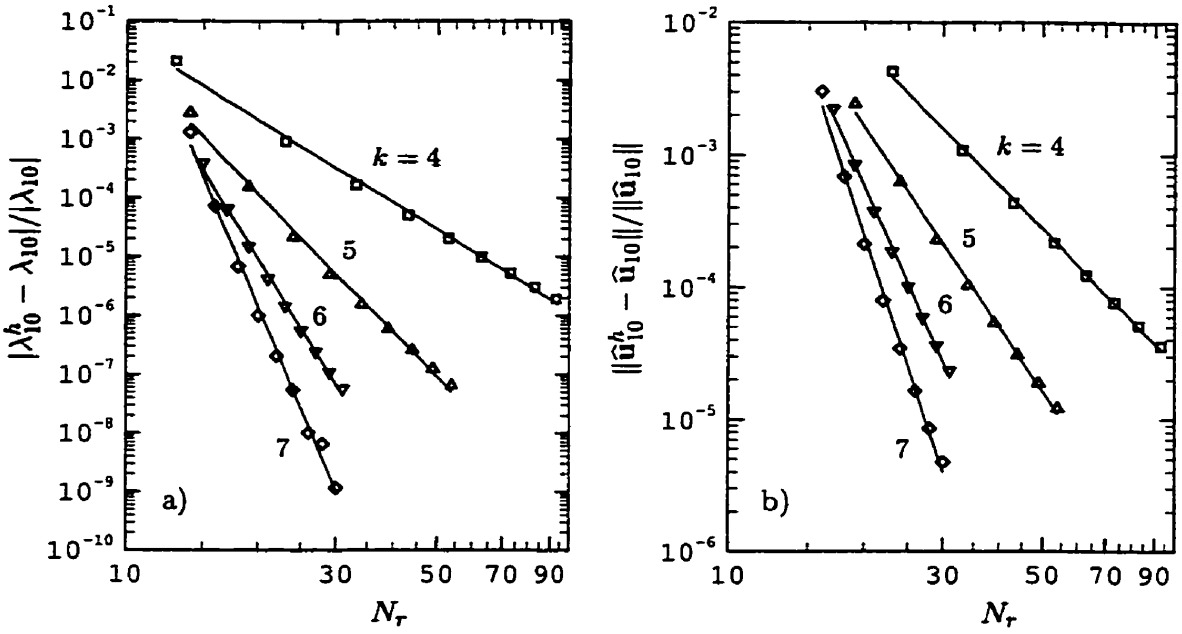

FIGURE 4.1. Relative error for a) the 10th eigenvalue, and b) its corresponding velocity eigenmode, as a function of N_r and k, for $k_\theta = 2$, $k_z = 3$. The lines are drawn from a best fit of the data; the corresponding convergence rates hence obtained are given in TABLE 4.1.

TABLE 4.1. Observed convergence rates in FIG. 4.1 vs. the theoretical estimates (4.5) and (4.6).

	$\lvert\lambda_{10}^h - \lambda_{10}\rvert/\lvert\lambda_{10}\rvert$		$\|\widehat{\mathbf{u}}_{10}^h - \widehat{\mathbf{u}}_{10}\|/\|\widehat{\mathbf{u}}_{10}\|$	
k	Observed	(4.5)	Observed	(4.6)
4	−4.67	− 4	−3.40	−3
5	−7.79	− 6	−5.03	−4
6	−12.1	− 8	−7.55	−5
7	−17.8	−10	−10.2	−6

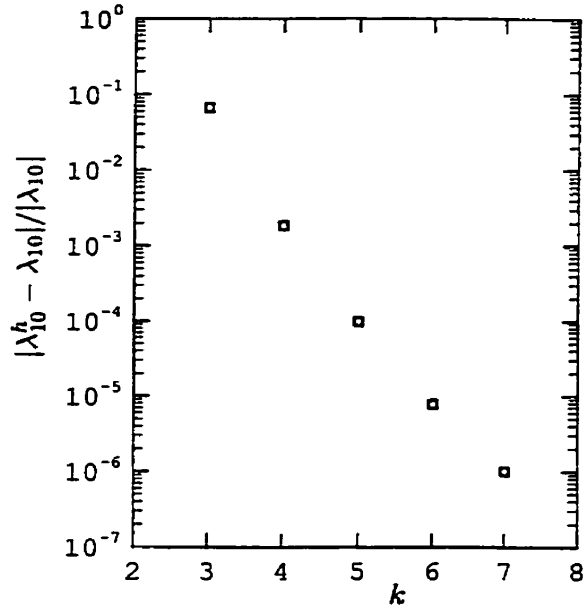

FIGURE 4.2. Relative eigenvalue error as a function of the B-spline order k ($N_r = 20$), for $k_\theta = 2$, $k_z = 3$. A straight line alignment of the data points on this "log-lin" graphics amounts to an exponential (spectral) convergence rate.

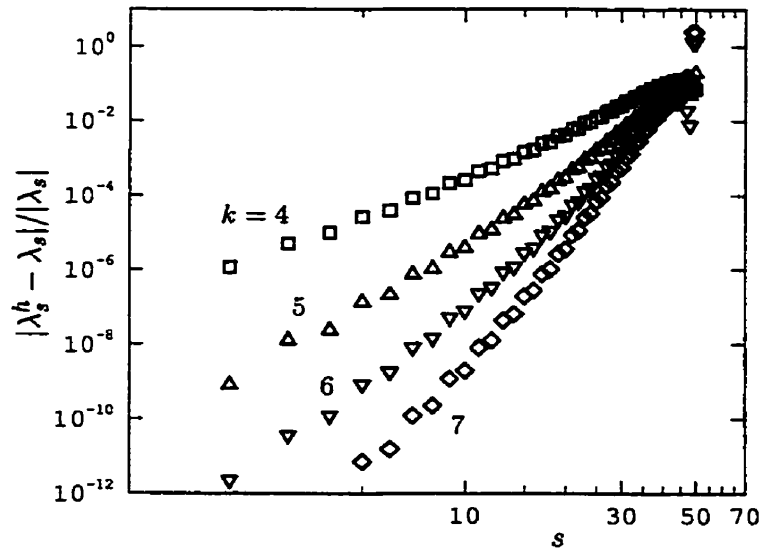

FIGURE 4.3. Relative eigenvalue error as a function of the index number s, for $k_\theta = 2$, $k_z = 3$. Results are obtained with $N_r = 30$ and different values of k, shown in the figure.

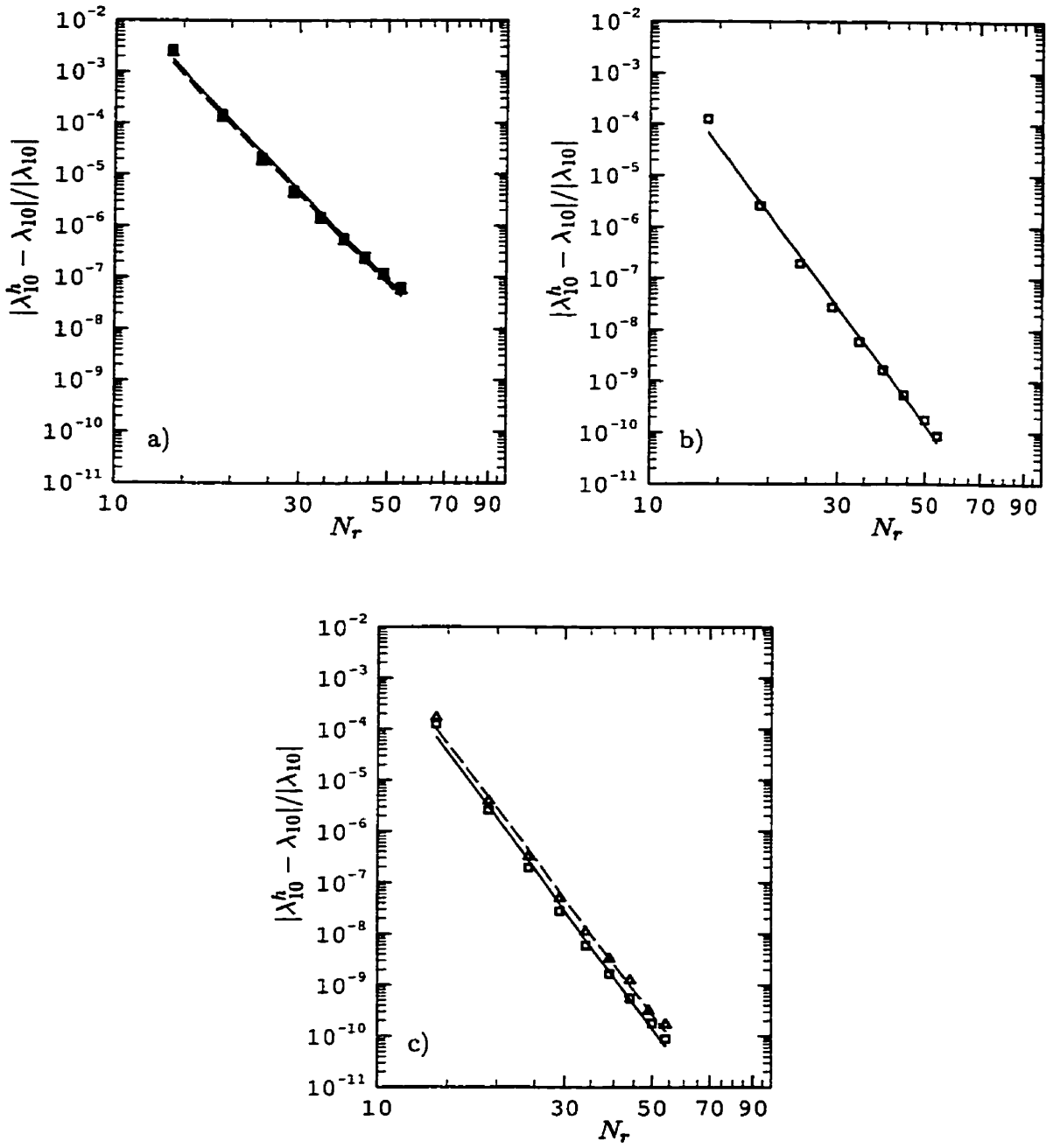

FIGURE 4.4. Relative error for the 5th eigenvalue of a) $k_\theta = 2$, $k_z = 0$; b) $k_\theta = 0$, $k_z = 2$; and c) $k_\theta = 0$, $k_z = 0$. Results are shown for $k = 5$ only. Here, the symbols "□" stand for "+" class and "△" for "−" class expansions except in b) where both classes are combined into one. The observed convergence rates are given in TABLE 4.2. The lines are drawn from a best fit of the data.

TABLE 4.2. Observed convergence rates in FIG. 4.4 vs. the theoretical estimate (4.5).

		$\lvert\lambda_5^h - \lambda_5\rvert/\lvert\lambda_5\rvert$	
k_θ	k_z	Observed	(4.5)
2	0	−7.78 (+)	−6
		−7.76 (−)	−6
0	2	−10.3	−6
0	0	−10.3 (+)	−8
		−10.1 (−)	−8

In terms of the accuracy of the radial approximation, the evidence so far certainly speaks in favor of the higher order B-splines. However, it is not so clear that this observation carries over directly to the general time marching procedure. One way to get a better idea on this question is by a rescaling of some of the above results. When discussing the computation of the nonlinear term (Sec. 3.2), the "radial" operation count of that procedure was shown to scale as $\mathcal{O}(N_r k^2)$. Let us use this value as an estimated cost for the nonlinear term, and rescale FIG. 4.1 accordingly, to see what happens.

The results are shown in FIG. 4.5 where we also present the error for the 20th eigenvalue. The behavior between the two eigenvalues is similar except for the level of the error itself (higher eigenvalues are more difficult to approximate). From this figure, the most efficient B-spline order is obtained by mentally drawing a horizontal line, from a given level of accuracy, and see which one of the different order curves is intercepted first, giving thus the lowest computing cost. Unless very high precision is sought, the error to cost ratio rather favors medium order splines with $k = 4$ or 5. These order values are consistent with the one used by LMMC for their turbulent pipe flow simulation ($k = 5$ in that case).

These observations clearly support the use of B-splines of orders of about $k = 5$ (or less) in practice for the Navier-Stokes solver. The possible stiffness problems, mentioned at the end of Sec. 3.3 in relation to the regularity condition at the center of the domain, are also much less likely to occur at these orders. Note however that values up to $k = 7$ were used with the eigenvalue solver without noticing such

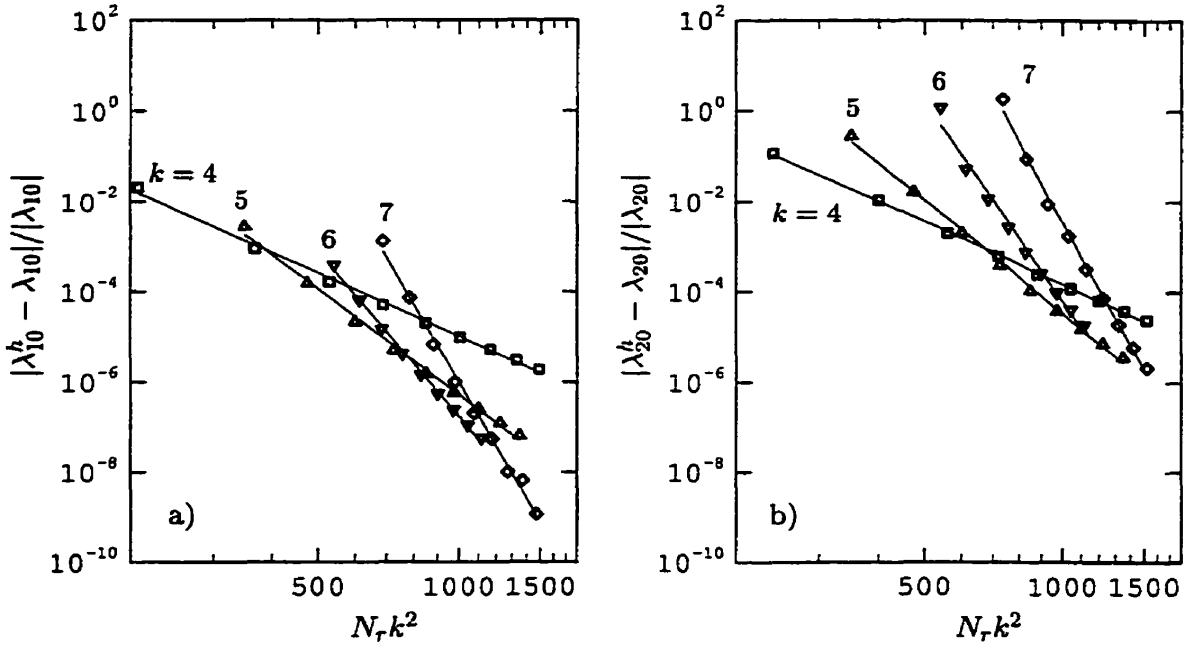

FIGURE 4.5. Relative error for the a) 10th eigenvalue and b) 20th eigenvalue as a function of the cost parameter $N_r k^2$, for $k_\theta = 2$, $k_z = 3$. The lines are drawn from a best fit of the data.

specific stiffness problems (see FIG. 4.1 and 4.4). Finally, recall from Chap. 2 that the minimum analytical requirements imposed by the present numerical method (see (2.46)) are satisfied provided $k \geq 3$.

4.1.2 Nonlinear term and time integration

The matrices of both codes, BOUNCYL and BOUNCYL-LS, have been convincingly validated in Sec. 4.1.1, using comparisons with analytical results for each family of vector expansions. For the validation of the nonlinear term, a different strategy must be devised for lack of general analytical solutions. Also, because of the explicit time integration of the latter term, the validation must be done while marching the solution in time. Note that the time marching algorithm could be validated independently of the nonlinear term via the Stokes flow problem but we choose here to do both at once. Besides comparing our numerical results with other benchmark (numerical or

experimental) data, a simple test can be devised from the time propagation of Orr-Sommerfeld waves, i.e., linear stability perturbations that are solutions of (3.27). This is the approach we use here and the procedure is explained in what follows.

Let us first introduce the Fourier-transformed perturbation vector $\widehat{\mathbf{u}}(r,t)$; the parametric dependence on the modal pair k_θ, k_z is implicitly assumed. If this perturbation is defined from the sth eigenmode $\widehat{\mathbf{u}}_s(r)$, then we have, from (3.26), that

$$\widehat{\mathbf{u}}(r,t) \equiv \widehat{\mathbf{u}}_s(r)\, e^{\lambda_s t} . \tag{4.7}$$

Let us use here the notation $\widehat{\mathbf{u}}^h(r,t)$ for the time approximation of $\widehat{\mathbf{u}}(r,t)$. Furthermore, let us also assume a given, sufficiently high level, radial resolution so that the spatial error in the approximate B-spline solution of (3.29) may be considered negligible. Without loss of generality, the radial discretization may thus also be implicitly assumed and we then write $\widehat{\mathbf{u}}^h(t)$ for short. It is known from standard temporal discretization error analysis that, for a scheme of order κ,

$$\frac{\| \widehat{\mathbf{u}}^h(t_n) - \widehat{\mathbf{u}}(t_n) \|}{\| \widehat{\mathbf{u}}(t_n) \|} = C\, t_n\, \Delta t^\kappa + \mathcal{O}(\Delta t^{\kappa+1}) \tag{4.8}$$

with $t_n = n\Delta t$ and C is some constant independent of Δt. For small Δt, the error should grow linearly in time.

From (4.8), the validation of both the nonlinear term and the time marching algorithm can be verified by testing the time propagation error of the initial condition

$$\widehat{\mathbf{u}}(r, t=0) \equiv \varepsilon\, \widehat{\mathbf{u}}_s(r) , \tag{4.9}$$

where ε is a small amplitude parameter, i.e., $\varepsilon \ll 1$. Indeed, since the Orr-Sommerfeld wave (4.7) is a solution of the linearized Navier-Stokes equations, this linearity of the solution should also be preserved by the fully nonlinear term. The implications of this statement are that: i) the evolution of the initial perturbation (4.9) is completely determined by the nonlinear interaction of the perturbation with the base flow field; and thus ii) all other nonlinear interactions, e.g., from the perturbation with itself, are negligibly small. For example,

$$\text{if} \quad \| \widehat{\mathbf{u}}(t; k_\theta, k_z) \| = \mathcal{O}(\varepsilon) , \quad \text{then} \quad \| \widehat{\mathbf{u} \times \boldsymbol{\omega}} \| \Rightarrow \| \widehat{\mathbf{u}}(t; 2k_\theta, 2k_z) \| = \mathcal{O}(\varepsilon^2) ,$$

and so on. As one would recall, the nonlinear interactions of two modal pairs, one in k_θ, k_z and the other in k'_θ, k'_z are four-fold: there is the "first harmonic" i) $k_\theta + k'_\theta$,

$k_z + k'_z$; the two "cross-interaction harmonics" ii) $k_\theta + k'_\theta$, $k_z - k'_z$; iii) $k_\theta - k'_\theta$, $k_z + k'_z$; and finally the "retrograde harmonic" iv) $k_\theta - k'_\theta$, $k_z - k'_z$.

That this test represents a necessary condition for the validation should not pose any problems. The fact that it also constitutes a sufficient condition may on the other side appear somewhat less obvious. We nevertheless believe that the following two part argument should help to remove any doubts about the sufficiency issue. In the first part, we want to establish that, by covering all the vector expansion families of TABLE 2.1, we do cover all the nonlinear interactions. The second part serves to establish that complying with the temporal error behavior (4.8) may be used to confirm the validity of the "spatial calculations".

For the eigenmode to grow or decay exponentially (the linear dynamics behavior), all modal nonlinear interactions should be negligible in comparison with the interaction of the base flow with the eigenmode. From this, we can see that there remain indeed some significant nonlinear interactions that need to be accounted for. The small parameter ε is only there to ensure the "exclusivity" of the interactions when evaluating the back and forth Fourier transforms, and the convolution sum discussed in Sec. 3.2. The fact that the convolution sum is evaluated in the physical space ensures in turn that indeed all the nonlinear interaction terms are covered, although the tests are made for one vector expansion family at a time; the whole four families of expansions obviously need to be checked for the verification to be complete.

To affirm that the "spatial evaluation" of the nonlinear term is done properly by monitoring the temporal error requires not only that (4.8) be satisfied, but also that the magnitude of this latter error remains very low. Indeed, complying with (4.8) only means that the total error is dominated by the temporal discretization error. A small magnitude requirement must therefore be added, and it is this combination of both conditions that guarantees in return the validity of the nonlinear term computation, i.e., an even much lower spatial computation error. Now, it is by putting together these two lines of reasoning that we may confidently arrive at considering the test, taken as a whole, as sufficient. Let us finally note that a similar validation procedure was also used by LMMC.

The reference eigenmode solution for each one of our tests is obtained via our

eigenvalue solver BOUNCYL-LS with the parabolic base flow profile

$$\mathbf{U}(r) \;=\; 0\,\hat{\mathbf{e}}_r \;+\; 0\,\hat{\mathbf{e}}_\theta \;+\; (1-r^2)\,\hat{\mathbf{e}}_z \tag{4.10}$$

at $Re = 9600$ (based on the centerline velocity and the pipe radius). In this case, the linear transport matrix $\widetilde{\mathsf{O}}$ of (3.29) is non-zero and the eigenvalue solver therefore requires an independent validation. Such a validation was previously carried out by comparing our results with other available benchmark data for the pipe flow case. Additional information on this extra validation procedure can be found in App. E.2.

For these tests, the (uniform) B-spline discretization was chosen to maintain the spatial discretization error very much under the temporal discretization one; $N_r = 35$ with $k = 7$ proved sufficient (more than six significant figures on the eigenvalue). This solution was given as an input to the code BOUNCYL (with $\varepsilon = 10^{-6}$) and advanced for 50 time steps. The error was then determined by comparing the computed eigenmode $\widehat{\mathbf{u}}^h(t_n)$ to the reference solution $\widehat{\mathbf{u}}(t_n)$, which was determined by

$$\widehat{\mathbf{u}}(t_n) \;=\; \varepsilon\,\widehat{\mathbf{u}}_s\,e^{\lambda_s t_n}\;.$$

In FIG. 4.6, we show the wave propagation error of the first eigenmode ($s = 1$) as a function of time, for the modal pair $k_\theta = 2$, $k_z = 3$. As expected, the error amplitude remains small and behaves linearly in time. Furthermore, the behavior of the first harmonic—the result of the nonlinear interaction of the eigenmode with itself—was verified to give

$$\|\,\widehat{\mathbf{u}}(t_n; 2k_\theta, 2k_z)\,\| \;\approx\; \|\,\widehat{\mathbf{u}}(t_n; k_\theta, k_z)\,\|^2\;,$$

also as expected.

In FIG. 4.7–4.9, similar results are shown for the other families of expansions (see again TABLE 2.1); all in agreement with the predicted behaviors. The following observations are worth adding. First, in FIG. 4.8, the time step size was set to a much larger value than for the other cases in order to keep the temporal error significantly higher than the spatial error. Note also that for this case, the error amplitude still remains much smaller than for the first two cases. Second, for the purely uniform axisymmetric case, $k_\theta = 0$, $k_z = 0$, the test was to measure how well the base flow profile maintained itself.

This indirectly brings us to the imposition of the forcing term required to preserve the mass flow. As we already mentioned in Sec. 3.2, any (linear) non-homogeneous forcing—such as the equivalent pressure gradient that maintains the mass flow here—can be taken into account by the addition of some background component (e.g., $\mathbf{u}_{\mathrm{nh}}$, $Re^{-1}\nabla^2\mathbf{u}_{\mathrm{nh}}$, etc.) in the nonlinear term. An illustration of a background flow application has been included in App. F. Here, we exceptionally use a slightly different procedure based directly on the conservation of the mass flow instead; the details of this latter approach can be found in LMMC's report. This choice was made for a matter of convenience and can be shown to have no effect on the solution.

Indeed, the use of a non-homogeneous parabolic background flow would be strictly equivalent to the imposition of an external pressure gradient in this case. By thus fixing the external forcing, the mass flow must be left free to adjust itself to some possible non-laminar dynamical equilibrium. The mass flow conservation algorithm of LMMC is based on a reversed approach for which the mass flow is the fixed parameter and the external forcing is the free one. For the linear stability dynamics considered here, this obviously makes no difference since the global base flow field always remains laminar. The point is additionally supported by the fact that the error between the computed $\widehat{\mathbf{u}}^h(t;0,0)$ and the base flow $\mathrm{U}(r)$, defined above in (4.10), remains close to the machine round-off error as indicated by the 10^{14} factor in FIG. 4.9.

The third and final point regards the order of the time integration scheme, κ in (4.8). Although the precise value is not necessary to conduct these tests, it is nevertheless worth noting that it can be determined "experimentally" by checking the variation of error curve slope as a function of the time step size. Recall that the time integration scheme is of third order (except for the diffusive terms, see App. D.1). This particular test was conducted on the benchmark case shown in App. E.2, and a value of $\kappa \approx 3$ was determined in accordance with the small diffusion Reynolds number chosen for the tests($Re = 9600$).

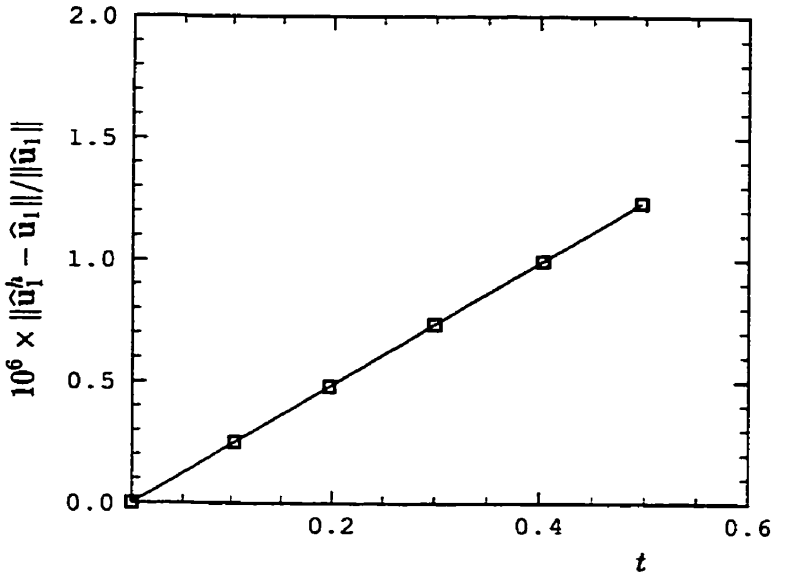

FIGURE 4.6. Relative eigenmode error as a function of time, for $k_\theta = 2$, $k_z = 3$. The discretization parameters are $k = 7$, $N_r = 35$ and $\Delta t = 9.4 \times 10^{-3}$ (CFL = 0.05).

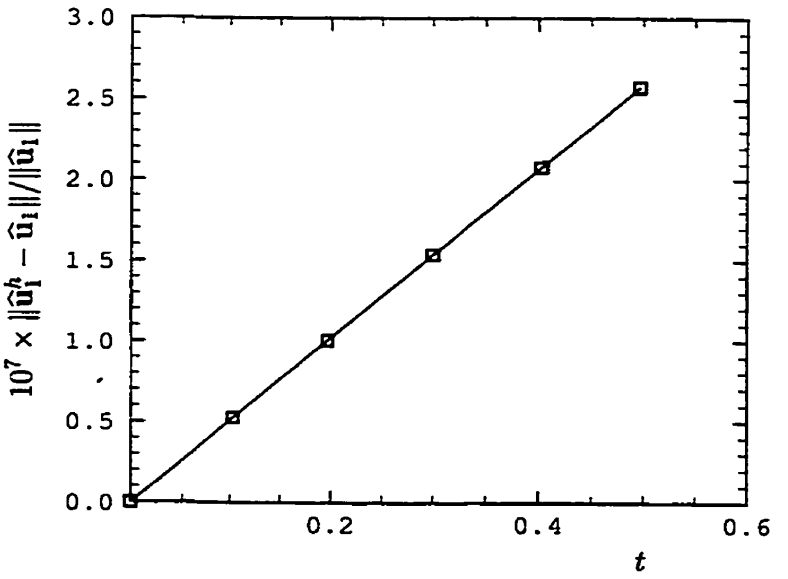

FIGURE 4.7. Relative eigenmode error as a function of time, for $k_\theta = 0$, $k_z = 2$. Discretization parameters as in FIG. 4.6.

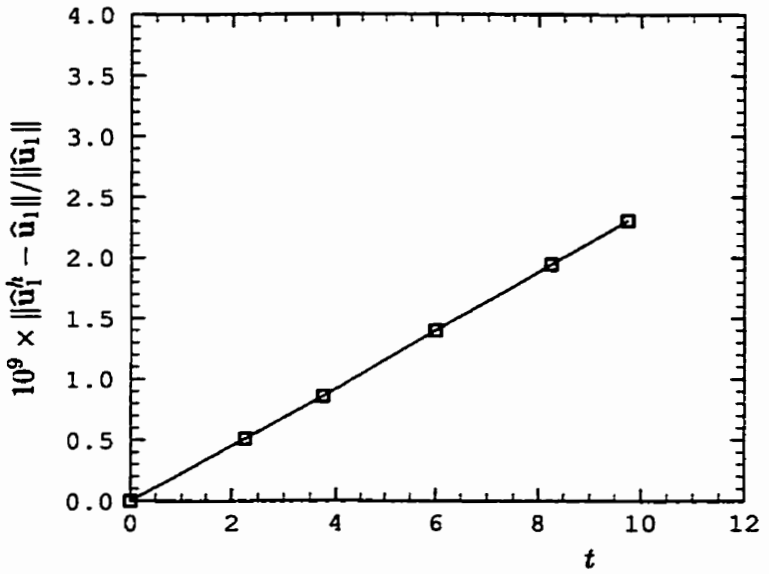

FIGURE 4.8. Relative eigenmode error as a function of time, for $k_\theta = 0$, $k_z = 2$. Discretization parameters as in FIG. 4.6, except for $\Delta t = 9.4 \times 10^{-1}$ (CFL = 5.0). See text for additional comments on the time step size value for this case.

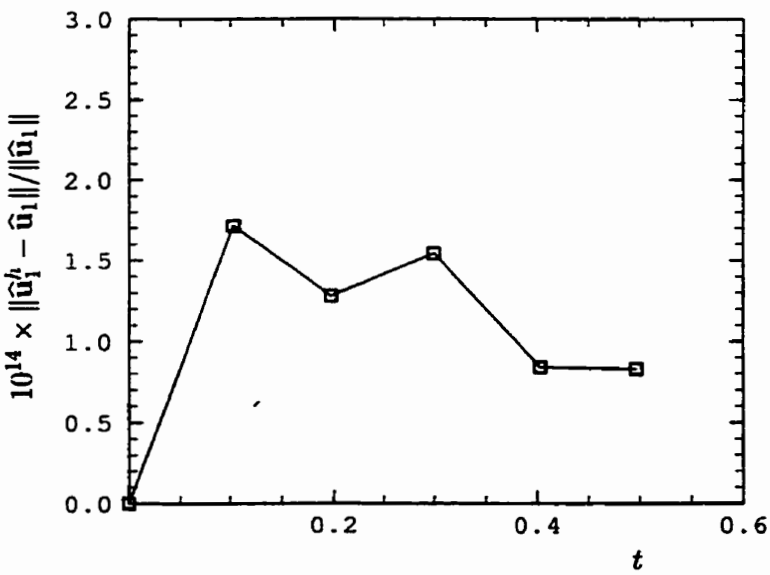

FIGURE 4.9. Relative eigenmode error as a function of time, for $k_\theta = 0$, $k_z = 0$. Discretization parameters as in FIG. 4.6. Notice that the error here is at about the machine round-off level.

4.2 Trailing line vortex

The preliminary validation presented in the last section was focussed on the bounded domain codes BOUNCYL and BOUNCYL-LS. This allowed comparisons of the numerical results of B-spline discretization with some closed form analytical solutions for the Stokes flow in a pipe. Additional results from the linear stability of Poiseuille flow served for the validation of the nonlinear term computation and the global time marching algorithm of the Navier-Stokes solver.

In this section, we proceed with the verification of the unbounded flow codes UNCYL and UNCYL-LS. Both Navier-Stokes solvers (bounded and unbounded) share the same algorithms for the time integration and the computation of the nonlinear term—validated in the preceding section—but clearly differ in the radial discretization and the outer boundary conditions. These differences have repercussions on both the inertia and viscous matrices as well as on the nonlinear term radial integrals (see Chap. 3). The objectives of this section are therefore focussed on the verification of these new radial terms.

More specifically, in this section emphasis is put on the expansion families for which $k_z \neq 0$ (see TABLE 2.1); the 2-D polar cases, i.e., with $k_z = 0$, being the object of next section. In the first part of the present section, we will be primarily concerned with the validation of the eigenvalue solver UNCYL-LS. The validation of the complete Navier-Stokes solver UNCYL will then be considered in the second part of the section, not only in relation with external reference data but also with its consistency with the eigenvalue solver. Finally, at the end of this section, a brief digression is made to comment on the use of the bounded B-spline formulation for the solution of unbounded flow problems.

4.2.1 Linear stability: Eigenvalue solver

To carry on with our task of validating the radial terms (and the code itself), we propose to consider the stability of trailing line vortices, more precisely of the Batchelor q-vortex. The problem is described in more details just below. Since there are again no closed form solution for this problem, validation will be done by comparing

our results with the predictions of Lessen et al. (1974), Mayer & Powell (1992) and Matsushima & Marcus (1997).

In order to better standardize our results with those found in the references, let us introduce the new variable N_r^*, that represents the number of "free" B-splines or equivalently the number of "radial modes". The terminology of radial mode comes from the global expansion approach. One may also recall that because of the divergence-free formulation used here, there are only two unknowns (complex valued) per computational nodes, namely α_{lmn}^+ and α_{lmn}^-. In that sense, N_r^* represents half the number of degrees of freedom per Fourier modal pair. The number of free B-splines N_r^* differs from the total number of B-splines N_r by the number of regularity/boundary conditions imposed, which in turn depends on the value of k_θ (see again Chap. 3).

The q-vortex flow was initially presented by Batchelor (1964) as a self-similar solution for an aircraft trailing line vortex. It is composed of a standard Gaussian (Lamb-Oseen) vortex to which is superposed an axial jet-like flow. As argued by Batchelor, this axial flow (relative to the free stream flow) comes as a dynamical necessity from the pressure differences within the vortex core (see also Saffman, 1992, for additional comments). This "basic flow" combination is not only a model problem of interest for aircraft vortices, but also for swirling jets. The difference between these two flow problems being only a matter of relative proportions. To describe the base flow field, we use the following normalization

$$\mathbf{U}(r) \;=\; 0\,\hat{\mathbf{e}}_r \;+\; \frac{q}{r}\,(1-e^{-r^2})\,\hat{\mathbf{e}}_\theta \;+\; h\,e^{-\beta r^2}\,\hat{\mathbf{e}}_z\;, \tag{4.11}$$

where q scales the swirl intensity, h the centerline axial velocity, and β the relative radial dimension of the axial flow to the vortex core size. The dimensional reference length and velocity scales that have been used for this normalization are respectively the vortex core size radius $\bar{a}$ and the fraction $1/h$ of the centerline axial velocity $\bar{U}_z(r=0)$. The corresponding Reynolds number is thus written

$$Re \;\equiv\; \frac{\bar{U}_z\,\bar{a}}{h\,\bar{\nu}}\;.$$

Note that the vortex core size radius $\bar{a}$ has been defined as $0.893\bar{r}_{U_{\theta\,\max}}$. The maximum swirl velocity $U_{\theta\,\max}$ therefore occurs at a non-dimensional radius of 1.12. These choices have been made in accordance with the convention used in the references.

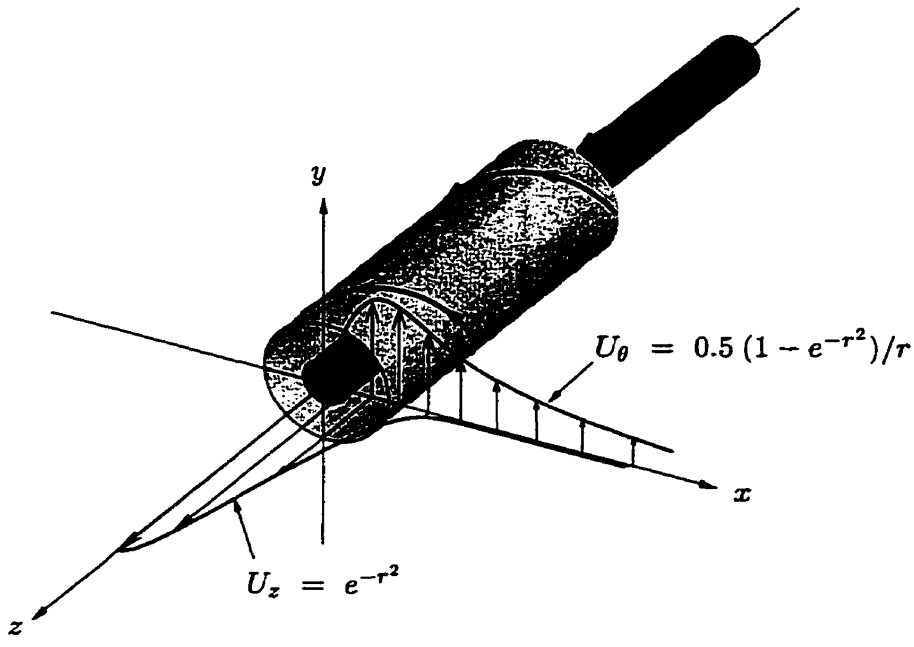

FIGURE 4.10. Perspective view of a q-vortex having parameter values of $q = 0.5$ and $h = \beta = 1$. The vortex tube is represented by the two iso-surfaces of longitudinal vorticity, $\omega_z = 0.8$ (inner surface) and $\omega_z = 0.2$ (outer surface). The spiral lines represent the fluid particle trajectories at the surface radius. Both azimuthal and longitudinal velocity profiles are also shown on the figure. [Figure by courtesy of R. Brochu]

To better illustrate the base flow field, we show in FIG. 4.10 a perspective view of a q-vortex with $q = 0.5$ and $h = \beta = 1$. The vortex tube is represented by two iso-surfaces of longitudinal vorticity: for the long inner surface, $\omega_z = 0.8$, while for the short outer one, $\omega_z = 0.2$. On each surface, the typical spiral path of the fluid particles is also shown. From inside out, the flow passes from purely axial, on the centerline z axis, to purely azimuthal at a sufficiently large radius. The variation of the pitch angle between these two extremes is determined by the value of the parameter q. The two velocity profiles U_θ and U_z are also included in the figure. A more formal graph of these specific velocity profiles is presented in FIG. 4.11 in terms of both the mapped coordinate η and the physical coordinate r.

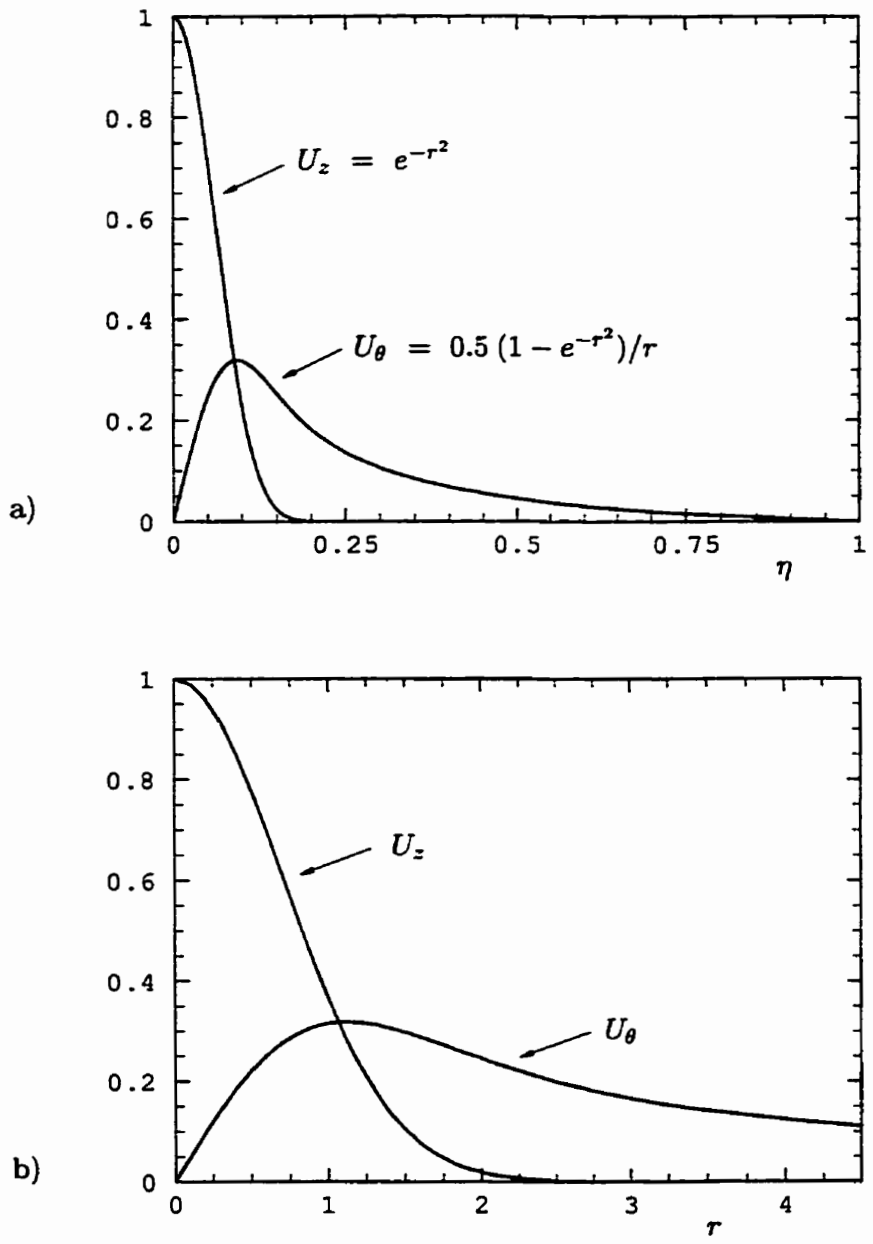

FIGURE 4.11. Axisymmetric base flow field for a q-vortex defined with $q = 0.5$ and $h = \beta = 1$. The profiles are plotted in relation to a) the mapped coordinate η with $L = 11$, and b) the radial coordinate r. See also FIG. 4.10.

Let us first consider the linear stability problem (3.27) for the q-vortex just defined above, i.e., with $q = 0.5$ and $h = \beta = 1$. We remind the reader that this test not only serves for the validation of the inertia and viscous matrices of the code UNCYL (via the eigenvalue solver UNCYL-LS), but it also serves for the validation of the linearized transport matrix. The importance of this point lies on the fact that later verifications of the complete Navier-Stokes solver will rest, in part, on these validation results.

Now, for the given set of parameters and a Reynolds number of $Re = 25$, it is known that the flow is unstable ($\mathrm{Re}(\lambda_s) > 0$) for perturbations in the modal pair $k_\theta = 1$, $k_z = 0.05$ (Mayer & Powell, 1992). Note that this stability problem is well suited for testing the radial discretization because it involves the slowest decaying rate of swirl velocity ($U_\theta \propto r^{-1}$ in the far field region), i.e., a wide spreading of the base flow, easily representable by the built-in decaying behavior, together with a smooth but relatively localized eigenmode. The computed most unstable eigenvalue λ_1 is given in TABLE 4.3 for different values of N_r^*. All values shown in the table were obtained with quintic B-splines ($k = 6$), uniformly distributed in the mapped domain η with $L = 11$. The corresponding values computed by Mayer & Powell and Matsushima & Marcus are given for comparison. Note that both of these reference values were obtained by global expansion approximations. In the first case, Chebyshev polynomials were used in combination with a no-slip condition imposed at a large but finite outer radius R_o. In the second case, radial discretization was done with rational Legendre functions on an unbounded domain, with similar boundary conditions as the ones used here.

The most unstable corresponding eigenmode ($\widehat{u}_\theta$) is shown in FIG. 4.12. The data used to make the figure are the ones of the $N_r^* = 70$ solution. Note that at $\eta = 0.5$ (or $r = 11$)[2], the eigenmode is practically zero. This means that there are in fact about only half the B-splines that are effectively used for resolving the eigenmode. A more efficient use of the local node positioning flexibility would rightly suggest to reduce some of the superfluous B-splines in the outer region.

[2]The reader may recall the quick rule of thumb, given in Chap. 2, for passing from the mapped coordinate η to the true radial coordinate r: $\eta = 0.25 \Leftrightarrow r = L/3$, $\eta = 0.5 \Leftrightarrow r = L$, and $\eta = 0.75 \Leftrightarrow r = 3L$.

TABLE 4.3. The most unstable eigenvalue of $k_\theta = 1$, $k_z = 0.05$, for $q = 0.5$ and $h = \beta = 1$ at $Re = 25$. The results are obtained with uniformly distributed B-splines (in η) with $k = 6$ and $L = 11$.

N_r^*	$\lambda_1 \times 10^4$
10	9.936040736 + i 22.40210147
20	9.885122155 + i 22.38851112
30	9.885158802 + i 22.38705093
40	9.885164246 + i 22.38703955
50	9.885164396 + i 22.38703911
60	9.885164411 + i 22.38703907
70	9.885164411 + i 22.38703907
MM†	9.8851644 + i 22.387039
MP‡	9.8851643 + i 22.387039

† Matsushima & Marcus (1997): $N_r^* = 60$ and $L = 12$
‡ Mayer & Powell (1992): $N_r^* = 300$ and $R_o = 200$

The present choice of using a uniform node distribution (in η) was made to allow for a standard point of comparison with the global expansion approximations, and also with the different B-spline results between themselves. In mapped global expansion approximations, e.g., as in Matsushima & Marcus, the radial resolution positioning (i.e., putting the degrees of freedom where they are needed) is determined only by the mapping parameter(s). In a mapped local method, such as this one, a great deal of flexibility is added by allowing for the independent adjustment of the mapping parameter and the node positioning. This certainly constitutes one of the original characteristics of the numerical method presented in this thesis. The resulting extra flexibility may lead to many possible combinations of mapping and domain partioning for practically similar effective resolution. This last point will be the object of further considerations in Sec. 4.2.4.

Assessment of the convergence rates for the mapped B-splines in this case is more difficult to carry out for lack of known analytical solutions. Instead, we make use of our new benchmark data of TABLE 4.3 (with $N_r^* = 70$) as a reference solution and compare lower resolution results with it. This, of course, constitutes more of a

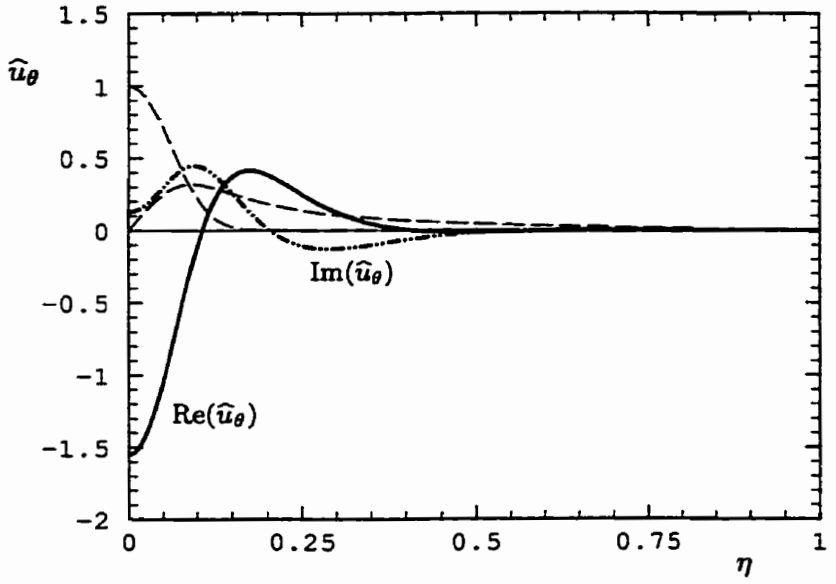

FIGURE 4.12. Most unstable computed eigenmode ($\widehat{u}_\theta$) corresponding to the problem of TABLE 4.3. The real part of the eigenmode is represented by the solid line, the imaginary part by the broken ("dash-dot-dot") line. The light dashed lines represent the base flow field, given as a reference.

consistency check than a true validation test for the radial interpolation.

The h- and p-convergence of the "approximated" solution hence obtained are shown in FIG. 4.13, again with a uniform node distribution in η. The h-convergence results shown in 4.13.a were obtained with $k = 5$ and $L = 11$. The convergence rate evaluated by a best-fit of the data is -7.19, which is in very good agreement with the results obtained in the Stokes pipe flow problem of TABLE 4.1. The p-convergence is shown in 4.13.b; the results were obtained with $N_r^* = 20$ and $L = 7$. These parameters were chosen to produce a significant and reliable difference between the approximated and the reference eigenvalues. In this case, the quasi-spectral convergence—a straight line alignment of the data points in a "log-lin" plot—is not as much apparent as it was in FIG. 4.2, but can nevertheless be considered relatively satisfactory. One should note that it is indeed not clear that if, by fixing the node distribution and the mapping parameter L in this error analysis, the resolution varies consistently with the B-spline order. We must also remember that these expected convergence behaviors

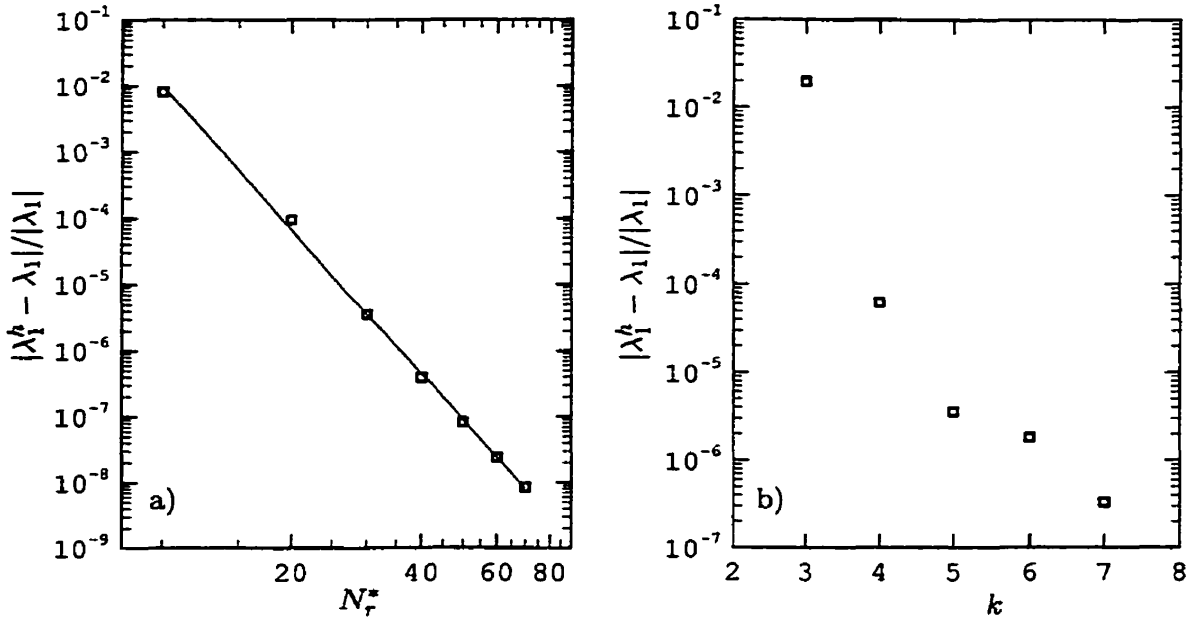

FIGURE 4.13. Relative error of the most unstable eigenvalue for the stability problem of TABLE 4.3. a) Results obtained with $k = 5$ and $L = 11$. The line represents a best-fit of the data for which $|\lambda_1^h - \lambda_1|/|\lambda_1| \propto N_r^{*\,-7.19}$, showing the h-type convergence. b) Results obtained with $N_r^* = 20$ and $L = 7$. The data show the p-type (quasi-spectral) convergence of the mapped B-splines.

may be observed only after a certain minimum level of resolution is achieved. Both of these considerations could help in explaining some of the observed fluctuations in the data points.

As another validation test for the eigenvalue solver UNCYL-LS, we computed the neutrally stable ($\lambda_r = 0$) asymmetric oscillations ($k_\theta = 1$) of an inviscid columnar vortex for different values of the defining parameters q, h and β. The results were obtained with $N_r^* = 20$ (uniformly distributed) and $k = 5$, and are shown in TABLE 4.4. All four digits shown are significant; computations with $N_r^* = 40$ were also carried out to check the accuracy. The mapping parameter L was chosen in order to minimize the difference between the two separate resolution sets of results, a procedure somewhat equivalent to the choice of optimal mapping parameter used by Matsushima & Marcus. For comparison, we include the values computed by Matsushima & Marcus

TABLE 4.4. The positive imaginary part of the eigenvalue ($k_\theta = 1$) of the neutrally stable ($\lambda_r = 0$) inviscid columnar vortex (4.11). The UNCYL-LS values were obtained with $N_r^* = 20$ and $k = 5$. As references, we include the equivalent results of Matsushima & Marcus and the theoretical predictions of Moore & Saffman given in (4.12).

					$\lambda_i/q \times 10^4$		
No	k_z	h/q	β	L	UNCYL-LS	MM†	(4.12)‡
1	0.4	0.0	–	4	897.0	897.0	779.4
2	0.2	0.0	–	5	344.1	344.1	333.5
3	0.1	0.0	–	7	118.9	118.9	118.0
4	0.05	0.0	–	10	38.24	38.24	38.17
5	0.025	0.0	–	15	11.71	11.71	11.71
6	0.025	2.0	1.0	11	5.127	5.127	5.125
7	0.025	1.0	1.0	11	9.865	9.865	9.861
8	0.025	−1.0	1.0	11	10.45	10.45	10.45
9	0.025	−2.0	1.0	11	5.832	5.832	5.828
10	0.025	2.0	0.5	–	*	*	−.9086
11	0.025	1.0	0.5	11	8.081	8.081	8.076
12	0.025	−1.0	0.5	11	9.150	9.150	9.145
13	0.025	−2.0	0.5	–	*	*	−.6475
14	0.025	2.0	2.0	8	8.353	8.353	8.349
15	0.025	1.0	2.0	10	10.78	10.78	10.78
16	0.025	−1.0	2.0	10	11.08	11.08	11.08
17	0.025	−2.0	2.0	9	8.835	8.835	8.831

† Matsushima & Marcus (1997): $N_r^* = 59$, see also TABLE V in the ref.
‡ Moore & Saffman (1972)
*: No positive eigenvalues were found

with 59 radial modes. Also, as a reference, we include the asymptotic solution results of Moore & Saffman (1972, cited from Matsushima & Marcus). Their long wavelength asymptotic solution gives the imaginary part of the eigenvalue as

$$\frac{\lambda_i}{q} = -\frac{k_z^2}{2}\left[\ln k_z + \frac{1}{2}(\gamma - \ln 2) + \frac{h^2}{2q^2\beta} + \frac{hk_z}{q\beta(1+\beta)}\right]\frac{1}{1+hk_z/q\beta} \qquad (4.12)$$

where $\lambda_i = \mathrm{Im}(\lambda)$ and $\gamma = 0.57721566\ldots$ (Euler's constant).

As reported by Matsushima & Marcus, this problem also constitutes a good test for the radial discretization since as k_z becomes smaller, the eigenfunctions have a slower radial decay, i.e., a wider extent. Technically the problem therefore becomes increasingly difficult as k_z decreases because of the scale difference between the base flow and the eigenfunction. This scale difference can also be accentuated as β increases, for example, because of the narrowing of the axial jet flow. At any rate, for the range of parameters shown, systematic agreement (all four significant digits) between the two numerical methods is observed. The agreement with the asymptotic predictions improves as expected when k_z diminishes, i.e., as k_z approaches the long wavelength limit of (4.12). It is worth noting how the B-spline discretization compares advantageously to the rational Legendre functions of Matsushima & Marcus in this particular case (our $N_r^* = 20$ vs. their $N_r^* = 59$). We must note however that is not entirely clear if the $N_r^* = 59$ results of Matsushima & Marcus do have more significant digits than the four shown in their table.

The stability of the inviscid q-vortex was also investigated numerically by Lessen et al. (1974). The method they used is based on a different approach than the one used by both Mayer & Powell and Matsushima & Marcus which are somewhat closer to ours. These last two methods, like ours, are based on some weighted residual formulation in combination with an eigenvalue solver of the QZ-type, as discussed in Sec. 3.6. Note that the precise details for the eigenvalue solver were not given by Matsushima & Marcus, but are presumed to follow this line of approach. As for Lessen et al., they first integrated the ordinary differential equation for the dispersion relation using a Runge-Kutta scheme and Frobenius power series. Then the eigenvalues were found as the zeros of this integrated equation using a Newton-Raphson method. With this approach, they identified a series of unstable "inviscid" modes from which, according to the azimuthal wavenumber k_θ, the maximum growth rates and the corresponding flow parameters are given in TABLE 4.5. Also shown in the table are the results from our code UNCYL-LS for the same parameters. The agreement between the two sets of results is again very satisfactory. Note that in this case, we used different radial discretizations (different values of N_r, k and L), according to the different sets of parameters, in order to obtain the four significant digits shown in the table.

TABLE 4.5. Maximum growth rates along with the corresponding longitudinal wavenumber k_z and swirl parameter q for different values of k_θ ($h = \beta = 1$). Our UNCYL-LS results are compared with the inviscid analysis values of Lessen et al.

			λ_r	
k_θ	k_z	q	UNCYL-LS	LSP[†]
1	−0.3	0.32	0.1494	0.1470
2	−1.2	0.70	0.3137	0.3138
3	−1.7	0.79	0.3544	0.3544
4	−2.15	0.82	0.3774	0.3777
5	−2.6	0.83	0.3906	0.3912
6	−3.2	0.83	0.4017	0.4008

[†] Lessen et al. (1974): see also TABLE 1 in the ref.

4.2.2 Linear stability: Navier-Stokes solver

Up to now, our q-vortex results served to verify the eigenvalue solver, for the general expansion family of $k_\theta > 0$, $k_z \neq 0$. At this point, we begin the second part of this section and make use of the validated eigenvalue solver—in conjunction with other external linear stability results—to verify the unsteady Navier-Stokes code UNCYL. The validation of the axisymmetric family of expansions, $k_\theta = 0$, $k_z \neq 0$ is also considered in the process. The verification procedure used in this part is separated in two. On one side, it involves the direct finding of the most unstable mode and its growth rate using the Navier-Stokes solver. An unsteady Navier-Stokes solution does indeed only provide information about the most unstable, or the least stable radial eigenmode solution (i.e., $s = 1$ in our ordering convention) for the given modal pair k_θ, k_z. On the other side, it involves the use of consistency verifications between both the Navier-Stokes and the validated eigenvalue solvers.

Longitudinal asymmetric modes: $k_\theta > 0$, $k_z \neq 0$.

In the linear stability problem (3.27), the base flow field was defined as an equilibrium solution of the Navier-Stokes equations, such as the parabolic profile (4.10) used in the pipe flow problem of Sec. 4.1.2. Because such solutions are seldom available for

unbounded domains, it is usually more convenient to work with equilibrium solutions of the less stringent (no diffusion) Euler equations. The present q-vortex problem is certainly a good example for this type of situation. Now, in order to formally recover the eigenvalue results associated with an Euler equilibrium solution, through a simulation of the complete Navier-Stokes equations, special care must be taken. The procedure used here to reproduce, and maintain, the Euler equilibrium state is simply to "freeze" the diffusion of the base flow. This simply amounts in skipping the time marching of the modal pair $k_\theta = 0$, $k_z = 0$. By doing so, the initial condition for that modal pair (the base flow) remains thus constant for the whole computation.

As a first test case, we study the stability of the q-vortex for the following set of base flow parameters:

$$q = 0.537 \quad ; \quad h = \beta = 1 \quad ; \text{ and } \quad Re = 40 \, .$$

Note that unless otherwise stated, the axial flow parameters will, for now on, remain fixed to $h = \beta = 1$. For the modal pair $k_\theta = 1$, $k_z = 0.436$, noted in its index form[3] $(1,1)$ for short, Mayer & Powell give a perturbation growth rate of $\lambda_r = 1.06 \times 10^{-2}$. As an initial condition for the Navier-Stokes solver, in addition to the base flow, we add a small amplitude white noise perturbation, with a modal energy of $E_{k_\theta,k_z} = 10^{-6}$, on all the computational modes; the modal energy is given by

$$E_{k_\theta,k_z} = \frac{1}{2}\int_0^\infty \widehat{\mathbf{u}}^*(r;\ k_\theta,k_z)\cdot\widehat{\mathbf{u}}(r;\ k_\theta,k_z)\, r\, dr \, . \tag{4.13}$$

The radial scalar fields are constructed from random B-spline coefficients values for $\eta \leq 0.5$, and zero afterward. An example of equivalent energy spectra is shown in FIG. 4.20 of Sec. 4.2.3.

Because we are here interested in the behavior of the specific modal pair $(1,1)$, low order spectral truncation is sufficient since that for linear stability dynamics, all nonlinear interactions besides those relating the perturbations with the base flow are of negligible order. Accordingly, the computation of the nonlinear term need not be done on a de-aliased collocation grid (see Chap. 3). Indeed, for this type of problems,

[3]Recall from Chap. 2 that the modal index pair (m,n), written in parenthesis, corresponds to the modal pair k_θ, k_z via $m = k_\theta L_\theta/2\pi$ and $n = k_z L_z/2\pi$. By choosing $L_\theta = 2\pi/k_\theta$ and $L_z = 2\pi/k_z$, the modal pair k_θ, k_z has the index values $(1,1)$.

TABLE 4.6. Comparison of modal growth rate results for the asymmetric mode $k_\theta = 1$, $k_z = 0.436$ with $q = 0.537$ ($h = \beta = 1$) and $Re = 40$. Navier-Stokes results are identified with the equation used to determine the values shown in the table.

	$\lambda_r \times 10^2$
MP†	1.06
UNCYL (I)	1.06
UNCYL (D)	1.055
UNCYL-LS	1.05565

† Mayer & Powell (1992)

the resolution effort mostly concerns the radial direction. The spatial discretization parameters used for the code UNCYL are:

$$N_r = 54 \quad ; \quad k = 5 \quad ; \quad N_\theta = 4 \quad ; \quad N_z = 6 \, .$$

The B-spline breakpoints are uniformly distributed in η with $L = 10$. For the time discretization, we used CFL $= 2$ ($\Delta t \approx 0.4$). Once the perturbation growth rate becomes relatively stable, the value is reduced to CFL $= 0.2$ for 25 time steps from which we determine the results appearing in TABLE 4.6. The number of digits shown in the table corresponds to the number of digits that remained constant over these last 25 time steps. The "(I)" and "(D)" labels associated with the UNCYL results, in the table, refer to method used to estimate the growth rate; the methodological details are supplied in Sec. D.6, in the appendices. For now, let us simply mention that method (I) is based on an instantaneous variation of modal energy (see (D.37)) while method (D) is based on a discrete estimate of this variation (see (D.38)). We make use of method (I) here because it is readily available from the Galerkin approximation (again see Sec. D.6). On the other hand, according to the level of energy at which the value is determined, method (D) may sometimes appear to be more precise, provided that the time step size Δt used in the evaluation of the estimate is small enough. To compare with the Navier-Stokes solver values, we give the result obtained with the eigenvalue solver for the same radial discretization. In that latter case the number of significant digits is, as previously, determined by comparison with other eigenvalue results obtained at higher resolution.

To illustrate how much of the B-spline resolution is effectively put to contribution, the corresponding eigenmode $\widehat{u}_\theta$ obtained from the Navier-Stokes solution is shown in FIG. 4.14. Eigenfunction values were amplified by a 3×10^4 factor to allow a comparison with the base flow velocity components shown in dashed lines. Also included in the figure are the uniformly distributed radial breakpoints. Since the eigenmode is non-zero for only approximately $r < 4.5$ ($\eta < 0.33$), a uniform radial resolution is clearly not the best choice in this case.

Owing to the very good agreement, in TABLE 4.6, of our Navier-Stokes results with those of the validated eigenvalue solver and of Mayer & Powell, we may directly infer the validity of the code UNCYL in regard to the general family of vector expansions having $k_\theta > 0$, $k_z \neq 0$.

This point is additionally supported by the monitoring of the modal energy $E_{k_\theta,kz}$ that was done during the simulation. The time variation of some of these modal energies is shown in FIG. 4.15. One may recall that a straight line on this "log-lin" figure represents an exponential growth/decay. The modal growth rate values (obtained with method (I) at $t = 125$) corresponding to the different curves are presented in TABLE 4.7; the UNCYL values of TABLE 4.6 are taken from the $(1,1)$ curve. For the selected modal pairs shown, the unstable predictions ($\lambda_r > 0$) from the eigenvalue solver are well reproduced by the Navier-Stokes results, confirming thus the consistency between both solvers. As for the discrepancies between the eigenvalue solver stable mode predictions ($\lambda_r < 0$) and the Navier-Stokes values, they can be shown to be the result of some significant nonlinear interactions. At $t = 125$, the energy level of the $(1,-1)$ and $(2,-2)$ modes has certainly become way too important for their nonlinear interactions to be considered negligible.

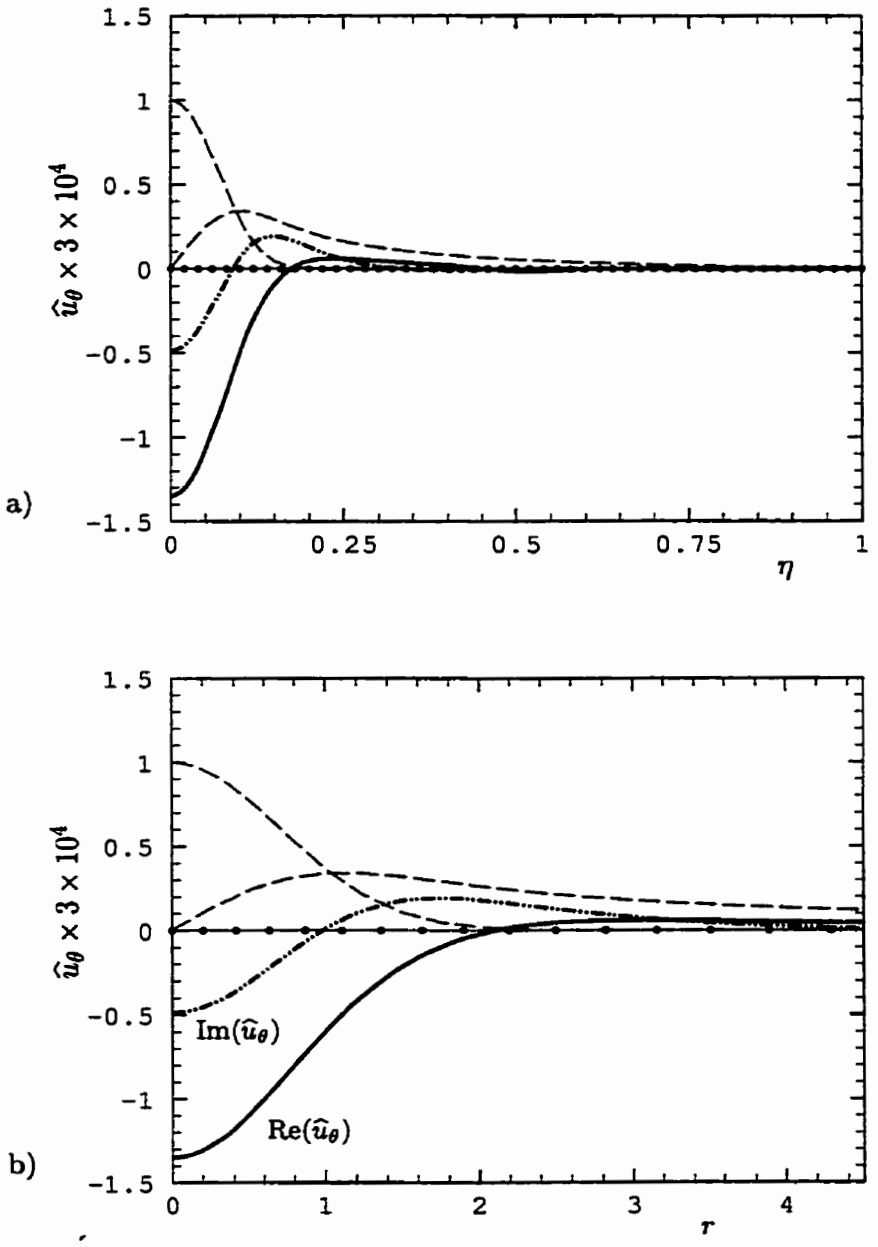

FIGURE 4.14. Asymmetric eigenmode ($\widehat{u}_\theta$) associated with the eigenvalue of TABLE 4.6. The eigenmode is shown as a function of a) the mapped coordinate η ($L = 10$), and b) the physical coordinate r. The eigenfunctions are amplified by a factor of 3×10^4 and the dashed lines represent the base flow field given as a reference. The points on the radial axis identify the B-spline breakpoints.

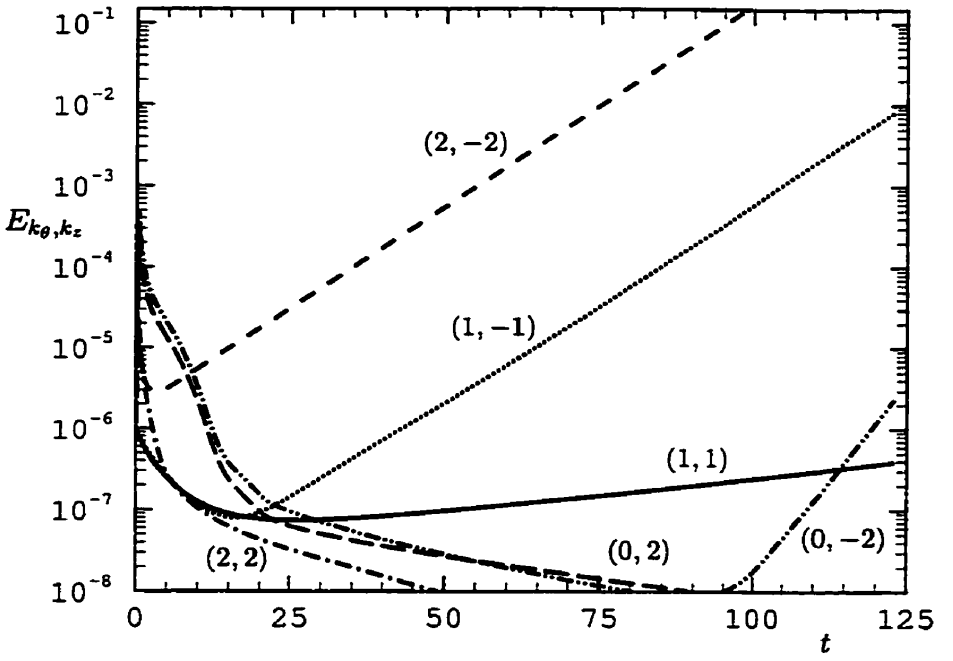

FIGURE 4.15. Modal energy as a function of time for $q = 0.537$ ($h = \beta = 1$) and $Re = 40$. The values in parenthesis identify the modal pair indices associated with the curves. The corresponding growth/decay rates are given in TABLE 4.7.

TABLE 4.7. Observed growth rates from Navier-Stokes simulations for the modal index pairs (m, n) shown in FIG. 4.15. The given values were taken at $t = 125$, when some of the modal pairs have left the linear regime. The corresponding eigenvalue solver results are given as a reference. See text for additional information.

	$\lambda_r \times 10^2$	
(m, n)	UNCYL	UNCYL-LS
(1, 1)	1.06	1.05565
(2, −2)	5.75	5.7388
(1, −1)	5.60	5.7351
(0, −2)	11.3	−1.90096
(0, 2)	−1.41	−1.90096
(2, 2)	−2.66	−1.9010

Longitudinal axisymmetric modes: $k_\theta = 0$, $k_z \neq 0$.

Let us now consider the verification of the axisymmetric family of expansions $k_\theta = 0$, $k_z \neq 0$ (see TABLE 2.1). The validation of both codes UNCYL and UNCYL-LS will be carried out simultaneously by considering this time the unstable growth rate values λ_r as a function of the swirl parameter q, again with $h = \beta = 1$. More specifically, the validation test will be realized for an axisymmetric perturbation with $k_z = 0.444$ at $Re = 1000$. The computed results are compared with those of Mayer & Powell (1992), and are presented in FIG. 4.16. In the reference, the q instability range for this specific set of parameters is given by

$$0.83 \; < \; q \; < \; 1.26 \, ,$$

with a maximum growth rate of $\lambda_r = 9.03 \times 10^{-4}$ occurring at $q = 1.05$; these three characteristic points are shown on the figure.

In this case, because the growth rates are quite small and the evolution from a random perturbation to a well structured eigenmode may be quite long, we directly use the eigenmode (from the eigenvalue solver) as the initial condition for the Navier-Stokes simulation (a 10^{-6} amplitude factor is used to maintain "secondary" nonlinear interactions negligible). Note that this test amounts, in a certain way, to the one done for the Orr-Sommerfeld wave propagation for the pipe flow problem of Sec. 4.1.2.

The growth rates evaluated with the Navier-Stokes solver agree to almost all significant digits with the values found by the eigenvalue solver, for the same radial discretization: $N_r = 54$, $k = 5$, with a uniform domain partition in η ($L = 5$). This certainly confirms that both solvers are consistent between themselves. Again, the number of significant digits of the UNCYL-LS growth rates is determined by comparison with higher order approximations ($N_r = 55$, $k = 6$). The maximum growth rate values λ_r hence obtained are shown in TABLE 4.8. The UNCYL value was computed with CFL = 1.7 ($\Delta t \approx 0.2$). All values are seen to be in very good agreement with each other. Furthermore, a linear interpolation between the two first and the two last data points gives the loci of the neutral stability ($\lambda_r = 0$) limit points, which yields an instability range of

$$0.83476 \; < \; q \; < \; 1.25448 \, , \tag{4.14}$$

also in very good agreement with the reference values given above.

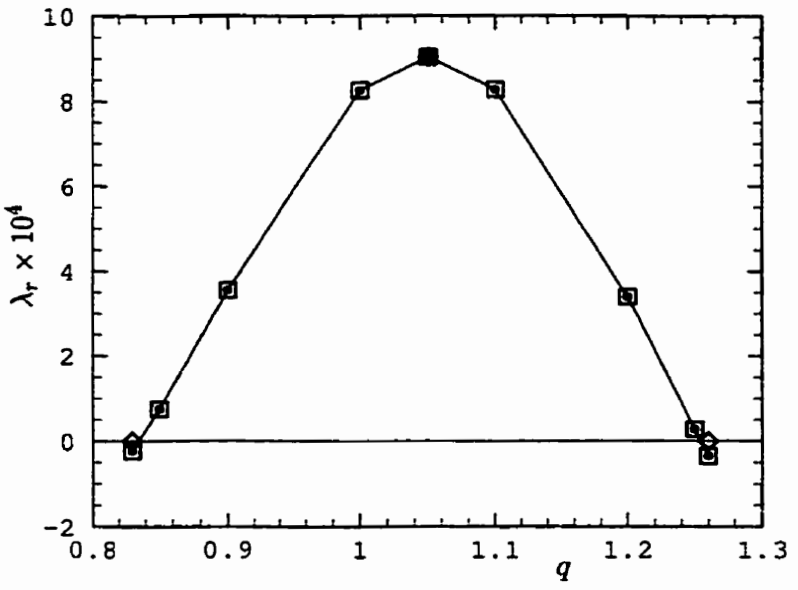

FIGURE 4.16. Growth rate value λ_r as a function of the swirl parameter q for the axisymmetric "viscous mode" $k_\theta = 0$, $k_z = 0.444$ at $Re = 1000$. The symbols identify the following results: "•" UNCYL-LS values; "□" UNCYL values; and "◇" Mayer & Powell reference values. The lines are drawn from the eigenvalue solver data points. Note that the maximum growth rate value at $q = 1.05$ coincides for all three sets of data points (see also TABLE 4.8).

TABLE 4.8. Comparison of modal growth rate results for the axisymmetric mode $k_\theta = 0$, $k_z = 0.444$ with $q = 1.05$ and $Re = 1000$ (see text for additional information).

	$\lambda_r \times 10^4$
MP†	9.03
UNCYL (D)	9.0281
UNCYL-LS	9.028086

† Mayer & Powell (1992)

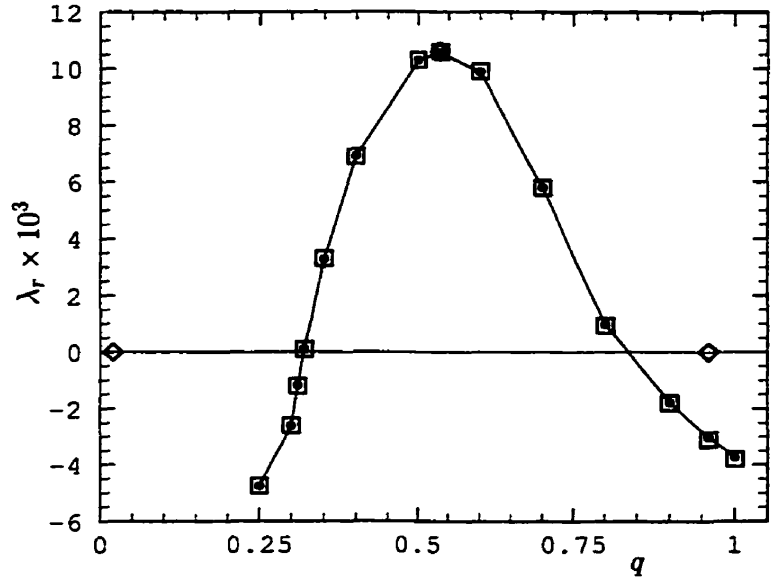

FIGURE 4.17. Growth rate λ_r as a function of the swirl parameter q for the asymmetric viscous mode $k_\theta = 1$, $k_z = 0.436$ at $Re = 40$. The symbol definition is the same as in FIG. 4.16. The maximum growth rate value at $q = 0.537$ coincides for the three sets of data points. See text for additional comments on the stability bounds.

Revisiting the longitudinal asymmetric case $k_\theta = 1$, $k_z = 0.436$.

The test just described above for the longitudinal axisymmetric modes was also carried out for the asymmetric case $k_\theta = 1$, $k_z = 0.436$ at $Re = 40$. Recall that for these parameters, the most unstable viscous mode computed with our method was in good agreement with the predictions of Mayer & Powell, as we showed in TABLE 4.6. In terms of the swirl parameter q, Mayer & Powell give the following instability bounds

$$0.02 < q < 0.96 .$$

Using a similar procedure as described precedently, we obtained the results shown in FIG. 4.17, with this time a much narrower instability range of

$$0.319 < q < 0.864 . \qquad (4.15)$$

Owing to the excellent standing of our results in all the different validation tests presented so far—including agreement with other results of Mayer & Powell—we are quite confident that our computed values provide a more accurate and reliable set of instability bounds for this specific case. A formal explanation for the discrepancy observed between both sets of values is however left to some further study.

4.2.3 Nonlinear dynamics

Having now established a good deal of confidence in the code UNCYL, let us leave the linear stability regime and make a brief "qualitative excursion" into some early stages of the nonlinear dynamics. For this purpose, we consider the low swirl case $q = 0.05$ at $Re = 1000$; the axial flow parameters are still $h = \beta = 1$ so that the flow of interest here is basically a swirling jet. The initial condition, besides the base flow, consisted of a white noise perturbation with an energy level of $E_{k_\theta,k_z} = 10^{-6}$. The spatial and temporal discretization parameters used were:

- $N_r = 54$, $k = 5$, uniform distribution of breakpoints in η $(L = 11)$;
- 4 modal zones $(L_\theta = 2\pi)$ with
  $N_\theta = 6$ $(0 \leq \eta < 0.075)$, $N_\theta = 10$ $(0.075 \leq \eta < 0.1)$,
  $N_\theta = 18$ $(0.1 \leq \eta < 0.5)$, $N_\theta = 10$ $(0.5 \leq \eta < 1.0)$;
- $N_z = 20$ $(L_z = 30)$; and
- CFL $= 1.7$ for which $\Delta t \approx 0.5$.

The time evolution of the solution is shown in FIG. 4.18. To illustrate the development of the instability, we show iso-surfaces of enstrophy $\frac{1}{2}|\omega|^2 = 0.1$; the "vortex tube" is shown for two longitudinal periodicity lengths. The energy variation (in time) of the most unstable modal pairs corresponding to FIG. 4.18 are also shown in FIG. 4.19.

Although we do not aim at making an in-depth study of this q-vortex dynamics, many interesting observations can be made from the simulation results. First, the most unstable modes have an azimuthal index number $m = 1$, combined with

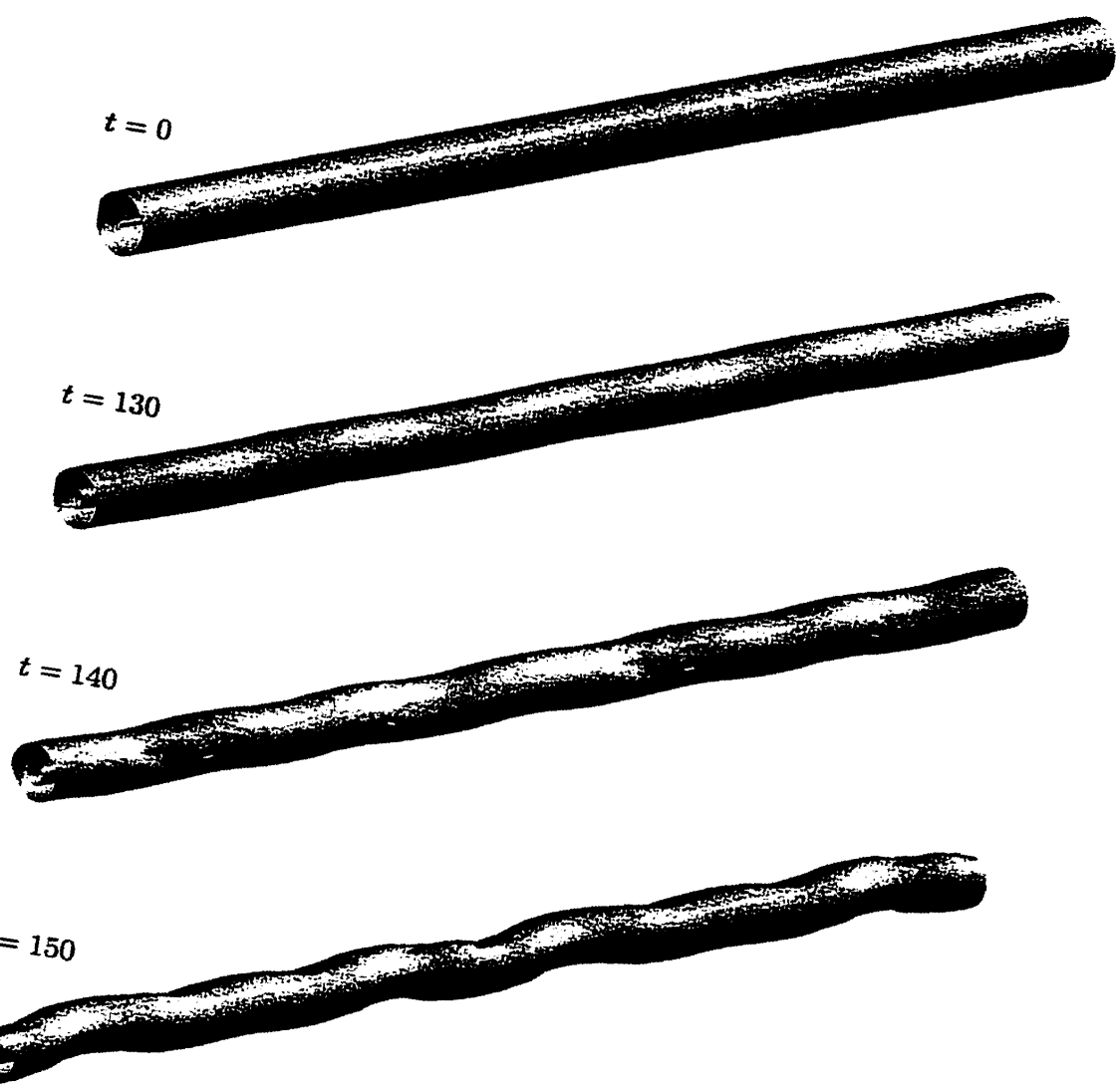

FIGURE 4.18. Time evolution of a randomly perturbed q-vortex with $q = 0.05$ ($h = \beta = 1$) at $Re = 1000$. The vortex tube is represented here by iso-surfaces of enstrophy $\frac{1}{2}|\omega|^2 = 0.1$. For visualization purposes, the representation is done with two longitudinal periodicity lengths.

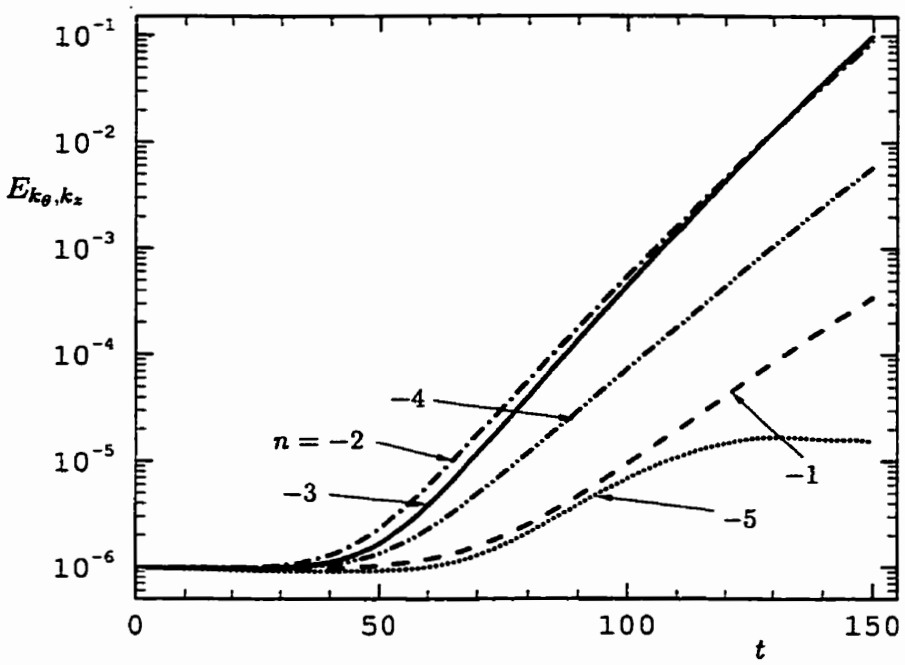

FIGURE 4.19. Time evolution of the perturbation energy for the five most unstable modal pairs (m, n) of the simulation shown in FIG. 4.18. Note that all curves are for $m = 1$, the index n is shown on the figure.

negative longitudinal index numbers n (see FIG. 4.19). This "asymmetric" character of the instability can also be partly observed from the azimuthal energy spectra (r and z integrated) in FIG. 4.20.a. The white noise perturbation is seen from the constant energy level in the spectrum at $t = 0$; the peak at $m = 0$ is associated with the base flow field. Continuing with FIG. 4.20.a, at $t = 50$, the unstable modes have started to grow (see FIG. 4.19) but still with a net decrease of the perturbation energy. At $t = 100$, the dominance of the $m = 1$ mode becomes apparent since an increase of the perturbation energy above the initial level is only seen for this azimuthal mode.

Also from FIG. 4.20.a, we can see some of the effects of the modal zoning. The sudden energy fall-off observed for $m \geq 10$ is one such effect, and is explained by what follows. When defining the white noise perturbation, a uniform amount of energy is assigned to each modal pair to obtain a uniform initial ($t = 0$) spectrum. Because of the (uniform) random character of the initial perturbation energy, there is no radial region

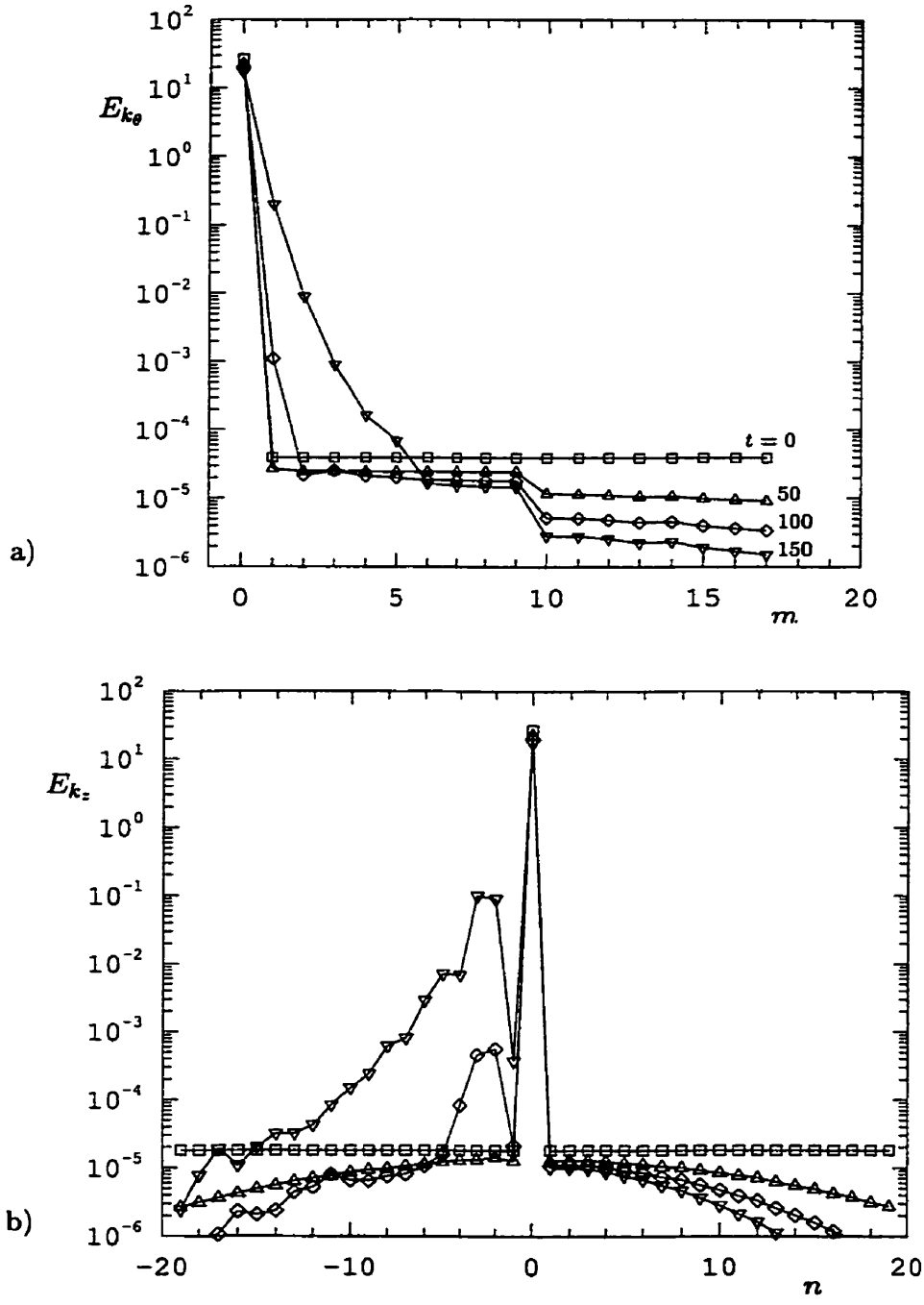

FIGURE 4.20. a) Azimuthal energy spectrum at different times for the q-vortex shown in FIG. 4.18. b) The corresponding longitudinal energy spectrum. Note that the time intervals are the same for a) and b) but different from those in FIG. 4.18. The step fall-off at $m = 10$ in a) is associated to a change of modal zone (see text for additional comments).

in which the modal truncation could be applied with only negligible losses of energy, as discussed by Houde et al. (2000). In other words, if the perturbation energy has a uniform random distribution in the radial direction, then applying directly the modal reduction would result in "step decreases", or energy losses in the initial spectrum. In the present case, we opted for a different strategy in which the perturbation energy density is augmented in the truncated zones, yielding the uniform radially integrated energy distribution at $t = 0$. No modal energy is therefore lost by the modal truncation. Note that for practical reasons, the perturbation energy was radially confined to $\eta \leq 0.5$, for all modes.

The important point of all this remains that, although different initial perturbations will obviously lead to different transient behaviors, the natural ensuing dynamics of the problem should not be affected (in most cases at least) as long as the initial perturbation does not exhibit any preferential structure. The spatial discretization, including the modal zoning, should be adequately devised to allow for the proper representation of all relevant eigenmodes. As can be seen by the shape of the different spectra and the energy level at which the step cut-off occurs, we may certainly feel confident that it has indeed no significant impact on the solution.

Let us now consider the longitudinal spectra (r and θ integrated) in FIG. 4.20.b, keeping in mind that the energy dominant modes have an azimuthal index of $m = 1$. There are many interesting points that can also be observed from that figure. First, one may note the k_z-asymmetry of the spectra. Even if the base flow is dominated by its "jet character", the slight presence of a swirl component results in a symmetry break-off, as discussed by Lessen et al.. Only in the case of a purely axisymmetric jet ($q = 0$), both the k_z and $-k_z$ modes have the same instability characteristics and, as Batchelor & Gill (1962) showed, the corresponding unstable modes are only possible for $k_\theta = 1$. Although this latter demonstration was made for a different velocity profile than the one in (4.11), it is also supposed to apply in this case.

For very low swirl values such as $q = 0.05$, Lessen et al. showed that there remain some positive ($k_z > 0$) unstable inviscid modes but with much smaller growth rates than those of the negative modes ($k_z < 0$). At finite Reynolds numbers, Mayer & Powell also showed that there is a possibility for some asymmetric ($m = 1$) positive viscous modes but again with significantly lower growth rates than those associated

with the inviscid-like modes observed here. None of these positive modes were however seen to emerge from the white noise perturbation we used, due precisely to the smallness of their growth rate. Another point worth noting is that, according to our results, the most unstable longitudinal mode (with $m = 1$) has a value $k_z \approx -0.6$, which is in good agreement with our linear stability predictions, as well as in good qualitative agreement with the inviscid analysis predictions of Lessen et al..

Finally, from the shape of the spectra and the relative amplitude of the modal energies, we are able to confirm that a truncation level $N_z = 20$ was sufficient to properly resolve the problem up to the considered time $t = 150$. With this, we conclude our brief illustrative excursion and at the same time, the verification of the $k_z \neq 0$ families of vector expansions. The reader may note that more complete nonlinear dynamics, with instability saturation, will be presented for the triangular vortex problem in the next section.

4.2.4 Radial direction: Domain truncation vs. mapping

As the reader will have noticed, most of the radial discretizations used so far were with a uniform distribution of breakpoints in the η-domain. The reason for this, as we already mentioned, was in part to allow for more standard comparisons with the global expansion results. Even if the local flexibility was not used to its full potential, the present method compared advantageously well with the other ones used as reference. The question that could naturally come to one's mind at this point is: how much could be gained by taking advantage of the additional flexibility offered by the variable node positioning?

Trying to give a relatively complete answer to this question is, in our view, a task that goes beyond the scope of the present work[4], and so we shall limit ourselves to some particular considerations only. More specifically, the use of a local method in unbounded domains may certainly call for a reconsideration of the truncated domain approach, briefly introduced in Sec. 2.3.2. As one may recall from that section, there are two main sources of error in the approximation of unbounded problems:

[4] As far as we are aware, mesh refinement and optimal node positioning—which is indeed the point of interest here—is still an active field of research of the "finite element community".

i) the approximation of the boundary conditions, and ii) the approximation of the continuum solution by a discrete set of values.

In the truncated domain approach, the outer radius R_o can always be chosen large enough as to bring the boundary condition error[5] to a negligibly small value compared to the other source(s) of spatial error. By doing so, the "double" approximation problem has now become one of spatial resolution only. This point is particularly well illustrated by the "bounded" results shown in TABLE 4.9. The significant differences observed between the error of our two B-spline values and the Chebyshev result of Mayer & Powell must indeed be attributable to differences in the spatial resolution since the boundary conditions are the same for all three cases.

Based on a similar argumentation, we may also conclude that the important difference, in the number of radial modes, between the solution of Matsushima & Marcus and that of Mayer & Powell (see TABLE 4.3) is again attributable to a difference in the spatial resolution. Following this, we can certainly see that the fixed and very regular resolution of global expansions, applied directly to the domain truncation approach does not seem so much appropriate, at least for the type of problems considered here. The mapped Legendre polynomials, or equivalently the rational Legendre functions, of Matsushima & Marcus come as marked improvement in terms of a more appropriate resolution positioning.

As opposed to global expansions methods, local methods with their intrinsic node or resolution positioning flexibility—which may vary according to the particular type local of interpolation chosen—thus appear to be naturally better fitted for the domain truncation approach. Regarding that point, let us mention that Houde (2001) has undertaken a more systematic validation and parametric study of some 2-D polar and axisymmetric versions of the code BOUNCYL. Many of the reference flows he successfully compared with were in fact unbounded flows. In this context, if unbounded problems can then seem to be efficiently approximated by a local interpolation bounded formulation, the question is then: how well does the mapped B-spline formulation of the code UNCYL compares to the standard B-spline one of the code BOUNCYL?

[5] As also mentioned in Sec. 2.3.2, the approximation can even be improved by considering other types of boundary conditions than the no-slip one, e.g., shear free, etc. By extension, mappings could

TABLE 4.9. Relative error for the most unstable eigenvalue λ_1 of $k_\theta = 1$, $k_z = 0.05$, for $q = 0.5$ ($h = \beta = 1$) at $Re = 25$ (see also TABLE 4.3 and text). In all cases, quartic ($k = 5$) B-splines are used.

Unbounded	N_r^*	L	$\lvert\lambda_1^h - \lambda_1\rvert/\lvert\lambda_1\rvert$
MM†	20	6	4.56×10^{-5}
UNCYL-LS	20	6	2.51×10^{-6}

Bounded	N_r^*	R_o	$\lvert\lambda_1^h - \lambda_1\rvert/\lvert\lambda_1\rvert$
MP‡	50	100	1.32×10^{0}
BOUNCYL-LS (I)	20	100	1.85×10^{-3}
BOUNCYL-LS (II)	20	100	8.42×10^{-6}

† Matsushima & Marcus (1997)
‡ Mayer & Powell (1992)

Note that because the new question only involves the radial discretization, it can as well be considered in terms of the eigenvalue solvers. Furthermore, since both general Navier-Stokes solvers share the same time marching procedure (including the computation of the nonlinear term), the linear stability comparison results are expected to carry over without restriction. Parts of these considerations are also included in Dufresne & Dumas (2000). Let us now revisit the benchmark case of TABLE 4.3 which will again serve as a reference. The procedure used here is similar to the one used for determining the convergence rates of FIG. 4.13.

In TABLE 4.9, we first compare the results obtained with UNCYL-LS, with those of Matsushima & Marcus for $N_r^* = 20$. Also shown in the table are the results of Mayer & Powell against those obtained with the code BOUNCYL-LS (both with a no-slip condition at $R_o = 100$). For that comparison, case-I corresponds to a simple but reasonable node distribution (4 regions of different but uniform node density) while case-II intends to mimic the (algebraically mapped) node distribution used for the unbounded calculation, with the mapping parameter set to $L = 12.5$. All B-splines results are obtained with $k = 5$. Looking at the error of the bounded cases, one can

even be seen as a different form of such "modified" boundary conditions.

easily see the advantages of local approximations. Indeed, for the large value of R_o used here, the imprecision of the Mayer & Powell and, to a lesser degree, of the case-I solutions can be attributed to a lack of resolution. As for the unbounded solutions, we see that the mapped B-spline method compares advantageously well with the method of Matsushima & Marcus, as it was already noted earlier in the section.

The main point of interest though, remains how the two B-spline codes compare between themselves. In order to assess that issue, a point of comparison needs to be established. The best comparison would obviously be at the lowest possible error for each method. Due to the inherent difficulties that are associated with the determination of such optimal results, we opted for a more accessible comparison point. Trying to approximately mimic the lowest error result on a comparable discretization, we used a similar but slightly different domain partitioning for each code. The breakpoints of the bounded code were uniformly distributed in a pseudo-mapped truncated domain $\eta \in [0, \eta_o]$ (with $\eta_o = R_o/(R_o + L)$ and consequently $\eta_o < 1$). These nodes were then projected back into the radial domain, and used as breakpoints. This is the case-II method used in TABLE 4.9. The unbounded solution was determined using a standard uniform distribution in the mapped η-domain. The mapping parameter L was chosen, in each case, to minimize the error. This choice was privileged over, say, an exact radial (minus the last point) domain partitioning because such breakpoints distribution do not lead to a minimum error simultaneously for both methods (recall that the effective radial interpolation functions are not the same).

Following this procedure, many comparison tests were done. The results of one such typical test are illustrated in FIG. 4.21, and are well representative of the whole series. Both eigenvalue and eigenmode (the scalar spline functions $g^{\pm}_{mn}$, instead of the the velocity $\widehat{\mathbf{u}}$, are used here) relative errors are shown as a function of the number of free B-splines N^*_r. Also for comparison purposes, the radial L^2-norm was evaluated over a finite radius ($r \leq 50$). The number of B-splines was limited to 20, to keep the relative error at a meaningful level; the reference data being the $N^*_r = 70$ solution of TABLE 4.3. Note that the leveling of the eigenvalue error, for the unbounded solution, is only associated with the fact that only a small number of B-splines were used, and that the discretization parameters are not identical for each point. At constant discretization parameters, the error value is not as small but does not level off. The proper behavior of the solution is nevertheless confirmed, even at varying discretization parameters, by the decay of the corresponding eigenmode error.

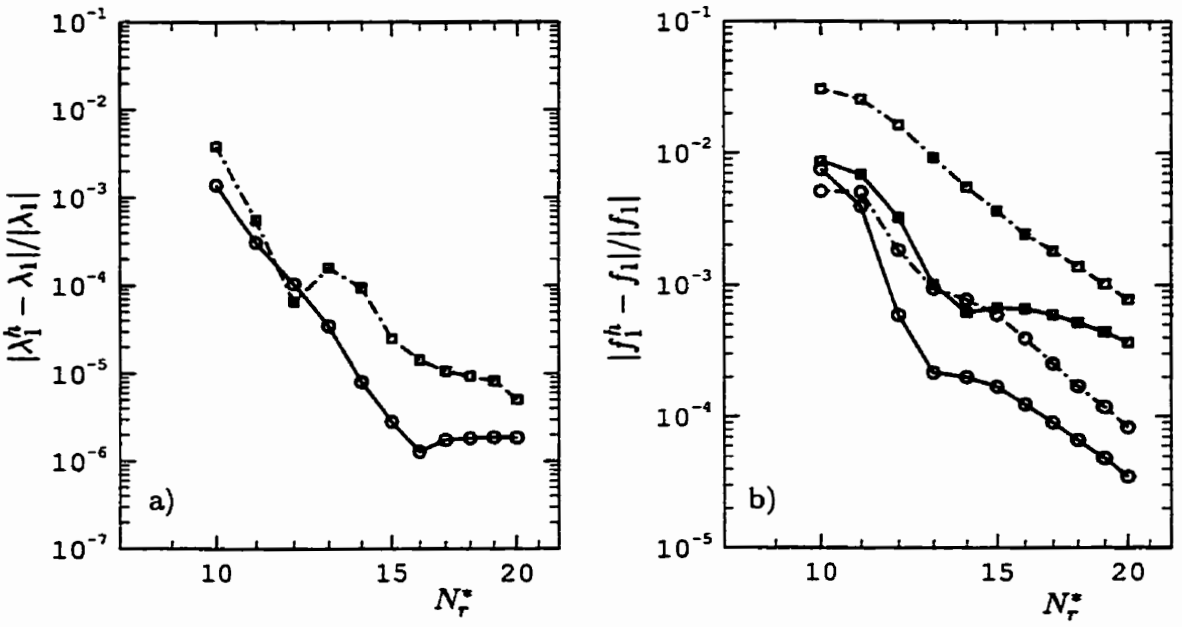

FIGURE 4.21. a) Relative eigenvalue error and b) scalar spline function eigenmode error, both as a function of N_r^*. The "□" symbols are for BOUNCYL-LS solutions while the "○" are for the UNCYL-LS ones. In b), the solid lines refer to the "+" class and the broken ("dash-dot") lines refer to the "−" class solutions error.

Globally, the unbounded solutions prove more precise for the tested cases, but this observation calls for additional comments. The tests were all with the slowest decaying base flow field ($U_\theta \propto r^{-1}$), which requires some resolution in the far field. For faster decaying fields the difference between the two solutions would probably not be so apparent. The bounded solution was also obtained with a no-slip condition at the outer radius. This is not the only possible choice, as we already mentioned, and other types of less stringent boundary condition approximations could have been used. These lasts points are certainly quite familiar to numericist who already very successfully used local interpolations on bounded domains approximating the infinity. It is nevertheless believed that—because of its built-in decaying behavior, and because whatever the distribution of standard B-spline breakpoints used, a similar distribution can always be obtained for the mapped B-splines—the present mapped B-spline formulation should always maintain itself a step ahead of the standard B-spline one. This difference may become marginal though, depending on the type of problems considered.

4.3 Triangular vortex

In this section, we now undertake the validation of the 2-D polar ($k_z = 0$) families of vector expansions of TABLE 2.1. To do so, we follow the same validation strategy used precedently an apply it to the stability and nonlinear dynamics of a circular vortex patch whose vorticity profile was given and studied by Kloosterziel & Carnavale (1999) and Carnavale & Kloosterziel (1994). In addition to the quantitative comparisons made with the linear stability results, the present validation tests also include qualitative comparisons with the nonlinear evolution of the flow structures. In view of our present verification objectives, this combination of quantitative and qualitative type of comparisons will prove sufficient.

Let us begin by a brief description of the problem. From the cited references, the non-dimensional vorticity and corresponding velocity profiles are respectively given by

$$\omega_z = \left(\frac{1}{2}\alpha r^\alpha - 1\right) e^{-r^\alpha} , \tag{4.16}$$

and

$$u_\theta = -\frac{1}{2} r\, e^{-r^\alpha} , \tag{4.17}$$

with $\alpha > 0$. These profiles define a basic axisymmetric flow which can be described as a negative vorticity core inscribed in a positive vorticity annulus of equal but opposite sign circulation; the resulting vortex patch having a zero net circulation. These profiles are shown in FIG. 4.22, for different values of the parameter α. The reference time and length scales used for normalization are defined by the inverse of the core center vorticity $\bar{\Omega}_0^{-1}$ (with $\bar{\Omega}_0 \equiv \bar{\omega}_z(\bar{r} = 0)$) and the velocity profiles "crossing point" $\bar{R}_c$. The velocity scale directly follows as $\bar{\Omega}_0 \bar{R}_c$ which in turn gives the Reynolds number

$$Re \equiv \frac{\bar{\Omega}_0 \bar{R}_c^2}{\bar{\nu}} .$$

It is worth noting that these "theoretical" profiles have an experimental counterpart (close to the $\alpha = 2$ profile) as mentioned by Kloosterziel & van Heijst (1991); they also are part of a group of model problems of interest in geophysical flows, and possibly in coherent structure dynamics of 2-D turbulence.

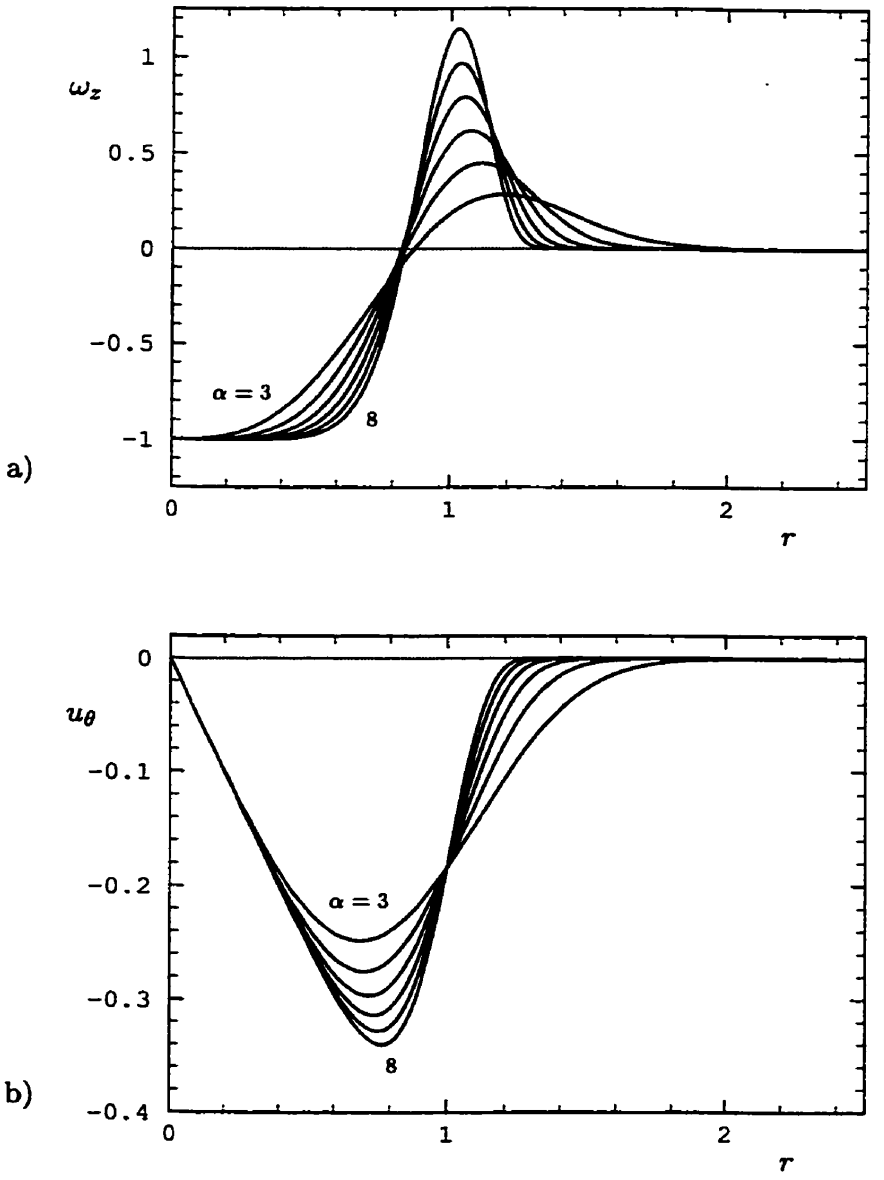

FIGURE 4.22. a) Vorticity and b) velocity profiles corresponding to (4.16) and (4.17) respectively. The curves are plotted for every unitary value of α between 3 (the smoothest) and 8 (the steepest).

For our validation purposes, we will limit ourselves to the study of the $\alpha = 7$ profile. At this parameter value, Carnavale & Kloosterziel have shown that the vortex is unstable to 2-D perturbations with azimuthal wavenumbers of $k_\theta = 2$, 3 and 4; the maximum growth rate being for $k_\theta = 3$. The velocity profile does indeed satisfy Rayleigh's inflexion point theorem that establishes the necessity of an inflexion point in the velocity profile for the existence of instabilities (Drazin & Reid, 1981). Note that the vortex may also be centrifugally unstable. Indeed, since the net circulation is zero, there must be a region in which the circulation (absolute value) decreases, violating thus Rayleigh's circulation criterion (Drazin & Reid, 1981). This second type of instability will however not be considered here since, as we already mentioned, we limit ourselves to perturbations with $k_z = 0$. We refer the reader directly to Kloosterziel & van Heijst (1991) for additional comments on these specific stability issues.

4.3.1 Linear stability

As a first test, we compare, in TABLE 4.10, the growth rate results given in Carnavale & Kloosterziel (1994) with the ones predicted by both our eigenvalue and Navier-Stokes solvers. Eigenvalue solutions were obtained with about 100 B-splines, uniformly distributed in the η-domain. The number of significant digits of the solution was determined by comparing the results obtained with $k = 5$ and 6, at different values of L ranging from 1 to 5 according to the specific case. The UNCYL results were obtained with the same radial discretization as the one used to obtain the UNCYL-LS results. Note that our "inviscid" values ($Re \to \infty$) were in fact computed with $Re = 10^8$ for both the eigenvalue and the Navier-Stokes solvers. For the eigenvalue solver, the choice of a finite value for Re instead of directly using the inviscid limit (setting the matrix $\widetilde{\mathsf{B}}$ to zero in (3.29)) was made because of some difficulties associated with the structure of the matrices in relation with the QZ algorithm. Small but non-zero values for the viscous term were necessary for the convergence of the solution. At any rate, this does not affect the ensuing results as can be seen by the good agreement between the different sets of values shown in TABLE 4.10. Let us additionally note that the results of Carnavale & Kloosterziel were obtained by numerical simulations, using a Cartesian Fourier spectral code (with a periodic array of

TABLE 4.10. Most unstable inviscid perturbation growth rate values for $k_\theta = 2$, 3, and 4, with $\alpha = 7$. The $Re = 10^4$ values are included for comparison.

	$Re \to \infty$			$Re = 10^4$	
	CK†	UNCYL-LS	UNCYL	UNCYL-LS	UNCYL
$k_\theta = 2$	0.220	0.220	0.21	0.21605	0.22
3	0.242	0.240	0.24	0.23461	0.234
4	0.197	0.194	0.19	0.18724	0.187

† Carnavale & Kloosterziel (1994): Data graphically interpolated

vortices), of the inviscid, linearized vorticity equation. These reference values were in turn found to be in agreement with those of Carton & McWilliams (1989, cited from Carnavale & Kloosterziel) who also worked on this problem.

Also included in TABLE 4.10 are the results for $Re = 10^4$, from both the eigenvalue and the Navier-Stokes solvers. These last two sets of values are found to be in good agreement between themselves and also with the inviscid results. This observation will allow us to use with confidence our $Re = 10^4$ flow fields to compare with the "inviscid" simulations of Kloosterziel & Carnavale (1999) in the following part (nonlinear dynamics) of the validation process. It is worth noting that in this latter work of Kloosterziel & Carnavale, a hyperviscosity dissipation term was used to prevent the built-up of small scale structures at high wavenumbers while in our case, we solely relied on standard physical dissipation (the Laplacian viscous term) to carry the same task. This is why we had to limit ourselves to only moderately high Reynolds numbers.

4.3.2 Nonlinear dynamics

The next validation test thus consists in comparing the ensuing nonlinear evolution of the specific perturbation mode $k_\theta = 3$ with the simulations of Kloosterziel & Carnavale. Their results show that the perturbation will maintain its linear growth regime for a certain time, but nonlinear interactions will eventually lead to a saturation of

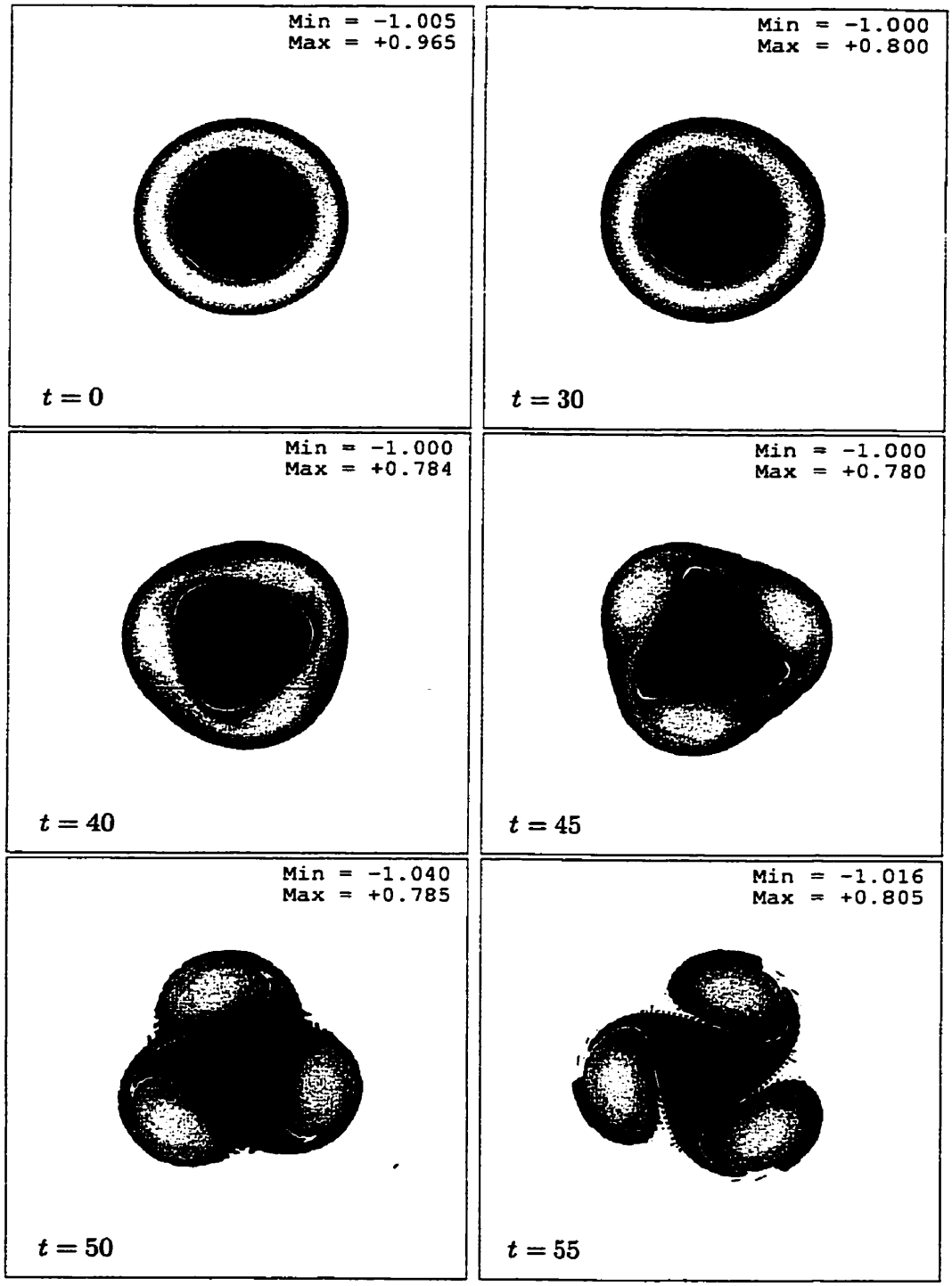

FIGURE 4.23. Formation of a triangular vortex with $\alpha = 7$ at $Re = 10^4$. Dark grey represents negative vorticity while light grey stands for positive values. The white region encompasses the near zero vorticity $-0.05 < \omega_z < 0.05$. See next page for continuation.

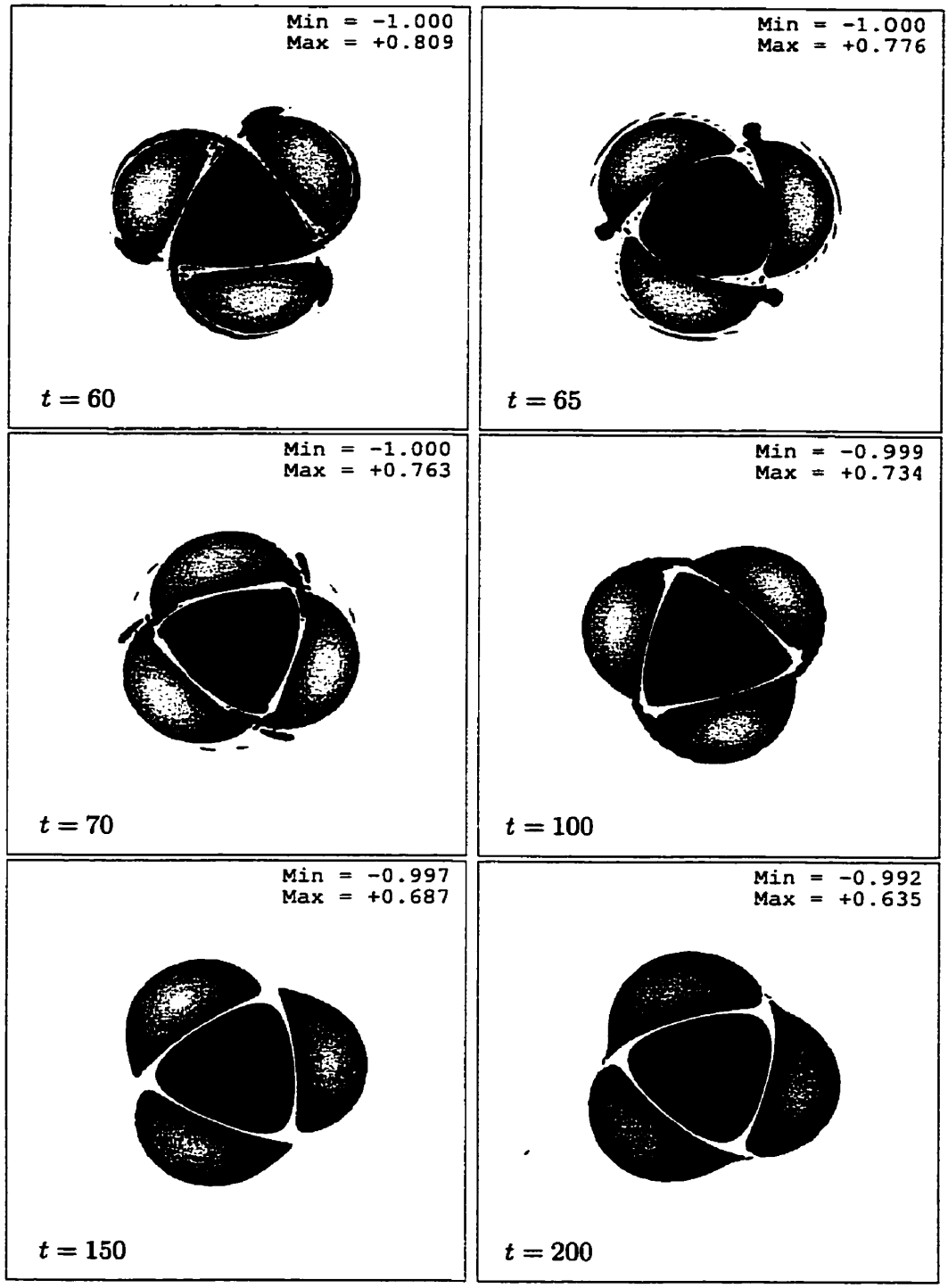

FIGURE 4.23. [Continued.] Minimum and maximum values of ω_z are shown on each frame, as well as the solution time t. The discretization parameters and the initial condition are described in the text.

this instability. A new state of time periodic equilibrium (for the Euler equations) is then reached in the form of a triangular vortex rotating as a whole about its central core. More specifically, the new vortex is constituted of a triangular central core of negative vorticity surrounded by three peripheral positive valued vortices[6]. This new system may in turn be subject to other types of instability (Kloosterziel & Carnavale, 1999) that are not considered here.

This dynamical behavior was well captured by our simulations, from which we show some general evolution illustrations in FIG. 4.23. Note that to save on computational time, these simulations were obtained with a specialized 2-D polar version of the code. Also, taking advantage of the natural periodic symmetry of the problem, we set $L_\theta = 2\pi/3$ so that in this case $k_\theta = 3m$ (with $m = 0, 1, \ldots, N_\theta$). The complete vorticity fields of FIG. 4.23 are thus simply produced by periodic extension of the basic "piece of pie" domain solution (see FIG. 4.24). As for the initial condition, we used a single mode $k_\theta = 3$ perturbation with a random radial structure (see FIG. 4.26). The discretization parameters are summarized in what follows:

- $N_r = 74$, $k = 5$, partially uniform distribution of breakpoints in η (45 points for $0 \leq \eta < 0.5$ and 25 points for $0.5 \leq \eta < 1$) with $L = 2$;
- 6 modal zones ($L_\theta = 2\pi/3$) with
  $N_\theta = 6$ $(0 \leq \eta < 0.1\ )$, $N_\theta = 12$ $(0.1 \leq \eta < 0.2\ )$,
  $N_\theta = 24$ $(0.2 \leq \eta < 0.25)$, $N_\theta = 32$ $(0.25 \leq \eta < 0.55)$,
  $N_\theta = 24$ $(0.55 \leq \eta < 0.75)$, $N_\theta = 12$ $(0.75 \leq \eta < 1.0\ )$;
- CFL $= 1.7$ for which $\Delta t \approx 3.5 \times 10^{-2}$.

An illustration of the pseudo-computational grid is shown in FIG. 4.24.

Note that the modal reduction used here mainly allows for an economy on the number of degrees of freedom (about 40% less for the present choice). The maximum CFL number that determines the critical time step only changes position—$r_{\text{CFL max}} \approx 0.5$ for the present multi-zone while $r_{\text{CFL max}} \approx 0.01$ in the single zone case—without

[6]It is interesting to note that this triangular and other multipolar vortices can be linked to some exact solutions of the Euler equations; see Crowdy (1999) for more details on such multipolar analytical solutions.

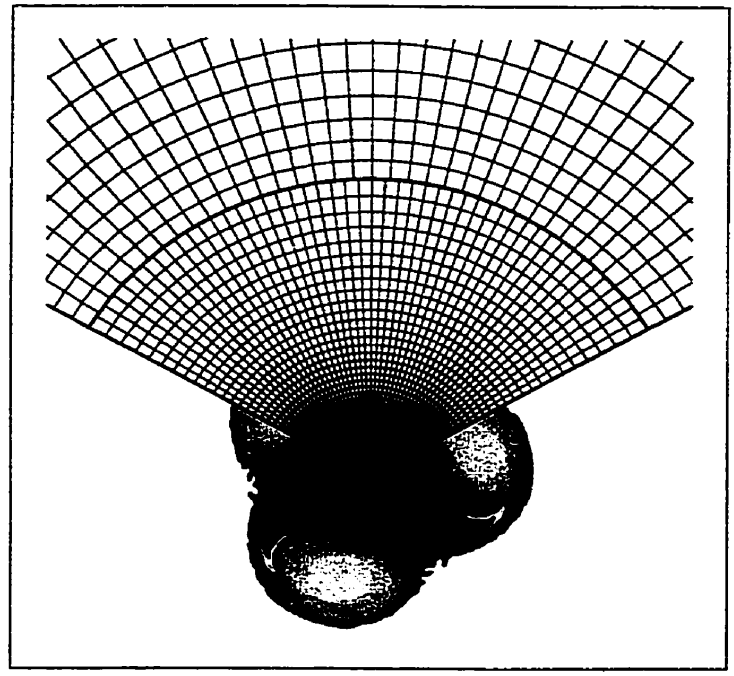

FIGURE 4.24. The pseudo-computational grid used to obtain the results shown in FIG. 4.23. For the radial discretization, we show the breakpoints (in r); for the azimuthal discretization, we use twice the number of computational modes to represent the pseudo-grid. Bold lines are used to show the frontiers of the modal zones (the fifth zone appears only partially and the sixth zone is not seen at all) and also of the periodic $(2\pi/3)$ domain. The discretization parameters are detailed in the text. The $t = 50$ solution of FIG. 4.23 is added for a scaling comparison.

practically changing the value of Δt. For a uniform azimuthal resolution in this type of problem (purely axisymmetric base flow field) we would expect the critical time step to be located at the point of maximum azimuthal velocity, which is indeed almost the case since for $\alpha = 7$, $u_{\theta\,\max}$ is located at $r = 0.757$. The agreement between the single (not shown here) and the multi-zone computations is better than five digits accuracy on the total energy, and no visual differences can be detected between the two flow fields.

4.3.3 Other results

Besides the global macroscopic agreement with the reference solution, other more specific verifications with the reference results of Kloosterziel & Carnavale were also undertaken. In FIG. 4.25, we show the time evolution of the modal components of kinetic energy E_{k_θ} and enstrophy $\mathcal{E}_{k_\theta}$. Following the definition of the modal kinetic energy in (4.13), we write for the modal enstrophy

$$\mathcal{E}_{k_\theta} = \frac{1}{2}\int_0^\infty \widehat{\omega}^*(r;\ k_\theta)\cdot\widehat{\omega}(r;\ k_\theta)\, r\, dr\ . \tag{4.18}$$

Since the velocity field is entirely rotational (no potential flow region) both E_{k_θ} and $\mathcal{E}_{k_\theta}$ behave similarly, and so observations from either one of two the quantities are almost directly transposable to the other. Because of the natural formulation of the problem in terms of vorticity, let us consider the modal enstrophy evolution.

From the initial condition to about $t = 5$, the mode-3 random perturbation—since we only speak of azimuthal modes here, let us use the simplified "mode-3" notation to designate the azimuthal wavenumber $k_\theta = 3$—is restructuring itself giving rise to the most unstable eigenmode. In FIG. 4.26, we show the ω_z contours of the initial perturbation, i.e., the total vorticity field minus the axisymmetric component $\widehat{\omega}_z^{(0)}$. Here, we use the notation $\widehat{\omega}_z^{(k_\theta)}$ to designate the specific modal component of the Fourier-transformed vorticity $\widehat{\omega}_z$. The radially unstructured character of the perturbation is still visible at $t = 5$ (just before the start of linear growth) as can be seen from the $\widehat{\omega}_z^{(3)}$ profile shown in FIG. 4.28.a. In FIG. 4.27.a, we show the vorticity contours at $t = 20$; the corresponding $\widehat{\omega}_z^{(3)}$ profile is shown in FIG. 4.28.b. Note that from FIG. 4.25, we see that the perturbation field is entirely dominated by mode-3 at that time. The contours of the corresponding eigenmode determined by Kloosterziel & Carnavale are shown in FIG. 4.27.b, for comparison purposes. Going back to FIG. 4.25.b, we observe that the linear growth regime extends to about $t = 40$, the time at which nonlinear interactions are seen to come into play by a rapid modification of the growth rates of the initially perturbed mode and its harmonics. At $t \approx 50$, a complete saturation of the instability is reached. After that, follows a readjustment of the modal vorticity components leading to the new (quasi-) equilibrium state.

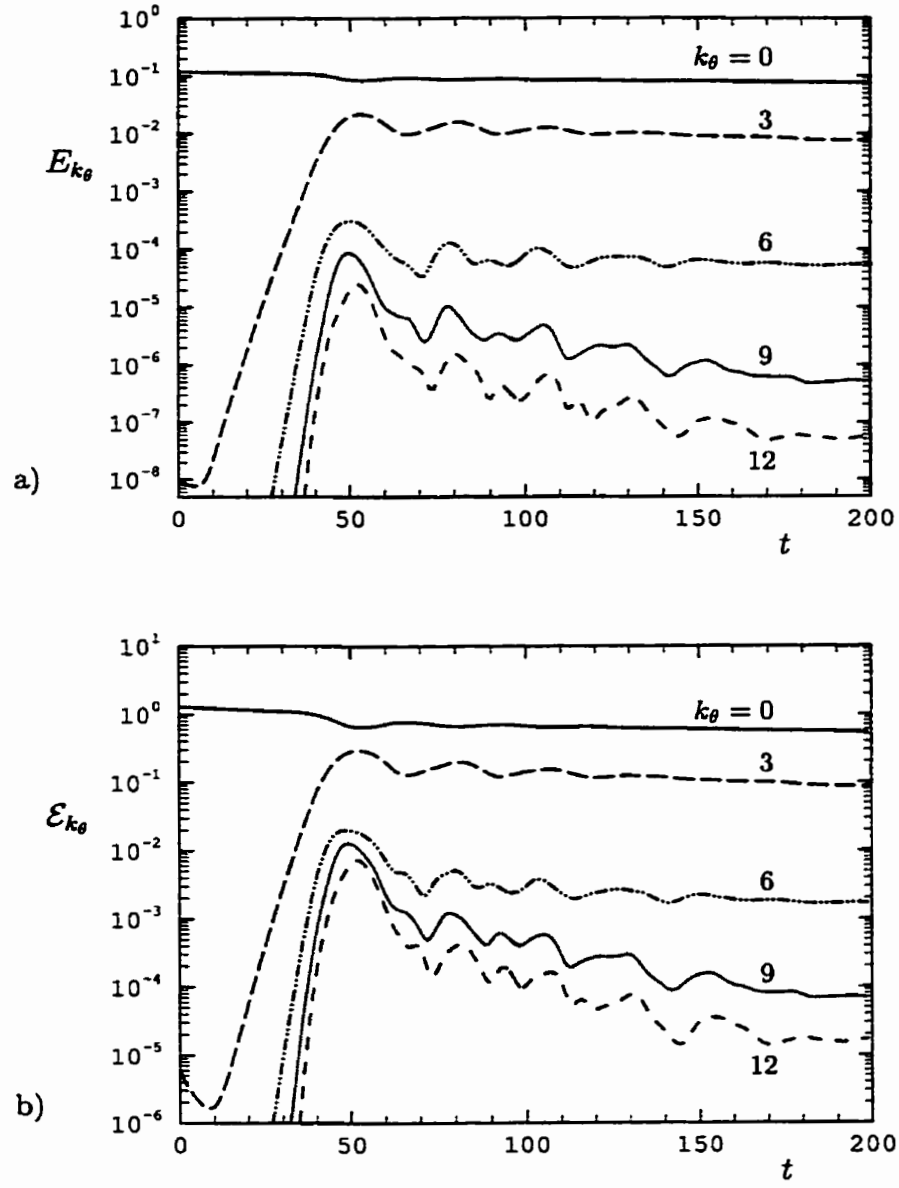

FIGURE 4.25. Time evolution of a) the modal kinetic energy E_{k_θ} and b) the enstrophy $\mathcal{E}_{k_\theta}$ corresponding to the vorticity fields shown in FIG. 4.23. Note that since L_θ was set to $2\pi/3$ for the simulations, the modal values of k_θ shown here correspond in fact to numerical indices $m = 0$, 1, 2, 3 and 4, i.e., the base flow field, the initially perturbed mode and its first three harmonics.

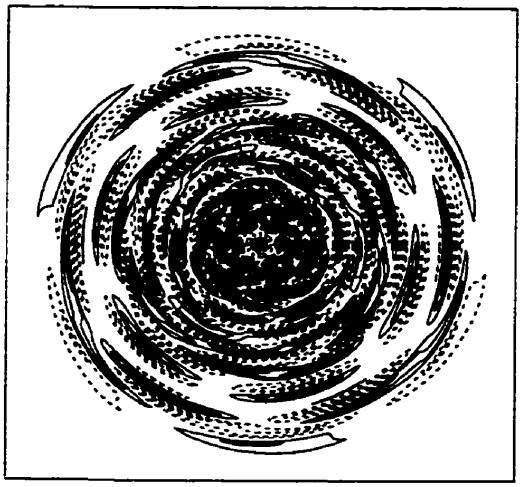

FIGURE 4.26. Initial mode-3 perturbation vorticity iso-contours with a random radial structure. The contours are given as follows: $\omega_{z\,\min} = -5 \times 10^{-3}$, $\omega_{z\,\max} = +5 \times 10^{-3}$ with increments of 5×10^{-4}. Solid lines are for positive values, dashed lines negative values. Note that for visibility reasons, the box dimensions are smaller than those of FIG. 4.23.

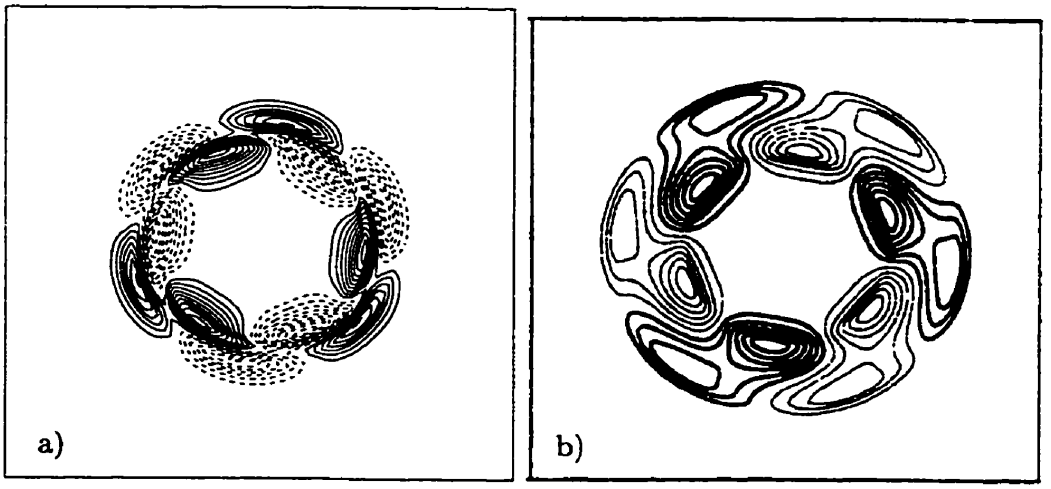

FIGURE 4.27. a) Computed perturbation vorticity field at $t = 20$. The contours are defined as follows: $\omega_{z\,\min} = -1.3 \times 10^{-2}$, $\omega_{z\,\max} = +1.3 \times 10^{-2}$, with increments of 1.3×10^{-3}. See also FIG. 4.26 for definitions, and FIG. 4.28.b for the corresponding $\widehat{\omega}_z^{(3)}$ profile. b) The eigenmode obtained by Kloosterziel & Carnavale (FIGURE 6.b in the reference paper), shown for comparison. In this case negative values are identified with thin lines while thick lines are for positive values. Not in scale with a).

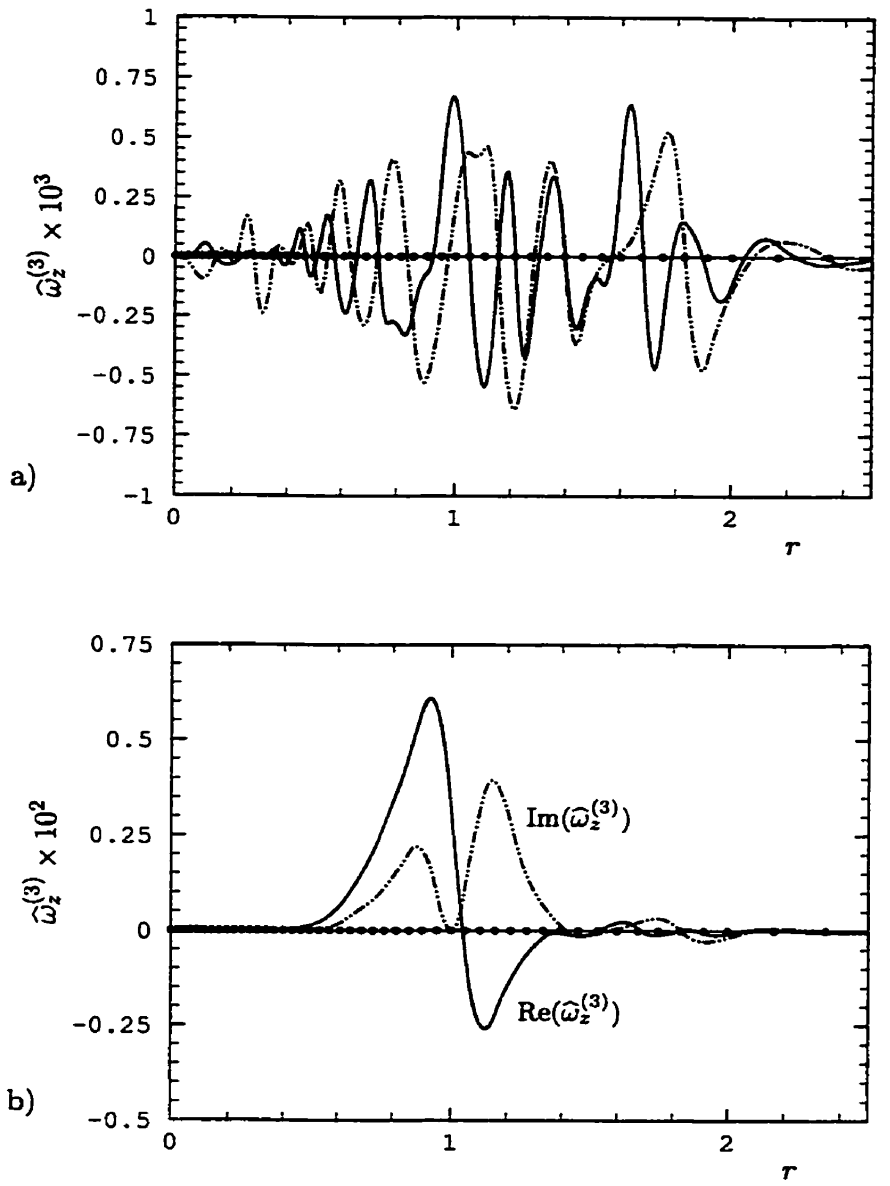

FIGURE 4.28. Radial profiles of the modal vorticity $\widehat{\omega}_z^{(3)}$. a) Computed solution at $t = 5$; the values are amplified by a factor of 10^3. Note that the initially random perturbation still retains a rather unorganized character. b) Computed solution at $t = 20$; the amplitude is now about 10 times that of a). The most unstable eigenmode has clearly emerged from the initially random perturbation. See also FIG. 4.27.a for corresponding ω_z contours. Finally, the "•" symbols identify the B-spline breakpoints used to compute the results shown.

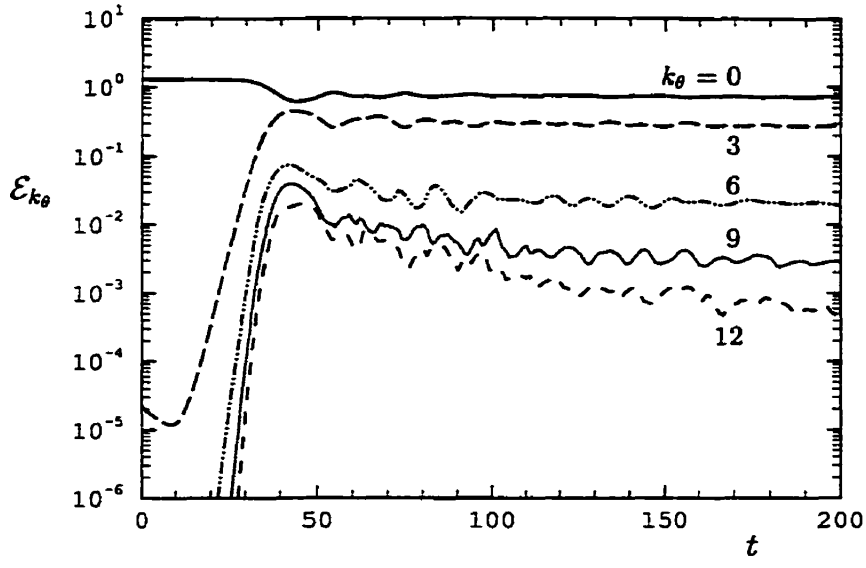

FIGURE 4.29. Time evolution of the modal enstrophy $\mathcal{E}_{k_\theta}$ at $Re = 10^5$. Even if the general behavior is quite similar to what was obtained for $Re = 10^4$ (see FIG. 4.25.b), the levels and ratios of modal enstrophy, e.g., $\mathcal{E}_0/\mathcal{E}_3$, have significantly changed.

Additional observations and comparisons with the results of Kloosterziel & Carnavale are worth mentioning. Indeed, if the good agreement observed so far between our results and those of the reference—quantitative for the linear and qualitative for the nonlinear dynamics—allows for a good level of confidence in the validity of the code UNCYL, the difference of equilibrium ratio values $\mathcal{E}_0/\mathcal{E}_3$ raised an interrogation. Kloosterziel & Carnavale obtained a value of $\mathcal{E}_0/\mathcal{E}_3 \approx 1.2$ while in our case this value is $\mathcal{E}_0/\mathcal{E}_3 \approx 6$! Without engaging in a thorough investigation of finite Reynolds number effects on such specific quantities, we nevertheless wanted to confirm that the modal enstrophy ratio was indeed "Reynolds dependent". We therefore ran other simulations, but this time at $Re = 10^5$, on a higher resolution "grid", from which we obtained $\mathcal{E}_0/\mathcal{E}_3 \approx 2.6$. The time evolution of the modal enstrophy for this case is shown in FIG. 4.29. Besides the $\mathcal{E}_0/\mathcal{E}_3$ ratio, the overall agreement with the equivalent reference results is better in this case than it was for $Re = 10^4$.

This last observation, combined with similar observations made by Kloosterziel & Carnavale for the inviscid vs the viscous vortex tripole (mode-2 instability) tends to confirm the dependence of some such specific quantities on the Reynolds number. If the global dynamics can be considered as inviscid, i.e., the convective time scales remain much smaller than all the relevant diffusive ones, the particular equilibrium

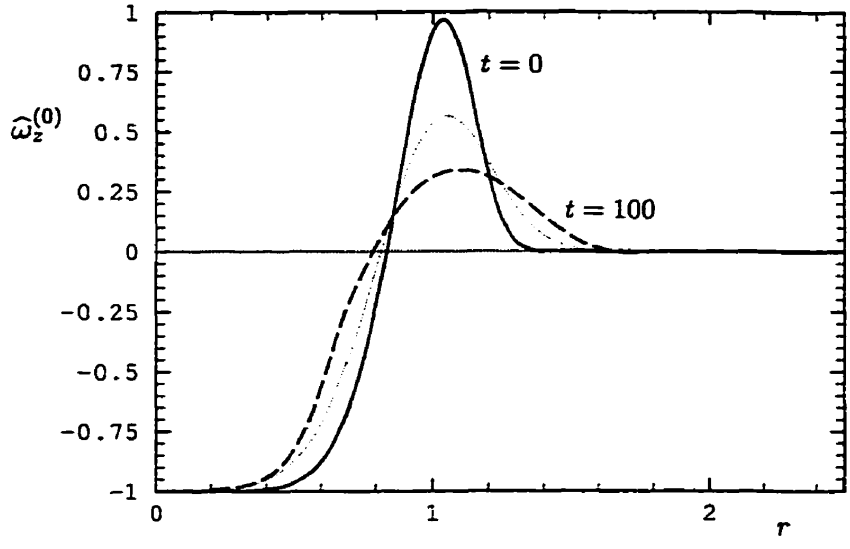

FIGURE 4.30. Radial profiles of $\widehat{\omega}_z^{(0)}$ corresponding to the results of FIG. 4.23. The full line represents the initial profile ($t = 0$); the dashed line, the solution at $t = 100$; the dotted line represents the profile for the case of pure diffusion, also at $t = 100$. Nonlinear interactions are seen to play a significant role in the modification of the base flow profile.

state that will be reached, on the other hand, depends on the complex interactions that occur during the saturation process which will in turn depend at some level on the viscous scales. Although this is a very interesting subject, which is also the object of the reference paper of Kloosterziel & Carnavale, we must put it aside for now since it brings us beyond the scope of our present objectives.

Let us continue with the comparison of our $Re = 10^4$ results with those of the reference. In FIG. 4.30, we show the axisymmetric base flow profile $\widehat{\omega}_z^{(0)}$ of FIG. 4.23 at $t = 0$ and 100. The profile that would have resulted if only diffusion would have come to play is also shown for comparison. From this, we see that nonlinear interactions have a noticeable effect in the modification of the base flow profile. This is again in agreement with the results of Kloosterziel & Carnavale. As a final verification step, we compare our $t = 200$ (equilibrium) results of FIG. 4.23 with the reference equilibrium solution. In FIG. 4.31, both global vorticity contours are shown, and in FIG. 4.32, we shown the mode-3 contours. The particular modal vorticity profiles corresponding to the mode-0 and the mode-3 components of our $t = 200$ solution are given in FIG. 4.33.

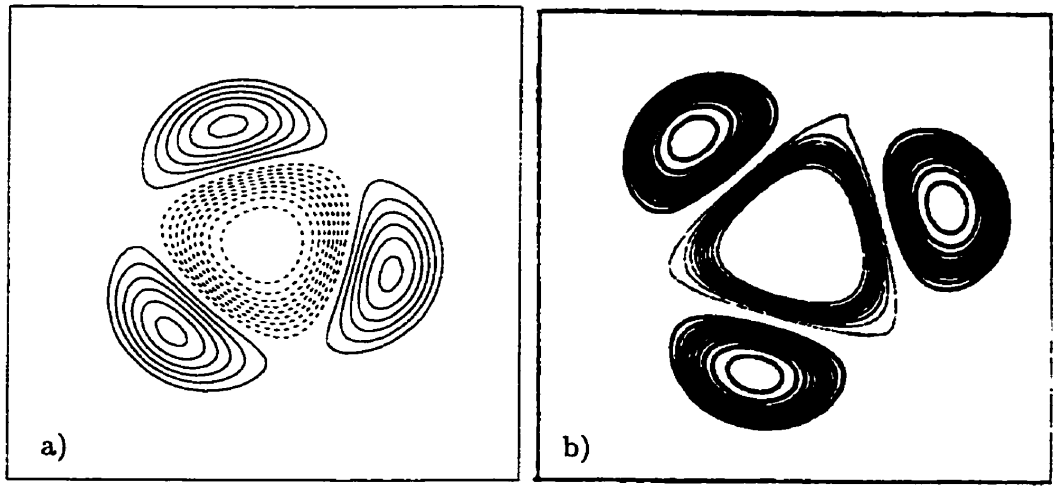

FIGURE 4.31. a) Global vorticity contours of the $t = 200$ solution of FIG. 4.23; the contours are shown for $\omega_{z\,\min} = -1$, $\omega_{z\,\max} = +0.3$, with increments of 0.05. b) The equivalent vorticity contours of the inviscid equilibrium solution of Kloosterziel & Carnavale (FIGURE 7.b of the reference paper), shown for comparison; the contours have an increment of $\Delta\omega_z = |\omega_z|_{\max}/10$. Again not in scale with a); the other usual definitions also apply.

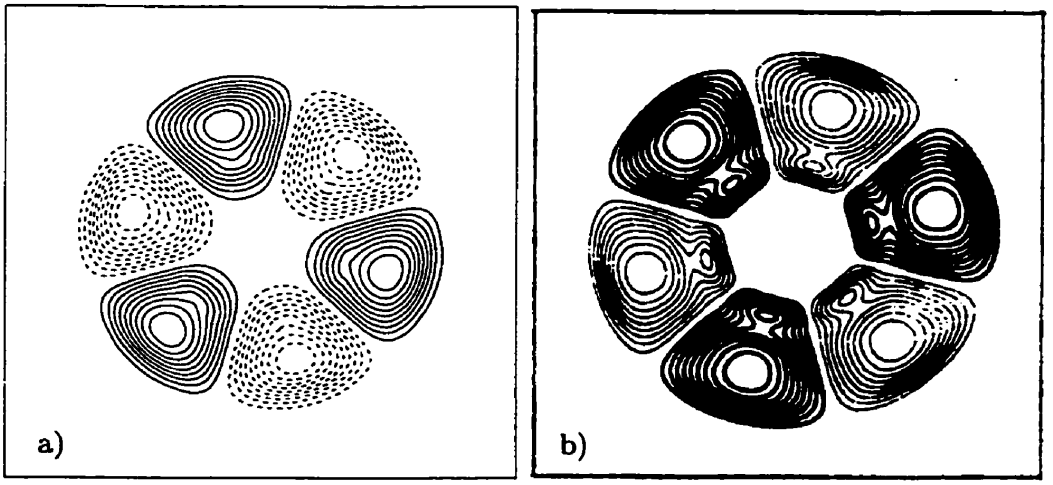

FIGURE 4.32. a) Mode-3 vorticity contours of the $t = 200$ solution of FIG. 4.23; the contours are shown for $\omega_{z\,\min} = -0.3$, $\omega_{z\,\max} = +0.3$, with increments of 0.03. b) The equivalent mode-3 vorticity contours of the inviscid equilibrium solution of Kloosterziel & Carnavale (FIGURE 7.e of the reference paper), shown for comparison; the contours have an increment of $\Delta\omega_z = |\omega_z|_{\max}/10$. Again not in scale with a); the other usual definitions also apply.

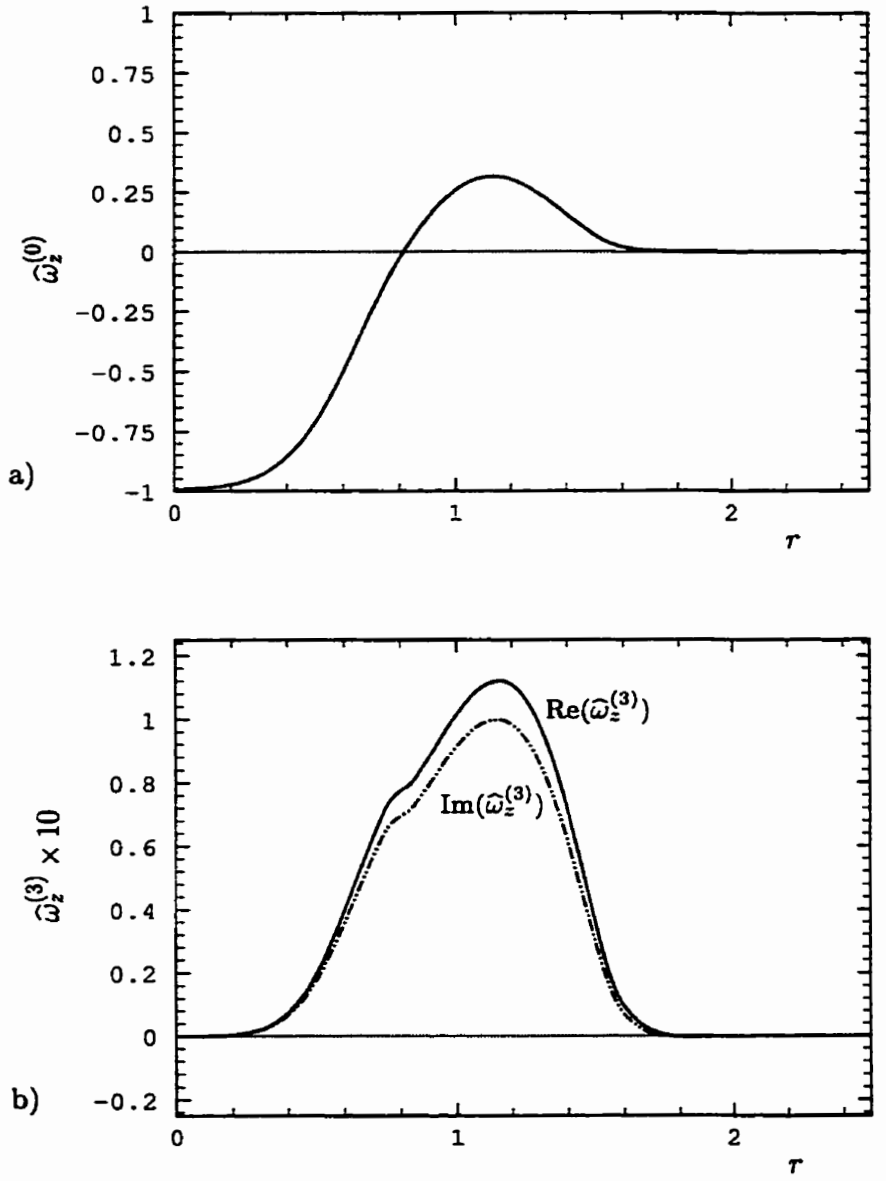

FIGURE 4.33. Radial profiles of the modal vorticity components $\widehat{\omega}_z^{(k_\theta)}$ at $t = 200$; in a) mode-0, and in b) mode-3. Note that the mode-3 values are amplified by a factor 10 in comparison with the mode-0 component. The usual definitions apply.

4.3.4 Complementary tests

In addition to the comparisons made with the reference results of Kloosterziel & Carnavale, we present here supplementary results that confirm the overall good behavior of the numerical method. More specifically, these extra verifications involve symmetry and symmetry brake off in the nonlinear evolution of the vortex problem discussed in Sec. 4.3.2. Since the points to be made here are very specific, we choose to use for this part a more direct "item by item" presentation.

In a first step, we verify how well the mode-3 "physical" symmetry is preserved when not explicitly imposed. Recall that the results presented in FIG. 4.23 were obtained on a computational domain where $L_\theta = 2\pi/3$, i.e., with a mode-3 forced periodicity. We show in FIG. 4.34 three different computations for the same physical problem: $\alpha = 7$, $Re = 10^4$, with a mode-3 initial perturbation. The following points provide a general description of the figure content:

- On the left, we show iso-contours of vorticity from $\omega_z = -1$ to $+1$, with steps of 0.1 (the zero contour is not shown); the solid lines refer to positive values while the broken ("dash") lines are for negative values.
- On the right, the corresponding modal entrophy spectrum is provided.
- The different solutions are given at comparable, though not identical, times that correspond approximately to the saturation of the instability, i.e., at about $t = 50$ in FIG. 4.25. This is the most demanding phase of the computation in terms of spatial resolution requirements due to the important "filamentation" of the three arms of negative vorticity.

The particular context of each simulation case is described below:

Case a) Solution obtained with the imposed symmetry $L_\theta = 2\pi/3$, as in FIG. 4.23. Thus, *all* the computational modes $m = 0, 1, 2, \ldots, N_\theta - 1$ (with $k_\theta = 3m$) are involved and "active" all along the simulation.

Case b) Solution obtained on a "full size" domain $L_\theta = 2\pi$, with the same initial perturbation in mode $k_\theta = 3$. In this case $k_\theta = m$, and only one third of the total

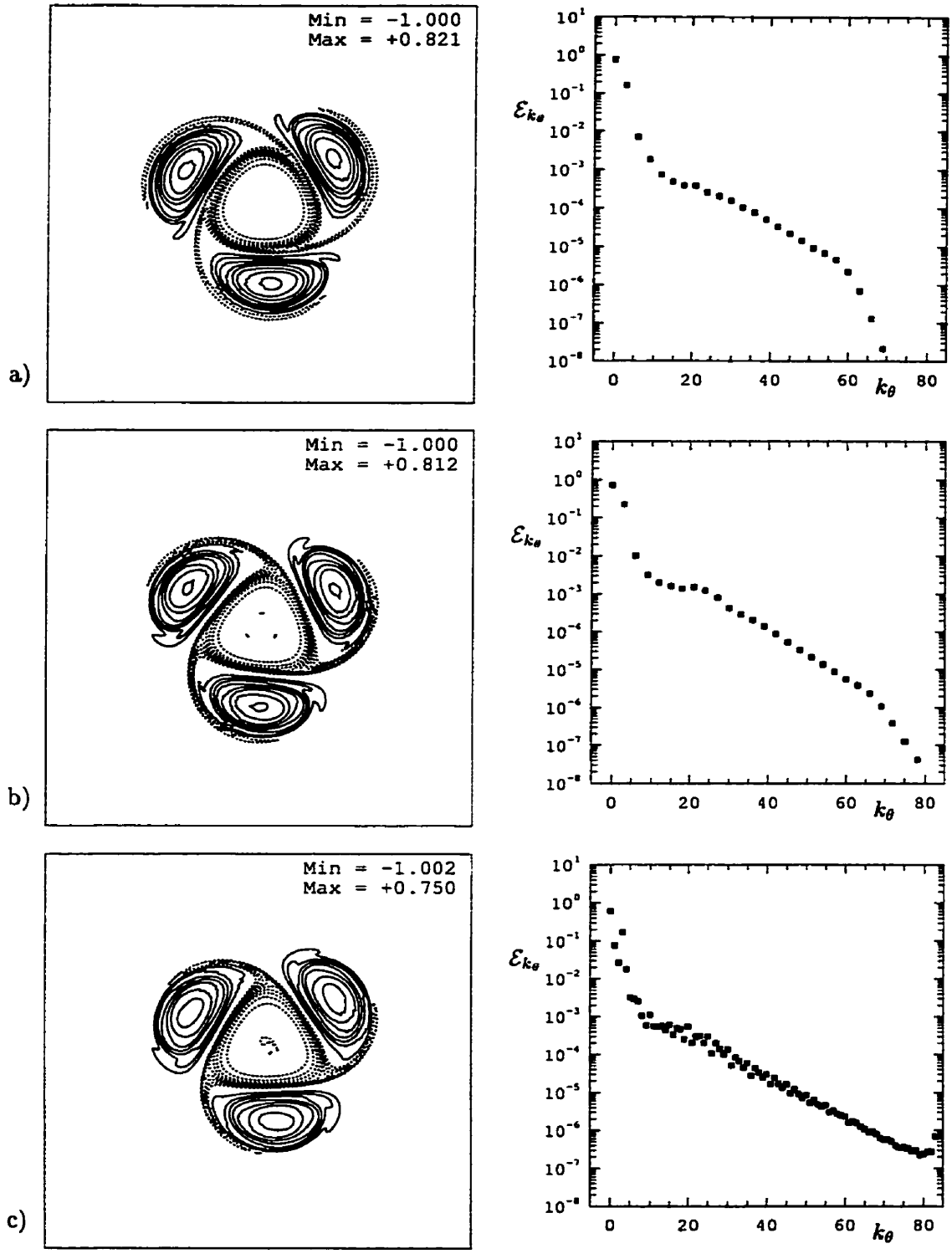

FIGURE 4.34. Comparison of different symmetry conditions for the triangular vortex ($\alpha = 7$) evolution at $Re = 10^4$. On the left, we show iso-contours of vorticity and on the right, the corresponding enstrophy spectrum. A more detailed description is provided directly in the text.

number of computational modes are effectively involved. Many more modes are therefore required to achieve the resolution of case a). Although present in the computation, the other "inactive" modes do not appear in the enstrophy spectrum because they remain at values of 10^{-28}, well below the limits of the figure.

Case c) Solution again obtained with $L_\theta = 2\pi$, but this time with the initial vortex having an offset of $\Delta x = \Delta y = 0.1$ relative to the center of the domain. The initial perturbation for this case is applied on the physical mode $k_\theta = 3$ based of the vortex center. Since there are no azimuthal symmetries left, the proper representation of the vorticity field requires all the computational modes.

All three solutions were obtained using the following radial discretization:

- $N_r = 99$, $k = 5$, partially uniform distribution of breakpoints in η (75 points for $0 \leq \eta < 0.5$ and 20 points for $0.5 \leq \eta < 1$) with $L = 2$;

while, according to the particular case, the following azimuthal truncations were used:

- Case a)
  6 modal zones ($L_\theta = 2\pi/3$) with
  $N_\theta = 6$ $(0 \leq \eta < 0.1$), $N_\theta = 12$ $(0.1 \leq \eta < 0.2$),
  $N_\theta = 24$ $(0.2 \leq \eta < 0.25)$, $N_\theta = 32$ $(0.25 \leq \eta < 0.55)$,
  $N_\theta = 24$ $(0.55 \leq \eta < 0.75)$, $N_\theta = 12$ $(0.75 \leq \eta < 1.0$);
- Cases b) and c)
  6 modal zones ($L_\theta = 2\pi$) with
  $N_\theta = 6$ $(0 \leq \eta < 0.1$), $N_\theta = 20$ $(0.1 \leq \eta < 0.2$),
  $N_\theta = 42$ $(0.2 \leq \eta < 0.25)$, $N_\theta = 84$ $(0.25 \leq \eta < 0.55)$,
  $N_\theta = 42$ $(0.55 \leq \eta < 0.75)$, $N_\theta = 12$ $(0.75 \leq \eta < 1.0$).

One may note that case a) has a slightly higher azimuthal resolution ($k_{\theta\,\max} = 95$ in comparison with $k_{\theta\,\max} = 83$ for cases b) and c)), but this does not affect the results shown. As for the time discretization, the CFL criterion was again set to 1.7. This

led to a general time step size of $\Delta t \approx 3.5 \times 10^{-2}$ (similar to the case of FIG. 4.23), except for case c)—because of the offset of the vortex and the presence of velocity at $r = 0$—for which the CFL limit imposes a lower $\Delta t \approx 6.5 \times 10^{-3}$.

From the above description and the results shown in FIG. 4.34, the following observations can be made:

- ⋆ All three results agree quite well confirming thus, once again, the overall good behavior of the method (including the modal reduction procedure).
- ⋆ Case a) was done with approximately one third of the number of degrees of freedom of cases b) and c). Taking advantage of the natural physical periodicity of the solution, when possible, therefore allows for an important gain in computational efficiency.
- ⋆ In a similar point of view, any departure from axial symmetry in the azimuthal direction leads to an increase in the resolution requirements (and computational costs) for that direction, as can be seen from the enstrophy spectrum of the off-centered vortex in case c).

To verify the level of spatial resolution used, besides looking at the modal enstrophy (or energy) spectrum, we may use the more "global" diagnosis

$$\frac{dE}{dt} = -2\,Re^{-1}\,\mathcal{E}\,, \tag{4.19}$$

the total energy E and enstrophy $\mathcal{E}$ being given by

$$E \equiv \frac{1}{2}\int_\Omega |\mathbf{u}|^2\,dV \quad \text{and} \quad \mathcal{E} \equiv \frac{1}{2}\int_\Omega |\boldsymbol{\omega}|^2\,dV\,.$$

It has been confirmed that (4.19) was satisfied to almost seven digit accuracy when applied to test case b) in FIG. 4.34. The time variation of the energy was evaluated for that check with the backward difference scheme

$$\frac{dE}{dt} = \frac{E(t+\Delta t) - E(t)}{\Delta t} + \mathcal{O}(\Delta t)\,,$$

and time step size of the order of 10^{-5} were used to maintain enough precision on this first order estimate. The "less accurate" results were observed during the saturation

phase of the instability, i.e., at about the time solution shown in FIG. 4.34.b; equation (4.19) was then satisfied with an accuracy of approximately six digits. These accuracy levels confirm the proper capturing of the small viscous scales for the discretization parameters used.

The triangular vortex solution represents only one of the possible outcomes of the initially unstable configuration with $\alpha = 7$. The mode-3 intability has indeed the highest growth rate, but mode-2 and mode-4 instabilities have similar, though slightly smaller, values (see TABLE 4.10). As another test, the case b) of FIG. 4.34 can be reconsidered, but this time with an initial white noise perturbation instead of a single mode-3. The partial evolution of the resulting vorticity field is shown in FIG. 4.35; the time evolution of the corresponding modal enstrophy (the first five modes) is in turn shown in FIG. 4.36. Although the mode-3 instability dominates the early stages of the evolution, the important nonlinear interactions with the other unstables modes do not lead to any equilibrium structures in this case. The results presented here—including the vortex merging observed in the sequence $t = 60$, 65, and 70 in FIG. 4.35—are once again in good agreement with the experimental and numerical results of Carnavale & Kloosterziel, as well as with the simulation results of Winckelmans (private communication) obtained with a 2-D vortex method.

This concludes our present section on the triangular vortex, and based on the quantitative agreement of our linear stability results, including the consistency of both codes UNCYL-LS and UNCYL, and the qualitative agreement of the overall nonlinear evolution, we feel confident in the complete verification of the $k_z = 0$ family of vector expansions. Also indirectly verified in this test case was the global modal reduction algorithm and the regularity conditions. Note that these were also indirectly verified in the q-vortex problem, with a restriction to the $k_\theta = 0$ and 1 cases. Because of the very confined nature of this flow field though—the velocity is effectively zero at some finite radius—the nature of the outer boundary conditions could not have been directly checked. We had to rely on a more specific, independent procedural verification to ensure that they were indeed correctly implemented for all cases of k_θ. An additional point regarding the very limited radial extent of this type of zero circulation vortex is the relevance of an unbounded method for computing such problems. In his parametric study of a 2-D version of the BOUNCYL code, Houde (2001) also very successfully computed the flow dynamics of this test case, showing that it is

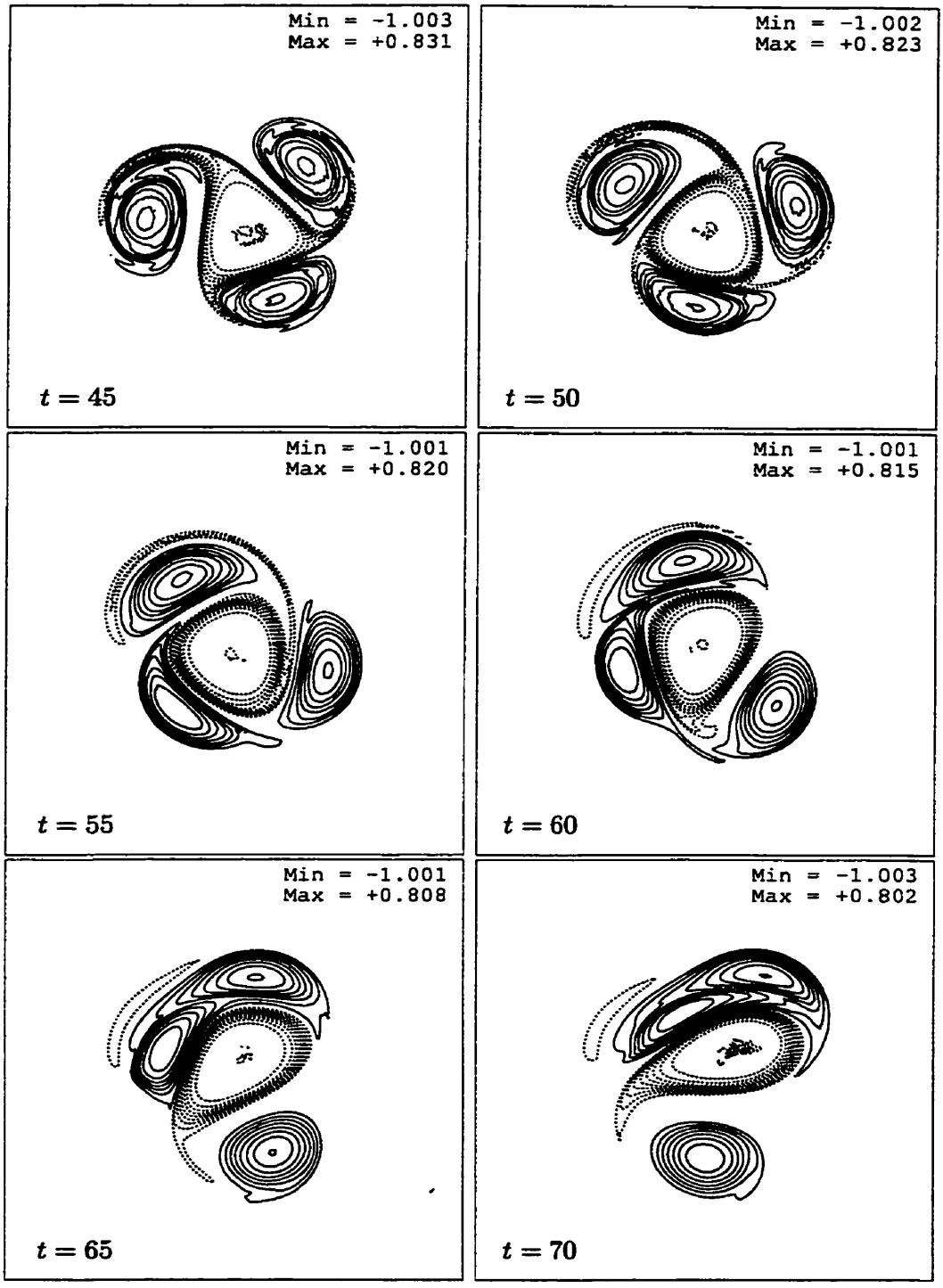

FIGURE 4.35. Partial evolution of the vortex of FIG. 4.23 ($\alpha = 7$ and $Re = 10^4$), but from this time an initial white noise perturbation. We show here the iso-contours of vorticity, from $\omega_z = -1$ to $+1$, with steps of 0.1 (the zero contour is not shown); solid lines are for positive values while broken ("dash") lines are for negative values. See FIG. 4.36 for the corresponding modal enstrophy evolution.

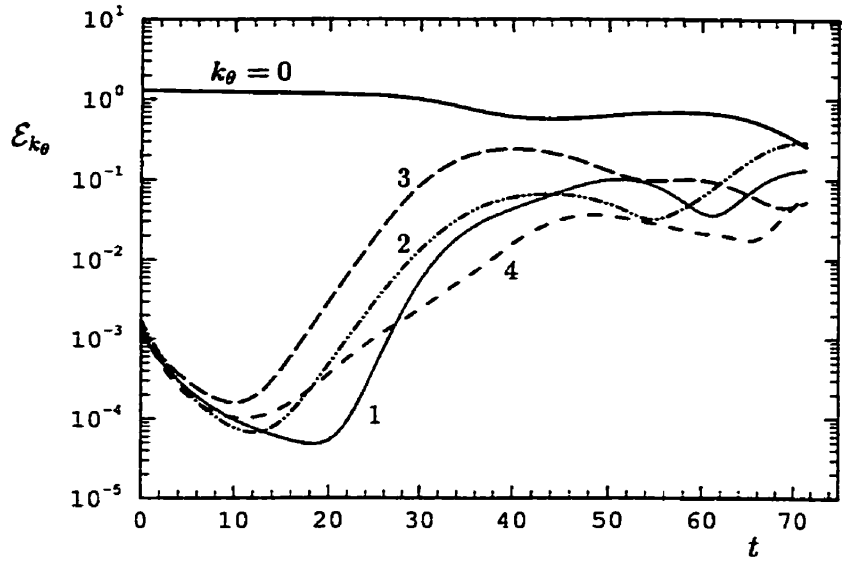

FIGURE 4.36. Time evolution of the modal enstrophy $\mathcal{E}_{k_\theta}$ associated with the vorticity fields shown in FIG. 4.35. The most unstable mode-3 perturbation is closely followed by mode-2 and the other low order modes.

almost insensitive to confinement effects, i.e., the distance R_o at which the no-slip boundary conditions are imposed. These particular considerations do obviously not affect, at any rate, our validation conclusions.

4.4 Summary

Before we bring this chapter to an end, let us summarize. In Sec. 4.1, we used the circular pipe Stokes flow analytical solution to verify the B-spline interpolation and the matrices of the bounded B-spline formulation (the codes BOUNCYL-LS and BOUNCYL). Linear stability results of the Poiseuille flow served in the verification of the nonlinear term computation and the time integration schemes of the Navier-Stokes solver BOUNCYL. Consistency between the eigenvalue and the Navier-Stokes solvers was used as a global validation test to verify the code as a whole.

Because both codes UNCYL and BOUNCYL make use of many common subroutines, some of the verifications presented in the first section, for the code BOUNCYL, were implicitly carried over to the code UNCYL. This led us, in Sec. 4.2, to focus on the unbounded radial discretization for the family of vector expansions for which $k_z \neq 0$. The radial interpolation and boundary conditions indeed represent the main difference between the present unbounded and bounded numerical methods. Linear stability results of the Batchelor q-vortex problem were used to first verify the eigenvalue solver UNCYL-LS. Then, using a slightly different procedure than the one used in Sec. 4.1, verification of the Navier-Stokes solver UNCYL was undertaken by direct computation of some of these linear stability results. Consistency between the Navier-Stokes and the eigenvalue solvers was also used as a complementary check.

The $k_z = 0$ family of vector expansions of the code UNCYL was in turn verified in Sec. 4.3, computing the complete nonlinear dynamics that leads to the formation of a triangular vortex. In that case, quantitative verifications through the corroboration of numerical linear stability results were of a more limited extent, but consistency between the eigenvalue and the Navier-Stokes solvers was again established. Qualitative verification of the complete nonlinear evolution of the mode-3 instability up to its saturation and the resulting triangular vortex formation also served as an additional confirmation.

Although not directly accounted for in the different tests, the regularity condition and the general modal reduction algorithm were implicitly verified in the series of flow problems considered. The verification of the harmonic decaying condition, on the other hand, was not directly nor indirectly involved, except for the base flow of

the q-vortex, i.e., only for $U_\theta \propto r^{-1}$. For the other cases examined, the solutions were found to decay much more rapidly than the minimal rates imposed by the condition. As it was the case for numerous algorithm tests that were carried out but not explicitly presented here, verification of the outer decaying boundary condition was nevertheless systematically performed.

As a final remark, anticipating the general discussion of the concluding chapter, let us note that in terms of radial interpolation, our B-spline results certainly compared very well and, in most cases, advantageously to the reference data found in the literature and obtained by global interpolation (spectral expansions) methods. On the other hand, our brief comparisons between the regular B-spline discretization of the code BOUNCYL-LS and the mapped B-splines of the code UNCYL-LS seem to show only a marginal advantage of the latter mapping approach over the former standard B-splines in the approximation of problems in unbounded domains.

Chapter 5

Conclusion

In this thesis, a novel extension of Leonard's divergence-free vector expansions method (Leonard, 1981) for the solution of the incompressible, unsteady Navier-Stokes equations in unbounded (cylindrical) domains has been proposed. The spatial discretization, presented in Chap. 2, is based on a series of vector expansions that intrinsically satisfy the divergence-free constraint. These vectors are constructed by a combination of Fourier series for both the longitudinal and azimuthal directions, and algebraically mapped B-splines for the semi-infinite radial direction. Special care has been taken to account for the particular analytical behaviors at the center of the domain ($r = 0$), and for the asymptotic behaviors as r tends to infinity. The implementation of this numerical method was discussed in Chap. 3, and its validation in Chap. 4.

The present, unbounded domain, B-spline formulation has also been modified to allow for the solution of the Navier-Stokes equations in radially bounded cylindrical domains (Sec. 3.5). For that particular instance, the resulting numerical method is similar to the one proposed by Loulou et al. (1997), except maybe for some few technical points. Also, as by-products of the two Navier-Stokes solvers, the genéral divergence-free Galerkin approximation was in turn used to develop two corresponding linear stability eigenvalue solvers; one for unbounded domains and one for bounded domains. Implementation and validation of these additional solvers were likewise considered in Chap. 3 and 4 respectively. Accordingly, all the thesis' main and secondary objectives presented in Chap. 1 have been successfully fulfilled.

We now conclude our work by first briefly discussing some of the issues that concern the use of local B-spline functions for the approximation of the unbounded radial direction, in light of the numerical tests presented in Chap. 4. Following this, we give some recommendations for future work related, on one hand, to the numerical methodology, and on the other hand, to some physical investigation that could be carried out following the results obtained in the various numerical tests.

5.1 Discussion

While testing our numerical method in Chap. 4, the comparisons made with the other numerical results obtained by global expansions methods proved the mapped B-splines to be an advantageous alternative for use as basis functions in the radial direction. Indeed, even without making use of any particularly refined distribution of radial breakpoints, the B-spline results were shown to be either more precise for a similar number of radial coefficients, or for a given error, usually required less degrees of freedom.

On the other hand, comparisons made between the unbounded B-spline code UNCYL-LS and its wall-bounded version BOUNCYL-LS did not prove as much advantageous, as may be recalled from TABLE 4.9 in Sec. 4.2.4. Despite this less favorable occurrence, we were nevertheless able to conclude—on the basis of our tested cases with a slow decaying base flow field (see FIG. 4.21)—that whatever the bounded B-spline discretization used, a similar unbounded mapped B-spline discretization could always be used to obtain better results. The gain of the latter approximation over the former may however be only marginal, particularly if the field solutions exhibit a fast decaying behavior. From this, we are led to admit that the present unbounded mapped B-spline method does not seem to provide a significant improvement over the more standard (wall-bounded) B-spline approach.

This last observation certainly comes in a marked contrast with the similar comparison made between the bounded domain Chebyshev polynomials of Mayer & Powell (1992), for example, and the unbounded rational Legendre functions of Matsushima & Marcus (1997). Since one of our motivations to include a mapping into the B-spline

formulation originated from the perspective of global expansions methods, we may clearly see that global expansions considerations do not necessarily carry over to local approximation formulations. Following this line of reasoning, one could legitimately raise doubts about the practical advantages—the theoretical advantages making no doubts—of imposing more complex regularity conditions at the center of the domain $r = 0$, i.e., from Chap. 2, imposing (2.11) instead of the more simple conditions given in (2.10). As we already mentioned, no special investigation was made in this work to supply a specific answer to this question. Such a task must therefore be considered as a recommendation for future work.

Although our comparison tests between both the bounded and the unbounded B-spline methods only led to partially satisfying conclusions in terms of the relevance of developing a special unbounded version, we are nevertheless convinced that the unbounded spectral/B-spline method presented in this thesis remains of great interest and usefulness. The successful and efficient stability results obtained, while testing both codes UNCYL-LS and UNCYL, do certainly allow us to conclude very positively on the efficiency of the mapped B-splines in comparison with the other global expansion approaches. The present method is indeed particularly well suited for flow problems having an intrinsic axial symmetry, as in the the q-vortex problem of Sec. 4.2, or the triangular vortex of Sec. 4.3.

5.2 Recommendations for future work

In the continuation of what has been initiated in this work, we suggest that the following elements be considered. Relating more specifically to the numerical method:

- The study of the effects of the regularity conditions (at $r = 0$) on the error of the solution, to see how effective are these conditions in practice;
- The development and implementation of a higher order dissipation term (e.g., like the biharmonic term $-\nu_4 \nabla^4 \mathbf{u}$) to allow for simulations at higher Reynolds number with only moderately high spatial resolution;
- The specialization and optimization of the modal truncation and nonlinear term

algorithms.

Other optimization considerations such as the development of a parallel version of the code should also be considered.

On a more physical point of view, the following lines of investigation could offer some interesting propects:

- Regarding the q-vortex problem presented in Sec. 4.2, the discrepancy observed between the results of Mayer & Powell (1992) and ours (see FIG. 4.17) was left unexplained. Further investigations on that matter could probably help solve this question.
- In the simulations of the triangular vortex of Sec. 4.3, finite Reynolds number effects were seen to have an influence on the final state of equilibrium. Up to what extent these effects come into play in the formation of the triangular vortex could also be studied using the codes presented in this thesis.
- Another problem of interest that could well be studied using the mapped B-splines codes, but that is not mentioned in this thesis, is related to the dynamics of a vortex tube in a straining field.

Note that since the present numerical method is particularly well suited for unbounded flow problems having an intrinsic axial symmetry, any problems falling into this category could also be considered.

Bibliography

ABRAMOWITZ, M. & STEGUN, I. A. 1964 *Handbook of Mathematical Functions with Formulas, Graphs and Mathematical Tables.* AMS 55. National Bureau of Standards, Washington D.C.

BATCHELOR, G. K. 1964 Axial flow in trailing line vortices. *J. Fluid Mech.*, **20**(4), 645–658.

BATCHELOR, G. K. 1967 *An Introduction to Fluid Dynamics.* Cambridge Univ. Press, Cambrdige (UK).

BATCHELOR, G. K. & GILL, A. E. 1962 Analysis of the stability of axisymetric jet. *J. Fluid Mech.*, **14**, 529–551.

BAYLY, B. J. 1986 Three-dimensional instability of elliptical flow. *Phys. Rev. Lett.*, **57**, 2160–2163.

BOYD, J. P. 1999 *Chebyshev and Fourier Spectral Methods.* Dover Publ., Mineola (electronic version from `http://www-personal.engin.umich.edu/~jpboyd/`), 2nd edition.

CADOT, O., DOUADY, S., & COUDER, Y. 1995 Characterization of the low-pressure filaments in a three-dimensional turbulent shear flow. *Phys. Fluids*, **7**(3), 630–646.

CANUTO, C., HUSSAINI, M. Y., QUARTERONI, A., & ZANG, T. A. 1988 *Spectral Methods in Fluid Dynamics.* Springer-Verlag, New-York.

CARNAVALE, G. F. & KLOOSTERZIEL, R. C. 1994 Emergence and evolution of triangular vortices. *J. Fluid Mech.*, **259**, 305–331.

CARTON, X. J. & MCWILLIAMS, J. C. 1989 Barotropic and baroclinic instabilities of axisymetric vortices in a quasi-geostrophic model. In Nihoul, J. C. J. & Jamart, B. M., editors, *Mesoscale/Synoptic Coherent Structures in Geophysical Turbulence*, 225–244. Elsevier.

CHORIN, A. J. 1969 On the convergence of discrete approximations to the Navier-Stokes equations. *Math. Comp.*, **23**, 341–353.

CHORIN, A. J. & MARSDEN, J. E. 1993 *A Mathematical Introduction to Fluid Mechanics*, Vol. 4 of *Texts in Applied Mathematics*. Springer-Verlag, New-York, 3rd edition.

COTTET, G. H. & KOUMOUTSAKOS, P. D. 2000 *Vortex Methods: Theory and Practice*. Cambridge Univ. Press, New-York.

CROWDY, D. 1999 A class of exact multipolar vortices. *Phys. Fluids*, **11**(9), 2556–2564.

DE BOOR, C. 1978 *A Practical Guide to Splines*. Springer-Verlag, New-York.

DRAZIN, P. G. & REID, W. H. 1981 *Hydrodynamic Stability*. Cambridge Univ. Press, New-York.

DUFRESNE, L. & DUMAS, G. 1998a A 3-D spectral/finite element method for the simulation of the wake vortices hydrodynamic instabilities. *CAS J.*, **44**(4), 223–230.

DUFRESNE, L. & DUMAS, G. 1998b A special finite element radial discretization for a Navier-Stokes solver in cylindrical coordinates. In *Proc. 6th Ann. Conf. CFD Soc. Canada CFD98*, VIII 123–128, Québec.

DUFRESNE, L. & DUMAS, G. 2000 DNS of free vortical flows in cylindrical coordinates: Boundary conditions and local radial interpolation. In *Proc. 8th Ann. Conf. CFD Soc. Canada CFD2K*, 407–412, Montréal.

DUMAS, G. & LEONARD, A. 1994 A divergence-free spectral expansions method for three-dimensional flows in spherical-gap geometries. *J. Comp. Phys.*, **111**(2), 205–219.

EBIN, D. G. & MARSDEN, J. 1970 Groups of diffeomorphisms and the motion of an incompressible fluid. *Ann. of Math.*, **92**, 102–163.

FERZIGER, J. H. 1981 *Numerical Methods for Engineering Application.* John Wiley & Sons, New-York.

GOLUB, G. H. & VAN LOAN, C. F. 1996 *Matrix Computations.* John Hopkins Univ. Press, Baltimore, 3rd edition.

GOTTLIEB, D. & ORSZAG, S. A. 1977 *Numerical Analysis of Spectral Methods: Theory and Applications.* CBMS-NSF Monograph 26. SIAM, Philadelphia.

GROSCH, C. E. & ORSZAG, S. A. 1977 Numerical solution of problems in unbounded regions: Coordinate transforms. *J. Comp. Phys.*, **25**, 273–296.

HAMMING, R. W. 1973 *Numerical Methods for Scientists and Engineers.* McGraw-Hill, New-York (reprinted by Dover Publ., 1986), 2nd edition.

HOUDE, S. 2001 Etude de Validation et d'Utilisation d'un Code Spectral/B-spline en Géométrie Cylindrique. Master's thesis, Université Laval, Québec.

HOUDE, S., DUMAS, G., & DUFRESNE, L. 2000 Utilisation et avantages d'une approche par zones modales pour un code quasi-spectral en géométrie cylindrique. In *Proc. 8th Ann. Conf. CFD Soc. Canada CFD2K*, 57–62, Montréal.

KLOOSTERZIEL, R. C. & CARNAVALE, G. F. 1999 On the evolution and saturation of instabilities of two-dimensional isolated circular vortices. *J. Fluid Mech.*, **388**, 217–257.

KLOOSTERZIEL, R. C. & VAN HEIJST, G. J. F. 1991 An experimental study of unstable barotropic vortices in a rotating fluid. *J. Fluid Mech.*, **223**, 1–24.

KRAVCHENKO, A. G. & MOIN, P. 1997 On the effect of numerical errors in large eddy simulations of turbulent flows. *J. Comp. Phys.*, **127**, 412–423.

KRAVCHENKO, A. G., MOIN, P., & MOSER, R. D. 1996 Zonal embedded grids for numerical simulations of wall-bounded turbulent flows. *J. Comp. Phys.*, **127**, 412–423.

LADYZHENSKAYA, O. A. 1975 Mathematical analysis of Navier-Stokes equations for incompressible liquids. *Ann. Rev. Fluid Mech.*, **7**, 249–272.

LEONARD, A. 1981 Divergence-free vector expansions for 3-D flow simulations. *Bull. Amer. Phys. Soc.*, **26**, 1247.

LEONARD, A. 1985 Computing three-dimensional incompressible flows with vortex elements. *Ann. Rev. Fluid Mech.*, **17**, 523–559.

LEONARD, A. & WRAY, A. 1982 A new numerical method for the simulation of 3-D flow in a pipe. In *Proc. 8th Int. Conf. Num. Meth. Fluid Dyn.*, Aachen.

LERAY, J. 1933 Étude de diverses équations intégrales nonlinéaires et de quelques problèmes que pose l'hydrodynamique. *J. Math. Pures Appl.*, **12**, 1–82.

LERAY, J. 1934a Essais sur les mouvements d'un liquide visqueux emplissant l'espace. *Acta Math.*, **63**, 193–248.

LERAY, J. 1934b Essais sur les mouvements plans d'un liquide visqueux que limitent des parois. *J. Math. Pures Appl.*, **13**, 331–418.

LESSEN, M., SINGH, P. J., & PAILLET, F. 1974 The stability of a trailing line vortex. Part 1. Inviscid theory. *J. Fluid Mech.*, **63**(4), 753–763.

LEWEKE, T. & WILLIAMSON, C. H. K. 1998 Collaborative elliptic instability of a vortex pair. *J. Fluid Mech.*, **360**, 85–119.

LOPEZ, J. M. & SHEN, J. 1998 An efficient spectral-projection method for the Navier-Stokes equations in cylindrical geometries. *J. Comp. Phys.*, **139**, 308–326.

LOULOU, P., MOSER, R. D., MANSOUR, N. N., & CANTWELL, B. J. 1997 Direct numerical simulation of incompressible pipe flow using a B-spline spectral method. Technical Memorandum TM-110436, NASA.

MATSUSHIMA, T. & MARCUS, P. S. 1997 A spectral method for unbounded domains. *J. Comp. Phys.*, **137**, 321–345.

MAYER, E. W. & POWELL, K. G. 1992 Viscous and inviscid instabilities of a trailing vortex. *J. Fluid. Mech.*, **245**, 91–114.

MILNE-THOMSON, L. M. 1968 *Theoretical Hydrodynamics.* Macmillan & Co., London (reprinted by Dover Publ., 1996), 5th edition.

MOORE, D. W. & SAFFMAN, P. G. 1972 The motion of a vortex filament with axial flow. *Phil. Trans.*, **272**, 403–429.

MORSE, P. M. & FESHBACH, H. 1953 *Methods of Theoretical Physics.* McGraw-Hill, New-York.

MOSER, R. D. & MOIN, P. 1984 Direct numerical simulation of curved turbulent channel flow. Technical Report TF-20, Thermosciences Div., Stanford Univ.

MOSER, R. D., MOIN, P., & LEONARD, A. 1983 A spectral numerical method for the Navier-Stokes equations with applications to Taylor-Couette flow. *J. Comp. Phys.*, **52**, 524–544.

OCKENDON, J., HOWISON, S., LACEY, A., & MOVCHAN, A. 1999 *Applied Partial Differential Equations.* Oxford Univ. Press, Oxford.

ORSZAG, S. A. 1969 Numerical method for the simulation of turbulence. *Phys. Fluids*, **12**(Suppl. II), 250–257.

ORSZAG, S. A. 1970 Transform method for the calculation of vector-coupled sums: Application to the spectral form of the vorticity equation. *J. Atmos. Sci.*, **27**, 890–895.

ORSZAG, S. A. 1971 Numerical simulation of incompressible flows within simple boundaries: I. Galerkin (spectral) representations. *Stud. Appl. Math.*, **50**, 293–327.

ORSZAG, S. A. 1974 Fourier series on sphere. *Mon. Weather Rev.*, **102**, 56–75.

ORSZAG, S. A. 1980 Spectral methods for problems in complex geometries. *J. Comp. Phys.*, **37**, 70–92.

PASQUARELLI, F., QUARTERONI, A., & SACCHI-LANDRIANI, G. 1987 Spectral approximations of the Stokes problem by divergence-free functions. *J. Sci. Comp.*, **2**(3), 195–225.

PATERA, A. T. 1984 A spectral element method for fluid dynamics: Laminar flow in a channel expansion. *J. Comp. Phys.*, **54**, 468–488.

PIERREHUMBERT, R. T. 1986 Universal short-wave instability of two-dimensional eddies in an inviscid fluid. *Phys. Rev. Lett.*, **57**, 2157–2159.

PLOUMHANS, P. 2001 *Simulation of High Reynolds Number Flows Past Bluff Bodies Using Vortex and Boundary Element Methods.* PhD thesis, Univ. cath. de Louvain, Louvain-la-Neuve.

SAFFMAN, P. G. 1992 *Vortex Dynamics.* Cambridge Univ. Press, New-York.

SALWEN, H., COTTON, F. W., & GROSCH, C. E. 1980 Linear stability of Poiseuille flow in a circular pipe. *J. Fluid Mech.*, **98**, 273–284.

SALWEN, H. & GROSCH, C. E. 1972 The stability of Poiseuille flow in a pipe of circular cross section. *J. Fluid Mech.*, **54**, 93–112.

SCHLICHTING, H. 1979 *Boundary Layer Theory.* McGraw-Hill, New-York, 7th edition.

SHEN, J. 1997 Efficient spectral-Galerkin methods III: Polar and cylindrical geometries. *SIAM J. Sci. Comp.*, **18**(6), 1583–1604.

SHILOV, G. E. 1973 *Elementary Real and Complex Analysis*, Vol. 1 of *Mathematical Analysis.* MIT Press, Cambridge (USA) (reprinted by Dover Publ., 1996).

SPALART, P. R. 1998 Airplane trailing vortices. *Ann. Rev. Fluid Mech.*, **30**, 107–138.

SPALART, P. R., MOSER, R. D., & ROGERS, M. M. 1991 Spectral methods for the Navier-Stokes equations with one or two periodic directions. *J. Comp. Phys.*, **96**, 297–324.

STANAWAY, S. K., CANTWELL, B. J., & SPALART, P. R. 1988 Navier-Stokes simulations of axisymetric vortex rings. AIAA Paper 88-0318.

STRANG, G. & FIX, G. J. 1988 *An Analysis of the Finite Element Method.* Wellesley-Cambridge Press, Wellesley (also edited by Prentice-Hall, 1973).

TEMAM, R. 1979 *Navier-Stokes Equations.* North-Holland Publ. Co., Amsterdam.

TEMAM, R. 1995 *Navier-Stokes Equations and Nonlinear Functional Analysis.* CBMS-NSF Monograph 66. SIAM, Philadelphia, 2nd edition.

VINCENT, A. & MENEGUZZI, M. 1991 The spatial structure and statistical properties of homogeneous turbulence. *J. Fluid Mech.*, **225**, 1–20.

WALEFFE, F. 1990 On the three-dimensional instability of strained vortices. *Phys. Fluids A*, **2**(1), 76–80.

WANG, C. Y. 1991 Exact solutions of the steady-state Navier-Stokes equations. *Ann. Rev. Fluid Mech.*, **23**, 159–177.

WINCKELMANS, G. S. 1989 *Topics in Vortex Methods for the Computation of Three- and Two-Dimensional Incompressible Unsteady Flows.* PhD thesis, Caltech, Pasadena.

ZIENKIEWICZ, O. C. & TAYLOR, R. L. 1989 *The Finite Element Method*, Vol. 1. McGraw-Hill, Maidenhead, 4th edition.

ZIENKIEWICZ, O. C. & TAYLOR, R. L. 1991 *The Finite Element Method*, Vol. 2. McGraw-Hill, Maidenhead, 4th edition.

Appendix A

Principal Differential Operators and Vector Field Representation in Cylindrical Coordinates

A.1 Principal differential operators

First, let us assume that the velocity vector $\mathbf{u}$ may be written as

$$\mathbf{u} = \widehat{\mathbf{u}}(r)\, e^{i k_\theta \theta} e^{i k_z z}\,, \tag{A.1}$$

then let " $\widehat{\ }$ " be the double Fourier transform operator in $(\theta,\, z)$ such that

$$\widehat{\mathbf{a}} = \frac{1}{4\pi^2} \iint \mathbf{a}\, e^{-i k_\theta \theta} e^{-i k_z z}\, d\theta\, dz\,, \tag{A.2}$$

where a period of 2π is assumed for both directions. The divergence, curl and Laplacian operators in cylindrical coordinates for both physical and spectral spaces are given as follows:

Divergence The divergence of the vector $\mathbf{u}$ is given by

$$\nabla \cdot \mathbf{u} \equiv \frac{1}{r}\frac{\partial r u_r}{\partial r} + \frac{1}{r}\frac{\partial u_\theta}{\partial \theta} + \frac{\partial u_z}{\partial z}\,. \tag{A.3}$$

In the spectral space this becomes

$$\boxed{\widehat{\nabla\cdot\mathbf{u}} = \frac{\widehat{u}_r}{r} + \widehat{u}_r' + i\,\frac{k_\theta}{r}\widehat{u}_\theta + i\,k_z\widehat{u}_z\,.} \tag{A.4}$$

Curl The curl operator applied to $\mathbf{u}$ gives

$$\boldsymbol{\omega} \equiv \nabla\times\mathbf{u} = \frac{1}{r}\begin{vmatrix} \hat{\mathbf{e}}_r & r\hat{\mathbf{e}}_\theta & \hat{\mathbf{e}}_z \\ \partial/\partial r & \partial/\partial\theta & \partial/\partial z \\ u_r & ru_\theta & u_z \end{vmatrix}. \tag{A.5}$$

The vorticity components are therefore written

$$\omega_r = \frac{1}{r}\frac{\partial u_z}{\partial\theta} - \frac{\partial u_\theta}{\partial z}\,; \tag{A.6}$$

$$\omega_\theta = \frac{\partial u_r}{\partial z} - \frac{\partial u_z}{\partial r}\,; \tag{A.7}$$

$$\omega_z = \frac{u_\theta}{r} + \frac{\partial u_\theta}{\partial r} - \frac{1}{r}\frac{\partial u_r}{\partial\theta}\,. \tag{A.8}$$

In the spectral space, we obtain

$$\boxed{\begin{aligned} \widehat{\omega}_r &= i\,\frac{k_\theta}{r}\widehat{u}_z - i\,k_z\widehat{u}_\theta\,; \\ \widehat{\omega}_\theta &= i\,k_z\widehat{u}_r - \widehat{u}_z'\,; \\ \widehat{\omega}_z &= \frac{\widehat{u}_\theta}{r} + \widehat{u}_\theta' - i\,\frac{k_\theta}{r}\,\widehat{u}_r\,; \end{aligned}} \tag{A.9}$$

which may be written in a more compact way by

$$\widehat{\boldsymbol{\omega}} = \widehat{\nabla\times\mathbf{u}}\,. \tag{A.10}$$

Laplacian Finally, the Laplacian of $\mathbf{u}$ is defined by

$$\nabla^2\mathbf{u} \equiv \frac{1}{r}\frac{\partial}{\partial r}\left(r\frac{\partial\mathbf{u}}{\partial r}\right) + \frac{1}{r^2}\frac{\partial^2\mathbf{u}}{\partial\theta^2} + \frac{\partial^2\mathbf{u}}{\partial z^2}\,, \tag{A.11}$$

with $\partial\,\hat{\mathbf{e}}_r/\partial\theta = \hat{\mathbf{e}}_\theta$ and $\partial\,\hat{\mathbf{e}}_\theta/\partial\theta = -\hat{\mathbf{e}}_r$. In the spectral space, the vector components thus become

$$\boxed{\begin{aligned}
\widehat{\nabla^2\,\mathbf{u}}\cdot\hat{\mathbf{e}}_r &= \frac{1}{r}\widehat{u}_r' + \widehat{u}_r'' - \left(\frac{k_\theta^2}{r^2} + k_z^2\right)\widehat{u}_r - \frac{\widehat{u}_r}{r^2} - i\,2\frac{k_\theta}{r^2}\widehat{u}_\theta\,; \\
\widehat{\nabla^2\,\mathbf{u}}\cdot\hat{\mathbf{e}}_\theta &= \frac{1}{r}\widehat{u}_\theta' + \widehat{u}_\theta'' - \left(\frac{k_\theta^2}{r^2} + k_z^2\right)\widehat{u}_\theta - \frac{\widehat{u}_\theta}{r^2} + i\,2\frac{k_\theta}{r^2}\widehat{u}_r\,; \\
\widehat{\nabla^2\,\mathbf{u}}\cdot\hat{\mathbf{e}}_z &= \frac{1}{r}\widehat{u}_z' + \widehat{u}_z'' - \left(\frac{k_\theta^2}{r^2} + k_z^2\right)\widehat{u}_z\,.
\end{aligned}} \tag{A.12}$$

Note the coupling between the radial and azimuthal components.

A.2 Analyticity at the origin

The equivalent of the following analyticity results, derived in a somewhat different manner, can also be found in Boyd (1999), or in Loulou et al. (1997).

The Taylor expansion theorem gives for an analytic vector function $\mathbf{u}$ in some neighborhood of the point $\mathbf{x} = \mathbf{0}$

$$\mathbf{u}(\mathbf{x}) = \sum_{a=0}^{\infty}\sum_{b=0}^{\infty}\sum_{c=0}^{\infty} \frac{x^a y^b z^c}{a!b!c!}\, D^n\mathbf{u}(\mathbf{x}=\mathbf{0})\,, \tag{A.13}$$

with the following definitions: $\mathbf{x} = \{x, y, z\}$; $\mathbf{u} = \{u_x, u_y, u_z\}$; $n = a + b + c$; and $D^n = \partial^n/\partial x^a \partial y^b \partial z^c$. Note that the series (A.13) is convergent within a "bounded sphere" $R = [x^2 + y^2 + z^2]^{1/2} < \infty$, that defined the region of analyticity. Because in Cartesian coordinates, the basis vectors are independent of position, we only need to consider one vector component at a time, namely u_z in the derivation shown below.

In (A.13), the terms $D^n\mathbf{u}(\mathbf{x} = \mathbf{0})$ act as constants so that if we rewrite for u_z in cylindrical coordinates ($\mathbf{x} = \{r, \theta, z\}$), we then get

$$u_z(\mathbf{x}) = \sum_{n=0}^{\infty} r^{a+b}\,\cos^a\theta\,\sin^b\theta\,z^c\,\xi_{a,b,c} \tag{A.14}$$

where the triple sum of (A.13) has been symbolically reduced to $\sum_{n=0}^{\infty}$ and

$$\xi_{a,b,c} = \frac{1}{a!b!c!} D^n u_z(\mathbf{x}=\mathbf{0}) .$$

Let us rewrite the "cos" and "sin" terms such that

$$\begin{aligned}
\cos^a\theta &= \frac{1}{2^a}[e^{i\theta}+e^{-i\theta}]^a \\
&= \frac{1}{2^a} \sum_{\substack{a_1=0 \\ a_2=0 \\ a_1+a_2=a}}^{a} \frac{a!}{a_1!a_2!} e^{i(a_1-a_2)\theta} \\
\sin^b\theta &= \frac{1}{(2i)^b}[e^{i\theta}-e^{-i\theta}]^b \\
&= \frac{1}{(2i)^b} \sum_{\substack{b_1=0 \\ b_2=0 \\ b_1+b_2=b}}^{b} \frac{b!}{b_1!b_2!} (-1)^{b_2} e^{i(b_2-b_1)\theta}
\end{aligned}$$

Replaced in (A.14), this gives

$$u_z(\mathbf{x}) = \sum_{n=0}^{\infty} r^{a+b} \chi_{a,b,c}(z) e^{id\theta} \xi_{a,b,c} , \tag{A.15}$$

with $d = a_1 - a_2 + b_2 - b_1$ and

$$\chi_{a,b,c}(z) = \frac{i^b}{2^{a+b}} \sum_{\substack{a_1=0 \\ a_2=0 \\ a_1+a_2=a}}^{a} \frac{a!}{a_1!a_2!} \sum_{\substack{b_1=0 \\ b_2=0 \\ b_1+b_2=b}}^{b} \frac{b!}{b_1!b_2!} (-1)^{b_2} z^c .$$

We now apply the double Fourier transform (in θ and z)

$$\widehat{u}_z(r;\ k_\theta, k_z) = \frac{1}{(2\pi)^2} \int_0^{2\pi}\int_0^{2\pi} u_z(\mathbf{x}) e^{-ik_\theta\theta} e^{-ik_z z} d\theta dz$$

to (A.15), to obtain

$$\widehat{u}_z(r;\ k_\theta, k_z) = \sum_{n=0}^{\infty} r^{a+b} \xi_{a,b,c} \widehat{\chi}_{a,b,c}(k_z) \delta_{d,k_\theta} . \tag{A.16}$$

Here δ_{d,k_θ} is the Kronecker delta, viz.,

$$\delta_{d,k_\theta} = \begin{cases} 0 & \text{if} \quad d \neq k_\theta \\ 1 & \text{if} \quad d = k_\theta \end{cases} .$$

Note that carring out explicitly the z Fourier transform on z^c gives, for $k_z \neq 0$ and $c > 0$,

$$\frac{1}{2\pi}\int_0^{2\pi} z^c\, e^{-ik_z z}\, dz \;=\; \frac{c!}{ik_z}\sum_{j=0}^{c-1}\frac{(-1)^{j+1}}{(c-j)!}\,\frac{(2\pi)^{c-j-1}}{(ik_z)^j}\;,$$

and when $k_z = 0$, it equals to $(2\pi)^c/(c+1)$. This is implicitly taken into account in $\widehat{\chi}_{a,b,c}(k_z)$. If we now take the sum of only the non-zero values in (A.16), for a given k_θ, we finally obtain

$$\widehat{u}_z(r;\; k_\theta, k_z) \;=\; \sum_{p=0}^{\infty}\sum_{c=0}^{\infty} r^{|k_\theta|+2p}\,\xi_{a,b,c}\,\widehat{\chi}_{a,b,c}(k_z)\;, \tag{A.17}$$

where p is a function of a and b or more specifically of $a_{1,2}$ and $b_{1,2}$. The functional relation between p and the set of all admissible values of $a_{1,2}$, $b_{1,2}$ is not so easily expressed but can be determined by the set of non-negative integer values satisfying

$$a_1 - a_2 + b_2 - b_1 \;=\; k_\theta\;, \tag{A.18}$$

$$a_1 + a_2 \;=\; a\;, \tag{A.19}$$

$$b_1 + b_2 \;=\; b\;. \tag{A.20}$$

Similar reasoning applied to $\widehat{u}_x$ and $\widehat{u}_y$ hence leads to the general form of the radial behavior:

$$\lim_{r\to 0}\{\,\widehat{u}_x, \widehat{u}_y, \widehat{u}_z\,\} \;=\; \mathcal{O}(r^{|k_\theta|+2p})\;, \tag{A.21}$$

with $p = 0, 1, 2, \ldots$.

In order to get the behavior of the cylindrical coordinates vector components $\{\,\widehat{u}_r, \widehat{u}_\theta, \widehat{u}_z\,\}$, we only need to apply, to the former result (A.21), the transformation rules

$$\begin{aligned} u_r &= u_x\cos\theta \;+\; u_y\sin\theta\;,\\ u_\theta &= u_y\cos\theta \;-\; u_x\sin\theta\;. \end{aligned} \tag{A.22}$$

Using the symbolic notation

$$u_x(r,\theta,z) \;=\; \sum_{k_\theta}\sum_{p} \tilde{u}_x(z; k_\theta, p)\; r^{|k_\theta|+2p}\; e^{ik_\theta\theta}\;,$$

we obtain after dropping the parametric dependence of the variables as well as the summation notation, for simplicity reasons, and after the θ-Fourier transform,

$$\begin{aligned} \widehat{u}_r &= \frac{1}{2}[\ \tilde{u}_x - i\tilde{u}_y\ ]\ r^{|k_\theta - 1|+2p} + \frac{1}{2}[\ \tilde{u}_x + i\tilde{u}_y\ ]\ r^{|k_\theta+1|+2p}\ , \\ \widehat{u}_\theta &= \frac{1}{2}[\ \tilde{u}_y + i\tilde{u}_x\ ]\ r^{|k_\theta - 1|+2p} + \frac{1}{2}[\ \tilde{u}_y - i\tilde{u}_x\ ]\ r^{|k_\theta+1|+2p}\ . \end{aligned} \tag{A.23}$$

Now, after combining the same powers of r, we finally get

$$\widehat{u}_r \pm i\widehat{u}_\theta = [\ \tilde{u}_x \pm i\tilde{u}_y\ ]\ r^{|k_\theta \pm 1|+2p}\ , \tag{A.24}$$

which can also be equivalently written in the more detailed form

$$\begin{aligned} r\ [\ \widehat{u}_r + i\widehat{u}_\theta\ ] &= \mathcal{O}(r^{k_\theta+2p+2}) \quad \text{for} \quad k_\theta \geq 0\ , \\ r\ [\ \widehat{u}_r + i\widehat{u}_\theta\ ] &= \mathcal{O}(r^{|k_\theta|+2p}) \quad \text{for} \quad k_\theta \leq -1\ , \\ r\ [\ \widehat{u}_r - i\widehat{u}_\theta\ ] &= \mathcal{O}(r^{k_\theta+2p}) \quad \text{for} \quad k_\theta \geq 1\ , \\ r\ [\ \widehat{u}_r - i\widehat{u}_\theta\ ] &= \mathcal{O}(r^{|k_\theta|+2p+2}) \quad \text{for} \quad k_\theta \leq 0\ , \end{aligned} \tag{A.25}$$

again with $p = 0, 1, 2, \ldots$.

A.3 The harmonic decaying behavior

We know from complex function analysis that if an analytic (or equivalently harmonic) complex valued function $f(\zeta)$ (of a complex variable $\zeta = re^{i\theta}$) is to tend to zero as $r \to \infty$, then $f(\zeta)$ can be written in terms of the principal part of a Laurent series such that (Shilov, 1973)

$$f(\zeta) = \sum_{m=-M}^{-1} c_m\, \zeta^m \tag{A.26}$$

where M may be infinite. There is a modulus $r_0 = |\zeta_0| > 0$ defining the domain of analyticity of $f(\zeta)$ to be for all $|\zeta| \geq r_0$ and accordingly

$$c_m = \frac{1}{2\pi i} \oint_C \frac{f(\zeta)}{\zeta^{m+1}}\, d\zeta\ ,$$

where C is some contour in the domain of analyticity. It is then a simple matter of changing variables to rewrite (A.26) as

$$f(r,\theta) \;=\; \sum_{m=-M}^{-1} c_m r^{-|m|}\, e^{im\theta} \;. \tag{A.27}$$

There are two real valued functions $g(r,\theta)$ and $h(r,\theta)$ such that

$$\begin{aligned} g &= f + f^* &&= 2\,\mathrm{Re}(f) \\ ih &= f - f^* &&= i\,2\,\mathrm{Im}(f) \end{aligned}$$

f^* being the complex conjugate of f. When applied to (A.27), this gives

$$g(r,\theta) \;=\; \sum_{\substack{m=-M \\ m\neq 0}}^{M} c_m r^{-|m|}\, e^{im\theta} \;, \tag{A.28}$$

$$ih(r,\theta) \;=\; \sum_{\substack{m=-M \\ m\neq 0}}^{M} -\mathrm{sgn}(m)\, c_m r^{-|m|}\, e^{im\theta} \;, \tag{A.29}$$

where we have defined $c_{-m} \equiv c_m^*$ $(m > 0)$ and $\mathrm{sgn}(m) \equiv m/|m|$. From (A.28), it is then possible to write

$$u_z(r,\theta,z) \;=\; \sum_{\substack{k_\theta=-M \\ k_\theta\neq 0}}^{M} \tilde{u}_z(z;k_\theta)\, r^{-|k_\theta|}\, e^{ik_\theta\theta} \;, \tag{A.30}$$

valid for $r \geq r_0 > 0$. Now, from (A.30) we may conclude that if the complex valued function $\widehat{u}_z(r;k_\theta,k_z)$ is to decay "harmonically" as $r \to \infty$, then we must have

$$\lim_{r\to\infty} \widehat{u}_z(r;k_\theta,k_z) \;=\; \mathcal{O}(r^{-|k_\theta|}) \;.$$

A similar argument applied to $\widehat{u}_x$ and $\widehat{u}_y$ leads to

$$\lim_{r\to\infty} \{\, \widehat{u}_x, \widehat{u}_y, \widehat{u}_z \,\} \;=\; \mathcal{O}(r^{-|k_\theta|}) \;. \tag{A.31}$$

Because u_x and u_y form an orthogonal pair in the plane r–θ, it is possible to write a complex valued function $f = u_x - iu_y$, in the same form as in (A.27). In the particular case of 2-D incompressible and irrotational velocity fields, the function f would be called the complex velocity and would be linked to the complex potential $\Pi = \phi + i\psi$

by $f = -d\Pi/d\zeta$ (where here $\mathbf{u} = -\nabla\phi = -\nabla \times \psi\hat{\mathbf{e}}_z$), following the notation of Milne-Thomson (1968). Now applying directly the definition of f in (A.27), or using the results of (A.28)–(A.29), we must then have that

$$\lim_{r\to\infty} \left[r^{|k_\theta|}\, \widehat{u}_x(r;\ k_\theta, k_z) \ = \ i\, \mathrm{sgn}(k_\theta)\, r^{|k_\theta|}\, \widehat{u}_y(r;\ k_\theta, k_z) \right] . \tag{A.32}$$

As for the cylindrical components u_r and u_θ, the transformation equation (A.22) is equivalent to

$$u_r \mp i u_\theta \ = \ \left[u_x \mp i u_y \right] e^{\pm i\theta} .$$

By applying this to the definition of f, we obtain that

$$\lim_{r\to\infty} \{ r\widehat{u}_r, r\widehat{u}_\theta, \widehat{u}_z \} \ = \ \mathcal{O}(r^{-|k_\theta|}) , \tag{A.33}$$

and

$$\lim_{r\to\infty} \left[r^{|k_\theta|+1}\, \widehat{u}_r(r;\ k_\theta, k_z) \ = \ i\, \mathrm{sgn}(k_\theta)\, r^{|k_\theta|+1}\, \widehat{u}_\theta(r;\ k_\theta, k_z) \right] . \tag{A.34}$$

Note that (A.32) and (A.34) are similar to the Cauchy-Riemann equations for the two vector components, and can also be seen as the equivalent form of a solenoidal and irrotational constraint (associated with the existence of the potential Π) in the $r-\theta$ plane.

Note also that although these results have been obtained for $k_\theta \neq 0$, the inclusion of $k_\theta = 0$ is somewhat straightforward and can be easily taken care of by extension of the above procedure (details are omitted). This would lead to the following asymptotic behavior:

$$\lim_{r\to\infty} \{ r\widehat{u}_r, r\widehat{u}_\theta, \widehat{u}_z \} \ = \ \mathcal{O}(1) . \tag{A.35}$$

Albeit this result is independent of k_z, a slight distinction should be made for the different cases of $k_z = 0$ and $k_z \neq 0$. In the former, $\widehat{u}_r \equiv 0$ while in the latter $\widehat{u}_r = \mathcal{O}(r^{-1})$ as for $\widehat{u}_\theta$ but independently of one another. Furthermore, since we assume that the flow is decaying at infinity the constant to which $\widehat{u}_z$ tends to must be zero.

Appendix B

B-spline Piecewise Polynomials

This appendix includes the information related the B-splines used for the discretization of the radial direction. It may be noted that most of the material presented here comes from the reference book of de Boor (1978), which should be consulted for a more complete presentation. We have chosen to include some of this material here for ease of access.

B.1 The truncated power basis

A function $f(\eta)$, if it is analytic in the neighborhood of a point η_0, has a Taylor series expansion around the point written

$$f(\eta) \;=\; f|_{\eta_0} + (\eta-\eta_0)\,\frac{d\,f}{d\eta}\bigg|_{\eta_0} + \frac{(\eta-\eta_0)^2}{2!}\,\frac{d^2\,f}{d\eta^2}\bigg|_{\eta_0} + \cdots + \frac{(\eta-\eta_0)^n}{n!}\,\frac{d^n\,f}{d\eta^n}\bigg|_{\xi}\;, \quad \text{(B.1)}$$

the last term on the right being called the remainder and with the point ξ being somewhere between the points η_0 and η. Assuming for example an expansion from the left, i.e., $\eta_0 \le \eta$, then $\eta_0 \le \xi \le \eta$. If $f(\eta)$ is a polynomial of order k, i.e., $f(\eta) \in \mathbb{P}^k$ we then have exactly

$$f(\eta) \;=\; \sum_{i=0}^{k-1} a_i(\eta-\eta_0)^i \quad \text{with} \quad a_i \;=\; \frac{1}{i!}\,\frac{d^i\,f}{d\eta^i}\bigg|_{\eta_0}\;. \quad \text{(B.2)}$$

Let us now introduce the "truncated" non-negative function

$$(\eta - \eta_0)_+ \equiv \max[\eta - \eta_0, 0] , \tag{B.3}$$

and extend its definition to the "truncated power basis"

$$(\eta - \eta_0)_+^k = [(\eta - \eta_0)_+]^k .. \tag{B.4}$$

When $k = 0$, this amounts to the step function (setting $0^0 = 1$), and for $k > 0$ to a polynomial function, for $\eta \geq \eta_0$, having $k-1$ continuous derivatives at η_0 (shown in figure VIII.2, p. 102 of de Boor, 1978). We can see that for $\eta \geq \eta_0$, and $f(\eta) \in \mathbb{P}^k$, that (B.2) is strictly equivalent to

$$f(\eta) = \sum_{i=0}^{k-1} a_i (\eta - \eta_0)_+^i . \tag{B.5}$$

Let us now consider an increasing sequence of points $\{\eta_i\}_{i=0}^{N_d}$, called *breakpoints*, such that

$$\eta_0 < \eta_1 < \eta_2 < \cdots < \eta_{N_d - 1} < \eta_{N_d} .$$

A piecewise polynomial (PP) function of order k for that given set of breakpoints is a function defined such that

$$f(\eta) \equiv P_i(\eta) \quad \text{if} \quad \eta \in]\eta_{i-1}, \eta_i[, \tag{B.6}$$

and $P_i(\eta) \in \mathbb{P}^k$. The set of all PP functions of order k for the given sequence of breakpoints $\{\eta_i\}$ will be noted $\mathbb{P}_\eta^k$. Before discussing the value of $f(\eta)$ at the breakpoints, let us consider first the "jump" of a function at a point, such that

$$\text{jump}_{\eta_0} f(\eta) \equiv f(\eta_0^+) - f(\eta_0^-) ,$$

where $\eta^+ = \lim_{\epsilon \to 0} \eta + \epsilon$ and $\eta^- = \lim_{\epsilon \to 0} \eta - \epsilon$. Continuity of a function at a point obviously requires that the jump at that point be 0. To the definition (B.6), we add a series of continuity conditions at the intermediary breakpoints $\{\eta_i\}_{i=1}^{N_d - 1}$, such that

$$\text{jump}_{\eta_i} D^{j-1} f = 0 \quad \text{for} \quad j = 1, 2, \ldots, \nu_i , \tag{B.7}$$

with $D^{j-1} f = d^{j-1} f / d\eta^{j-1}$. We can now restrict the PP space $\mathbb{P}_\eta^k$ with a set of continuity conditions (B.7) symbolized by the set of integers $\{\nu_i\}_{i=1}^{N_d - 1}$. The set of

all PP functions of order k on $\{\eta_i\}_{i=0}^{N_d}$, under the continuity constraints given by $\{\nu_i\}_{i=1}^{N_d-1}$, will be noted $\mathbb{P}_{\eta,\nu}^k$. Clearly $\mathbb{P}_{\eta,\nu}^k \subseteq \mathbb{P}_\eta^k$.

Let us now define the linear functional λ_{ij} and the function ϕ_{ij} such that

$$\lambda_{ij} f \equiv \begin{cases} D^j f(\eta_i) & ; \ i = 0 \\ \text{jump}_{\eta_i} D^j f & ; \ i = 1, \ldots, N_d - 1 \end{cases}$$

$$\phi_{ij} \equiv \begin{cases} (\eta - \eta_i)^j / j! & ; \ i = 0 \\ (\eta - \eta_i)_+^j / j! & ; \ i = 1, \ldots, N_d - 1 \end{cases}$$

for $j = 0, 1, \ldots, k-1$. We also note that $\phi_{ij} \in \mathbb{P}_\eta^k$ and that

$$\lambda_{ij} \phi_{pq} = \delta_{ip} \delta_{jq} ,$$

with δ_{ij} as the Kronecker delta. Consequently, the kN_d functions ϕ_{ij} are linearly independent and therefore form a basis for $\mathbb{P}_\eta^k$. A function $f \in \mathbb{P}_\eta^k$ has therefore a unique representation

$$f = \sum_i \sum_j (\lambda_{ij} f) \phi_{ij} ,$$

which is given in detailed form by

$$f(\eta) = \sum_{j=0}^{k-1} \frac{(\eta - \eta_0)^j}{j!} D^j f(\eta_0) + \sum_{i=1}^{N_d-1} \sum_{j=0}^{k-1} \frac{(\eta - \eta_i)_+^j}{j!} \left[\text{jump}_{\eta_i} D^j f(\eta_i)\right] . \quad \text{(B.8)}$$

By restricting the basis ϕ_{ij} with the continuity conditions (B.7), which can be directly applied in (B.8), it can be shown that the set

$$\phi_{ij} \quad \text{for} \quad j = \nu_i, \ldots, k-1 \ \text{and} \ i = 0, 1, \ldots, N_d ,$$

form a basis for the space $\mathbb{P}_{\eta,\nu}^k$, i.e., for every $f \in \mathbb{P}_{\eta,\nu}^k$ there is a unique representation

$$f = \sum_{i=0}^{N_d-1} \sum_{j=0}^{k-1} \alpha_{ij} \phi_{ij} . \quad \text{(B.9)}$$

Although of great theoretical interest, this result is not so easily applicable in practice because of the possible stiffness problems that may result from the use of the truncated power basis in numerical computations.

TABLE B.1. The divided difference table corresponding to (B.10).

t_1	$f(t_1)$					
		$[t_1, t_2]f$				
t_2	$f(\eta_2)$		$[t_1, t_2, t_3]f$			
		$[t_2, t_3]f$			$[t_1, \ldots, t_{n-1}]f$	
t_3	$f(t_3)$		$\vdots$	$\cdots$		$[t_1, \ldots, t_n]f$
$\vdots$	$\vdots$	$\vdots$			$[t_2, \ldots, t_n]f$	
t_{n-1}	$f(t_{n-1})$		$[t_{n-2}, t_{n-1}, t_n]f$			
		$[t_{n-1}, t_n]f$				
t_n	$f(t_n)$					

B.2 Generalized B-splines

The B-spline formulation, used here in its general sense, comes as an efficient and practical way of circumventing the stiffness problems associated with the truncated power basis described in the previous section.

Let us first begin by considering a new set of of non-decreasing points $\{ t_i \} \subseteq [\eta_0, \eta_{N_d}]$, called *knots*; the relation between the breakpoints and the knots will be specified only after the introduction of a few more definitions (see TABLE B.2). These knots are ordered so that the repeated points occur together, i.e., if $t_i = t_{i+r}$, then $t_i = t_{i+1} = \cdots = t_{i+r-1} = t_{i+r}$. Furthermore, let us also introduce the divided differences of f, noted $[t_i, \ldots, t_{i+r}]f$, and such that either $t_i = t_{i+r}$ and then

$$[t_i, \ldots, t_{i+r}]f = \frac{1}{r!} \frac{d^r f}{d\eta^r}\bigg|_{t_i} ,$$

or else $t_i \neq t_{i+r}$ and

$$[t_i, \ldots, t_{i+r}]f = \frac{[t_{i+1}, \ldots, t_{i+r}]f - [t_i, \ldots, t_{i+r-1}]f}{t_{i+r} - t_i} . \tag{B.10}$$

See TABLE B.1, for an example of the set of divided differences corresponding to (B.10).

TABLE B.2. Knot multiplicity according to the number of continuity conditions imposed at each breakpoint.

η_0	η_1	η_2	$\cdots$	η_{N_d-1}	η_{N_d}
$\nu_1 = 0$	ν_2	ν_3	$\cdots$	ν_{N_d-1}	$\nu_{N_d} = 0$
$k - \nu_1 = k$	$k - \nu_2$	$k - \nu_3$	$\cdots$	$k - \nu_{N_d-1}$	$k - \nu_{N_d} = k$
t_1	t_{k+1}	$t_{2k-\nu_2+1}$	$\cdots$	$\cdot$	t_{N_r+1}
$\vdots$	$\vdots$	$\vdots$		$\vdots$	$\vdots$
t_k	$t_{2k-\nu_2}$	$t_{3k-\nu_2-\nu_3}$	$\cdots$	t_{N_r}	t_{N_r+k}

The lth normalized (and generalized) B-spline of order k for the given knot sequence $\{ t_i \}$ is denoted by $B_{l,t}^{(k)}(\eta)$, and is defined by

$$B_{l,t}^{(k)}(\eta) \equiv (t_{l+k} - t_l)[t_l, \ldots, t_{l+k}](\cdot - \eta)_+^{k-1} , \quad \forall \eta \in \mathbb{R} . \tag{B.11}$$

The notation $(\cdot - \eta)_+^{k-1}$ is used to express that the kth ordered divided difference of $(t - \eta)_+^{k-1}$ is considered as a function of t alone, at a given fixed value of η. From (B.11), and the definition of the truncated power basis, we may see that the B-splines $B_l = B_{l,t}^{(k)}$ have a local support, viz.,

$$B_l(\eta) = 0 \quad \text{for} \quad \eta \notin [t_l, t_{l+k}] .$$

The notation B_l is used for short when the set $\{ t_i \}$, and the order k can be inferred from the context.

An important theorem, due to Curry & Schoenberg, states that for the previously defined set of breakpoints $\{ \eta_i \}_{i=0}^{N_d}$, and for the given set of non-negative integers $\{ \nu_i \}_{i=0}^{N_d}$ with $\nu_i \leq k$—from which the sequence of knots $\{ t_i \}_{i=1}^{N_r+k}$ is determined with the relations in TABLE B.2—the B-splines functions introduced in (B.11) form a *basis* for the PP space $\mathbb{P}_{\eta,\nu}^k$. Consequently, the dimension N_r of the resulting B-spline space is given by

$$N_r = k + \sum_{i=2}^{N_d} (k - \nu_i) = kN_d - \sum_{i=2}^{N_d} \nu_i = \dim \mathbb{P}_{\eta,\nu}^k , \tag{B.12}$$

where N_r is equal to the total number of piecewise polynomial coefficients minus the number of continuity conditions defined by the set of integers $\{ \nu_i \}$.

In a more technical description, the set of knots is equal to the set of breakpoints, in terms of values, with an additional possible redundancy of values according to the continuity level imposed at the breakpoint. The maximum number of continuity conditions that can be imposed at a breakpoint, without degeneracy, is $k-1$, as can be seen from TABLE B.2. In that case we obtain that $B_l \in C^{k-2}$, as it was considered for the development of the numerical method presented in Chap. 2.

The definition of B-splines given in (B.11) is also formulated in terms of the truncated power basis. As it was mentioned in the previous section this may lead to some stiffness problems. De Boor showed that the following recurrence relation (see the development in chapter X of his book)

$$B_l^{(k)}(\eta) = \frac{\eta - t_l}{t_{l+k-1} - t_l} B_l^{(k-1)}(\eta) + \frac{t_{l+k} - \eta}{t_{l+k} - t_{l+1}} B_{l+1}^{(k-1)}(\eta) , \tag{B.13}$$

with

$$B_l^{(1)}(\eta) = \begin{cases} 1 & ; \quad t_l \leq \eta < t_{l+1} \\ 0 & ; \quad \text{otherwise} \end{cases} , \tag{B.14}$$

does lead to the same result without the stiffness drawbacks.

Amongst the other important results that can be derive from the above definitions, we have that the B-spline basis form a partition of unity, viz.,

$$\sum_l B_l^{(k)} = 1 \quad \text{and} \quad \frac{d}{d\eta}\left(\sum_l B_l^{(k)}\right) = 0 .$$

Also, the derivative of a B-spline function of order k can be exactly represented by B-splines of order $k-1$ such that

$$\frac{d}{d\eta}\left(\sum_l \alpha_l B_l^{(k)}\right) = \sum_l (k-1)\frac{\alpha_l - \alpha_{l-1}}{t_{l+k-1} - t_l} B_l^{(k-1)} .$$

This last result can be used to determine each one of the k piecewise polynomials that form a B-spline. An example is given in FIG. B.1, in which we have represented the 4th order spline of FIG. 2.2 with its four constituting polynomials.

The B-spline projection of some function $f(\eta)$ can be done in various ways, here we use an integral-type projection in which the B-spline coefficients α_l can be determined

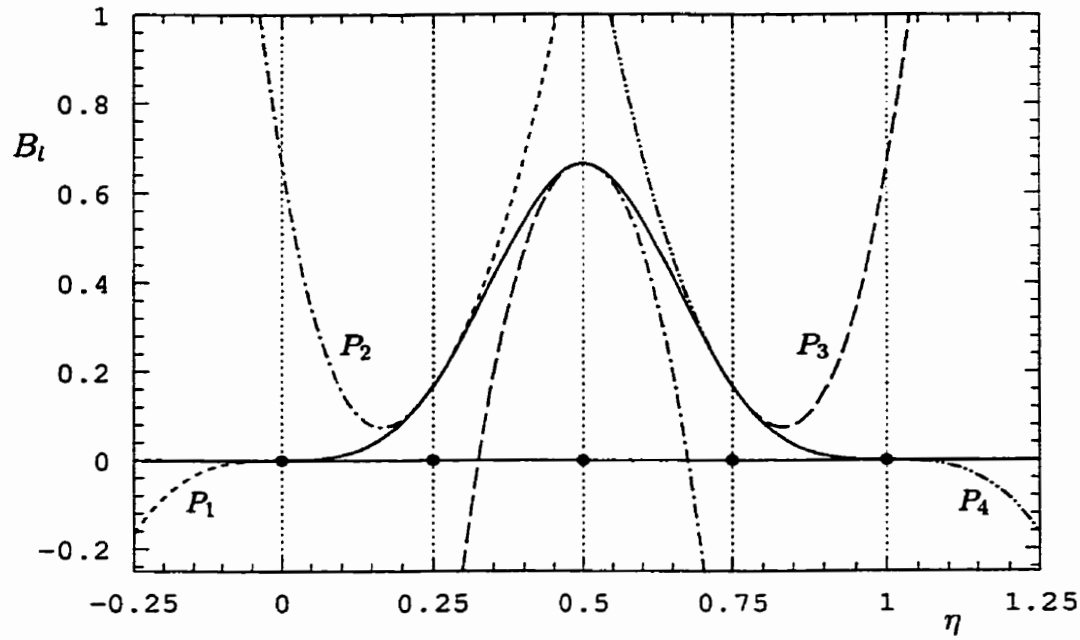

FIGURE B.1. The 4th order B-spline of FIG. 2.2 and its constituting polynomials P_i $(i = 1, \ldots, 4)$. The sub-domains that define the support of the B-spline are identified with the "•" symbols.

according to

$$\sum_l \alpha_l \int_{\eta_0}^{\eta_{N_d}} B_{l'} B_l \, d\eta = \int_{\eta_0}^{\eta_{N_d}} B_{l'} f(\eta) \, d\eta \, .$$

Furthermore, since the B-splines are formed from piecewise polynomials, we can use this property to decompose the domain integral into a sum of sub-domain integrals, such that

$$\int_{\eta_0}^{\eta_{N_d}} [\ldots] \, d\eta = \sum_{d=1}^{N_d} \int_{\eta_{d-1}}^{\eta_d} [\ldots]_d \, d\eta \, .$$

The integrand in each sub-domain being formed from polynomial expressions, the integrals can thus be evaluated numerically by some Gaussian-type quadrature (see also App. C). At the end, results an algebraic system of equations

$$[\mathsf{P}_{l'l}] \, \{\alpha_l\} = \{\mathsf{f}_{l'}\} \, ,$$

from which solution the spline coefficients are determined (see also App. D.5).

Appendix C

Matrices and Nonlinear Term

In this appendix, we include in the first part the detailed expressions related to the construction of the inertia and diffusion matrices introduced in Chap. 2, and also discussed in Sec. 3.3. In the second part of the appendix, we give the detailed form of the various expressions related to the computation of the nonlinear term, in complement of the discussion of Sec. 3.2. Some of the material presented here is redundant with what can be found in the report of Loulou et al. (1997). We have nevertheless chosen to include it here for ease of access, and also for self-containment reasons.

C.1 Inertia and diffusion matrices

The inertia and viscous matrices can be parametrically expressed in terms of purely radial matrices. Before giving their definition, let us first introduce the following notation:

$$\left[M^k_{i,j}\right]_{l',l} \equiv \int_0^\infty G^{(i)}_{l'}(r) G^{(j)}_l(r)\, r^k\, dr\ , \tag{C.1}$$

with $G^{(j)}_l = d^j\, G_l / dr^j$. We furthermore have

$$\frac{d^0\, G_l}{dr^0} \;=\; G_l(r(\eta)) \;=\; B_l(\eta)$$

$$\frac{d^1 G_l}{dr^1} = \frac{d\eta}{dr}\frac{d B_l}{d\eta} ,$$
$$\frac{d^2 G_l}{dr^2} = \frac{d^2\eta}{dr^2}\frac{d B_l}{d\eta} + \left(\frac{d\eta}{dr}\right)^2 \frac{d^2 B_l}{d\eta^2} ,$$

and so on. Whenever the context leaves no ambiguities, we will drop the variable dependence of the different functions to alleviate the notation. Replacing these values in (C.1), the matrix is now written in terms of the η coordinate only, such that

$$\left[M^k_{i,j}\right]_{l',l} = \int_0^1 G^{(i)}_{l'} G^{(j)}_l \; r^k \; \frac{dr}{d\eta} d\eta \; . \tag{C.2}$$

In the next step, we use the domain partition to write

$$\begin{aligned}\left[M^k_{i,j}\right]_{l',l} &= \sum_{q=1}^{N_d} \int_{\eta_q}^{\eta_{q+1}} G^{(i)}_{l'} G^{(j)}_l \; r^k \; \frac{dr}{d\eta} d\eta \\ &\approx \sum_{q=1}^{N_d} \left[\sum_{p=1}^{P_M} \left[G^{(i)}_{l'} G^{(j)}_l \; r^k \; \frac{dr}{d\eta} \right]_{\eta=\eta_p} \left(\frac{d\eta}{d\xi}\right)_q \; w_p \right] ,\end{aligned}$$

with for each q,

$$\eta_p = \left[\frac{\eta_{q+1} - \eta_q}{2}\right] \xi_p + \left[\frac{\eta_{q+1} + \eta_q}{2}\right] . \tag{C.3}$$

The ξ_p ($\in [-1, 1]$) and w_p are respectively the coordinates and weight factors for the Gauss-Legendre quadrature (for numerical values, see e.g., Abramowitz & Stegun (1964)). The number of integration points P_M is chosen, according to the order of the B-spline used, to approximate the integral as close as possible to machine accuracy.

We define two additional "boundary" matrices, namely

$$M_{B1} = G_{l'}(\eta = 1) G_l(\eta = 1) , \tag{C.4}$$
$$M_{B2} = G'_{l'}(\eta = 0) G'_l(\eta = 0) . \tag{C.5}$$

Consequently, these matrices will be non-zero only for $l' = l = N_r$ in the case of M_{B1} and l', $l \in \{1, 2\}$ for M_{B2}.

C.1.1 Inertia matrices

According do the definition of the inertia matrix in (2.44), for each modal family (see TABLE 2.1), we have:

- $k_z \neq 0,\ k_\theta > 0$

$$\begin{aligned}
\mathsf{A}_+^+ &= k_z^2\left[(k_\theta^2-1)M_{0,0}^1 + M_{1,1}^3 + M_{B1}\right]\\
\mathsf{A}_+^- &= k_z^2\left[(k_\theta+1)M_{0,0}^1 + M_{1,0}^2\right]\\
\mathsf{A}_-^- &= 2k_z^2 M_{0,0}^1 + (k_\theta-1)^2 M_{0,0}^{-1} + M_{1,1}^1\\
\mathsf{A}_-^+ &= k_z^2\left[(k_\theta+1)M_{0,0}^1 + M_{0,1}^2\right]
\end{aligned}$$

- $k_z = 0,\ k_\theta > 0$

$$\begin{aligned}
\mathsf{A}_+^+ &= (k_\theta^2-1)M_{0,0}^1 + M_{1,1}^3 + M_{B1}\\
\mathsf{A}_+^- &= 0\\
\mathsf{A}_-^- &= (k_\theta-1)^2 M_{0,0}^{-1} + M_{1,1}^1\\
\mathsf{A}_-^+ &= 0
\end{aligned}$$

- $k_z \neq 0,\ k_\theta = 0$

$$\begin{aligned}
\mathsf{A}_+^+ &= k_z^2 M_{0,0}^1\\
\mathsf{A}_+^- &= k_z^2 M_{0,0}^1\\
\mathsf{A}_-^- &= 2k_z^2 M_{0,0}^1 + M_{0,0}^{-1} + M_{1,1}^1\\
\mathsf{A}_-^+ &= k_z^2 M_{0,0}^1
\end{aligned}$$

- $k_z = 0,\ k_\theta = 0$

$$
\begin{aligned}
\mathsf{A}_{+}^{+} &= M_{0,0}^{1} \\
\mathsf{A}_{+}^{-} &= 0 \\
\mathsf{A}_{-}^{-} &= M_{0,0}^{-1} \\
\mathsf{A}_{-}^{+} &= 0
\end{aligned}
$$

C.1.2 Diffusion matrices

In a similar manner to what was done for the inertia matrix, the viscous matrix definition (2.45) gives us for each modal family (see TABLE 2.1):

- $k_z \neq 0,\ k_\theta > 0$

$$
\begin{aligned}
\mathsf{B}_{+}^{+} &= -\frac{k_z^2}{Re}\left[k_z^2\left[(k_\theta^2-1)M_{0,0}^{1}+M_{1,1}^{3}+M_{B1}\right]+(k_\theta^2-1)^2M_{0,0}^{-1}+\right. \\
&\qquad \left.(2k_\theta^2+1)M_{1,1}^{1}+M_{2,2}^{3}\right] \\
\mathsf{B}_{+}^{-} &= -\frac{k_z^2}{Re}\left[k_z^2\left[(k_\theta+1)M_{0,0}^{1}+M_{1,0}^{2}\right]+(k_\theta-1)^2\left[(k_\theta+1)M_{0,0}^{-1}+M_{1,0}^{0}\right]+\right. \\
&\qquad \left.(k_\theta+2)M_{1,1}^{1}+M_{2,1}^{2}\right] \\
\mathsf{B}_{-}^{-} &= -\frac{1}{Re}\left[2k_z^4M_{0,0}^{1}+(k_\theta^4-4k_\theta^3+2k_\theta^2+4k_\theta-3)(M_{0,0}^{-3}-M_{B2})+\right. \\
&\qquad \left.3k_z^2\left[(k_\theta-1)^2M_{0,0}^{-1}+M_{1,1}^{1}\right]+(2k_\theta^2-4k_\theta+3)M_{1,1}^{-1}+M_{2,2}^{1}\right] \\
\mathsf{B}_{-}^{+} &= -\frac{k_z^2}{Re}\left[k_z^2\left[(k_\theta+1)M_{0,0}^{1}+M_{0,1}^{2}\right]+(k_\theta-1)^2\left[(k_\theta+1)M_{0,0}^{-1}+M_{0,1}^{0}\right]+\right. \\
&\qquad \left.(k_\theta+2)M_{1,1}^{1}+M_{1,2}^{2}\right]
\end{aligned}
$$

- $k_z = 0,\ k_\theta > 0$

$$
\begin{aligned}
\mathsf{B}_+^+ &= -\frac{1}{Re}\left[(k_\theta - 1)^2 M_{0,0}^{-1} + (2k_\theta^2 + 1)M_{1,1}^1 + M_{2,2}^3\right] \\
\mathsf{B}_+^- &= 0 \\
\mathsf{B}_-^- &= -\frac{1}{Re}\left[(k_\theta^4 - 4k_\theta^3 + 2k_\theta^2 + 4k_\theta - 3)(M_{0,0}^{-3} - M_{B2}) + \right. \\
&\qquad \left. (2k_\theta^2 - 4k_\theta + 3)M_{1,1}^{-1} + M_{2,2}^1\right] \\
\mathsf{B}_-^+ &= 0
\end{aligned}
$$

- $k_z \neq 0,\ k_\theta = 0$

$$
\begin{aligned}
\mathsf{B}_+^+ &= -\frac{k_z^2}{Re}\left[k_z^2 k_z^2 M_{0,0}^1 + M_{0,0}^{-1} + M_{1,1}^1\right] \\
\mathsf{B}_+^- &= -\frac{k_z^2}{Re}\left[k_z^2 k_z^2 M_{0,0}^1 + M_{0,0}^{-1} + M_{1,1}^1\right] \\
\mathsf{B}_-^- &= -\frac{1}{Re}\left[2k_z^4 M_{0,0}^1 - 3(M_{0,0}^{-3} - M_{B2} - M_{1,1}^{-1}) + 3k_z^2(M_{0,0}^{-1} + M_{1,1}^1) + M_{2,2}^1\right] \\
\mathsf{B}_-^+ &= -\frac{k_z^2}{Re}\left[k_z^2 k_z^2 M_{0,0}^1 + M_{0,0}^{-1} + M_{1,1}^1\right]
\end{aligned}
$$

- $k_z = 0,\ k_\theta = 0$

$$
\begin{aligned}
\mathsf{B}_+^+ &= -\frac{1}{Re}\left[M_{0,0}^{-1} + M_{1,1}^1\right] \\
\mathsf{B}_+^- &= 0 \\
\mathsf{B}_-^- &= -\frac{1}{Re}\left[M_{1,1}^{-1} - M_{1,1}^{-3} + M_{B2}\right] \\
\mathsf{B}_-^+ &= 0
\end{aligned}
$$

C.2 Nonlinear term and related arrays

The computation of the nonlinear term $\{\mathsf{F}^{\pm}\}$ involves the evaluation of the integral (see (3.3))

$$\langle \mathbf{V}_j , \mathbf{F} \rangle \;=\; \frac{1}{L_\theta L_z} \int_0^{L_\theta} \int_0^{L_z} \int_0^{\infty} (\mathbf{V}_j)^* \cdot \mathbf{F}\; r\, dr d\theta dz \;,$$

which writes in long (see (3.5))

$$\begin{aligned} \frac{1}{L_\theta L_z} \iiint \mathbf{W}^{\pm\,*}_{l'm'n'}\, e^{-ik'_\theta \theta} e^{-ik'_z z} \cdot \Bigg[\sum_l \sum_m \sum_n \alpha^{\pm}_{lmn} \mathbf{W}^{\pm}_{lmn}\, e^{ik_\theta \theta} e^{ik_z z} \times \\ \nabla \times \left(\sum_{l_*} \sum_{m_*} \sum_{n_*} \alpha^{\pm}_{l_* m_* n_*} \mathbf{W}^{\pm}_{l_* m_* n_*}\, e^{ik_{\theta *} \theta} e^{ik_{z *} z} \right) \Bigg]\; r\, dr\, d\theta\, dz \;. \end{aligned} \tag{C.6}$$

for both "+" and "−" classes and for every indices l', m' and n'. The sequential evaluation of all sums and products can be simplified by proper reordering of the different terms.

Let us first consider the physical components of the vorticity and velocity vectors. From the vector functions in TABLE 2.1, we have

$$\omega_r(r,\theta,z,t) \;=\; a_l G_l(r) + b_l r G'_l(r) + c_l r^{-2} G_l(r) + d_l r^{-1} G_l(r) \;, \tag{C.7}$$

$$\omega_\theta(r,\theta,z,t) \;=\; e_l G_l(r) + f_l (r^{-1} G'_l(r) - r^{-2} G_l(r)) + g_l G''_l(r) \;, \tag{C.8}$$

$$\omega_z(r,\theta,z,t) \;=\; h_l r^{-1} G_l(r) + (m_l + 2j_l) G'_l(r) + j_l r G''_l(r) \;, \tag{C.9}$$

and

$$u_r(r,\theta,z,t) \;=\; k_l G_l(r) \;, \tag{C.10}$$

$$u_\theta(r,\theta,z,t) \;=\; j_l r G'_l(r) + m_l G_l(r) \;, \tag{C.11}$$

$$u_z(r,\theta,z,t) \;=\; -g_l G'_l(r) - f_l r^{-1} G_l(r) \;, \tag{C.12}$$

where it is understood that each component $a_l, b_l, \ldots$ is a function of θ, z and t, i.e., $a_l \equiv a_l(\theta,z,t)$, etc., and that summation over l is implied, i.e.,

$$a_l G_l(r) \equiv \sum_{l=1}^{N_r} a_l G_l(r) \;.$$

These are the detailed forms of the symbolic expressions introduced in (3.6) and (3.7). The Fourier transformed scalar components are given by

$$
\begin{aligned}
\widehat{a}_l &= -ik_z^2(\alpha^+_{l,m,n} + \alpha^-_{l,m,n}) \\
\widehat{b}_l &= \begin{cases} -ik_z^2\alpha^+_{lmn} \\ \quad 0 \qquad ; \quad k_\theta = 0 \end{cases} \\
\widehat{c}_l &= -ik_\theta(k_\theta - 1)\alpha^-_{lmn} \\
\widehat{d}_l &= -ik_\theta\alpha^-_{lmn} \\
\widehat{e}_l &= k_z^2(k_\theta\alpha^+_{lmn} + \alpha^-_{lmn}) \\
\widehat{f}_l &= (k_\theta - 1)\alpha^-_{lmn} \\
\widehat{g}_l &= \begin{cases} -\alpha^-_{lmn} \\ \quad 0 \qquad ; \quad k_\theta = k_z = 0 \end{cases} \\
\widehat{h}_l &= \begin{cases} k_z(1 - k_\theta)\left[(1 + k_\theta)\alpha^+_{lmn} + \alpha^-_{lmn}\right] \\ \qquad (1 - k_\theta^2)\alpha^+_{lmn} \qquad ; \quad k_z = 0 \end{cases} \\
\widehat{j}_l &= \begin{cases} k_z\alpha^+_{lmn} \\ \alpha^+_{lmn} \quad ; \quad k_z = 0 \text{ and } k_\theta > 0 \\ \quad 0 \qquad ; \quad k_\theta = 0 \end{cases} \\
\widehat{k}_l &= \begin{cases} -ik_z(k_\theta\alpha^+_{lmn} + \alpha^-_{lmn}) \\ \quad -ik_\theta\alpha^+_{lmn} \qquad ; \quad k_z = 0 \text{ and } k_\theta > 0 \\ \qquad 0 \qquad\qquad ; \quad k_z = k_\theta = 0 \end{cases} \\
\widehat{m}_l &= \begin{cases} k_z(\alpha^+_{lmn} + \alpha^-_{lmn}) \\ \quad \alpha^+_{lmn} \qquad ; \quad k_z = 0 \end{cases}
\end{aligned}
$$

for which we have implicitly assumed the variable dependence on t, k_θ and k_z, viz. $\alpha^-_{lmn} \equiv \alpha^-_{lmn}(t)$ and $\widehat{d}_l \equiv \widehat{d}_l(t; k_\theta, k_z)$.

Because the radial integration introduced in (3.12) involves only B-splines functions, it can be precomputed at once before entering into the time marching procedure. Recall that the related radial integrals involve triple products of B-splines having a generic definition in the form of

$$
\left[F^k_{i,j,s}\right]_{l',l,l_*} \equiv \int_0^\infty G^{(i)}_{l'}(r)G^{(j)}_{l}(r)G^{(s)}_{l_*}(r)\, r^k\, dr\ . \tag{C.13}
$$

The global topology of one such typical three-dimensional array is shown in FIG. C.1

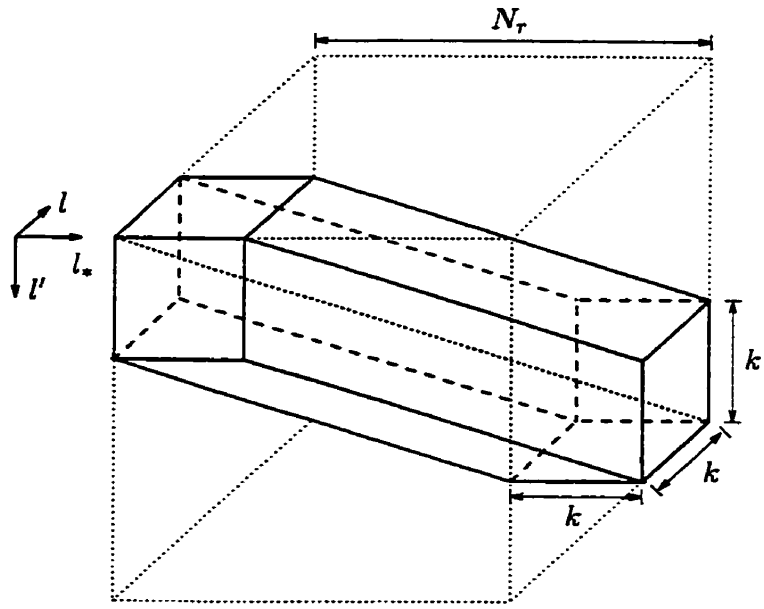

FIGURE C.1. Topology of a generic three-dimensional array $F^k_{i,j,s}$. The global cube is of dimension N_r. The non-zero entries are identified by the shaded volume. For a given value l', the two-dimensional array of non-zero entries associated with l_* and l is sketched in FIG. C.2.

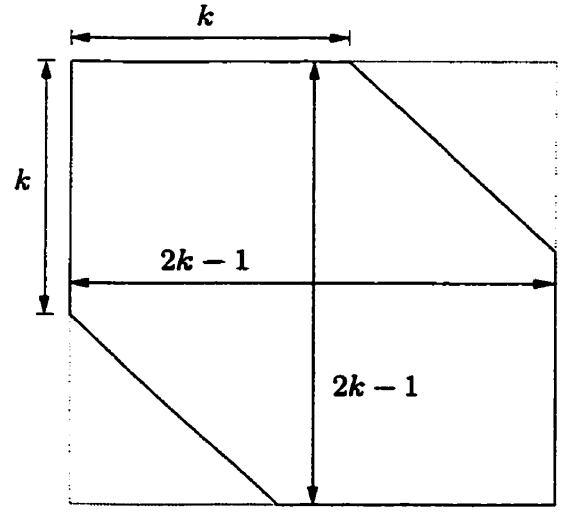

FIGURE C.2. A two-dimensional "cut", for a constant value of l' away from the edges, from the three-dimensional array shown in FIG. C.1. The non-zero entries, for the values of l_* and l, are represented by the shaded area.

and C.2. The numerical evaluation of the 22 resulting particular arrays is carried out according to the same procedure as for the $M^k_{i,j}$ matrices, but this time with a higher number P_F of integration points. The number P_F is chosen, according to the B-spline order, to bring the integration result to machine precision accuracy.

Now, the equivalent radial convolution sum, symbolized by (3.13), is detailed in the following expressions:

$$\begin{aligned}
\Pi_{l'} &= (e_{l.}f_l + h_{l.}m_l)F^0_{0,0,0} + (e_{l.}g_l + h_{l.}j_l)F^1_{0,1,0} + \\
&\quad (m_{l.} + 2j_{l.})(m_lF^1_{0,0,1} + j_lF^2_{0,1,1}) + \\
&\quad f_{l.}\left[f_l(F^{-1}_{0,0,1} - F^{-2}_{0,0,0}) + g_l(F^0_{0,1,1} - F^{-1}_{0,1,0})\right] + \\
&\quad g_{l.}(f_lF^0_{0,0,2} + g_lF^1_{0,1,2}) + j_{l.}(m_lF^2_{0,0,2} + j_lF^3_{0,1,2})
\end{aligned}$$

$$\begin{aligned}
\Upsilon^+_{l'} &= (a_{l.}m_l - e_{l.}k_l)F^0_{0,0,0} + (c_{l.}m_l + f_{l.}k_l)F^{-2}_{0,0,0} + a_{l.}j_lF^1_{0,1,0} + \\
&\quad c_{l.}j_lF^{-1}_{0,1,0} + d_{l.}j_lF^0_{0,1,1} - g_{l.}k_lF^0_{0,0,2} + b_{l.}(m_lF^1_{0,0,1} + j_lF^2_{0,1,1}) + \\
&\quad (d_{l.}m_l - f_{l.}k_l)F^{-1}_{0,0,1}
\end{aligned}$$

$$\begin{aligned}
\Upsilon^-_{l'} &= (a_{l.}m_l - e_{l.}k_l)F^1_{1,0,0} + (c_{l.}m_l + f_{l.}k_l)F^{-1}_{1,0,0} + a_{l.}j_lF^2_{1,1,0} + \\
&\quad c_{l.}j_lF^0_{1,1,0} + d_{l.}j_lF^1_{1,1,1} - g_{l.}k_lF^1_{1,0,2} + b_{l.}(m_lF^2_{1,0,1} + j_lF^3_{1,1,1}) + \\
&\quad (d_{l.}m_l - f_{l.}k_l)F^0_{1,0,1}
\end{aligned}$$

$$\begin{aligned}
\Phi^+_{l'} &= (a_{l.}f_l + h_{l.}k_l)F^0_{0,0,0} + a_{l.}g_lF^1_{0,1,0} + c_{l.}(f_lF^{-2}_{0,0,0} + g_lF^{-1}_{0,1,0}) + \\
&\quad b_{l.}g_lF^2_{0,1,1} + (b_{l.}f_l + m_{l.}k_l + 2j_{l.}k_lF^1_{0,0,1}) + \\
&\quad d_{l.}(f_lF^{-1}_{0,0,1} + g_lF^0_{0,1,1}) + j_{l.}k_lF^2_{0,0,2}
\end{aligned}$$

$$\begin{aligned}
\Phi^-_{l'} &= (a_{l.}f_l + h_{l.}k_l)F^1_{1,0,0} + a_{l.}g_lF^2_{1,1,0} + c_{l.}(f_lF^{-1}_{1,0,0} + g_lF^0_{1,1,0}) + \\
&\quad b_{l.}g_lF^3_{1,1,1} + (b_{l.}f_l + m_{l.}k_l + 2j_{l.}k_lF^2_{1,0,1}) + \\
&\quad d_{l.}(f_lF^0_{1,0,1} + g_lF^1_{1,1,1}) + j_{l.}k_lF^3_{1,0,2}
\end{aligned}$$

evaluated in the physical space. Note that in these last terms, the double summation

over the indices l and l_* is assumed, i.e.,

$$e_{l_*} f_l F^0_{0,0,0} \equiv \sum_{l_*=1}^{N_r} \sum_{l=1}^{N_r} e_{l_*} f_l \left[F^0_{0,0,0}\right]_{l',l,l_*} .$$

Finally, the nonlinear term is obtained, after the Fourier transforms, by the last following expressions:

$$\left\{\mathsf{F}^+\right\}_{l'} = \gamma_+(ik_\theta \widehat{\Pi}_{l'} - \widehat{\Phi}^+_{l'}) - \delta \widehat{\Phi}^-_{l'} , \tag{C.14}$$

$$\left\{\mathsf{F}^-\right\}_{l'} = \gamma_-(i\widehat{\Pi}_{l'} - \widehat{\Phi}^+_{l'}) + \chi_+ \widehat{\Upsilon}^+_{l'} - \chi_- \widehat{\Upsilon}^-_{l'} , \tag{C.15}$$

with

$$\gamma_+ = \begin{cases} k_z \\ 1 \quad ; \quad k_z = 0 \end{cases} \qquad \delta = \begin{cases} k_z \\ 1 \quad ; \quad k_z = 0 \text{ and } k_\theta > 0 \\ 0 \quad ; \quad k_\theta = 0 \end{cases}$$

$$\gamma_- = k_z \qquad \chi_+ = k_\theta - 1 \qquad \chi_- = \begin{cases} 1 \\ 0 \quad ; \quad k_z = k_\theta = 0 \end{cases}$$

Appendix D

Complementary Notes on Implementation

Thi appendix includes a series of miscellaneous topics related to the implementation considerations discussed in Chap. 3.

D.1 Time integration

The time integration scheme used was first presented by Spalart et al. (1991). We identify it here as the SMR (for Spalart, Moser and Rogers) scheme. Following the presentation done by Spalart et al., the scheme can be derived by considering the model equation

$$\frac{\partial \mathbf{u}}{\partial t} \;=\; L(\mathbf{u}) + N(\mathbf{u}) \;\equiv\; R(\mathbf{u}) \;. \tag{D.1}$$

The operator $L(\mathbf{u})$ stands for a general linear operator and $N(\mathbf{u})$ for a nonlinear one. The nonlinear operator can in turn be linearized by the following Taylor-type expansion

$$N(\mathbf{u}+\delta\mathbf{u}) \;=\; N(\mathbf{u}) \;+\; \mathcal{D}\delta\mathbf{u} \;+\; \frac{1}{2}\mathcal{E}\delta\mathbf{u}^2 \;+\; O\left(\delta\mathbf{u}^3\right) \;,$$

where

$$\mathcal{D} \;\equiv\; \left.\frac{\partial N}{\partial \mathbf{u}}\right|_{\mathbf{u}} \qquad , \qquad \mathcal{E} \;\equiv\; \left.\frac{\partial^2 N}{\partial \mathbf{u}^2}\right|_{\mathbf{u}} \;,$$

and are respectively linear and bilinear in $\delta\mathbf{u}$. For example, the linear operator $\mathcal{D}$ also appears in the generalized Newton-Raphson method, and the discrete version of $\mathcal{D}$ is associated with the so called "tangent" matrix (Zienkiewicz & Taylor, 1991).

Let us now consider the Taylor expansion in time of (D.1) around the point t such that

$$\mathbf{u}(t+\Delta t) = \mathbf{u} + \Delta t\frac{\partial \mathbf{u}}{\partial t} + \frac{\Delta t^2}{2}\frac{\partial^2 \mathbf{u}}{\partial t^2} + \frac{\Delta t^3}{6}\frac{\partial^3 \mathbf{u}}{\partial t^3} + O(\Delta t^4)\ . \tag{D.2}$$

After a few manipulations of the above definitions, it can be shown without much trouble that

$$\frac{\partial^2 \mathbf{u}}{\partial t^2} = [L+\mathcal{D}]R(\mathbf{u})$$

and that

$$\frac{\partial^3 \mathbf{u}}{\partial t^3} = [L+\mathcal{D}]^2 R(\mathbf{u}) + \mathcal{E}[R(\mathbf{u})]^2\ .$$

Replacing in (D.2) we obtain

$$\begin{aligned}\mathbf{u}(t+\Delta t) = \mathbf{u} + \Delta t R(\mathbf{u}) + \frac{\Delta t^2}{2}[L+\mathcal{D}](R(\mathbf{u})) + \\ \frac{\Delta t^3}{6}\left[[L+\mathcal{D}]^2(R(\mathbf{u})) + \mathcal{E}[R(\mathbf{u})]^2\right] + O(\Delta t^4)\ .\end{aligned} \tag{D.3}$$

A fully third order scheme in time should match this Taylor expansion exactly. Spalart et al. proposed a general scheme in the form of

$$\mathbf{u}_* = \mathbf{u}_n + \Delta t\left[L(\alpha_1\mathbf{u}_n + \beta_1\mathbf{u}_*) + \gamma_1 N(\mathbf{u}_n)\right]\ , \tag{D.4}$$

$$\mathbf{u}_{**} = \mathbf{u}_* + \Delta t\left[L(\alpha_2\mathbf{u}_* + \beta_2\mathbf{u}_{**}) + \gamma_2 N(\mathbf{u}_*) + \zeta_1 N(\mathbf{u}_n)\right]\ , \tag{D.5}$$

$$\mathbf{u}_{n+1} = \mathbf{u}_{**} + \Delta t\left[L(\alpha_3\mathbf{u}_{**} + \beta_3\mathbf{u}_{n+1}) + \gamma_3 N(\mathbf{u}_{**}) + \zeta_2 N(\mathbf{u}_*)\right]\ , \tag{D.6}$$

where the first substep amounts to a CN/BE[1] scheme but with modified coefficients. The other two substeps are in turn equivalent to modified CN/AB2[2] schemes. There are 11 coefficients but exact matching between (D.3) and (D.2) would require 17 equations. These equations can be obtained in a very straightforward but also very

[1]The "CN" stands for the Crank-Nicolson scheme while "BE" is for Backward Euler.

[2]Here, "AB2" is for the second order Adams-Bashforth scheme.

tedious manner by properly expanding (D.4)–(D.5) and equating with the correspondent terms in (D.3); a task well suited for a symbolic mathematics software such as MATHEMATICA. We do not write the full system of equations but rather a reduced one which is obtained after imposing the same time interval length for L and N such that

$$\alpha_1 + \beta_1 = \gamma_1 \quad ; \quad \alpha_2 + \beta_2 = \gamma_2 + \zeta_1 \quad ; \quad \alpha_3 + \beta_3 = \gamma_3 + \zeta_2 \tag{D.7}$$

hence leading to 8 equations for 8 unknowns. More Specifically, for 1st order:

$$\gamma_1 + \gamma_2 + \gamma_3 + \zeta_1 + \zeta_2 = 1 \tag{D.8}$$

for 2nd order

$$\gamma_3(\gamma_1 + \gamma_2 + \zeta_1) + \gamma_1(\zeta_2 + \gamma_2) = \frac{1}{2} \tag{D.9}$$

$$\begin{aligned} &\gamma_1\beta_1 + \gamma_1(\gamma_2 + \zeta_1) + (\gamma_2 + \zeta_1)\beta_2 + \\ &\quad (\gamma_3 + \zeta_2)(\gamma_1 + \gamma_2 + \zeta_1) + \beta_3(\gamma_3 + \zeta_2) = \frac{1}{2} \end{aligned} \tag{D.10}$$

and finally, for 3rd order

$$\gamma_1\gamma_2\gamma_3 = \frac{1}{6} \tag{D.11}$$

$$\gamma_1^2(\gamma_2 + \zeta_2) + \gamma_3(\gamma_1 + \zeta_1 + \gamma_2)^2 = \frac{1}{3} \tag{D.12}$$

$$\beta_3[\gamma_3(\gamma_1 + \gamma_2 + \zeta_1) + \gamma_1\zeta_2] + \gamma_1\gamma_2(\gamma_3 + \zeta_2) + \gamma_1\gamma_2\beta_2 = \frac{1}{6} \tag{D.13}$$

$$\gamma_3[\gamma_1\beta_1 + (\gamma_2 + \zeta_1)(\gamma_1 + \beta_2)] + \gamma_1\beta_1(\gamma_2 + \zeta_2) = \frac{1}{6} \tag{D.14}$$

$$\begin{aligned} &[(\gamma_1 + \beta_3 + \beta_2)(\zeta_1 + \gamma_2) + (\beta_3 + \beta_1)\gamma_1 + \beta_3^2]\zeta_2 + \\ &\quad [(\gamma_1 + \beta_3 + \beta_2)\gamma_3 + (\beta_3 + \beta_1)\gamma_1 + \beta_2^2]\zeta_1 + \\ &\quad\quad [(\gamma_1 + \beta_3 + \beta_2)\gamma_2 + (\beta_3 + \beta_1)\gamma_1 + \beta_3^2]\gamma_3 + \\ &\quad\quad\quad [(\beta_2 + \beta_1)\gamma_1 + \beta_2^2]\gamma_2 + \beta_1^2\gamma_1 = \frac{1}{6} \end{aligned} \tag{D.15}$$

This system of nonlinear equations (D.8)–(D.15) does not seem to have a unique "workable" solution. The authors still proposed the following set of coefficients:

$$\alpha_1 = \frac{29}{96} \qquad \beta_1 = \frac{37}{160} \qquad \gamma_1 = \frac{8}{15}$$

$$\alpha_2 = -\frac{3}{40} \qquad \beta_2 = \frac{5}{24} \qquad \gamma_2 = \frac{5}{12} \qquad \zeta_1 = -\frac{17}{60}$$

$$\alpha_3 = \frac{1}{6} \qquad \beta_3 = \frac{1}{6} \qquad \gamma_3 = \frac{3}{4} \qquad \zeta_2 = -\frac{5}{12}$$

which satisfy all but the last equation. In (D.15) the RHS term actually equals 119/640 which gives a mismatch of 37/1920 (≈ 0.0193). The resulting scheme is therefore of 3rd order on the convective and the mixed terms while being formally of 2nd order on the diffusive term.

The curve of the marginal stability of this scheme is shown next in FIG. D.1[3]. The curve is given in terms of the simple model equation

$$\frac{du}{dt} = \lambda u \,,$$

in which λ is complex. The imaginary part of the coefficient λ can be associated to some transport/convective term while the real part can be associated with some diffusive term. Note that in the asymptotic limit of very viscous problems, the scheme tends to unconditional stability (implicit integration of the diffusive term) so it will not close on the left. Furthermore, it crosses the imaginary axis at $\sqrt{3}$ and very slightly overboard in the positive region as for RK3 schemes (Canuto et al., 1988). Inviscid flow computations are theoretically stable but in the absence of any dissipation term, energy cascade to smaller structures can rapidly saturate the spatial resolution. Nonetheless, this allows for maintaining relatively large time steps even at moderate values of *Re* and therefore proves more advantageous than the CN/AB2 as will be seen in the comparison below. In practice, CFL numbers of 2 and possibly higher according to the value of the Reynolds number can be used.

Comparisons have been made between the SMR and the CN/AB2 schemes and are illustrated in the following figures. The results were obtained by considering the solution of a linear transport/diffusion equation (i.e., a linear version of the Burgers

[3]The data used to plot the curve were kindly provided by R. Brochu.

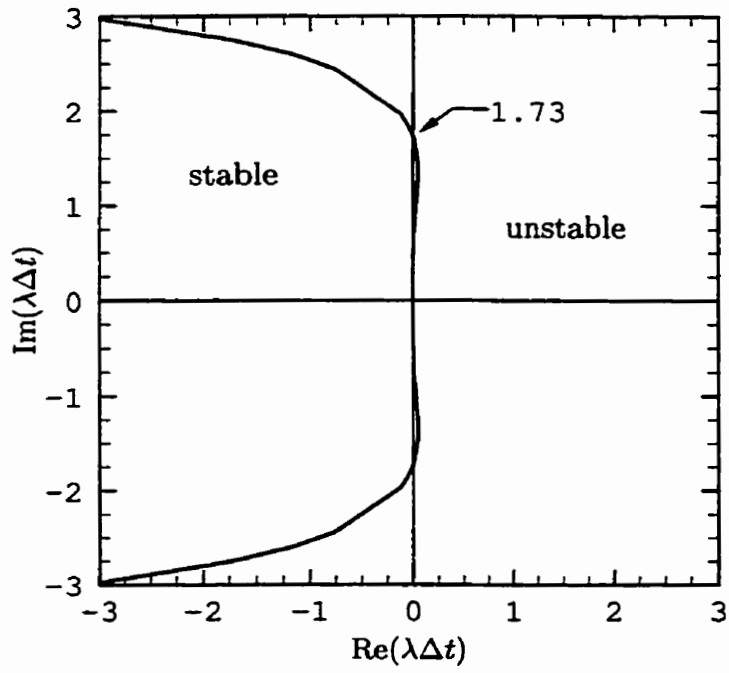

FIGURE D.1. Marginal stability curve for the SMR scheme. The scheme is stable in the region at the left of the curve.

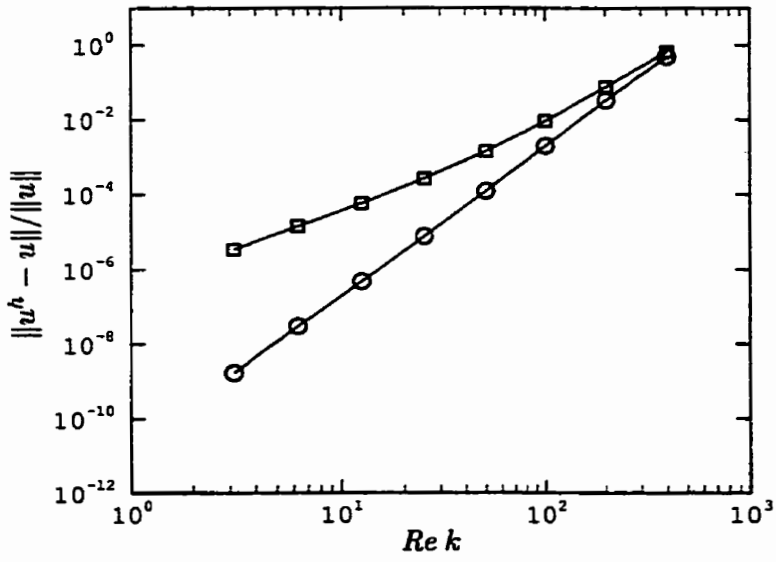

FIGURE D.2. Comparison or error between the CN/AB2 ("□" symbols) and the SMR ("o" symbols) schemes. The total solution error is computed in the physical space. See text for additional comments.

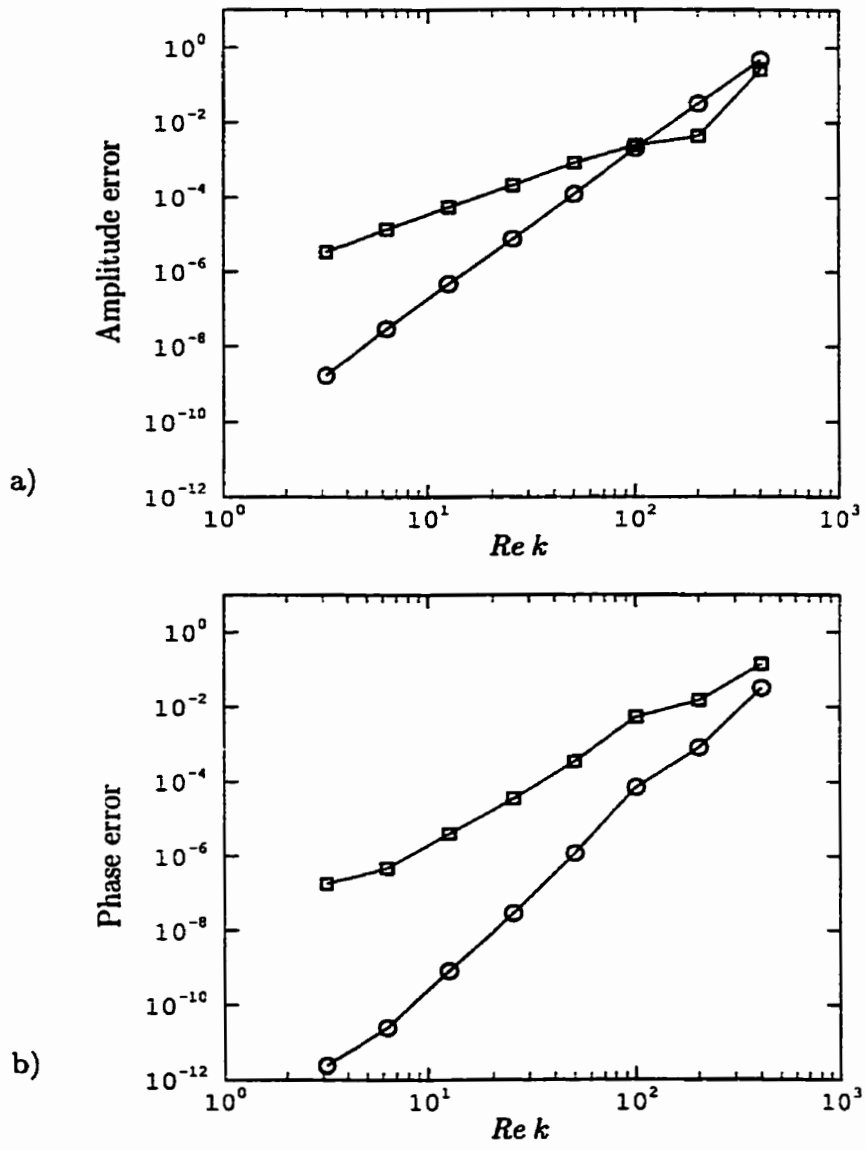

FIGURE D.3. Comparison or error between the CN/AB2 and the SMR schemes. The total solution error of FIG. D.2 has been decomposed in a) its amplitude component, and b) its phase component. These results are computed in the spectral space. The symbols are the same as in FIG. D.2.

equation). In terms of a non-dimensional wavenumber k and a Reynolds number Re, we show in FIG. D.2 the total solution error. In FIG. D.3 we show the decomposition of the solution error of FIG. D.2 in terms of its amplitude and its phase component.

D.2 Regularity conditions

In this section, we give the different expressions related to the imposition of the regularity conditions at $r = 0$. Again some of this material is redundant with what is presented in Loulou et al. (1997); the same considerations about ease of access and self-containment applies here too.

Note that the clever construction of vector functions of Loulou et al. allows form an identical implementation of conditions for both the + and − classes. This is one of the main factor for which we opted for these expansions rather than the ones of Leonard & Wray, for example.

Before discussing the direct implementation, recall some properties of the B-spline functions (results derived from App. B). More specifically, the partition of unity

$$\sum_{l=1}^{N_r} B_l(\eta) \;=\; 1\;. \tag{D.16}$$

Summation over any order of derivatives will obviously gives 0, i.e.,

$$\sum_{l=1}^{N_r} \frac{d^n}{d\eta^n} B_l(\eta) \;=\; 0\;, \tag{D.17}$$

for $0 < n < k$; for $n \geq k$, the result is trivial since $d^k B_l/d\eta^k = 0$ for all l.

The regularity conditions (2.11) are formulated in terms of the true radial coordinate r but can be considered in terms of η without loss of generality since the two coordinates coincide at $r = 0$ (the Jacobian is equal to 1). The regularity conditions can therefore be written

$$\sum_{l=1}^{N_r} \alpha^{\pm}_{lmn} B_l(\eta) \;\sim\; \eta^{k_\theta - 1} P(\eta^2)\;, \tag{D.18}$$

as $\eta \to 0$ and with $P(\eta^2)$ being a polynomial of the appropriate order (without the constant factor when $k_\theta = 0$). This parity condition is imposed by constraining the odd (even) derivatives to zero, at $\eta = 0$, for odd (even) values of k_θ.

The regularity conditions are imposed on a linear combination of weight vectors formed by

$$\widetilde{\mathbf{W}}_{l'}^{\pm} = \sum_{n=1}^{N_r} \beta_{nl'} \mathbf{W}_n^{\pm} , \tag{D.19}$$

such that $\widetilde{\mathbf{W}}_{l'}^{\pm}$ must be regular. This vectorial condition can again be directly brought down to the spline function level so that we now have

$$\sum_{n=1}^{N_r} \beta_{nl'} B_n(\eta) \sim \eta^{k_\theta - 1} P(\eta^2) . \tag{D.20}$$

Following the same principle as for the basis vectors, the proper linear combinations of weight vectors, satisfying the required conditions, can be determined by the following sets of equations:

- k_θ odd
  - k even

$$\begin{bmatrix} B_1' & B_2' & 0 & 0 & 0 & \cdots & 0 & 0 \\ B_1''' & B_2''' & B_3''' & B_4''' & 0 & \cdots & 0 & 0 \\ \vdots & \vdots & \vdots & \vdots & \vdots & \ddots & \vdots & \vdots \\ B_1^{(p)} & B_2^{(p)} & B_3^{(p)} & B_4^{(p)} & B_5^{(p)} & \cdots & B_q^{(p)} & 0 \end{bmatrix} \begin{bmatrix} 1 & 0 & \cdots & 0 \\ \beta_{11} & 0 & \cdots & 0 \\ 0 & 1 & \cdots & 0 \\ \beta_{12} & \beta_{21} & \cdots & 0 \\ 0 & 0 & \cdots & 0 \\ \vdots & \vdots & \ddots & \vdots \\ \beta_{1d} & \beta_{2(d-1)} & \cdots & 0 \\ 0 & 0 & \cdots & 1 \end{bmatrix} = [0] ; \tag{D.21}$$

- k odd

$$\begin{bmatrix} B_1' & B_2' & 0 & 0 & 0 & \cdots & 0 \\ B_1''' & B_2''' & B_3''' & B_4''' & 0 & \cdots & 0 \\ \vdots & \vdots & \vdots & \vdots & \vdots & \ddots & \vdots \\ B_1^{(p)} & B_2^{(p)} & B_3^{(p)} & B_4^{(p)} & B_5^{(p)} & \cdots & B_{q+1}^{(p)} \end{bmatrix} \begin{bmatrix} 1 & 0 & \cdots & 0 \\ \beta_{11} & 0 & \cdots & 0 \\ 0 & 1 & \cdots & 0 \\ \beta_{12} & \beta_{21} & \cdots & 0 \\ \vdots & \vdots & \ddots & \vdots \\ 0 & 0 & \cdots & 1 \\ \beta_{1d} & \beta_{2(d-1)} & \cdots & \beta_{d1} \end{bmatrix} = [0] \; ; \tag{D.22}$$

- k_θ even

  - k even

$$\begin{bmatrix} B_1 & 0 & 0 & 0 & 0 & \cdots & 0 \\ B_1'' & B_2'' & B_3'' & B_4'' & 0 & \cdots & 0 \\ \vdots & \vdots & \vdots & \vdots & \vdots & \ddots & \vdots \\ B_1^{(p)} & B_2^{(p)} & B_3^{(p)} & B_4^{(p)} & B_5^{(p)} & \cdots & B_{q+1}^{(p)} \end{bmatrix} \begin{bmatrix} 1 & 0 & \cdots & 0 \\ \beta_{11} & 0 & \cdots & 0 \\ 0 & 1 & \cdots & 0 \\ \beta_{12} & \beta_{21} & \cdots & 0 \\ \vdots & \vdots & \ddots & \vdots \\ 0 & 0 & \cdots & 1 \\ \beta_{1d} & \beta_{2(d-1)} & \cdots & \beta_{d1} \end{bmatrix} = [0] \; ; \tag{D.23}$$

  - k odd

$$\begin{bmatrix} B_1 & 0 & 0 & 0 & 0 & \cdots & 0 & 0 \\ B_1'' & B_2'' & B_3'' & B_4'' & 0 & \cdots & 0 & 0 \\ \vdots & \vdots & \vdots & \vdots & \vdots & \ddots & \vdots & \vdots \\ B_1^{(p)} & B_2^{(p)} & B_3^{(p)} & B_4^{(p)} & B_5^{(p)} & \cdots & B_q^{(p)} & 0 \end{bmatrix} \begin{bmatrix} 1 & 0 & \cdots & 0 \\ \beta_{11} & 0 & \cdots & 0 \\ 0 & 1 & \cdots & 0 \\ \beta_{12} & \beta_{21} & \cdots & 0 \\ 0 & 0 & \cdots & 0 \\ \vdots & \vdots & \ddots & \vdots \\ \beta_{1d} & \beta_{2(d-1)} & \cdots & 0 \\ 0 & 0 & \cdots & 1 \end{bmatrix} = [0] \; ; \tag{D.24}$$

Let us briefly consider an example on the system of equations

$$\mathsf{A}\,\alpha \;=\; b\,. \tag{D.25}$$

If we consider the particular case of $k_\theta = 1$, the for cubic B-splines ($k = 4$) the set of linear relations is determined by

$$\begin{bmatrix} B_1' & B_2' & 0 \end{bmatrix} \begin{bmatrix} 1 & 0 \\ \beta_{11} & 0 \\ 0 & 1 \end{bmatrix} \;=\; [0]\,. \tag{D.26}$$

In terms of the weight vectors, this gives

$$\begin{aligned} \widetilde{\mathbf{W}}_1 &= \mathbf{W}_1 + \beta_{11}\mathbf{W}_2\,, \\ \widetilde{\mathbf{W}}_3 &= \mathbf{W}_3\,, \end{aligned} \tag{D.27}$$

and results in a coupling relation for the first two lines of matrix A. More specifically, if the matrix is initially given by

$$\begin{bmatrix} a_{11} & a_{12} & a_{13} & a_{14} & 0 & 0 & \cdots \\ a_{21} & a_{22} & a_{23} & a_{24} & a_{25} & 0 & \cdots \\ a_{31} & a_{32} & a_{33} & a_{34} & a_{35} & a_{36} & \cdots \\ \vdots & \vdots & \vdots & \vdots & \vdots & \vdots & \ddots \end{bmatrix} \begin{Bmatrix} \alpha_1 \\ \alpha_2 \\ \alpha_3 \\ \vdots \end{Bmatrix} = \begin{Bmatrix} b_1 \\ b_2 \\ b_3 \\ \vdots \end{Bmatrix}, \tag{D.28}$$

applying the regularity conditions of the weight vectors gives the following modified matrix

$$\begin{bmatrix} \tilde{a}_{11} & \tilde{a}_{12} & \tilde{a}_{13} & \tilde{a}_{14} & \tilde{a}_{15} & 0 & \cdots \\ a_{21} & a_{22} & a_{23} & a_{24} & a_{25} & 0 & \cdots \\ \tilde{a}_{31} & \tilde{a}_{32} & \tilde{a}_{33} & \tilde{a}_{34} & \tilde{a}_{35} & \tilde{a}_{36} & \cdots \\ \vdots & \vdots & \vdots & \vdots & \vdots & \vdots & \ddots \end{bmatrix} \begin{Bmatrix} \alpha_1 \\ \alpha_2 \\ \alpha_3 \\ \vdots \end{Bmatrix} = \begin{Bmatrix} \tilde{b}_1 \\ b_2 \\ \tilde{b}_3 \\ \vdots \end{Bmatrix}, \tag{D.29}$$

where $\tilde{a}_{1j} = a_{1j} + \beta_{11}a_{2j}$ and $\tilde{b}_1 = b_1 + \beta_{11}b_2$. Now, because the second equation (line) is linearly dependent, it needs to be suppressed. In this case, we rather choose to replace it with the regularity condition of the B-spline coefficients α_l. Thus, we finally obtain

$$\begin{bmatrix} \tilde{a}_{11} & \tilde{a}_{12} & \tilde{a}_{13} & \tilde{a}_{14} & \tilde{a}_{15} & 0 & \cdots \\ B_1' & B_2' & 0 & 0 & 0 & 0 & \cdots \\ \tilde{a}_{31} & \tilde{a}_{32} & \tilde{a}_{33} & \tilde{a}_{34} & \tilde{a}_{35} & \tilde{a}_{36} & \cdots \\ \vdots & \vdots & \vdots & \vdots & \vdots & \vdots & \ddots \end{bmatrix} \begin{Bmatrix} \alpha_1 \\ \alpha_2 \\ \alpha_3 \\ \vdots \end{Bmatrix} = \begin{Bmatrix} \tilde{b}_1 \\ 0 \\ \tilde{b}_3 \\ \vdots \end{Bmatrix}. \tag{D.30}$$

An example of the modification that result from the application of the regularity conditions on the effective matrix, with $k = 3$, is shown in FIG. D.4.

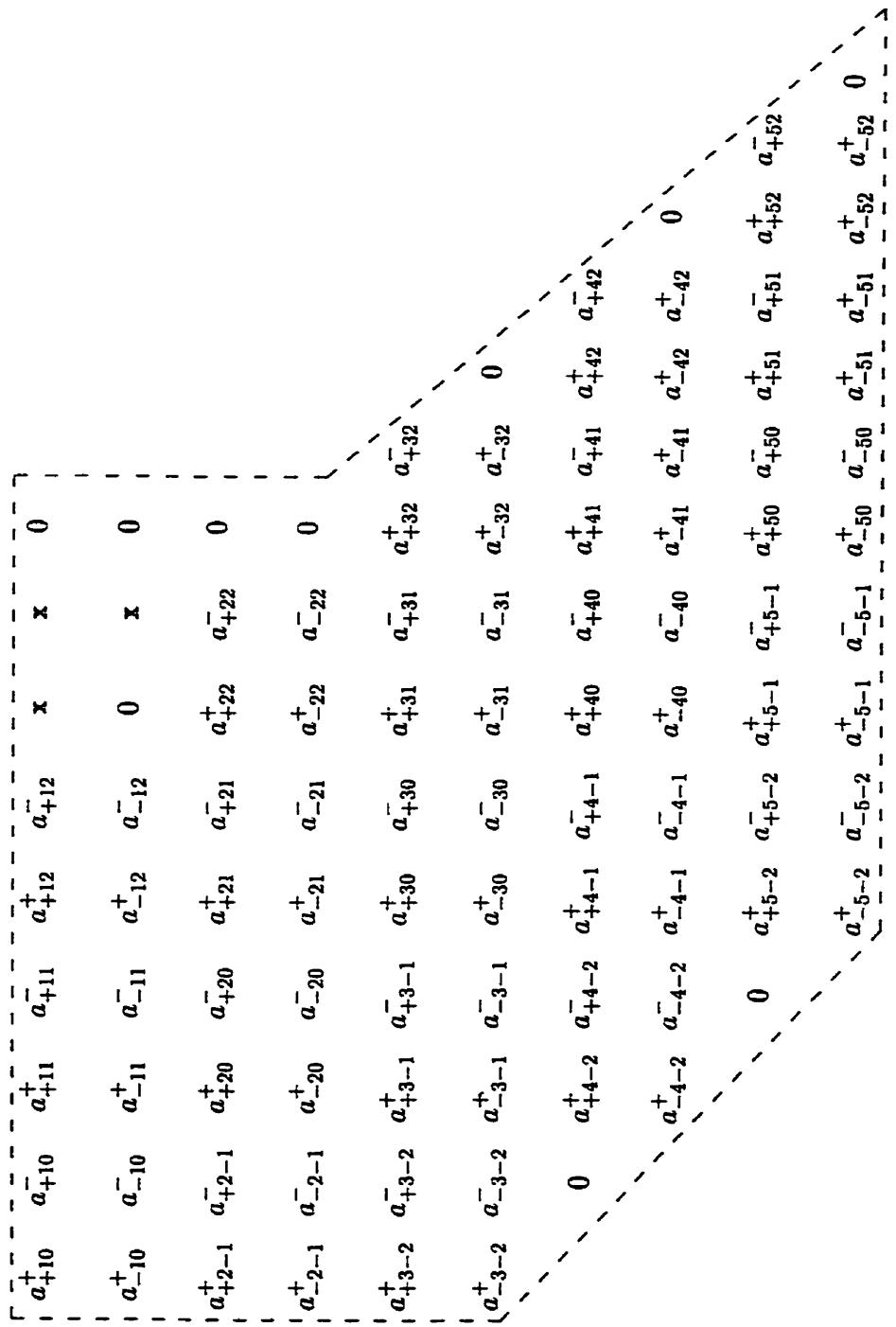

FIGURE D.4. Effective matrix head with proper reordering of the different coefficients according to the "+" and "−" classes. The example is for quadratic ($k = 3$) B-splines. The initially zero values that would be modified by the imposition of the regularity conditions are identified by an "x".

D.3 Boundary conditions

In this section we give a brief synthesis of the boundary conditions that need to be imposed in both the unbounded and the bounded cases. As it was already discussed in Chap. 3, the boundary conditions amount in all cases to the imposition of a series of zeros.

TABLE D.1. B-spline coefficients for the harmonic decaying boundary conditions of Ψ_l at $\eta = 1$. The conditions apply equally to $k_z = 0$ and $k_z \neq 0$.

	$k_\theta = 0$	$k_\theta > 0$
k_z	$\alpha^+_{N_r} = 0$ $\alpha^-_{N_r} = 0$	$\alpha^+_{N_r-k_\theta} = \cdots = \alpha^+_{N_r} = 0$ $\alpha^-_{N_r-k_\theta} = \cdots = \alpha^-_{N_r} = 0$

TABLE D.2. B-spline coefficients for the no-slip boundary conditions at $r = R_o$

	$k_\theta = 0$	$k_\theta > 0$
$k_z = 0$	$\alpha^+_{N_r} = 0$ $\alpha^-_{N_r} = 0$	$\alpha^+_{N_r-1} = \alpha^+_{N_r} = 0$ $\alpha^-_{N_r-1} = \alpha^-_{N_r} = 0$
$k_z \neq 0$	$\alpha^+_{N_r} = 0$ $\alpha^-_{N_r-1} = \alpha^-_{N_r} = 0$	$\alpha^+_{N_r-1} = \alpha^+_{N_r} = 0$ $\alpha^-_{N_r-1} = \alpha^-_{N_r} = 0$

D.4 Modal groups and FFT's

The modal groups discussed in this section come as a generalization of the modal zones presented in LMMC's report, and allow for an arbitrary variation of the azimuthal truncation in the radial direction. Because of the general character of this approach, an extension to include the variation of the longitudinal truncation N_z could relatively easily be made, but this would come with an extra price to pay in the computation of the nonlinear term.

In the first part of this section, a set formulation is used to present the modal groups, briefly introduced in Chap. 3. In the second part, we give some brief informations related to the FFT used for the computation of the nonlinear term.

D.4.1 Modal groups

We begin by the introduction of some definitions. First, a modal zone is defined as a (mapped) radial sub-interval $[\eta_i, \eta_{i+1}[$, with $\eta_i < \eta_{i+1}$ to which is assigned a given truncation N_θ. The B-spline breakpoints are a convenient choice for the η_i. More specifically, let us define a modal zone p as the interval $[\eta_{p-1}, \eta_p[$ with the corresponding zonal truncation $N_{\theta Z}^{(p)}$. Let us now introduce an associated set of zonal B-spline indices $I_{\eta Z}^{(p)} = \{ l_i \}$, such that

$$l_i \in I_{\eta Z}^{(p)} \quad \text{if} \quad \tau_{l_i} \in [\eta_{p-1}, \eta_p[\, .$$

An illustrative example of such a set will be given a little later on; as for the τ_{l_i}, they are the collocation points associated with the B-splines B_{l_i}. There is some arbitrariness in the choice of definition of the τ_l, as long as $\tau_l \in [t_l, t_{l+k}]$, here we use

$$\tau_l \;=\; \frac{1}{k-1} \sum_{j=1}^{k-1} t_{l+j} \, .$$

The set of all zonal sub-intervals $[\eta_{p-1}, \eta_p[$ form a partition of the radial domain, viz.,

$$\bigcup_i [\eta_{i-1}, \eta_i[= [0,1[\qquad \text{and} \qquad [\eta_{p-1}, \eta_p[\cap [\eta_{q-1}, \eta_q[= \emptyset \quad \text{if} \quad p \neq q \, ,$$

where $\emptyset$ is the empty set. Consequently the $I_{\eta Z}^{(p)}$ form a partition of the set of B-splines indices $I_\eta = \{ 1, 2, \ldots, N_r \}$, i.e.,

$$\bigcup_i I_{\eta Z}^{(i)} = I_\eta \qquad \text{and} \qquad I_{\eta Z}^{(p)} \cap I_{\eta Z}^{(q)} = \emptyset \quad \text{if} \quad p \neq q \, .$$

For computation purposes, instead of working with the modal zones we rather form *modal groups*. The qth modal group $I_{\theta G}^{(q)}$ is defined such that

$$I_{\theta G}^{(q)} = \bigcup_i I_{\eta Z}^{(i)} \qquad \text{with} \qquad N_\theta^{(i)} > N_{\theta G}^{(q)}$$

where $N_{\theta G}^{(q)}$ is the qth value of the set $N_{\theta G}$ of "distinct" truncation levels $N_{\theta Z}^{(i)} \in N_{\theta Z}$, in ascending order. More specifically, this gives $N_{\theta G}^{(i)} = N_{\theta Z}^{(j)}$ for some j, but $N_{\theta G}^{(i)} < N_{\theta G}^{(i+1)}$ (equal values of $N_{\theta Z}^{(j)}$ for different zones are considered as being the same for a group), and also with $N_{\theta G}^{(1)} = 0$.

Let us use an example to better illustrate the matter. Suppose that we have a radial discretization formed of 12 B-splines divided into 4 zones, with $N_{\theta Z} = \{ 4, 6, 8, 6 \}$. Suppose furthermore that the application of the collocation point criterion exposed above gives the following correspondence between the truncation levels $N_{\theta Z}^{(i)}$ and the B-spline indices l,

$$\begin{aligned}
&\text{Zone } 1: \quad N_{\theta Z}^{(1)} = 4 \, , \quad I_{\eta Z}^{(1)} = \{ 1, 2, 3, 4 \} \, ; \\
&\text{Zone } 2: \quad N_{\theta Z}^{(2)} = 6 \, , \quad I_{\eta Z}^{(2)} = \{ 4, 5, 6 \} \, ; \\
&\text{Zone } 3: \quad N_{\theta Z}^{(3)} = 8 \, , \quad I_{\eta Z}^{(3)} = \{ 7, 8 \} \, ; \\
&\text{Zone } 4: \quad N_{\theta Z}^{(4)} = 6 \, , \quad I_{\eta Z}^{(4)} = \{ 9, 10, 11, 12 \} \, .
\end{aligned}$$

From this, we start by constructing the set of ordered truncation levels such that $N_{\theta G} = \{ 0, 4, 6, 8 \}$. The 4 zonal sets $I_{\eta Z}^{(i)}$ will hence give 3 modal groups $I_{\theta G}^{(q)}$ (the 4th one being obviously an empty set), such that

$$I_{\theta G}^{(q)} = \bigcup_{i=1}^{4} I_{\eta Z}^{(i)} \qquad \text{with} \qquad N_\theta^{(i)} > N_{\theta G}^{(q)}$$

whence

$$\begin{aligned}
I_{\theta G}^{(1)} &= \{ 1, 2, 3, 4, 5, 6, 7, 8, 9, 10, 11, 12 \} \, , \\
I_{\theta G}^{(2)} &= \{ 4, 5, 6, 7, 8, 9, 10, 11, 12 \} \, , \\
I_{\theta G}^{(3)} &= \{ 7, 8 \} \, .
\end{aligned}$$

Now, because of the B-spline overlapping, when computing the FFT's related to the convolution sum in the nonlinear term (see Chap. 3), the "effective" modal groups must be extended with $k-1$ indices from higher to lower azimuthal resolution. Assuming that in the example above we have quadratic B-splines, this means extending the modal groups by two index values, such as to finally obtain

$$\begin{aligned} I_{\theta G}^{(1)} &= \{1,2,3,4,5,6,7,8,9,10,11,12\}, \\ I_{\theta G}^{(2)} &= \{2,3,4,5,6,7,8,9,10,11,12\}, \\ I_{\theta G}^{(3)} &= \{5,6,7,8,9,10\}. \end{aligned}$$

These modal groups are pre-organized in look-up tables for the code so that for each value of l', in TABLE 3.3, the dimension of the FFT's (line 1.(b) and 1.(d) in the table) are directly available.

D.4.2 FFT's and the collocation grid

The two-dimensional FFT introduced in Chap. 3 (Sec. 3.2) is carried out by two successive one-dimensional complex FFT's, from the FFTPACK library. The dimension N of each transform must be such that $N = 2^q 3^r 4^s 5^t$, or otherwise a "slow" DFT is used. Note also that since the transforms are executed on a collocation grid, the dimension N is therefore associated with the "de-aliased" truncation; the effective number of computational modes (N_θ or N_z) is thus determined by $\frac{2}{3}N$. In the implementation, the number of collocation modes is set independently of the number of computational modes so that partially, or even fully, aliased calculations may also be done.

D.5 Projection of the initial condition

The projection of the initial condition onto the spectral/B-spline space coefficients may be done from various types of field. In the following subsections, we give the different matrices required for projections from vorticity and velocity fields; the corresponding boundary conditions are also given. The stream function fields mention

in the last subsection apply for either axisymmetric or 2-D polar flows. In these latter cases, the projection is simply a standard B-spline integral projection (see Sec. B), and no boundary condition need be specified. In all cases, the initial field quantities are assumed to satisfy the regularity conditions near the point $r = 0$; no regularity conditions (Sec. D.2) are therefore imposed on the projection matrices.

D.5.1 Vorticity field

This initial condition projection is defined in terms of the vorticity $\boldsymbol{\omega}$. Because this vector field is divergence-free, only two components are required to completely defined it and consequently to define its projection onto the scalar spectral/B-splines space coefficients. Because of their appearance in the definition of most basic flows, we use the θ and z components. We then end up with an algebraic system of equations given by

$$\begin{aligned} \mathsf{V}_\theta^- \alpha^- + \mathsf{V}_\theta^+ \alpha^+ &= \widetilde{\omega}_\theta \ ; \\ \mathsf{V}_z^- \alpha^- + \mathsf{V}_z^+ \alpha^+ &= \widetilde{\omega}_z \ . \end{aligned} \tag{D.31}$$

The definition of the matrices and the RHS term depends on the type of projection used. We use here an integral projection such that

$$\widetilde{\omega}_\theta(l', k_\theta, k_z) = \int_0^\infty G_{l'}(r) \widehat{\omega}_\theta(r;\ k_\theta, k_z)\ dr \tag{D.32}$$

$$\widetilde{\omega}_z(l', k_\theta, k_z) = \int_0^\infty G_{l'}(r) \widehat{\omega}_z(r;\ k_\theta, k_z)\ dr \tag{D.33}$$

with the following set of matrices (see (C.1) for the definitions of the $M_{i,j}^k$ matrices), defined according to the different families of modes (see Sec. C.2):

1) (0, 0) mode

$$\begin{aligned} \mathsf{V}_\theta^- &= M_{0,0}^{-2} - M_{0,1}^{-1} \\ \mathsf{V}_\theta^+ &= 0 \\ \mathsf{V}_z^- &= 0 \\ \mathsf{V}_z^+ &= M_{0,0}^{-1} + M_{0,1}^{0} \end{aligned}$$

TABLE D.3. Outer boundary conditions for the vorticity projection: number of zeros imposed.

	V_θ^-	V_θ^+	V_z^-	V_z^+
$(0,0)$	1	n/a	n/a	1
$(k_\theta,0)$	2	n/a	n/a	2
$(0,k_z)$	2	n/a	1	1
(k_θ,k_z)	2	0	1	2

2) $(k_\theta,\,0)$ modes

$$\begin{aligned} V_\theta^- &= (k_\theta-1)[M_{0,0}^{-1}-M_{0,0}^{-2}]-M_{0,2}^0 \\ V_\theta^+ &= 0 \\ V_z^- &= 0 \\ V_z^+ &= (1-k_\theta^2)M_{0,0}^{-1}+3M_{0,1}^0+M_{0,2}^1 \end{aligned}$$

3) $(0,\,k_z)$ modes

$$\begin{aligned} V_\theta^- &= k_z^2M_{0,0}^0-M_{0,1}^{-1}+M_{0,0}^{-2}-M_{0,2}^0 \\ V_\theta^+ &= 0 \\ V_z^- &= k_z[M_{0,0}^{-1}+M_{0,1}^0] \\ V_z^+ &= k_z[M_{0,0}^{-1}+M_{0,1}^0] \end{aligned}$$

4) $(k_\theta,\,k_z)$ modes

$$\begin{aligned} V_\theta^- &= k_z^2M_{0,0}^{-1}+(k_\theta-1)[M_{0,1}^0-M_{0,0}^{-2}]-M_{0,2}^0 \\ V_\theta^+ &= k_z^2k_\theta M_{0,0}^{-1} \\ V_z^- &= k_z[M_{0,0}^{-1}+M_{0,1}^0] \\ V_z^+ &= k_z[(1-k_\theta^2)M_{0,0}^{-1}+3M_{0,1}^0+M_{0,2}^1] \end{aligned}$$

The integrals (D.32)–(D.33) are computed through a Gauss-Legendre quadrature. This requires that the Fourier-transformed components $\widehat{\omega}_\theta$, $\widehat{\omega}_z$ have to be stored for every quadrature points. The set of boundary conditions required to close the system of equations is outlined in TABLE D.3, above.

D.5.2 Velocity field

The initial conditions can be given in terms of the velocity vector components in a similar manner as for the vorticity. In this case the projection matrices are given by:

1) (0, 0) mode

$$\begin{aligned} \mathsf{U}_\theta^- &= 0 \\ \mathsf{U}_\theta^+ &= M_{0,0}^0 \\ \mathsf{U}_z^- &= M_{0,0}^{-1} \\ \mathsf{U}_z^+ &= 0 \end{aligned}$$

2) (k_θ, 0) modes

$$\begin{aligned} \mathsf{U}_\theta^- &= 0 \\ \mathsf{U}_\theta^+ &= M_{0,1}^1 + M_{0,0}^0 \\ \mathsf{U}_z^- &= M_{0,1}^0 + (1 - k_\theta) M_{0,0}^{-1} \\ \mathsf{U}_z^+ &= 0 \end{aligned}$$

3) (0, k_z) modes

$$\begin{aligned} \mathsf{U}_\theta^- &= k_z M_{0,0}^0 \\ \mathsf{U}_\theta^+ &= k_z M_{0,0}^0 \\ \mathsf{U}_z^- &= M_{0,1}^0 + M_{0,0}^{-1} \\ \mathsf{U}_z^+ &= 0 \end{aligned}$$

4) (k_θ, k_z) modes

$$\begin{aligned} \mathsf{U}_\theta^- &= k_z M_{0,0}^0 \\ \mathsf{U}_\theta^+ &= k_z [M_{0,1}^1 + M_{0,0}^0] \\ \mathsf{U}_z^- &= M_{0,1}^0 + (1 - k_\theta) M_{0,0}^{-1} \\ \mathsf{U}_z^+ &= 0 \end{aligned}$$

The boundary conditions corresponding to the velocity projection are given in TABLE D.4.

TABLE D.4. Outer boundary conditions for the velocity projection: number of zeros imposed.

	U_θ^-	U_θ^+	U_z^-	U_z^+
$(0,0)$	n/a	0	0	n/a
$(k_\theta,0)$	n/a	1	1	n/a
$(0,k_z)$	0	0	1	n/a
(k_θ,k_z)	0	1	1	n/a

D.5.3 Stream functions

The vector potentials $\mathbf{\Psi}_l^\pm$ used to construct the velocity vector expansions $\mathbf{W}_l^\pm$ cannot be directly linked, in general, to stream functions since $\widehat{\nabla\cdot}\mathbf{\Psi}_l^\pm \neq 0$. Stream function fields can nevertheless be used to define the initial condition, in the polar and axisymmetric cases, by making use of the following considerations.

For 2-D polar flows, there is a stream function $\psi_p(r,\theta)$ such that

$$u_r = \frac{1}{r}\frac{\partial \psi_p}{\partial \theta} \quad ; \quad u_\theta = -\frac{\partial \psi_p}{\partial r} .$$

For axisymmetric flows, there is a stream function $\psi_a(r,z)$ such that

$$u_r = -\frac{1}{r}\frac{\partial \psi_a}{\partial z} \quad ; \quad u_z = \frac{1}{r}\frac{\partial \psi_a}{\partial r} .$$

If we consider, for the axisymmetric case, a velocity vector $\mathbf{u}$ such that $\mathbf{u} = \nabla\times\psi_\theta\hat{\mathbf{e}}_\theta$, we then obtain $\psi_a = r\psi_\theta$. For the 2-D polar case, with $\mathbf{u} = \nabla\times\psi_z\hat{\mathbf{e}}_z$, we directly have $\psi_p = \psi_z$. Both ψ_θ and ψ_z can be used to define the the initial spline function coefficients. Note also that for the particular case where $k_\theta = k_z = 0$, we have

$$\psi_p = \psi_z = -\int_0^r u_\theta(\varrho)\, d\varrho ,$$

and

$$\psi_a = \int_0^r u_z(\varrho)\varrho\, d\varrho ,$$

or equivalently

$$\psi_\theta = \frac{1}{r}\int_0^r u_z(\varrho)\varrho\, d\varrho .$$

Without loss of generality, we may assume here that $\psi_z(0) = \psi_\theta(0) = 0$, to overcome the indeterminateness mentioned in TABLE 2.1.

D.6 Modal energy and growth rate value

Let us briefly look, in this section, at how we evaluate the instability growth rate values λ_r, used in Chap. 4, from the Navier-Stokes solutions. Taking advantage of the Galerkin formulation, we certainly may use of the following relation. For the radially integrated modal kinetic energy, defined by

$$E_{k_\theta,k_z} \equiv \frac{1}{2}\int_0^\infty \widehat{\mathbf{u}}^*(r;\ k_\theta,k_z)\cdot\widehat{\mathbf{u}}(r;\ k_\theta,k_z)\,r\,dr\ , \tag{D.34}$$

the integral can directly be expressed in terms of the $\alpha^{\pm}_{lmn}$ by

$$\int_0^\infty \widehat{\mathbf{u}}^*\cdot\widehat{\mathbf{u}}\,r\,dr \;=\; (\alpha^+)^*\left[\mathsf{A}^+_+\alpha^+ + \mathsf{A}^-_+\alpha^-\right] \;+\; (\alpha^-)^*\left[\mathsf{A}^-_-\alpha^- + \mathsf{A}^+_-\alpha^+\right]\ . \tag{D.35}$$

Furthermore, since

$$\widehat{\mathbf{u}}^*\cdot\frac{d\,\widehat{\mathbf{u}}}{dt} \;=\; \frac{d}{dt}\,\frac{1}{2}|\widehat{\mathbf{u}}|^2\ ,$$

we can also expressed the time derivative of the kinetic energy as (see (2.25))

$$\frac{d}{dt}E_{k_\theta,k_z} \;=\; (\alpha^+)^*\left[\mathsf{B}^+_+\alpha^+ + \mathsf{B}^-_+\alpha^- + \mathsf{F}^+\right] \;+\; (\alpha^-)^*\left[\mathsf{B}^-_-\alpha^- + \mathsf{B}^+_-\alpha^+ + \mathsf{F}^-\right]\ . \tag{D.36}$$

The instantaneous growth rate λ_r can then be obtained by combining (D.35) and (D.36) to give

$$\lambda_r \;=\; \frac{1}{E_{k_\theta,k_z}}\,\frac{d}{dt}E_{k_\theta,k_z}\ . \tag{D.37}$$

This is the procedure identified with the label "(I)" in Chap. 4.

When the modal energy E_{k_θ,k_z} is small (i.e., small values of $\alpha^{\pm}_{lmn}$), (D.36) may suffer from accuracy losses and the following first order estimate

$$\lambda_r(t_n) \;=\; \frac{\ln E_{k_\theta,k_z}(t_n) - \ln E_{k_\theta,k_z}(t_{n-1})}{2\Delta t} \;+\; \mathcal{O}(\Delta t) \tag{D.38}$$

may prove more reliable, provided that the time step Δt is small enough. This is method "(D)".

For sufficiently well resolved problems, both results should obviously tend to the same value. According to the particular case tested and the resolution used, an agreement to about five significant digits can be reasonably obtained. Such an agreement between the two values gives an indication of consistent resolution between the inertia, the viscous and nonlinear terms.

Let us simply end by noting the following relations for the "modally integrated" energies

$$E_{k_\theta} = \sum_{n=-N_z+1}^{N_z-1} E_{k_\theta,k_z} \qquad \text{and} \qquad E_{k_z} = \sum_{m=0}^{N_\theta-1} E_{k_\theta,k_z} \,. \tag{D.39}$$

Appendix E

Linear Stability of Poiseuille/Stokes Flow

In the first part of this appendix, we briefly review the analytical closed form solution of the stability of Stokes flow in a circular pipe. In the second part, we discuss the construction and partial validation of the linearized transport matrix $\widetilde{\mathsf{O}}$, introduced in Sec. 3.6, in the context of a uniform, axisymmetric base flow.

E.1 Eigensolutions for Stokes flow in a circular pipe

We provide here the analytical closed form solution of the Stokes eigenproblem for circular pipe flow, defined as the solution of

$$\lambda \mathbf{u} \;=\; -\nabla p \;+\; \frac{1}{Re}\nabla^2 \mathbf{u}\;, \tag{E.1}$$

with

$$\mathbf{u}(\mathbf{x},t) \;=\; \widehat{\mathbf{u}}(r)\, e^{i(k_\theta \theta + k_z z)}\, e^{\lambda t} \;+\; \text{c.c.}\;,$$

and $\mathbf{u} = \mathbf{0}$ at $r = R_o = 1$. The vector field $\mathbf{u}$ is always understood to be divergence-free.

The solution of (E.1), for $k_z \neq 0$, was given by Salwen & Grosch (1972) (see also

Loulou et al., 1997), as

$$\lambda_s = -\frac{1}{Re}\left(k_z^2 + \beta_s^2\right) , \tag{E.2}$$

with β_s being the sth root of

$$\beta\left[\frac{J'_{k_\theta}(\beta)}{J_{k_\theta}(\beta)}\right]\left[\frac{J'_{k_\theta}(\beta)}{\beta J_{k_\theta}(\beta)} + \frac{I'_{k_\theta}(k_z)}{k_z I_{k_\theta}(k_z)}\right] = \frac{k_\theta^2(k_z^2+\beta^2)}{k_z^2\beta^2} . \tag{E.3}$$

J_{k_θ} and I_{k_θ} are respectively the Bessel and the modified Bessel functions of the first kind of order k_θ (Abramowitz & Stegun, 1964). Note that here the Reynolds number in (E.2) is only present as a scaling factor for the eigenvalue λ_s. The corresponding eigensolutions are:

$$\widehat{u}_r^{(s)}(r;\ k_\theta,\ k_z) = k_z I'_{k_\theta}(k_z r) + \alpha_1 J_{k_\theta+1}(\beta_s r) - \alpha_2 J_{k_\theta-1}(\beta_s r) , \tag{E.4}$$

$$\widehat{u}_\theta^{(s)}(r;\ k_\theta,\ k_z) = \frac{k_z}{r} I_{k_\theta}(k_z r) - \alpha_1 J_{k_\theta+1}(\beta_s r) - \alpha_2 J_{k_\theta-1}(\beta_s r) , \tag{E.5}$$

and

$$\begin{aligned}\widehat{u}_z^{(s)}(r;\ k_\theta,\ k_z) = {} & k_z I_{k_\theta}(k_z r) + \\ & \frac{\alpha_1}{k_z}\left[\frac{k_\theta+1}{r} J_{k_\theta+1}(\beta_s r) + \beta_s J'_{k_\theta+1}(\beta_s r)\right] + \\ & \frac{\alpha_2}{k_z}\left[\frac{k_\theta-1}{r} J_{k_\theta-1}(\beta_s r) - \beta_s J'_{k_\theta-1}(\beta_s r)\right] .\end{aligned} \tag{E.6}$$

The constants α_1 and α_2 are respectively given by

$$\alpha_1 = \frac{k_\theta I_{k_\theta}(k_z) - k_z I'_{k_\theta}(k_z)}{2J_{k_\theta+1}(\beta_s)}$$

and

$$\alpha_2 = \frac{k_\theta I_{k_\theta}(k_z) + k_z I'_{k_\theta}(k_z)}{2J_{k_\theta-1}(\beta_s)} .$$

In the particular case of $k_\theta = 0$, we have

$$\widehat{u}_\theta^{(s)}(r;\ 0,\ k_z) = J_1(j_1^{(s)} r) , \tag{E.7}$$

with $j_n^{(s)}$ being the sth zero of J_n, i.e., $J_n(j_n^{(s)}) \equiv 0$.

Extension of these solutions to the particular case of $k_z = 0$, can be found in Loulou et al. (1997). Because of the uncoupling between the "+" and the "−" classes, two different sets of solutions are obtained, namely,

$$\lambda_s^+ = -\frac{[j_{k_\theta+1}^{(s)}]^2}{Re} \quad \text{and} \quad \lambda_s^- = -\frac{[j_{k_\theta}^{(s)}]^2}{Re} , \tag{E.8}$$

with

$$\widehat{u}_r^{(s)}(r;\, k_\theta,\, 0) = k_\theta r^{k_\theta-1} - k_\theta \frac{J_{k_\theta}(j_{k_\theta+1}^{(s)} r)}{r J_{k_\theta}(j_{k_\theta+1}^{(s)})} , \tag{E.9}$$

$$\widehat{u}_\theta^{(s)}(r;\, k_\theta,\, 0) = k_\theta r^{k_\theta-1} - j_{k_\theta+1}^{(s)} \frac{J'_{k_\theta}(j_{k_\theta+1}^{(s)} r)}{J_{k_\theta}(j_{k_\theta+1}^{(s)})} , \tag{E.10}$$

$$\widehat{u}_z^{(s)}(r;\, k_\theta,\, 0) = J_{k_\theta}(j_{k_\theta}^{(s)}) . \tag{E.11}$$

E.2 Eigenvalue solver

We present here some complementary informations related to the construction of the linearized transport matrix $\widetilde{\mathsf{O}}$ used in the eigenvalue solver introduced in Sec. 3.6. More specifically, we give the details of the different arrays that arise when considering an axisymmetric, uniform base flow field, i.e., for

$$\mathbf{U}(\mathbf{x}) = 0\,\hat{\mathbf{e}}_r + U_\theta(r)\,\hat{\mathbf{e}}_\theta + U_z(r)\,\hat{\mathbf{e}}_z . \tag{E.12}$$

Let us first decompose the general integral (3.30) in two parts such that

$$\mathsf{O}_\delta^\gamma = \mathsf{I}_\delta^\gamma + \mathsf{II}_\delta^\gamma , \tag{E.13}$$

and where

$$[\mathsf{I}_\delta^\gamma]_{l',l} = \int_0^\infty (\mathbf{W}_{l'}^\delta)^* \cdot \left(\mathbf{W}_l^\gamma \cdot \widehat{\nabla}\widehat{\mathbf{U}}\right) r\, dr , \tag{E.14}$$

and

$$[\mathsf{II}_\delta^\gamma]_{l',l} = \int_0^\infty (\mathbf{W}_{l'}^\delta)^* \cdot \left(\widehat{\mathbf{U}} \cdot \widehat{\nabla}\mathbf{W}_l^\gamma\right) r\, dr . \tag{E.15}$$

Here again δ and γ take the the values "+" and "−" according to the combination of vector expansions (see TABLE 2.1). Following the above notation, the different matrices O_δ^γ can be formulated, after replacing the various appropriate terms, by some parametric combinations of purely radial arrays, having the generic form

$$\left[N_{i,j,k}^{p,q} \right]_{l',l} \equiv \int_0^\infty G_{l'}^{(i)}(r)\, G_l^{(j)}(r)\, U_p^{(q)}(r)\, r^k\, dr \ , \tag{E.16}$$

with

$$U_p^{(q)} = \frac{d^q}{dr^q}\, \mathbf{U}(r) \cdot \hat{\mathbf{e}}_p \ .$$

A total of 20 arrays is required for the complete definition of all the terms in I_δ^γ and $\mathrm{II}_\delta^\gamma$. For each family of modal pairs k_θ, k_z, we obtain (using MATHEMATICA) the following specific expressions:

- $k_z \neq 0,\ k_\theta > 0$

$$\begin{aligned}
\mathrm{I}_+^+ &= -ik_z^2 k_\theta \left[(N_{0,0,0}^{\theta,0} + N_{0,0,1}^{\theta,1} + N_{0,1,1}^{\theta,0} + N_{1,0,2}^{\theta,1} \right] \\
\mathrm{I}_+^- &= -ik_z^2 \left[k_\theta N_{0,0,0}^{\theta,0} + N_{0,0,1}^{\theta,1} + N_{1,0,2}^{\theta,1} \right] \\
\mathrm{I}_-^+ &= -ik_z \left[k_\theta((1-k_\theta)N_{0,0,0}^{z,1} + N_{1,0,1}^{z,1}) + k_z(N_{0,0,0}^{\theta,0} + k_\theta N_{0,0,1}^{\theta,1} + N_{0,1,1}^{\theta,0}) \right] \\
\mathrm{I}_-^- &= -ik_z \left[(1-k_\theta)N_{0,0,0}^{z,1} + k_z(N_{0,0,0}^{\theta,0} + N_{0,0,1}^{\theta,1}) + N_{1,0,1}^{z,1} \right]
\end{aligned}$$

$$\begin{aligned}
\mathrm{II}_+^+ &= ik_z^2 \Big[k_\theta((k_\theta^2-1)N_{0,0,0}^{\theta,0} + N_{1,1,2}^{\theta,0}) + \\
&\qquad k_z((k_\theta^2+1)N_{0,0,1}^{z,0} + N_{0,1,2}^{z,0} + N_{1,0,2}^{z,0} + N_{1,1,3}^{z,0}) \Big] \\
\mathrm{II}_+^- &= ik_z^2 \left[(k_\theta-1)(N_{1,0,1}^{\theta,0} + (k_\theta+1)N_{0,0,0}^{\theta,0}) + k_z((k_\theta+1)N_{0,0,1}^{z,0} + N_{1,0,2}^{z,0}) \right] \\
\mathrm{II}_-^+ &= ik_z^2 \left[(k_\theta-1)((k_\theta+1)N_{0,0,0}^{\theta,0} + N_{0,1,1}^{\theta,0}) + k_z((k_\theta+1)N_{0,0,1}^{z,0} + N_{0,1,2}^{z,0}) \right] \\
\mathrm{II}_-^- &= i \Big[k_\theta((1-k_\theta)((1-k_\theta)N_{0,0,-2}^{\theta,0} + N_{0,1,-1}^{\theta,0} + N_{1,0,-1}^{\theta,0}) + N_{1,1,0}^{\theta,0}) + \\
&\qquad k_z((1-k_\theta)((1-k_\theta)N_{0,0,-1}^{z,0} + N_{0,1,0}^{z,0} + N_{1,0,0}^{z,0}) + \\
&\qquad N_{1,1,1}^{z,0} + 2k_z((k_\theta-1)N_{0,0,0}^{\theta,0} + k_z N_{0,0,1}^{z,0})) \Big]
\end{aligned}$$

- $k_z = 0,\ k_\theta > 0$

$$
\begin{aligned}
\mathsf{I}_+^+ &= -ik_\theta \left[N_{0,0,0}^{\theta,0} + N_{0,0,1}^{\theta,1} + N_{1,0,2}^{\theta,1} \right] \\
\mathsf{I}_+^- &= 0 \\
\mathsf{I}_-^+ &= ik_\theta \left[(k_\theta - 1) N_{0,0,0}^{z,1} - N_{1,0,1}^{z,1} \right] \\
\mathsf{I}_-^- &= 0
\end{aligned}
$$

$$
\begin{aligned}
\mathsf{II}_+^+ &= ik_\theta \left[(k_\theta^2 - 1) N_{0,0,0}^{\theta,0} + N_{1,1,2}^{\theta,0} \right] \\
\mathsf{II}_+^- &= 0 \\
\mathsf{II}_-^+ &= 0 \\
\mathsf{II}_-^- &= ik_\theta \left[(1 - k_\theta) N_{0,0,-2}^{\theta,0} + N_{0,1,-1}^{\theta,0} + N_{1,0,-1}^{\theta,0} + N_{1,1,0}^{\theta,0} \right]
\end{aligned}
$$

- $k_z \neq 0,\ k_\theta = 0$

$$
\begin{aligned}
\mathsf{I}_+^+ &= 0 \\
\mathsf{I}_+^- &= -ik_z^2 N_{0,0,1}^{\theta,1} \\
\mathsf{I}_-^+ &= -ik_z^2 N_{0,0,0}^{\theta,0} \\
\mathsf{I}_-^- &= -ik_z^2 \left[N_{0,0,0}^{\theta,0} + N_{0,0,1}^{\theta,1} + N_{0,0,0}^{z,1} + N_{1,0,1}^{z,1} \right]
\end{aligned}
$$

$$
\begin{aligned}
\mathsf{II}_+^+ &= ik_z^3 k_z N_{0,0,1}^{z,0} \\
\mathsf{II}_+^- &= ik_z^2 \left[k_z N_{0,0,1}^{z,0} - N_{0,0,0}^{\theta,0} \right] \\
\mathsf{II}_-^+ &= ik_z^2 \left[k_z N_{0,0,1}^{z,0} - N_{0,0,0}^{\theta,0} \right] \\
\mathsf{II}_-^- &= ik_z \left[N_{0,0,-1}^{z,0} + N_{0,1,0}^{z,0} + N_{1,0,0}^{z,0} + N_{1,1,1}^{z,0} + \right. \\
&\qquad \left. 2(k_z N_{0,0,1}^{z,0} - N_{0,0,0}^{\theta,0}) \right]
\end{aligned}
$$

TABLE E.1. Validation of the linearized transport matrix for a Poiseuille flow in a pipe at $Re = 9600$. The first eigenvalue for the (1,1) mode. Top results h-convergence with $k = 7$; bottom p-convergence with $N_r^* = 35$.

	$\lambda_1 \times 10^1$
N_r^*	
15	$-0.27416712598 - i\ 9.62134530607$
20	$-0.23148573319 - i\ 9.50489579729$
25	$-0.23170798840 - i\ 9.50481392765$
30	$-0.23170795895 - i\ 9.50481396363$
35	$-0.23170795764 - i\ 9.50481396669$
k	
3	$-0.22978913980 - i\ 9.50260578466$
4	$-0.23168978039 - i\ 9.50481730271$
5	$-0.23170786642 - i\ 9.50481424618$
6	$-0.23170796329 - i\ 9.50481396951$
7	$-0.23170795764 - i\ 9.50481396669$
LW†	$-0.23170795764 - i\ 9.50481396668$
SCG‡	$-0.2317 - i\ 9.5048$

† Leonard & Wray (1982): $N_r^* = 37$
‡ Salwen et al. (1980)

For the particular modal pair $k_\theta = 0$ and $k_z = 0$, all expressions are naturally zero. One may finally note that the radially bounded version of these expressions can be easily obtained by making use of the appropriate modifications discussed in Sec. 3.5.

The validation of the different expressions given above has been carried out for both the bounded and the unbounded formulations; the general results were presented in the different sections of Chap. 4. A more systematic algorithmic validation of the assembly of the effective matrices and other relevant technical procedures had nevertheless been previously undertaken by, among other things, comparisons with the benchmark data of Leonard & Wray (1982). These latter validations results are shown in TABLE E.1. The test was made for the first eigenvalue λ_1 with $k_\theta = 1$ and

$k_z = 1$ of a Poiseuille flow (i.e., with the bounded formulation of the code BOUNCYL-LS), where

$$\mathbf{U}(\mathbf{x}) \;=\; 0\,\hat{\mathbf{e}}_r \;+\; 0\,\hat{\mathbf{e}}_\theta \;+\; (1-r^2)\,\hat{\mathbf{e}}_z \;.$$

The Reynolds number considered—based on the centerline velocity and the pipe radius—was $Re = 9600$. The uniform B-spline discretization used is seen to compare quite well with the Jacobi method of Leonard & Wray.

Appendix F

Use of a Background Flow

The superposition of a background flow $\mathbf{u}_{\rm nh}$ to the homogeneous field $\mathbf{u}$ (the subscript "h" is implicitly assumed here) has been tested with the counter-rotating vortex pair problem. The initial basic flow is defined in terms of two counter-rotating Lamb-Oseen vortices, such that

$$\omega_z \;=\; \mathrm{G}(x-\frac{1}{2}\,,y\,;\,a) \;-\; \mathrm{G}(x+\frac{1}{2}\,,y\,;\,a)\;, \tag{F.1}$$

where

$$\mathrm{G}(x,y\,;\,a) \;=\; \frac{2}{a^2}\,\exp\left(-\frac{x^2+y^2}{a^2}\right)\;. \tag{F.2}$$

The parameter a is the characteristic length associated with the vortex core size; at a radius $r = a$, around the vortex center, the ratio of the partial to the total circulation of the vortex "tube" hence defined is 0.632. The dimensional length and velocity scales are respectively chosen as the vortices inner spacing $\bar{b}$ and the vortex pair self-induced velocity (in the filament limit $a \to 0$), i.e.,

$$\bar{L}_{\rm ref} \;=\; \bar{b} \quad \text{and} \quad \bar{U}_{\rm ref} \;=\; \frac{\bar{\Gamma}}{2\pi\bar{b}}\;.$$

The nondimensional circulation Γ of a single vortex is accordingly given by

$$\Gamma \;=\; \frac{\bar{\Gamma}}{\bar{U}_{\rm ref}\bar{L}_{\rm ref}} \;=\; 2\pi\;.$$

In FIG. F.1, we show iso-contours of vorticity for a vortex pair defined by (F.1), with $a = 0.1$; in FIG. F.2, we show the corresponding initial energy (E_{k_θ}) spectrum. Note that for simplicity, we limit here our considerations to 2-D polar flow fields.

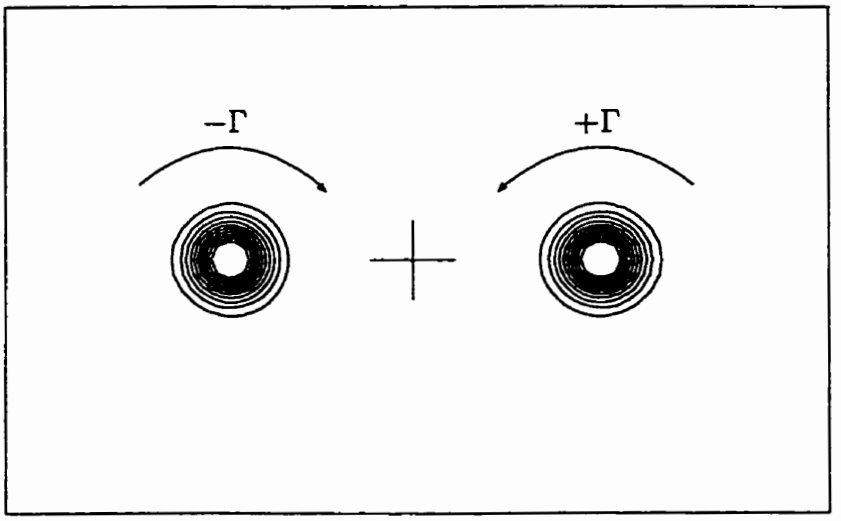

FIGURE F.1. Iso-vorticity contours for the initial counter-rotating vortex pair defined in (F.1), with $a = 0.1$. The contours are shown for $|\omega_z|_{\max} = 150$ with increments of $\Delta\omega_z = 15$ (the zero contour is skipped); the left and right vortices have respectively negative and positive vorticity, as indicated by the arrows. The cross indicates the center of the computational domain.

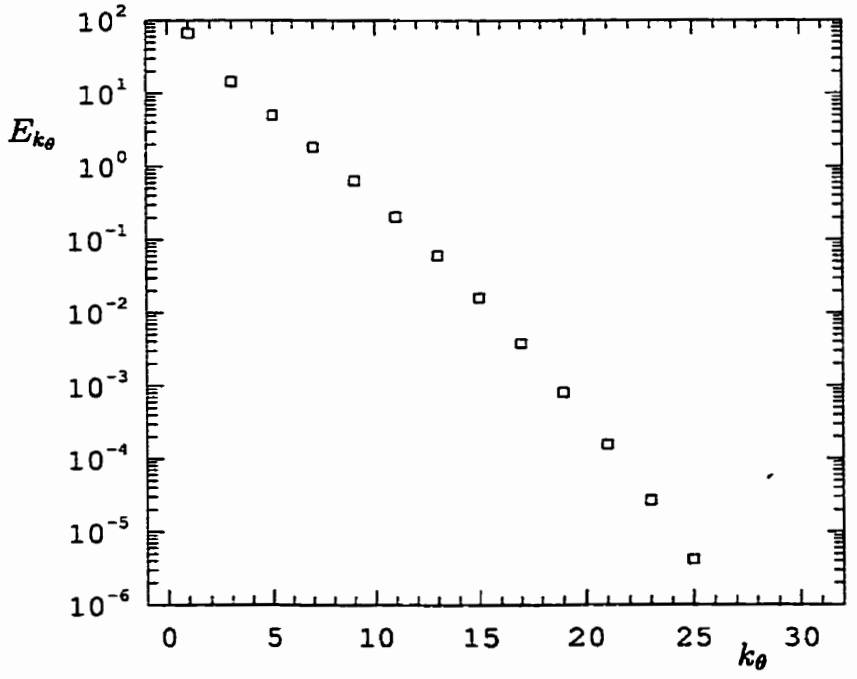

FIGURE F.2. Azimuthal energy spectrum corresponding to the flow field shown in FIG. F.1. One may note the "odd symmetry" in the distribution of modal energy; only odd value wavenumbers have a non-zero energy content.

The vortex pair shown in FIG. F.1 will naturally convect itself downward with with a velocity close to

$$u_y = \frac{\Gamma}{2\pi b} = 1 ,$$

since we can consider that $a = 0.1 \ll 1$. As a first step, we show the self-induced translation of the counter-rotating vortex pair, computed with the code UNCYL and using the following discretization:

- $N_r = 77$, $k = 4$, partially uniform distribution of breakpoints in η with
  4 points for $0 \leq \eta < 0.02$, 6 points for $0.02 \leq \eta < 0.08$,
  54 points for $0.08 \leq \eta < 0.55$, 6 points for $0.55 \leq \eta < 0.7$, and
  4 points for $0.7 \leq \eta \leq 1.0$,
  with $L = 1.5$;
- 6 modal zones ($L_\theta = 2\pi$) with
  $N_\theta = 4$ $(0 \leq \eta < 0.01)$, $N_\theta = 8$ $(0.01 \leq \eta < 0.03)$,
  $N_\theta = 16$ $(0.03 \leq \eta < 0.05)$, $N_\theta = 30$ $(0.05 \leq \eta < 0.5)$,
  $N_\theta = 16$ $(0.5 \leq \eta < 0.7)$, $N_\theta = 8$ $(0.7 \leq \eta < 1.0)$;
- CFL = 2.0 for which Δt varies according to the particular case considered (see details below).

The Reynolds number, based on an individual vortex circulation, was set to $Re = \bar{\Gamma}/\bar{\nu} = 6280$; the diffusive time scale is $T_\nu = 10$, based on the vortex core radius, while the convective time scale is $T_U = 1$, based on the reference length and the velocity scale.

In FIG. F.3, we show the vortex pair at $t = 0.5$; the corresponding energy spectrum is given in FIG. F.4. As the vortex pair moves away from the center of the computational domain (indicated by the "light" cross in FIG. F.3), the energy content shifts from lower to higher wavenumbers. For obvious practical reasons, one would wish to maintain the principal flow structures "stationary" in the computational domain. This can be achieved, in this case, by superposing an upward, uniform background flow $\mathbf{u}_{\rm nh}$, such that

$$\mathbf{u}_{\rm nh} = u_y \sin\theta\, \hat{\mathbf{e}}_r + u_y \cos\theta\, \hat{\mathbf{e}}_\theta . \qquad \text{(F.3)}$$

The only additional "extra forcing" that results from this procedure is $\mathbf{F_e} = \mathbf{u_{nh}} \times \boldsymbol{\omega}$ (see (3.4)).

The stationary vortex pair is illustrated in FIG. F.5 where a background flow (F.3) has been added with $u_y = 1$. The solution is shown at $t = 1.0$, and the pair has remained very close to its initial position. From the spectrum in FIG. F.6, we see that the initial "odd symmetry" is preserved, and the higher wavenumber structures have diffused. The appearance of energy in the lower even wavenumbers is associated with the deformation of the vortex cores. Each vortex induced velocity field, combined with the uniform flow translation, results in the generation of a straining field, centered at the adjacent vortex location. Vortices of finite core size will therefore deform under the action of this straining field. Note that the time scale associated with the straining field is $T_\epsilon = 2\pi b^2/\Gamma = 1$, i.e., of the same order as the time at which the solution is shown. Supporting the observation that the even wavenumbers are directly associated with the vortex core deformation, is the Stokes flow solution shown in FIG. F.7 and F.8. In that latter case, each vortex tube diffuses independently of the other and remain circular. The comparison of both spectra (FIG. F.6 and F.8), in which the energy content of the odd wavenumbers is practically identical, thus confirms the observation.

All the computations shown here were carried out with a time step size criterion of CFL = 2.0. According to the particular case treated, this resulted in different values of Δt, that we consider in what follows. First, since the velocities are important near the center of the domain, the use of modal reduction to alleviate the time step size (see Sec. 3.4) is of critical importance here. For example, a single zone (with $N_\theta = 30$) for the computation shown in FIG. F.5 would have required that $\Delta t \approx 2. \times 10^{-4}$ whereas the present multi-zone discretization gives $\Delta t \approx 1.1 \times 10^{-3}$, a factor 5 difference. For the free vortex pair in FIG. F.3, the initial time step size (with the same multi-zone discretization) was $\Delta t \approx 8. \times 10^{-4}$. This is because the use of an upward background flow reduces the effective velocity near the center, where the CFL constraint is highest, and higher velocities are therefore encountered in the absence of the background flow. On the other hand, as the free vortices move away from the center, so do the important velocities. The time step size is thus relaxed to $\Delta t \approx 1.4 \times 10^{-3}$ for the displaced vortex pair shown in FIG. F.3, at $t = 0.5$.

This brings us to our second point, which is seeking a compromise between the spatial and the temporal resolutions, leading to a globally more efficient computation for this test case. A comparison between the two spectra in FIG. F.3 and F.5 show that for a given cut-off energy level, $E_{k_\theta} = 10^{-5}$ say, the displaced pair requires about 3/2 more computational modes than the centered pair. Adding the upward background flow $u_y = 1$ to the displaced pair of FIG. F.3 however relaxes the time step size to a value of $\Delta t \approx 3.3 \times 10^{-3}$; a factor 3 compared to the centered pair computation that also includes the background flow. If one recalls that the computation of the nonlinear term—the most demanding part of the calculation—scales with $\mathcal{O}(N_\theta \log N_\theta)$, then the 3/2 factor just mentioned above can be transformed into an increment of approximately 1.7 in the computational effort (keeping the same radial and temporal discretizations). On the other hand, the factor 3 on the time step size directly translates into a saving of a factor 3. Thus, in this case it is more advantageous to compute the vortex pair (with the background flow) in its displaced position rather than its centered one: a reduction factor of about $3/1.7 = 1.8$ in the CPU cost.

The evolution of the displaced vortex pair of FIG. F.3, from $t = 0.5$ to $t = 1.0$, with this time the addition of the background flow $u_y = 1$, is shown in FIG. F.9 and F.10. It may be noted that this new $t = 1.0$ solution could have also been obtained by directly offsetting the vortex pair in the initial condition (F.1). As a last comment, let us only say that the most "efficient" combination of spatial and temporal resolution, for a given problem, depends on many factors, and it is in this author's opinion that some "heuristic" approach remains inevitable, at one point or another, to find this best compromise.

We conclude this appendix by showing the results of a displaced and a stationary vortex pair with $a = 0.2$; all the other parameters remain equal. The results are respectively given in FIG. F.11 and F.12; and in FIG. F.13 and F.14. In this case, the viscous time scale becomes $T_\nu = 40$. Also, because the vortices are bigger, the deformation effects are more apparent, and the departure from the asymptotic self-induced velocity $u_y = 1$ can be felt, although only slightly for the solution time shown.

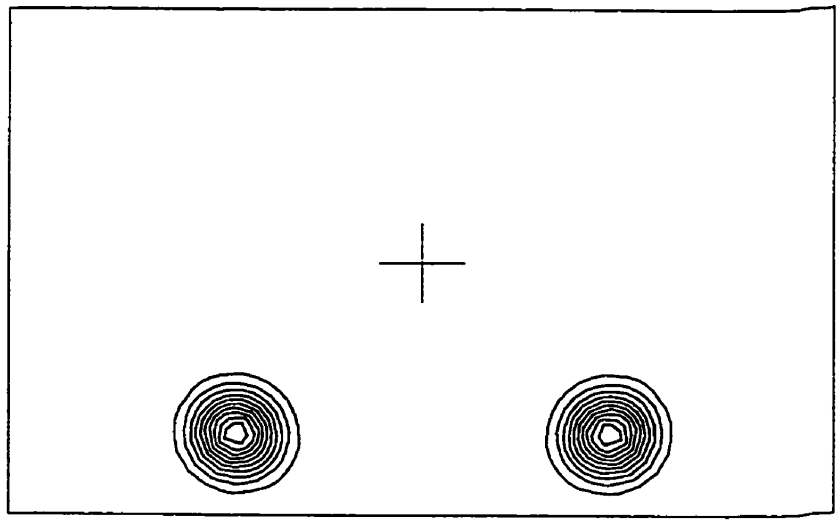

FIGURE F.3. The vortex pair of FIG. F.1 shown at $t = 0.5$, with the same iso-vorticity contours. After that short time, the vortex cores have only partially diffused, but the pair has moved downward, as a whole, with a distance of $t \times u_y = 0.5$. See the corresponding energy spectrum in FIG. F.4.

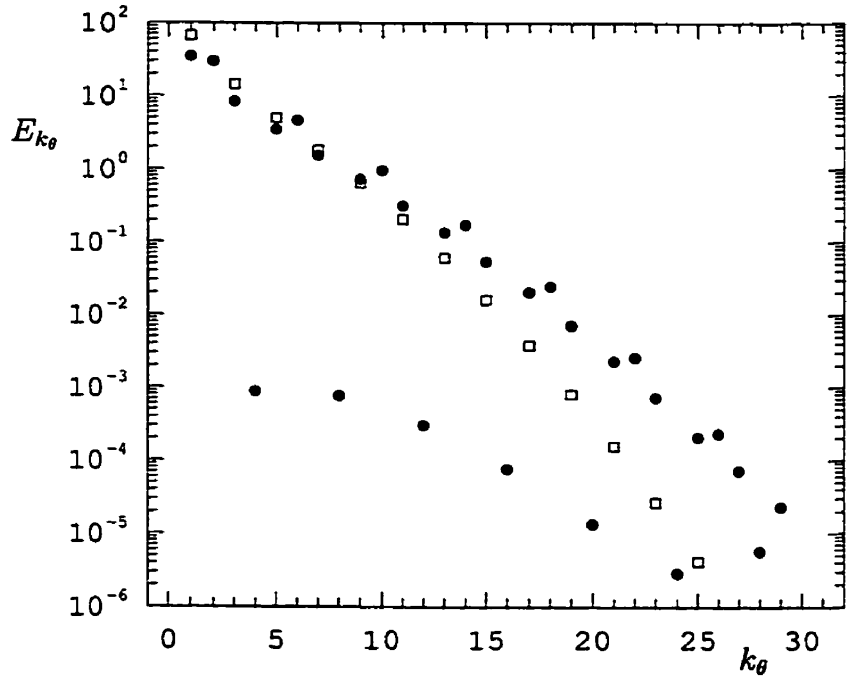

FIGURE F.4. The energy spectrum corresponding to the $t = 0.5$ solution shown in FIG. F.3 (the "•" symbols). The initial spectrum of FIG. F.2 is also shown as a reference (the "□" symbols). The initial "odd symmetry" is lost, and as the vortices move away from the center of the computational domain, the modal energy shifts towards higher wavenumbers.

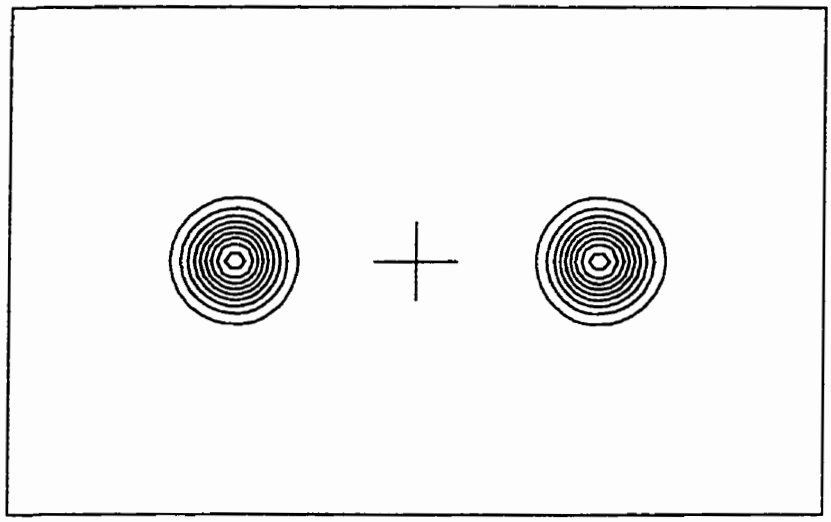

FIGURE F.5. The vortex pair of FIG. F.1 shown at $t = 1.0$, with the same iso-vorticity contours. The addition of a uniform, upward background flow $u_y = 1.0$ maintains the vortex pair close to its initial position. The slight diffusion acting on the vortex cores has the effect, here, to relax the resolution requirement, as can be seen from the corresponding spectrum shown below.

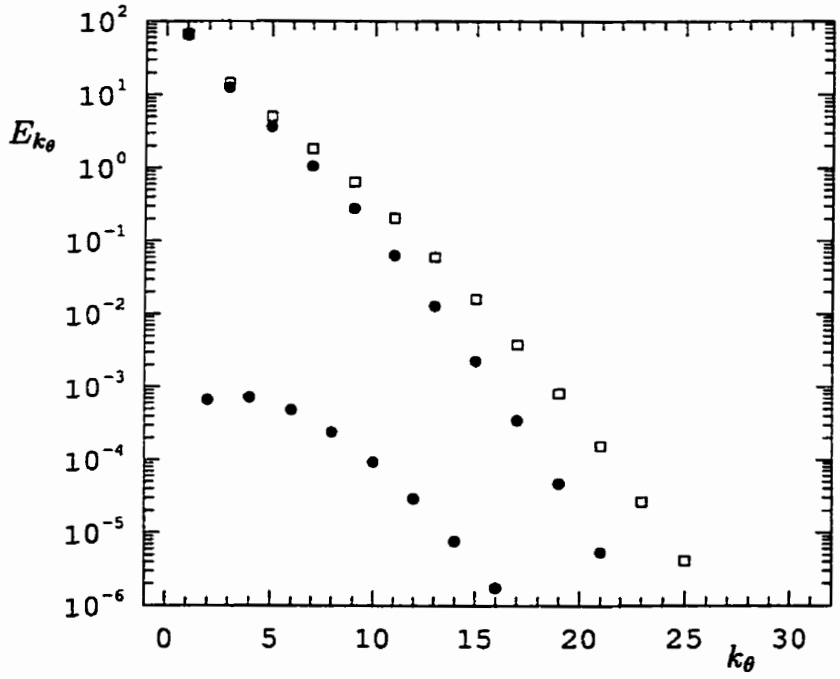

FIGURE F.6. The energy spectrum corresponding to the $t = 1.0$ solution shown in FIG. F.5 (the "•" symbols); the "□" symbols are for the initial spectrum. The diffusion reduces the energy content at higher odd wavenumbers, but the deformation of the vortex cores gives rise to the energy content of the even wavenumbers. Compare with the purely diffusive case shown in FIG. F.8.

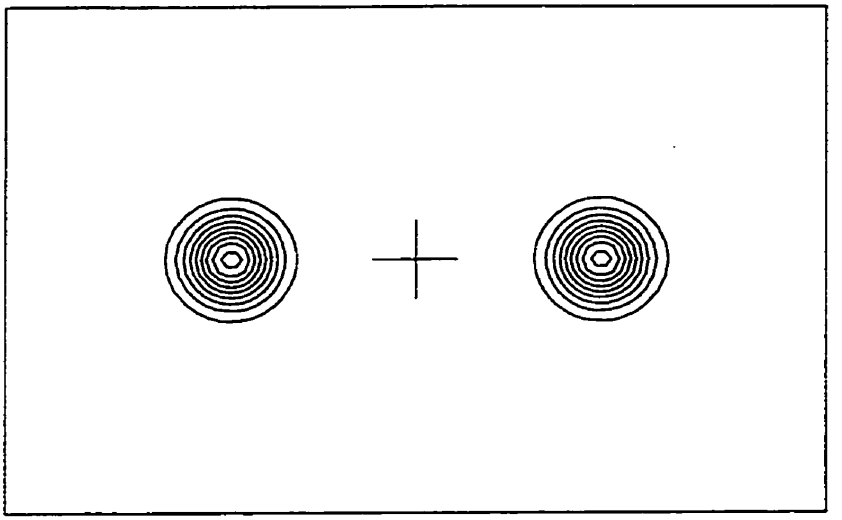

FIGURE F.7. The vortex pair of FIG. F.1 shown at $t = 1.0$, but with pure diffusion only, i.e., the Stokes flow solution. The visual difference with the Navier-Stokes solution (the slight deformation of the vortex cores) of FIG. F.5 is not so much apparent here, but is better illustrated by the energy spectrum below.

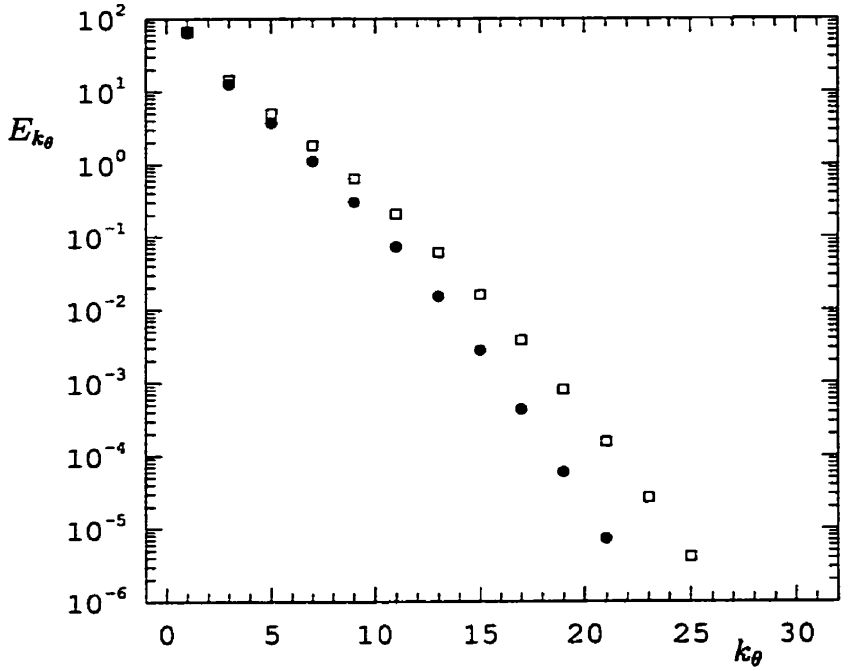

FIGURE F.8. The energy spectrum corresponding to the $t = 1.0$ solution shown in FIG. F.7 (the "•" symbols); the "□" symbols are for the initial spectrum. Both vortices diffuse independently of one another; they remain circular and the "odd symmetry" is preserved. There is thus no energy on the even modes, as opposed to FIG. F.6.

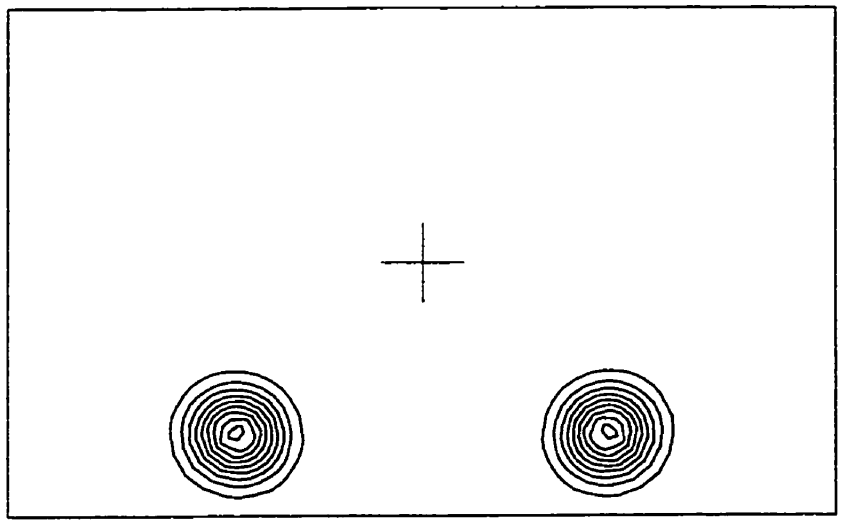

FIGURE F.9. The vortex pair of FIG. F.3 shown at $t = 1.0$, with the same iso-vorticity contours. The evolution from $t = 0.5$ to 1.0 has been done with the addition of an upward background flow ($u_y = 1$). See the corresponding energy spectrum in FIG. F.10.

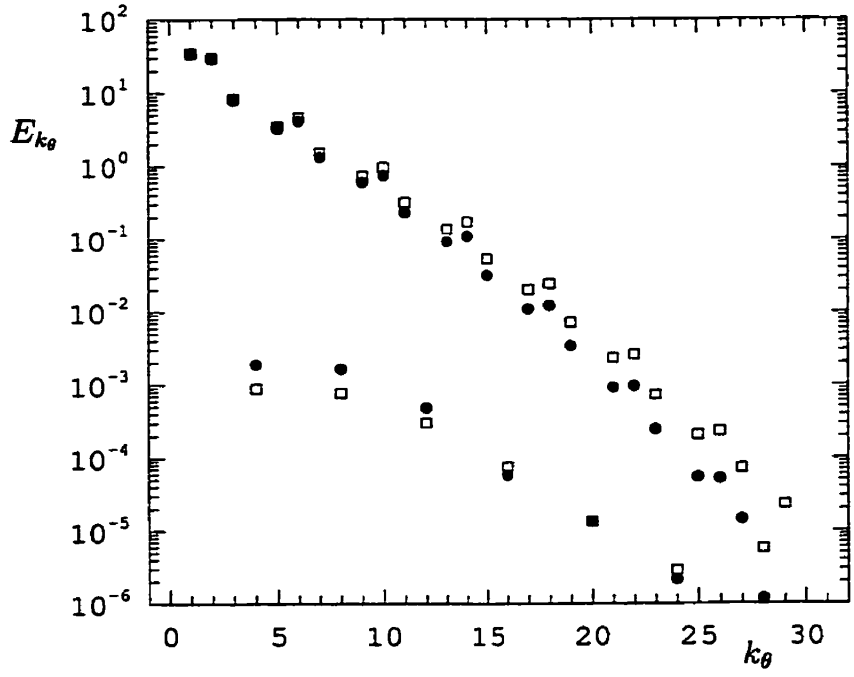

FIGURE F.10. The energy spectrum corresponding to the $t = 1.0$ solution shown in FIG. F.9 (the "•" symbols). The $t = 0.5$ spectrum of FIG. F.4 is also shown as a reference (the "□" symbols).

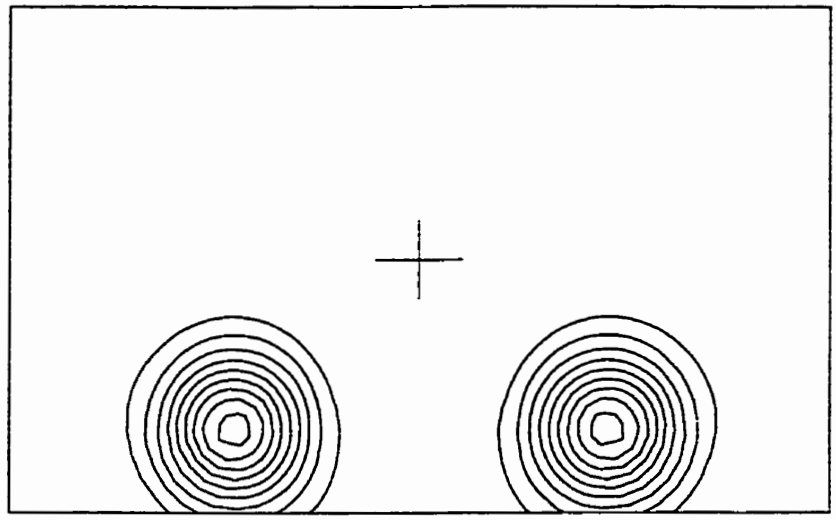

FIGURE F.11. Same as in FIG. F.3, but this time with $a = 0.2$. The iso-vorticity contours are shown for $|\omega_z|_{\max} = 50$ with increments of $\Delta\omega_z = 5$ (the zero contour is skipped). The corresponding energy spectrum is shown in FIG. F.12.

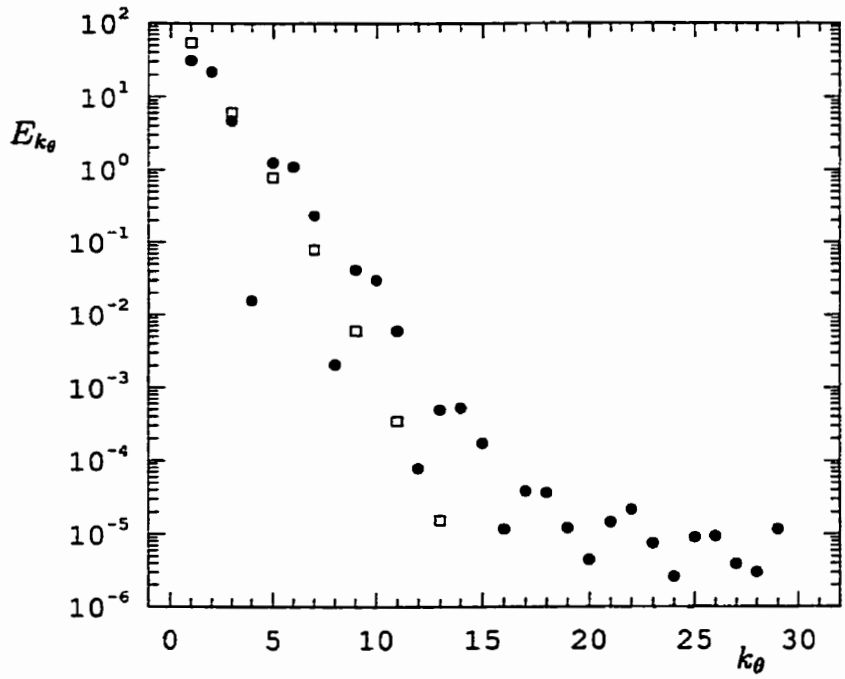

FIGURE F.12. The energy spectrum corresponding to the $t = 0.5$ solution shown in FIG. F.11 (the "•" symbols); the "□" symbols are for the initial spectrum. Compare with the equivalent $a = 0.1$ spectrum shown in FIG. F.4. The energy content of the initial spectrum falls off more rapidly in this case, but again the energy content shifts towards the higher wavenumbers as the vortices move away from the center.

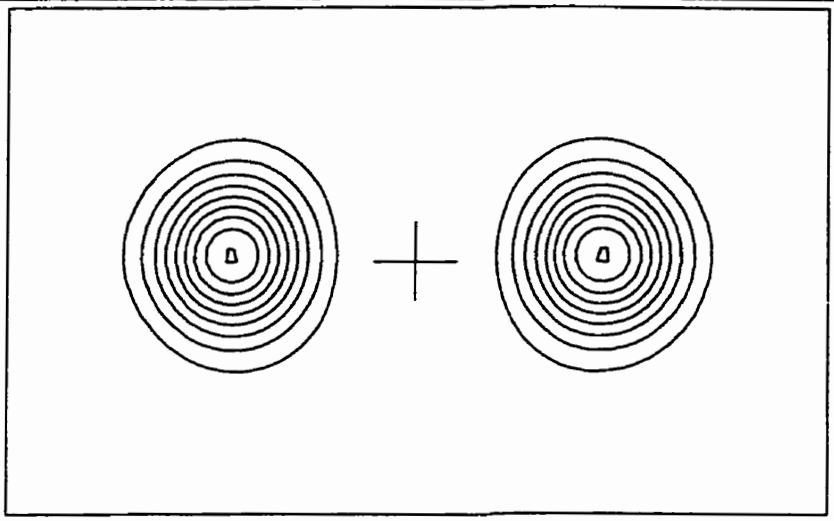

FIGURE F.13. The equivalent of the vortex pair of FIG. F.11 shown at $t = 1.0$, with the same iso-vorticity contours, and the addition of. the upward background flow $u_y = 1.0$. Because the self-induced velocity is slightly smaller than 1 in this case, the vortex pair has moved up, but not of a significant amount for this short time. See also the corresponding energy spectrum in FIG. F.14.

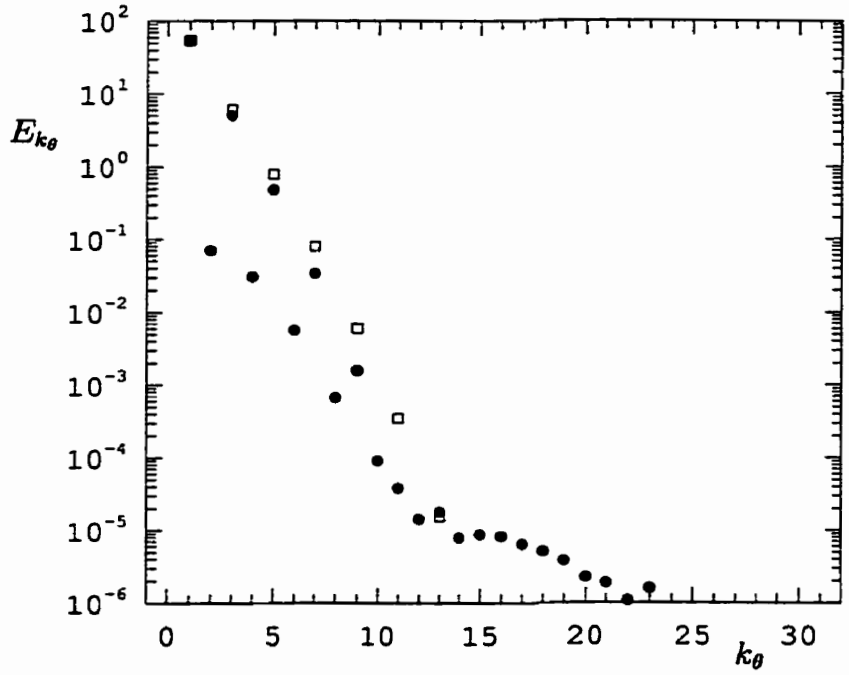

FIGURE F.14. The energy spectrum corresponding to the $t = 1.0$ solution shown in FIG. F.13 (the "•" symbols); the "□" symbols are for the initial spectrum. Diffusion is seen in the decay of the intermediate odd modes, vortex core deformation is seen in the appearance of energy on the low even modes, and the slight translation of the vortex pair is seen in the "tail" of the spectrum at higher wavenumbers ($k_\theta > 12$).